Characterization of Mixture Formation, Ignition and Combustion Processes of Ethanol-Gasoline Blends Injected by Hole-Type Nozzle for DISI Engine

(直噴火花点火機関用ホールノズルから噴射したエタノール－ガソリン混合燃料の混合気形成，点火，燃焼過程に関する研究)

by

CHEN Run

Dissertation

Submitted to the Graduate School of Engineering

University of Hiroshima

in Partial Fulfillment of the Requirements

for the Degree of

Doctor of Engineering

University of Hiroshima

September, 2014

ABSTRACT

Automobile industry is now playing more attention to the development of fuel direct injection in a spark ignition (SI) engine in order to lower fuel consumption and reduce pollutant emissions. Thanks to the development of injection, combustion and engine control system, the direct-injection spark ignition (DISI) technology has made a great progress. Spray-guided concept (namely the narrow spacing between the injector and spark plug) and the multi-hole injector are currently receiving considerable attention due to their great potential to achieve the favorable fuel consumption and engine-out emissions. However, the ever growing demands for the fossil fuel and increase of CO_2 emission in the atmosphere from automobiles make it necessary to develop alternatives of conventional fuels. Moreover, gasoline and diesel have high carbon atom and long chemical chain, which produce more carbon dioxide. Future researches may focus on the using of renewable fuel, such as ethanol which is well known as the most promising substitute of gasoline in SI engine. Therefore, it is worth providing added insight into (1) whether or not ethanol-gasoline blends can be accepted by the DISI engines, especially the spray-guided concept, and (2) how the DISI engines fed by ethanol-gasoline blends perfectly works, and (3) the mechanism/behavior of spray and combustion characteristics under DISI-like conditions using ethanol-gasoline blends.

This study focuses on the clarification of spray mixture, ignition and combustion characteristics injected by a hole-type nozzle in a constant volume vessel. The quiescent-steady conditions were set to simulate the typical thermodynamic environment of near top dead center (TDC) in DISI engines. The fuels with different ethanol blending ratios, E0 (100% gasoline), E85 (85% ethanol and 15% gasoline) and E100 (100% ethanol) were used in this study.

The mixture formation of spray, especially the different components in the E85, was quantitatively measured by a dual-wavelength ultraviolet-visible laser absorption scattering (LAS) technique which was able to simultaneously measure the liquid and vapor phase distributions. Different spray mixing characteristics of fuel composition in ethanol-gasoline blends were investigated. In addition, the non-vaporizing and vaporizing spray of E85 also were tested by using Mie scattering to clarify the spray characteristics, such as penetration length, spray angle and liquid volume, during the spray development based on the momentum theory. Furthermore, the impinging spray of different imping distance (30 and 45mm) and wall temperature (273 and 298K) were investigated by the LAS measurement to clarify the mixing process of ethanol-gasoline blends spray under cold-start condition.

Thereafter, different ignition strategies, consisting of ignition position and timing, were conducted in the combustion experiment. The range of ignition probability for ethanol-gasoline blends were clarified using the Z-type shadowgraph and the comparisons of those were made. Also, the effect of spark energy

on the flame development was studied. Moreover, the flame visualization and development, such as flame color, flame radius, ignition delay and combustion variability were qualitatively and quantitatively characterized by the high-speed imaging of OH* chemiluminescence and natural luminosity. Also, the effect of spray evaporation on the combustion performance was examined. Soot formation during the combustion was analyzed based on the natural luminosity. A further discussion of using E85 in DISI engine was conducted and compared with other previous studies. The result showed that the optimal ignition strategies proposed by this study was able to achieve the favorable combustion performance.

TABLE OF CONTENTS

iv

NOMENCLATURES

A_f	surface area of liquid droplet
AEOI	time after end of injection, (ms)
AF_{stoich}	stoichiometric air/fuel
AF_V	local stoichiometric air/fuel
ASOI	time after start of injection, (ms)
AFR	air/fuel ratio
C_a	area contraction coefficient
C_{amb}	ambient gas concentration
C_v	Velocity coefficient
C_V	Vapor concentration, (mg/cm^2)
C_d	Discharge coefficient
CCD	charge-coupled device
CI	compression ignition
CFD	calculation fluid dynamic
CH_2O	formaldehyde
CoV	coefficient of variation
CO	monoxides of carbon
CO_2	carbon dioxides
D	nozzle hole diameter, (mm)
D_{imp}	Impinge distance, (mm)
D_{aimp}	distance after impinging, (mm)
d	diameter of liquid droplet, (μm)
DISI	direct-injection spark ignition
EOI	end of injection
FWHM	full width at half-maximum
GDI	gasoline direct injection
HBP	high boiling point
HC	hydrocarbon
HCCI	homogenous charge compression ignition
I	pixel intensity
I_l	luminosity intensity

I_t	total intensity in flame
I_0	intensity of incident light
I_t	intensity of transmitted light
K	cavitation number
LAS	laser absorption scattering
LDSA	laser diffraction size analyzer
LBP	low boiling point
LDA	laser doppler anemometer
LEA	laser extinction/absorption
LHV	lower heat value, MJ/kg
LIEF	laser-induced exciplex fluorescence
LIF	laser-induced fluorescence
LIR	luminosity intensity ratio
L/D	orifice length to diameter ratio
M_{inj}	injected fuel mass, (mg)
MW	molar weight, (g/mol)
N_l	pixel number of luminous flame
N_t	pixel number of total flame
NL	natural luminosity
NO_x	oxides of nitrogen
OH	hydroxyl
P_a	ambient pressure, (MPa)
P_{inj}	injection pressure, (MPa)
P_{vap}	vapor pressure, (kPa)
PDPA	phase Doppler particle anemometer
PFI	port fuel injection
Q_{ext}	extinction efficiency
R	equivalent flame radius, (mm)
Re	Reynold number
RGB	red-green-blue
RoHR	rate of heat release, (J/deg CA)
r	radius distance from spray axis, (mm)
S	penetration length, (mm)
S_L	liquid penetration length, (mm)

S_{imp}	Spray penetration of impinging spray, (mm)
SI	spark ignition
SC-DISI	stratified-combustion direct-injection spark ignition (SC-DISI)
SG-DISI	spray-guided direct-injection spark ignition
SMD	sauter mean diameter, μm
SOIg	start of ignition, (ms)
TCP	Texaco Combustion Process
TDC	top dead center
T_w	wall temperature, (K)
t_{ASOI}	time after start of injection, (ms)
t_{AEOI}	time after end of injection, (ms)
t_d	spark charge duration, (ms)
t_{inj}	injection duration, (ms)
t_{aign}	time after start of ignition, (ms)
t_{ign}	spark timing, (ms, AEOI)
UHC	unburned hydrocarbon
UV	ultraviolet
V_L	liquid volume, (mm^3)
VCO	valve cover orifice
v_{rel}	relative velocity, (m/s)
We_g	gas phase weber number
Z	axial distance from nozzle tip, (mm)
α	spray angle
$θ_L$	liquid spray angle, (°)
$θ_w$	impinge angle
σ	surface tension, (mN/m)
$ρ_0$	air density in standard condition
$ρ_a$	ambient gas density, (kg/m^3)
$ρ_l$	liquid density, (kg/m^3)
$ρ_f$	fuel density, (kg/m^3)
Φ	equivalence ratio
$Φ_V$	vapor equivalence ratio
$Φ_L$	liquid equivalence ratio

λ	excess air ratio
λ_A	absorption wavelength, nm
λ_T	transparent wavelength, nm
ε	molar absorption coefficient
τ	ignition delay, (ms)
ν	kinematic viscosity,(mm^2/s)
ΔP	pressure drop from orifice, (Pa)

CHAPTER 1 INTRODUCTION

1.1 BACKGROUND AND MOTIVATION

1.1.1 Direct-injection Spark Ignition (DISI) Engines

The most significant engineering achievement of the 20th century in society is attributed to the automobiles. In every year, about 60 million new personal automobiles and light trucks are built and sold. Nearly all of those are powered by reciprocating-piston internal combustion (IC) engines, which mainly burns petroleum-derived hydrocarbon fuels: gasoline. Since the first gasoline engine was produced by Daimler in 1883, the great engineering advances led to the widespread adoption in society applications by the late 19th century, such as in automobiles. In early gasoline engines, the mixture formation was realized with an aid of a carburetor, which tended to a worse engine-out emissions and fuel consumption. Thereafter, the multi-port fuel injection (PFI) system was introduced into gasoline engines with the development of electrical controlling. Although PFI engines are able to ensure the equivalence ratio Φ=1.0 in chamber, which is required to the work of three-way oxidation/reduction catalysts, they still have several disadvantages. The relative low pressure fuel injector installed in the intake port can cause fuel films on the port walls, even on the intake valves leading problems during cold start (excess of fuel require to form favorable fuel vapor mixing in cylinder for robust ignition). Large-scale swirl and tumble flow induced by the intake movement can result in an intense turbulent flows in cylinder, and hence decrease cycle-to-cycle variability as a result of the distortion of flame kernel formation. In order to prevent the in-cylinder knocking, the compression ratio is limited to ~10:1. Moreover, a decrease of fuel economy at part load occurs in the consequence of the pumping (throttling) losses [1-3].

Therefore, as a greatly potential alternative to conventional PFI gasoline engines, direct-injection spark ignition (DISI) engines become more and more interests for their significant advantages of (1) volumetric efficiency, owing to the decrease of in-cylinder temperature induced by fuel direct injection, and (2) enhanced thermal efficiency because of less pumping losses during intake stroke, and (3) increased specific output at part load due to stratified mixture formation and combustion in cylinder, and (4) improved fuel economy by precisely fuel injection in transient response. All of these factors are considered as the reasons to ensure the high efficiency in DISI gasoline engines, as shown in Fig.1.1.
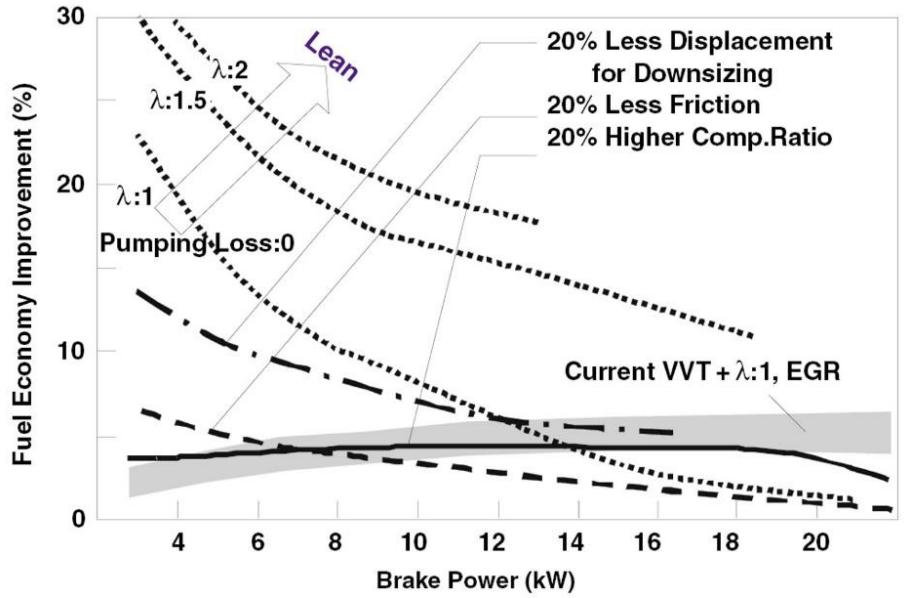
Figure 1.1 Factors of Fuel Economy Improvements
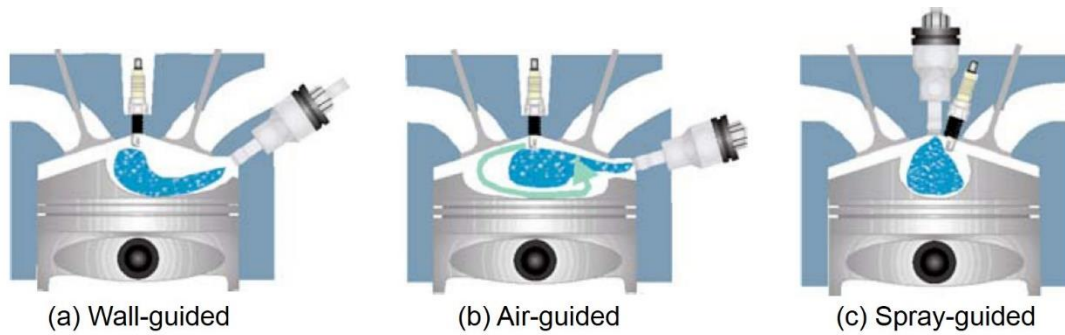
	(a) Wall-guided	(b) Air-guided	(c) Spray-guided
Fuel Economy	0	+	++
HC Emission	0	+	++
Smoke	0	+	++
Power	0	−	0 to +
Robustness	0	−	−

Figure 1.2 Characteristics of Gasoline Direct-Injection Concept

For DISI engines, one of the most crucial issues is the spray and mixture formation process. Since whether the injected fuel can be atomized and formed an ignitable mixture at the spot of spark plug during discharge time will greatly plays a significant role on the whole combustion process and engine performance. The research of in-cylinder stratified-charge combustion system started from Mid-1940 by Texaco Combustion Process (TCP) in America. Nevertheless, since the equivalence ratio is not able to be controlled so favorable that the emission could not meet to the three-way catalysts, the production of DISI engines were disturbed and far behind the practical application. Although this type of concept has proven

2

rather difficult in practice, much progress has been made within the last decade through the great advances in the fuel injector, the exhaust after-treatment and the engine control system [4]. Modern direct-injection spark ignition engines have been in production for ten years, and advanced gasoline engines are expected to remained research in vehicle application for many years to come. The DISI systems fall into three categories according to the dominant approach of the stratified-charge process: wall-guided, flow guided and spray guided [5], as shown in Fig. 1.2.

The first generation of commercial DISI engines have been designed as the wall-guided concept as shown in Fig.1.2 (a), in which the fuel is targeted at the hot piston surface and fuel-vapor mixing is forced to direct towards the spark plug. This type interaction of the fuel spray with a piston-bowl geometry and strong in-cylinder bulk flow helps to form and stabilize a suitable fuel-air distribution around the spark plug. In the case of wall-guided concept, the mixture formation during engine operation can be separated at least two aspect, depending on load and speed. First, at low/part load, fuel is introduced into the chamber at the later stages of compression stroke (late injection) to form the over-rich mixture near the spark plug (Stratified Charge). Hence, the initial flame kernel is able to be yielded successfully. While the surrounding environment is under over-lean available for the fast flame propagation and the decrease of fuel consumption. Secondly, at the high/full load, fuel is injected during the early stages of intake stroke to form the homogenous mixture in cylinder, which ensures the more power output (Homogenous Charge). Since most of automobile are worked at the low/part load, thereby lots of researches focus on the utility of stratified-charge operation in wall-guided DISI engines under that condition. Mitusbishi Co. firstly proposed a gasoline direct-injection (GDI) engine in 1996 as shown in Fig. 1.3. They suggested using a high-pressure swirl injector coupled with the curved-top piston was able to realize an unprecedented stratified-charge model (40:1) in engines. The main advantage of this concept is that the spark plug fouling problem has been resolved since the fuel directs to the piston instead of the spark plug [6]. Thereafter, Toyoda [7], Nissan [8], Volkswagen [9] and Peugeot Citroen [10] et al. presented their wall-guided DISI engines. All of those showed different types of piston shape combining with the in-cylinder movement to form the desirable fuel vapor around the spark plug, and demonstrated the potential to a decrease of fuel consumption (~50% fuel saving at low/part load compared with PFI engines). However, in this system, due to the fuel directly targeted at the piston cavity wall, a fuel film is formed on the wall inevitably, hence leading to an increase of soot and unburned hydrocarbon (UHC) emission [11-13]. Flow-guided is a fuel-air mixing way of using a strong in-cylinder airflow to force the fuel vapor to the near spark plug. To ensure the ignition occurs successfully at a thermodynamic optimum timing, the stable airflow is required to improve the mixture formation and transport this compact spray cloud to the spark plug. During the stratified operation model, however, it is difficult to maintain such a stable flow within the lean-burn

operation range, thus resulting in a high cycle-to-cycle variability. In addition, the vigorous swirl and tumble airflow in cylinder also reduce fuel economy due to increased throttling losses.
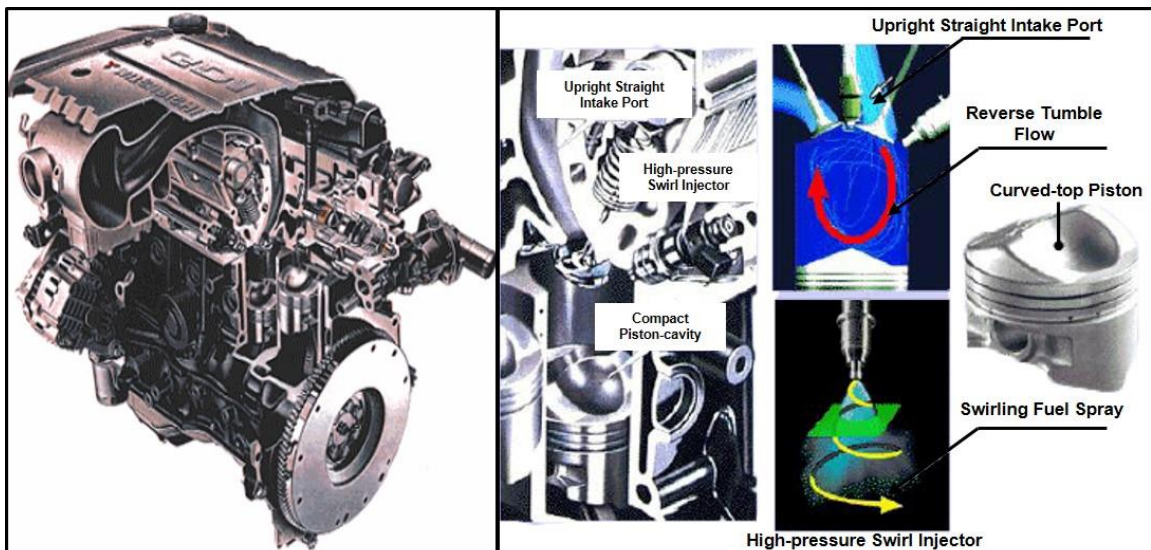
Figure 1.3 Mitusbishi Co. Gasoline Direct-injection Engine (GDI)

Both wall-guided system and flow-guided system sufficiently utility the in-cylinder airflow interacted with a special-built structure in piston crown, yet resulting in a heat loss due to the complex shape of piston crown increasing the surface area. In addition, the knock resistance decreases as a result of the sharp edges of the piston, and the compression ratio is limited in comparison to a flat piston to prevent knock at full load [14]. However, the spray-guided concept (Fig.1.2(c)) which is regarded as the next generation DISI system, shows its potential of solving the problems above in wall-guided and flow-guided engines [15]. In spray-guided direct-injection spark ignition (SG-DISI) engines, a centrally mounted injector directs the spray along the cylinder axis towards a closely spaced spark plug, whose electrodes are located carefully located at the edge of the spray. Due to the narrow injector/spark plug spacing and narrow injection/ignition timing, the fuel-vapor stratified process is greatly better than wall-guided system, hence allowing a compact fuel could at the vicinity of spark plug, and leading to a fast burn and shorten combustion duration with less cyclic variability [16]. Therefore, the lower engine-out smoke and UHC emissions can be realize and meet the strict emission regulation. Overall, SG-DISI engines have more significant advantages over the wall-guided system on fuel economy under a wider stratified-charge operating range [17-20]. BMW, Co. developed a new engine with a spray-guided concept, as shown in Fig.1.4 [21]. The pintle-type outwards opening piezo injector up to 20MPa, was centrally installed in the chamber and provide a precisely high-pressure spray. Combining a split injection strategy under the stratified-charge combustion model, it can achieve the ultra-low fuel consumption compared with the conventional stoichiometric combustion DISI engines, as expressed in Fig. 1.5 [22].

4
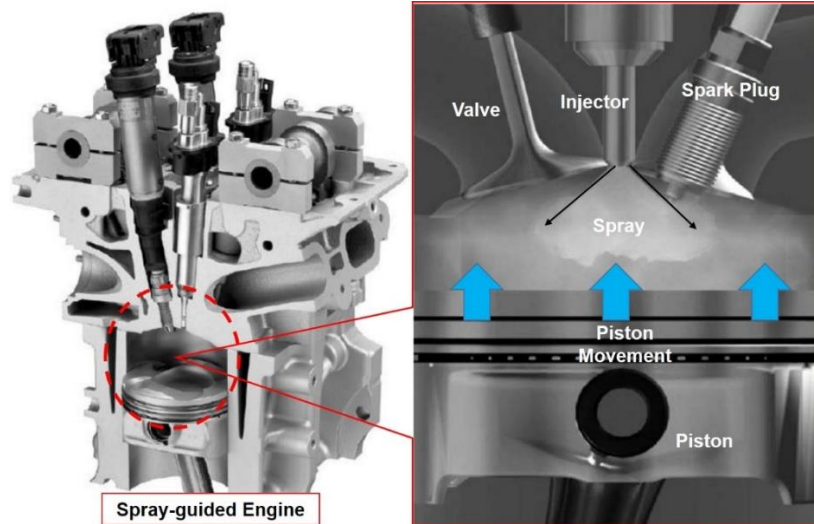
Figure 1.4 Structure Characteristics of Stratified Spray-guided DISI Engines of BMW
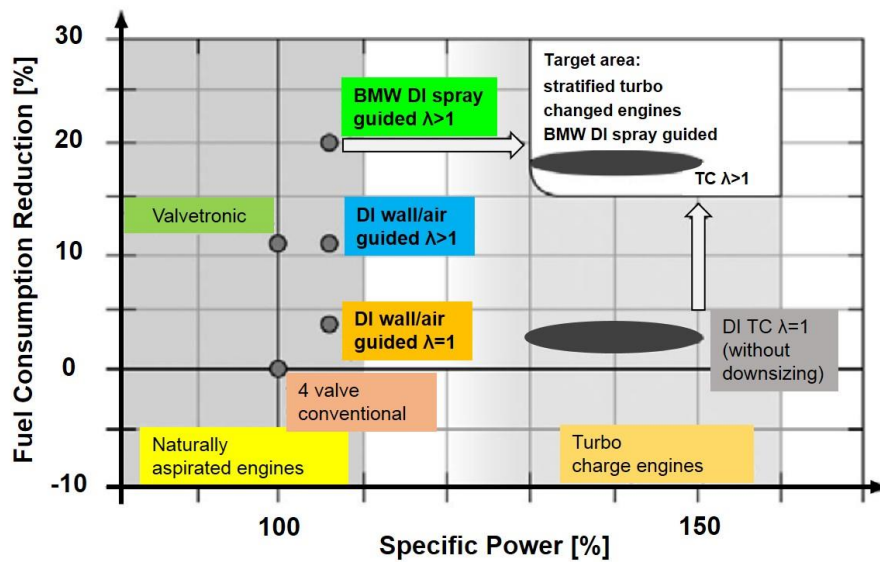
Figure 1.5 Technology Comparison for Fuel Efficiency and Specific Power

However, a potential for inferior mixing in the vicinity of the spark plug occurs as a result of the short time interval between the end of injection (EOI) and the start of ignition (SOIg) [23-25]. High spray velocity (strong velocity fluctuation), large fuel vapor fluctuation and the presence of liquid droplet fouling on the spark plug can cause a problem of ignition (e.g., partial combustion and random misfire). Large spatial gradients of velocity and fuel-air mixing ratio require a stable and repeatable spray structure and accurate spark plug arrangement. Large temporal gradients at the spark gap requires a more precise injection and ignition timing. Wetting of the spark electrodes by liquid droplet can lead to a fuel fouling on the spark plug. Therefore, it can be argued that the mixture formation and distribution in cylinder, especially at the

close proximity of the injector to spark plug, has a great effect on the flame formation and development. Moreover, characteristics of the fuel injection system also play the significant role on the spray structure and the subsequent combustion process. All of these factors will determine the success of the spray-guided stratified charge DISI engine concept as a mass-production technology for vehicle application.

1.1.2 Injectors of Direct-injection Spark Ignition Engines

Compared to the conventional diesel injection near top dead center (TDC), the direct injection of gasoline occurs either already during the induction stroke in the case of homogenous mixture formation (full load), or at late stage of compression stroke in the case of stratified charge combustion (low/part load) as described previous section. Therefore, the in-cylinder gas pressure varies significantly, thus fuel injectors should be carefully considered to produce a desired spray quality. During the evolution of DISI engines, most of researches lay emphasis on these four types of gasoline direct-injection injector: swirl injector, slit injector, outward-opening injector and multi-hole injector. The swirl injector and slit injector were mainly applied in the wall-guided DISI engines as shown in Fig.1.6.
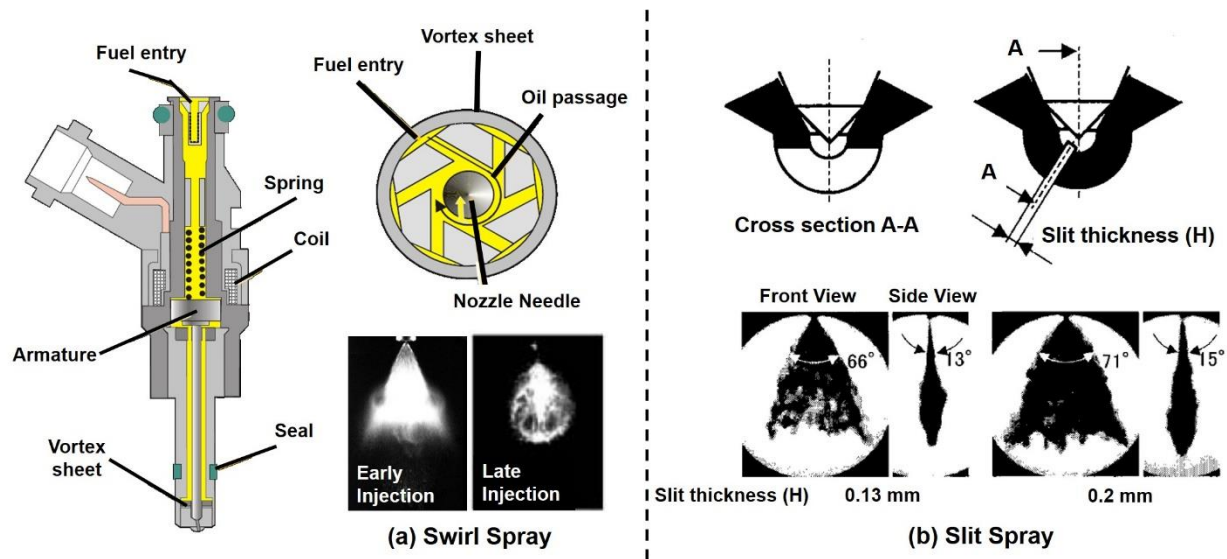
Figure 1.6 Swirl Injector and Slit Injector [26] for GDI Engines

In a high-pressure swirl injector (Fig.1.6 (a)), fuel traverses tangentially arranged swirl ports and gets a rotational motion inside the swirl chamber. After passing through the nozzle, fuel is formed a free cone-shaped liquid sheet inside the chamber. By this way, the injection pressure in swirl injector is converted to the rotational moment to promote the spray atomization and limit the spray penetration to prevent wall impingement. Therefore, the swirl injector can provide the desirable spray structure to meet the wall-guided DISI engines. However, this type injector requires the strong swirling or tumbling generated by the suction

6

port, which sometimes decreases the volumetric efficiency compared with the straight port. In order to maintain higher output performance, the improved injector, namely slit injector as shown in Fig.1.6 (b), is developed and adopted in a straight suction port. The advantage of this type injector is that (1) it can enable the spray to be guided to the near spark plug without the help of air motion，and that (2) it also provide a thin fan-shaped wide dispersion spray to ensure the fine atomization. In comparison to the swirl injector, the typical spray characteristics of break up, dispersion, sauter mean diameter (SMD) and penetration, for slit injector are enhanced and show a good practice in GDI engines [26-27]. Nevertheless, the spray structures of these two type injectors are significantly influenced by the surrounding gas pressure, in particular the spray spread of swirl injector can decrease extremely and be forced to a "collapse" shape with increasing ambient gas pressure [28-29]. Although the pressure-swirl injector is the most-used injector in the first generation of series production DISI engines, the SG-DISI engines as an effective way to realize the full benefit of direct injection and maxing fuel economy, require sprays whose general structure and spray angle are independent of backpressure.

Figure 1.7 Electric Outward-opening Pintle Injector and Spray Patten under Different Backpressure [30]

Two types of fuel injector have been developed specifically for SG-DISI gasoline engines: electric outward-opening pintle injectors and solenoid-actuated multi-hole injectors. In the system of outward-opening pintle nozzle, fuel from the high-pressure rail is introduced into the nozzle gallery and guided
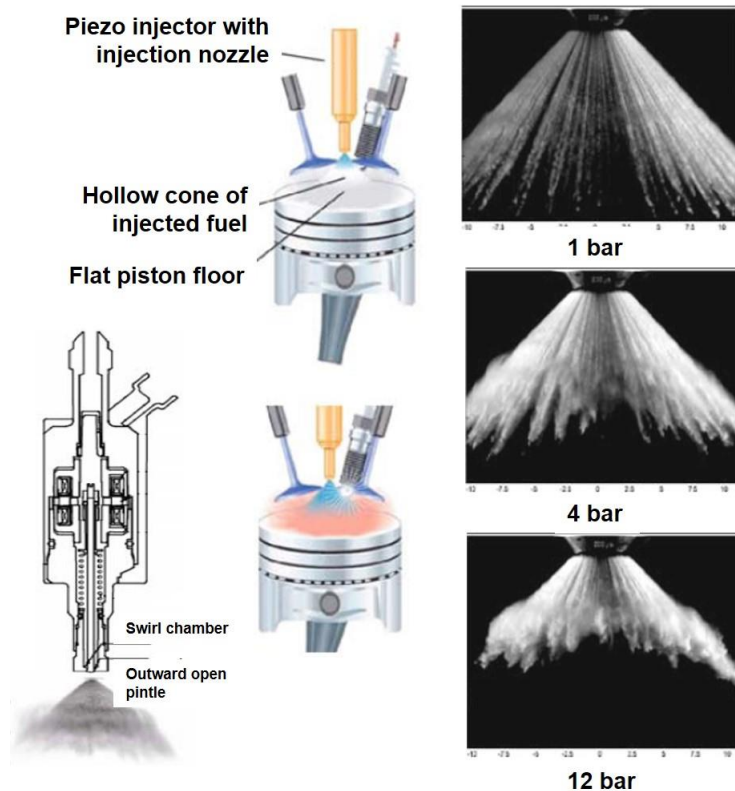
7

towards the nozzle exit through three or four flow passages. A dead volume at the nozzle exit can collect those high speed jets mixing, then in turn forming a hollow-cone spray when the fuel is injected into chamber. The penetration of this structure in engine cylinder is function of the prevailing thermodynamic conditions (pressure/density/temperature). As Fig. 1.7 shows, the "streaky" like structure of spray under nearly atmosphere conditions gradually diminishes with the increase of ambient gas pressure, leading to a more compact spray cloud with clearly edge vortices. Numerous studies have been conducted to investigate the interaction between the edge vortices creation and spark plug positioning, and found that the formed vortices can provide some flexibility in the arrangement of spark plug for both stratified and homogeneous operating condition which is the key to the success of the spray-guided concept [31-33]. Although the outward opening pintle injector generating the hollow-cone spray has an enhanced atomization because of the high area-to-volume ratio, the piezoelectric actuation of needle results in much higher cost and the significant "make value" should be carefully considered to the mass-production in the SG-DISI engine application.
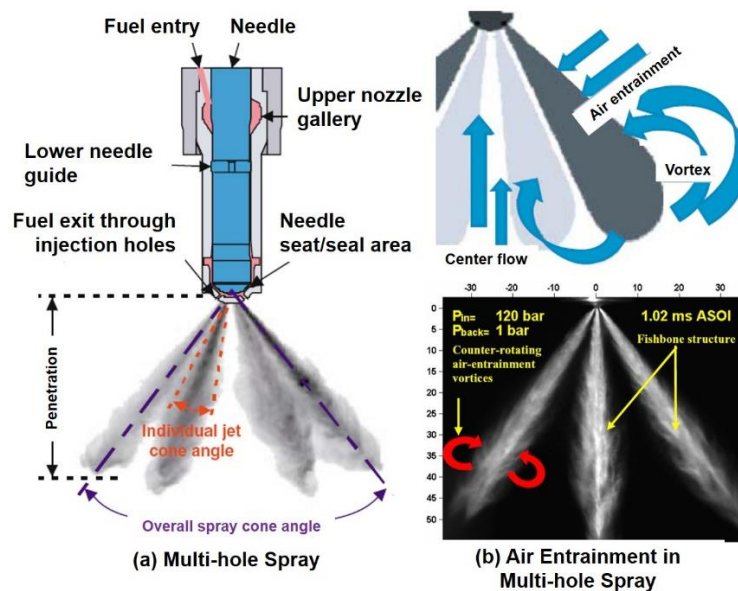
Figure 1.8 Multi-hole Spray and Its Typical Air Entrainment [32, 34]

Compared with the outward-opening pintle injector, the multi-hole injector is very familiar to the automotive industry due to its shape and structure of individual spray similar to the high-pressure diesel nozzle used in direct-injection diesel engines. The great benefits from the multi-hole injectors employed in SG-DISI engines are attributed to that (1) the spray structure and spray angle do not change with the increase of backpressure in cylinder [35-36], which is an important criterion for the realization in spray-guided concept, and (2) the enhanced geometric flexibility in the number and arrangement of the nozzle holes to acquire the desirable spray plumes at potentially much lower cost [4, 34, 37-39].

8

This type of injector produces sprays with narrow high-velocity and compact plumes as shown in Fig. 1.8 (a). The fishbone structure of multi-hole spray has been studied for many years which is similar to diesel spray, finding that it has great influenced not only by internal nozzle flow but also by air entrainment pattern. High velocity of spray can induce the downstream air vortex, thus leading the airflow re-enter into the upstream spray. In addition, because of the low pressure inside the speedy spray, other airflow can be introduced into the center of the spray. Both of these effects help the breakup process of liquid droplet faster, thus achieve the favorable spray atomization. In multi-hole injector, there are two main nozzle types: the sac hole nozzle and the valve covered orifice (VCO) nozzle, are used, see Fig.1.9. In comparison to the VCO nozzle, the mass flow through different holes does not influenced by the eccentricity or radial motion of the needle tip in sac hole nozzle, thus a satisfied symmetric overall spray can be produced. However, the sac volume should be kept as small as possible to prevent the additional fuel from entering the chamber, which tends to result in a UHC emission. The VCO nozzle can be used to solve the problem of sac hole nozzle, yet the eccentricity motion induced by needle tip should be considerably control to prevent the spray quality from deteriorating because of the fluctuated mass flow in different nozzle holes.
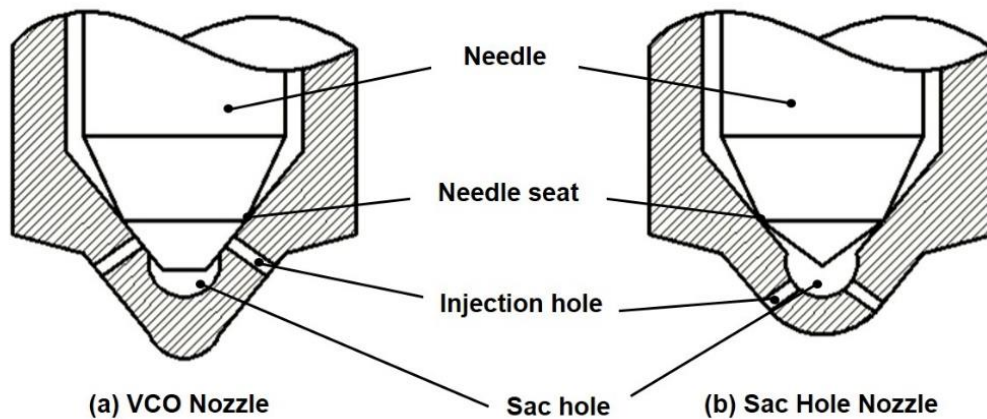
Figure 1.9 Structure of Hole-type Nozzle

Although the multi-hole injectors have lots of advantages to meet with success in DI diesel engines, at the early development of DISI engines, they tends to result in some problems. Their excess of spray penetration is accessible to cause the fuel fouling on the spark plug due to the closed proximity between the injector and spark plug. Some speedy plumes of spray from multi-hole injector can strike the ground electrode leading to a large droplets on the spark plug and the discharge distortion, thus result in a decreased ignition stability which affects the initial flame kernel formation. In addition, the compact fuel cloud near the spark plug tends to form a large fuel-air gradients which has an impact on the spark and flame propagation. In the worst case, misfire would take place if the strong fluctuation of fuel vapor mixture and

ignition present in cylinder. All of those cases above also can produce more emissions of soot, CO and UHC [40-41]. However, thanks to the emergence of the high pressure gasoline fuel injection system and advanced controlling strategies, it is possible to apply the multi-hole nozzle in SG-DISI engines again and can achieve lower hydrocarbon emissions and fuel consumption compared with the pizeo outward-opening nozzle system [42].

1.1.3 Ethanol Alternative Fuel and Its Utility in DISI Engines

In 20th century, with the great development of economy, automobiles have become more popular in all over the world and be regarded as the most important transportation method in society. Especially from 1980s, the automobile market have been growing gradually and shows a steep increase up to 850 million in the future scenario. In the new developing countries, the potential in vehicle demand remains large, where shows China is predicted to overtake the vehicles fleet of the United Sates by around 2030 (see Fig.1.10 [43]).
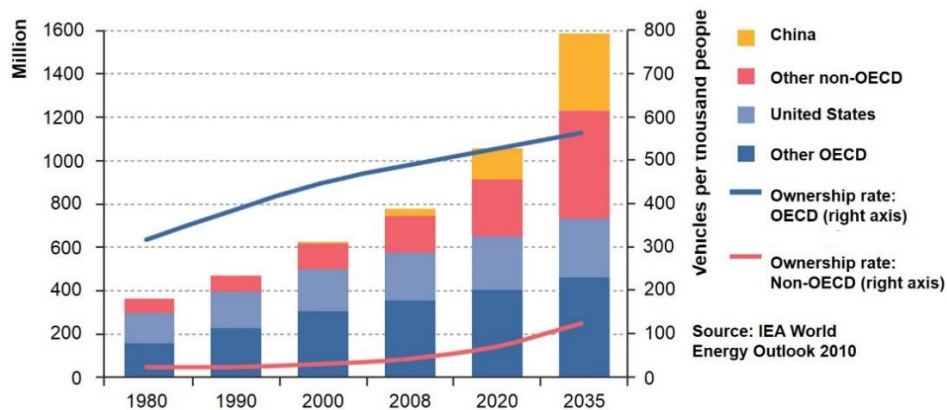
Figure 1.10 Vehicle Fleet and Ownership Rates by Region
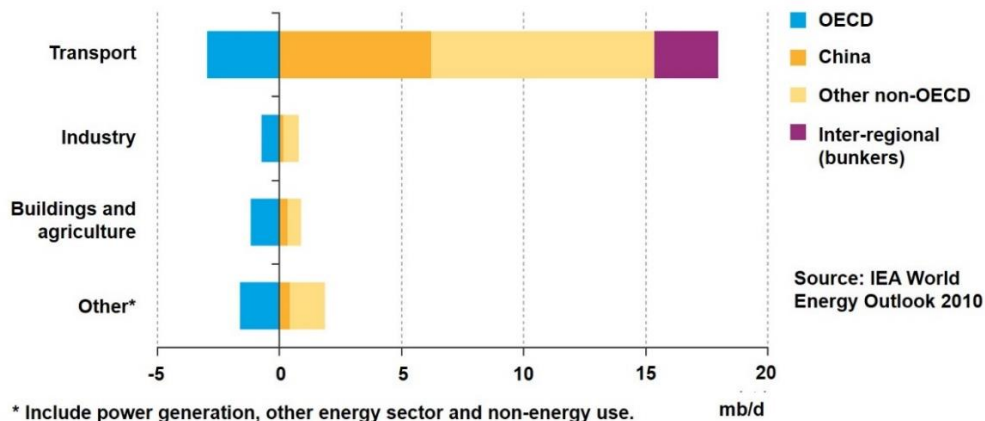
Figure 1.11 Change in Primary Oil Demand by Sector and Region (2009-2035)

10

Figure. 1.11 shows a state of change in primary oil in society sector and region. The transport is expected to continue to drive the growth in global oil demand. Within the predicted scenario (2009 to 2035), transport takes up almost all of the increase in oil demand, which suggests an aggregate expanding compared with other sectors. Road transport (passenger cars and freight trucks) will continue to dominate overall transport energy and oil use. This great growth of transport, especially in automobile, promotes the increase of crude oil production rather than discoveries from the last decade. The global oil production would reaches 96 mb/d in 2035 on the back of rising output of natural gas liquid and unconventional oil, as crude oil production range [43].
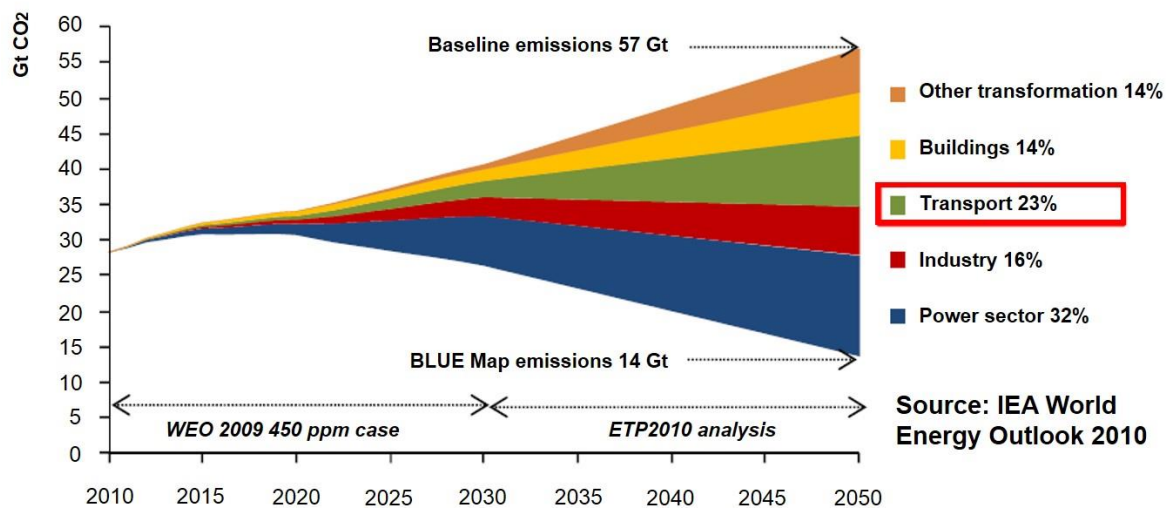
Figure 1.12 CO_2 Emissions Abatement by Region

Because a large amount of greenhouse gas, in particular for carbon dioxide (CO_2) can be produced when the oil (mainly gasoline or diesel) is burned. The transport sector accounting about 19% of global energy use and 23% of oil-fuel-burnt CO_2 emissions (see Fig. 1.12), is considered to be one of the most reasons for failing to meet the Kyoto targets. In addition, it also as a significant factor to the greenhouse effect due to the heavy, and increasing traffic level. Irrespective of some improvements made to promote energy efficiency, the transport sector is still generating increases in CO_2 emissions. While in order to decrease the greenhouse effect, both developed and emerging countries have similar tendencies in commercial vehicles and passenger cars, to enhanced CO_2 regulation whose blue-map shows a significant CO_2 abatement from >200g/km in 2004 to <100g/km in 2020, even a prospect of reducing one to three according to the base line in 2050 (see Fig. 1.13). To approach this goal, drastic political decisions could be implemented to address in region, especially in developing countries. Furthermore, the shortage of crude oil supply has an outlook of reduction and becomes a limiting factor lately.
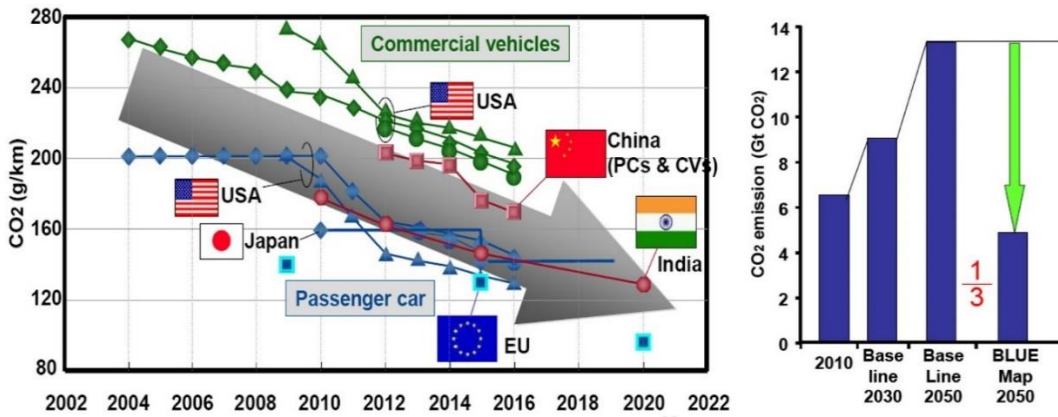
Figure 1.13 CO_2 Regulation Trends in Transport Sector
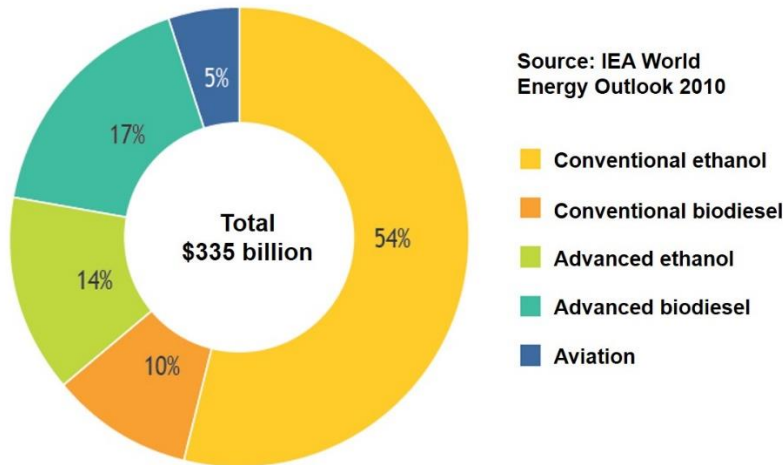
Figure 1.14 Cumulative Investment in Biofuel Production Facilities, 2010-2035 (in year-2009 dollars)

One important step in the efforts to moderate the problems above is to replace the conventional energy fuels with alternative fuels for internal combustion (IC) engines. Both of cleaner emissions and improved fuel consumption with IC engines are the significant issues taking account CO_2 exhaust regulations and limited supply of crude oil. In term of these issues, the development of new clean-burn gasoline engines, such as direct injection fueled with alternative fuels, is important due to the advantages of higher thermal efficiency as a result of direct fuel injection, and high power output over conventional engines [44-45].

Ethanol can be considered as the excellent alternatives for conventional fuels, since it can be used as a fuel extender for petroleum-derived fuels, oxygenate, an octane enhancer, and a pure fuel. Ethanol was first introduced as an automobile fuel in USA in the 1930s, yet was widely popularized only after 1970 in respond to the oil embargoes in 1973-1979. Then its application was focused on special market, mainly in Brazil, Sweden and as a gasoline additive for octane number enhancement in USA, Canada and India [46-

48]. Nowadays, in all of alternative fuels, ethanol has become a most significant surrogate as shown in Fig. 1.14 where demonstrates a large share (up to nearly 70%) of investment in biofuel production.

Table 1.1 Chemical and Physical Properties of Ethanol and Gasoline

Fuel Property	Ethanol	Gasoline
Formula	CH_3CH_2OH	C4-C12
Molecular weight (g/mol)	46.07	100-105
Carbon (mass %)	52.2	85-88
Hydrogen (mass %)	13.1	12-15
Oxygen (mass %)	34.7	2.7
Density (kg/m³) at 25°C	796	<783
Boiling point (°C)	79	27-225
Vapor pressure (kPa) at 25°C	7.3	48-103
Specific heat (KJ/kg·K)	2.4	2
Kinetic viscosity (mm²/s)	1.37	0.68
Low heating value (MJ/kg)	27	44.4
Autoigntion temperature (°C)	423	257
Flammability limitation (Vol %)	4.3/19	1.4/7.6
Stoichiometric air/fuel	9	14.7
Research octane number	92	87
Sulfur content (ppm)	0	<200

Many differences of physical properties between ethanol and gasoline are reported in Table 1.1. In particular, although the heating value of ethanol is lower than that of gasoline (~66% that of gasoline in volume basis) which adds the difficulties for the cold start [49], the amount of energy per kg of stoichiometric mixture is closed for both fuels. In addition, ethanol has a higher octane number (RON) which can shows the excellent knock resistance in high-compression-ratio combustion and higher boost in turbo-charge engines. Ethanol also has a higher vaporization heat available for making approximately three times of cooling effect at the suction stroke bigger than gasoline. This would increase volumetric efficiency mainly in naturally aspirated engines with PFI system, or in direct-injection gasoline engines and turbo-charge engines. Because ethanol can be identified as the most promising alternative for gasoline in automobile [50-52]. If using this surrogate in direct-injection gasoline engines, especially in spray-guided concept, it should be examined considerably to optimize the combustion performance that exceeds gasoline engine efficiency and take full benefits from ethanol's higher octane number and enthalpy of vaporization.

To understand the mixture formation and combustion behavior of ethanol-gasoline blends in DISI engines, some optical diagnostics measurements in constant volume vessel or cylinder must be performed so that the chemical and physical process in the combustion of ethanol-gasoline blend can be evaluated. Spray structure and in-nozzle cavitation of ethanol alternative fuels injected by multi-hole type nozzle, were examined in "bomb" and optical DISI engine by Aleiferis and Serras-Pereira et al. [53-56], finding the spray plume was induced to "collapse" shape due to the low boiling point components in blend fuels, even though the fuel was not on the flash boiling condition. In order to improve the spray atomization, over-heated ethanol in nozzle up to 90°C was needed at early injection during the intake stroke. In addition, larger liquid droplet for E85 than gasoline was observed which indicated a lower evaporation appeared in the case of the ethanol addition. However, Oh and Bae [57] demonstrated that a faster evaporation for ethanol than gasoline spray injected by a piezo actuated outward-opening injector was found by the measurement of planar laser-induced fluorescence. Furthermore, different ethanol blending ratio fuels spray using a GDI swirl injector were tested by Park [58] and Gao [59] under normal atmosphere condition. Their results reported that main spray tip penetration would decrease with increasing ethanol ratio in low ambient pressure, yet became inconspicuous when the ambient pressure increased.

For combustion characteristics of ethanol-gasoline blend, numerous researches focused on the overall performance in engine tests. Chen et al. [60-61] used a multi-hole injector in a DISI engine to study the particle matter (PM) emissions of fuel with different ethanol ratio. They reported that the PM emissions could be decreased with increasing ethanol addition under the rich mixture (λ=0.9) condition, due to the presence of oxygen in fuel molecule reducing the required intermediate species for the production of soot precursors. While in the stoichiometric condition, ethanol addition led to an increase of PM emissions because of higher mixture heterogamous resulted from its higher latten heat at the early injection during intake stroke. Combustion stability and efficiency of ethanol-gasoline blend in DISI engine were examined by Turner et al [62], in which showed the result of higher stable combustion and efficiency appearing with ethanol addition as a result of better evaporation and mixing in cylinder. NO_x emissions were reduced due to the higher enthalpy of vaporization lowing the combustion temperature, which was similar to the result carried out by Wallner and Miers [50]. In addition, the hydrocarbon emissions also could be decreased with the increase of ethanol blending [63].

Although lots of researches have offered valuable information on the spray and combustion of ethanol-gasoline blend, there are still less knowledge on mixture formation, flame chemiluminescence and development of that blends in DISI condition. Few works have been carried out in evaporations of different component as gasoline is blend with ethanol. In a PFI engine, a clearly difference of spatial distributions of high and low boiling point fractions was found [64]. When fuel was injected into a direct-injection engine,

14

the distributions of different components in blends were able to be neglected under the normal operating temperature [65]. Moreover, literature from Andersson et al [66-67] was found to use gasoline-like and ethanol-based fuels in hollow-cone spray to confirm evaporation processes of different component in ethanol-gasoline blends. They successfully distinguished the vapor and liquid phase of different fuel compositions by means of Mie/LIF simultaneously imaging and revealed that the heavy components in blend still remain in fuels with increasing ambient temperature up to 473K. They also pointed out that the evaporation is not fast enough to generate an equal distribution of different fuel compositions. However, due to the Mie/LIF technique's limitations of the mechanism difference between Mie scattering and LIF signal which can produce errors in dense spray area and be influenced by surrounding gas, it is difficult to understand the evaporation of different components at early injection. For combustion, also few studies have been found to focus on the visual characteristics of ethanol-base compared with gasoline. An opaque appearance of E85 flame compared with gasoline was proposed and possibly attributed to the different carbon chain length in fuel content [55]. Recently, optical characteristics of spray and combustion in a two-wheel small GDI engine has been examined by Sementa and Catapano [68-69]. They suggested that different combustion behaviors of bio-ethanol occurred in stratified and homogenous operating conditions. Moreover, it pointed out the need of a careful optimization on engine controlling and fuel injection due to the ethanol was especially sensitive to the in-cylinder thermodynamic environment and fuel injection timing. However, the ignition process and the correction of flame chemiluminescence and soot formation using ethanol-based fuels are still not so clear. Therefore, in order to exploit the ethanol's properties in DISI engine and develop its full benefits, it is necessary to provide a deeper insight into the spray and combustion using ethanol-gasoline blends.

1.2 OBJECTIVE AND APPROACHES

This work focuses on the fundamental investigations on the spray evaporation and combustion characteristics of ethanol-gasoline blends, consisting of E0 (100% gasoline), E85 (85% ethanol and 15% gasoline) and E100 (100% ethanol), injected by a hole-type nozzle in a quiescent constant volume vessel under DISI-like conditions. Main objectives were concentrated on the following aspects.

(1) Mixing process and vapor distribution of ethanol-gasoline blends, especially the different components in E85 spray, were quantitatively analyzed. Map of blending ratio distribution in E85 mixture was clarified to provide clear evolution of mixture formation process for E85 with time escape. Also, the evolution of E85 free spray was evaluated based on the spray-momentum theory.

(2) Fuel-mixture formation of spray impingement under cold/ultra-cold start condition was tested.

(3) Ignition robustness when increasing ethanol ratio in gasoline were examined. In addition, effect of local mixture on the ignition, and the interaction of spray and spark charge also were investigated.

(4) Different ignition strategies, which included ignition position and timing, were conducted in fuels with different ratio of ethanol. Combustion characteristics also were analyzed to confirm the flame development.

(5) Flame visualization and soot luminosity were studied. The correlation of chemiluminescence and soot formation was investigated.

The laser absorption scattering (LAS) technique was applied to investigate the liquid and vapor phase distributions of different fuels. Surrogate fuels were used to simulate the real gasoline, ethanol and its blends in LAS experiments. Based on the theory of light extinction, the evaporation process of different components in blended fuel can be recorded and analyzed quantitatively. Mie scattering was used to study the effect of ambient gas density and temperature on the spray characteristics, such as penetration and spray angle. High-speed shadowgraph was implemented to identify the ignition robustness and the interaction of spray with spark discharge. Combustion behaviors were examined by the simultaneously imaging of natural luminosity and OH* chemiluminescence. The soot formation also was clarified by the means of natural luminosity.

1.3 OUTLINES

The outlines of this dissertation are shown as following. Firstly, a review of the previous studies on the development of DISI engines, ethanol alternative fuels, optical diagnostics of spray and combustion for gasoline and ethanol, as well as its related simulation was introduced in Chapter 1. The experimental setup and corresponding theory description of measured approaches were introduced in Chapter 2. Chapter 3 investigated the spray evolution of E85 spray by Mie scattering and the corrected empirical equation of spray tip penetration was proposed. Chapter 4 showed the results of free spray and impinged spray about mixture formation for fuels with different ethanol. The vapor and liquid phase distributions were distinguished respectively by the measurement of LAS technique. The blending ratio distribution of E85 spray was proposed and analyzed. In Chapter 5, ignition process was evaluated by high-speed visualization of shadowgraph and OH* chemiluminescence. The combustion characteristics of different ethanol blends were measured in Chapter 6. Also, the effect of spray evaporation on combustion characteristics was discussed. Finally, the general conclusions of the spray mixture formation and its effect on the combustion behavior, as well as the impact of ignition strategy on the burning performance were summarized in Chapter 7. The future prospect also was proposed in this section.

1.4 STUDIES REVIEW

1.4.1 Spray Mixture Formation in DISI Engines

1.4.1.1 Free Spray

In internal combustion engines, the characterization of the diesel and gasoline sprays have a great effect on the evaluation of mixture formation to improve combustion efficiency. The spray structure formed by various DISI injectors are quite different with each other. However, they can be generally categorized in two kinds of spray structures: full-cone sprays and hollow-cone sprays. Hollow-cone sprays are mainly formed by swirl injector and outwardly opening injector. While full-cone spray is generated by hole-type nozzle. Researches of spray injected by hole-type nozzles were greatly investigated in diesel engines since the spray mixture formation plays a most significant role on the diesel combustion before the direct-injection concept being proposed in DISI gasoline engines. The simple theory of spray break-up mechanism and classic descriptions of spray parameter for full-cone sprays are reviewed in the following.
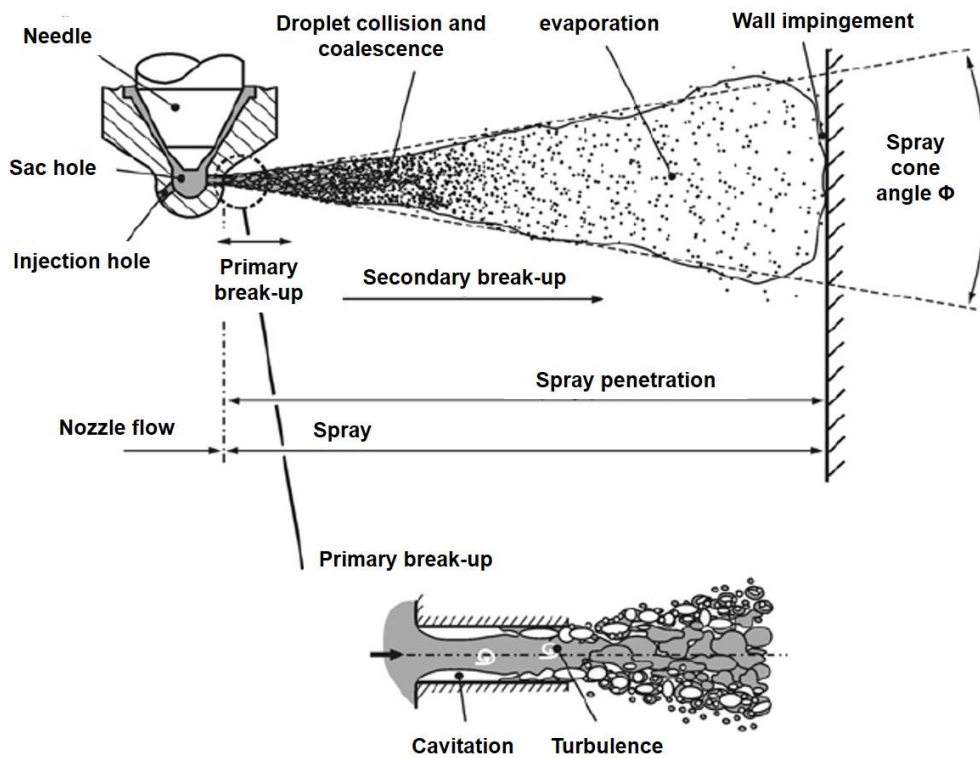
Figure 1.15 Typical Schematic of Spray Structure from Full-cone Spray

A typically schematic descriptions of the full-cone sprays injected from the hole-type injector is presented by Baumgartenin in Fig.1.15 [70]. It is believe that the disintegration process of the liquid core region appears even before the spray comes out of the nozzle hole due to the turbulence and cavitation. This process occurs at the early stage of spray development which is called as primary break-up. During this

17

period, the turbulent-induced disintegration is considered as one of the most dominant factor on the liquid break-up. For the liquid fuel, the increasing turbulent eddy inside the nozzle would be able to overcome the surface tension of droplet, then leading to an initial disintegration into ligaments [71]. The cavitation occurs since the abrupt acceleration of the liquid flow inside the nozzle results in a greatly decreasing of local pressure. Thus, the bubbles can be produced when the local pressure is lower than the vapor pressure. Geometry of nozzle hole, especially in the curvature of the joint of sac hole and hole inlet, and the movement of needle (open/close) have an effect on the increase of cavitation. Previous works [72-74] have been conducted and suggested the cavitating flow could result in an increase of spray angle and decrease of spray tip penetration. The implosion of those cavitation bubbles inside the nozzle holes can enhance the following disintegration of spray due to the increase of turbulent level. The flow cross section area inside the nozzle hole, however, is reduced because of the cavitation locating near the wall field especially in high-pressure injection condition, hence tends to the unstable flow in subsequent spray. Consequently, the level of cavitation in nozzle hole should be carefully considered and controlled in an acceptable range. A range of cavitation number which can be used to describe the extent of cavitation, have been quoted in some literature relating to diesel injectors for a variety of nozzle-hole geometries and injection parameters. However, the most well-known definition of a dimensionless characteristics number, namely cavitation number K, is shown as follows [75]:

$$K = \frac{P_{inj} - P_a}{P_a - P_{vap}} \qquad (1.1)$$

Where P_{inj} is the injection pressure, P_a is the ambient gas pressure, and P_{vap} is the vapor pressure. This factor is not so strictly correct from a fluid dynamics perspective but makes comparisons with data from different experimental arrangements simple. The non-cavitation flow can occurs unless the K value is lower than the critical cavitation number K_{cr}, which is dependent on the pressure drop and the orifice geometry.

Downstream disintegration process of liquid fuel is defined as secondary break-up, which is significantly governed by the counteraction of aerodynamic force (friction and pressure) and liquid surface tension. The whole liquid droplet can be kept in its shape because of the surface tension. While the aerodynamic force is generated by the relative velocity interaction in liquid/gas surface, hence induces a growth of instable wave on that surface. As a result, the liquid ligaments broken up in the primary stage, would further disintegrate into smaller droplets. Those droplets can be more easily led to deformation and disintegration owing to the great interaction of surface tension force and critical relative velocity. The gas phase Weber number We_g is used to describe the secondary break-up process, which is defined as the ratio of the aerodynamic force and surface tension force:

$$We_g = \frac{\rho_a \cdot v^2_{rel} \cdot d}{\sigma} \qquad (1.2)$$

Where ρ_a is the ambient gas density, v_{rel} is the relative velocity of liquid and gas phase, and d is the liquid droplet's diameter, σ is the surface tension of liquid fuel. In general, the break-up level and length are improved with increasing the jet velocity. Reitz and Bracco [76] concluded that the with the increase of jet velocity, the spray process can be distinguished into four regimes, namely Rayeigh break-up regime, first and second wind-induced regime, and the atomization regime.

During the secondary break-up, the more and more liquid droplets are formed and move towards downstream of the spray. The droplets at spray front also lost their momentum gradually, then the following droplets with higher momentum probably purse the precedent ones and push them forward. Therefore, the spray propagates continuously downwards, and the large ambient gas vortex is induced re-entrain to the spray plumes which further enhances the spray atomization. However, the droplet collide with each other can produce the droplet coalescence effect and result in a formation of larger droplet. The liquid fuel at the downstream spray is mainly influenced by the ambient gas conditions, such as pressure, temperature and density. When the ambient temperature increases over the room temperature, the liquid droplet set out to vaporize. In the well-used DISI engines of the wall-guided concept, when the gasoline is lately injected into the chamber to form the stratified mixture, it is inevitable that a fraction of fuel would impinge on the piston crown and probably form a fuel film on that wall. This would cause an inferior UHC and soot emission as describe in section 1.1. Therefore, the interaction of liquid droplet and piston wall needs to be investigated to reduce the impact of the spray impingement.

With the great progress on the optical diagnostic technique, it is possible to study the spray break-up and evolution more intuitively by the state-of-the-art high-speed imaging. The macroscopic characteristics of spray, such as spray morphology, droplet's size distribution and equivalence ratio distribution have been studied aggressively, and numerous semi-empirical equations and theories also have been summarized.

The spray tip penetration of diesel spray was examined by Hiroyasu et.al [77] by using high-speed films. They separated the spray evolution into two aspects. First, the penetration length is proportion to the time as the liquid core region moves without break-up. Second, during the spray evolution, the momentum of liquid droplet is influenced by the surrounding gas in the result of the slower droplets at the tip region. The equations which describe these two regimes can be summarized as follows.

$$S = 0.39 \cdot \left(\frac{2\Delta P}{\rho_f}\right)^{0.5} \cdot t \qquad (t < t_{break}) \qquad (1.3)$$

$$S = 2.95 \cdot \left(\frac{\Delta P}{\rho_a}\right)^{0.25} \cdot (D \cdot t)^{0.5} \qquad (t > t_{break}) \tag{1.4}$$

$$t_{break} = \frac{28.65 \cdot \rho_f \cdot D}{(\rho_a \cdot \Delta P)^{0.5}} \tag{1.5}$$

Where ΔP is the pressure drop at the nozzle exit in [Pa], ρ_f is the liquid density in [kg/m³], D is the nozzle hole diameter in [m]. The influence of the ambient gas temperature T_a (K) was took into account and pointed out that the increasing ambient gas temperature can reduce the length of spray penetration. The improved equation is shown below as:

$$S = 3.07 \cdot \left(\frac{\Delta P}{\rho_a}\right)^{0.25} \cdot (D \cdot t)^{0.5} \cdot \left(\frac{294}{T}\right)^{0.25} \tag{1.6}$$

In 1957, Wakuri et al [78] proposed the three hypothesis of (1) radially uniform velocity and fuel concentration of spray, and (2) no velocity slip between the liquid and gas phase at any cross section, and (3) the same total mass and momentum fluxes at any cross section. Based on this theory, the modified equation of spray penetration which took the cavitation into account, was presented in Eq. (1.7).

$$S = \left(\frac{2C_a \cdot \Delta P}{\rho_a}\right)^{0.25} \cdot \left(\frac{D \cdot t}{\tan(\alpha/2)}\right)^{0.5} \tag{1.7}$$

Recently, Narber and Siebers et al. [79-80] developed the scaling law of non-evaporating spray based on the idealized, isothermal, incompressible "model" jet suggested by Wakuri et al. as shown in Fig. 1.16. The dimensional forms of the spray tip penetration can be described as follows:

in near field: $\quad S = C_v \cdot \sqrt{\dfrac{2(P_{inj} - P_a)}{\rho_f}} \cdot t \tag{1.8}$

in far field: $\quad S = \sqrt{\dfrac{C_v \cdot \sqrt{2C_a}}{\tan(\alpha/2)}} \cdot \sqrt{\sqrt{\dfrac{P_{inj} - P_a}{\rho_a}} \cdot D \cdot t} \tag{1.9}$
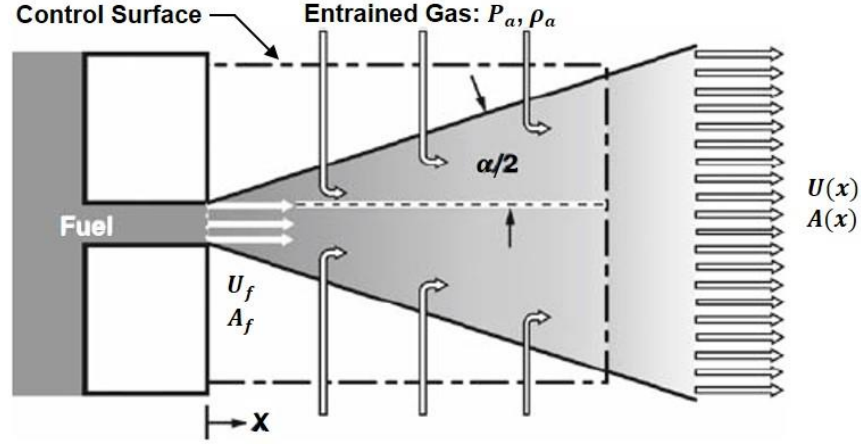
Figure 1.16 Schematic of the Idealized Model Fuel Jet

The transition position S_r from the near field to the far field, is related to the place where the dominant factor transfers from the injected fuel to the ambient gas. And it can be shown in:

$$S_r = \frac{\sqrt{C_a} \cdot D}{\tan(\alpha/2)} \cdot \sqrt{\frac{\rho_l}{\rho_a}} \tag{1.10}$$

It seems to be similar to the equations (1.3 to 1.5) proposed by Hiroyasu et al., however, the coefficient is focused on the internal nozzle flow where the C_v is the velocity coefficient accounting for the effects of factors such as friction loss and cavitation on the flow velocity through the orifice. While the C_d, which is the ratio of the mass flow rate injected in the cylinder to the theoretical mass flow rate computed from the Bernoulli equation can be calculated by:

$$C_d = C_a \cdot C_v \tag{1.11}$$

Beside the spray tip penetration, the sature mean diameter (SMD) is usually used to quantitatively characterize the droplet size. It is defined as the diameter of a "modeled droplet whose volume-surface area ratio equals the ratio of the volume of all the droplets in the spray to the surface area of all the droplets. The definition of SMD is described as follow.

$$\text{SMD} = \frac{\sum_{i=1}^{n} d_i^3}{\sum_{i=1}^{n} d_i^2} \tag{1.12}$$

The semi-empirical equation of SMD also was presented by Hiroyasu et al as below.

$$\frac{\text{SMD}}{D} = 0.38 \cdot Re^{0.25} \cdot We_l^{-0.32} \cdot \left(\frac{\mu_l}{\mu_a}\right)^{0.37} \cdot \left(\frac{\rho_l}{\rho_a}\right)^{-0.47} \tag{1.13}$$

SMD is in [m] and μ is dynamic viscosity in [N•s/m^2]. Reynold number Re is a dimensionless number which characterizes the effects of viscosity. When the ambient density is increased, the result of SMD also becomes larger due to the higher droplet's collision. Based on this equation, it can be seem that the spray atomization can be significantly improved in terms of increasing injection pressure and reducing size of nozzle hole. It should be noticed that the statistical result of SMD is able to give an overall imaging of the droplet distribution and excellently evaluate the spray atomization of different fuels.

Another significant factor is the local fuel/air mixture ratio, which is more meaningful used in the real application. Wakuri et al presented a classic semi-equation to predict the equivalence ratio at a certain cross section of a "modeled" steady diesel spray with infinite long injection duration according to the ratio of mass flow rate of fuel and gas. L_{th} is the stoichiometric air/fuel ratio. And the local equivalence ratio decreases with the increase of distance from nozzle tip linearly.

$$\emptyset_{inst} = \frac{L_{th}\sqrt{C_a}}{2\tan(\alpha/2)} \cdot \sqrt{\frac{\rho_l \cdot D}{\rho_a \cdot x}} \qquad\qquad (1.14)$$

In the case of a swirl injector, a cylindrical and strongly rotating liquid film emerges from the nozzle as an annular sheet which spreads radially outward to form an initially hollow-cone spray as shown in Fig.1.17 [70, 81]. Pressure energy is effectively transformed into the rotational momentum, which leads to enhance the atomization. The primary break-up is similar to the full-cone spray, yet the spray angle α is decreased due to the conversation of mass when the fuel is departed from the nozzle. The initial spray angle range between 25°~150° and SMD varies from 14~23μm. It produces a spray with a narrower distribution of droplet sizes (DV90~DV10) than one obtained from a standard hole-type nozzle [82-85]. The sac spray which induced by the less rotational motion, leaves the nozzle with nearly zero swirl and penetrates away from the nozzle tip for about 50 mm in less than 20ms. The air inside the spray is enhanced and accelerated in the axial direction because of the momentum transfer between liquid droplets and gas. Therefore, a low static pressure region is formed inside the hollow cone, hence leading to a secondary airflow development which transports gas from outside the spray into its center. Whereas, a decrease of spray angle β with increasing distance from the nozzle, is attributed to the reduced velocity component of droplet induced by the secondary gas flow. Hence, a bell-shaped spray is formed with decreased spray width b and increased spray penetration.
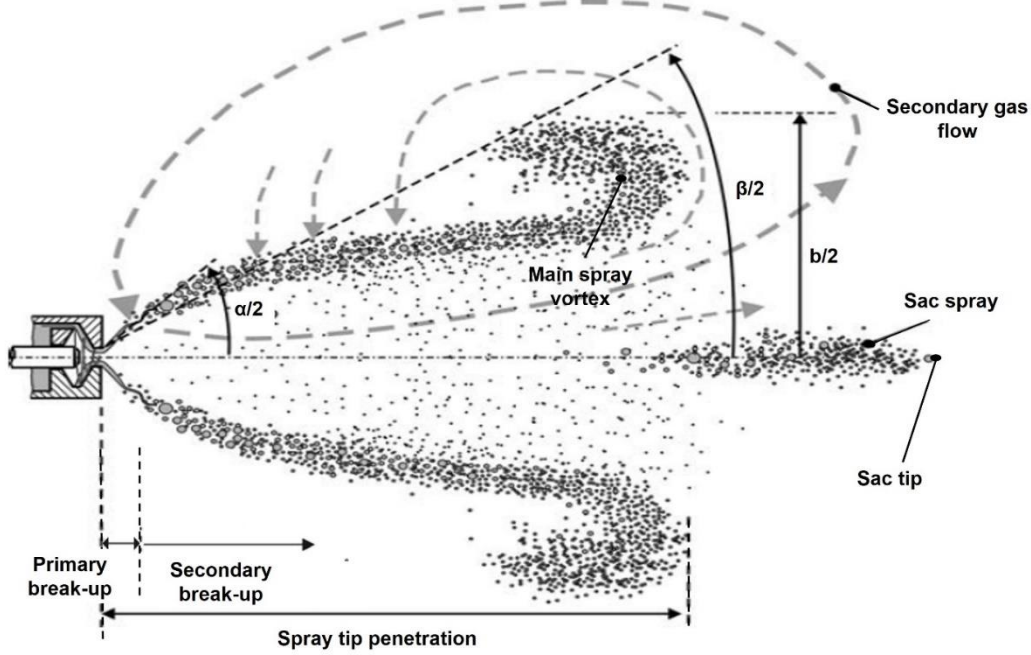
Figure 1.17 Schematic of Spray Structure for Pressure-swirl Injector

Although few studies relative to describing the significant spray parameters have been found in contrast to the full-cone spray, the size of liquid droplet was focused in published literature [86-89] in which showed first, that the SMD increased with elevated ambient density, and second, that the SMD decreased with the increase of injection pressure. The most-used semi-empirical relation of SMD in the pressure-swirl atomizer also was proposed by Lefebvre [90] and can be expressed in:

$$SMD = 2.25 \cdot \sigma^{0.25} \cdot \mu_l^{0.25} \cdot \dot{m}_l^{0.25} \cdot \Delta P^{-0.5} \cdot \rho_g^{-0.25} \tag{1.14}$$

The above equation could be used for other swirl nozzle with special design as long as amending the exponents of the dimension parameters. If taking account of the effect of spray angle, a modified equation can be expressed as:

$$SMD = 4.52 \cdot \left[\frac{\sigma \mu_l^2}{\rho_g \Delta P^2}\right]^{0.25} \cdot \left(hcos\frac{\alpha}{2}\right)^2 + 0.39 \cdot \left[\frac{\sigma \dot{\mu}_l^2}{\rho_g \Delta P}\right]^{0.25} \cdot \left(hcos\frac{\alpha}{2}\right)^{0.75} \tag{1.15}$$

$$h = 2.7 \cdot \left[\frac{D\dot{m}_l \mu_l}{\rho_l \Delta P_l}\right]^{0.25} \tag{1.16}$$

where α is the spray angle, and D is the diameter of nozzle hole. More detail respect to the SMD calculation of pressure-swirl injector was given in [90]. Although the swirl injector has a better atomization with smaller droplet size, its spray structure with temporal development is strongly influenced by the boundary

23

conditions, especially by the ambient gas density. Gindele et al [91] suggested that the increase of gas density was able to reduce the spray tip penetration in the case of lower injection pressure, but not changed in the higher or moderate injection pressure. However, the results of Homberg et al [92] revealed that the spray tip penetration length did greatly reduce in the higher backpressure (1MPa~3MPa), even was forced to collapse into a full-cone-like spray as the ambient gas pressure was sufficiently high. This behavior is regarded as the grate disadvantage to be applied in the new generation of DISI engines as discussed in section 1.1.2.

The spray structure formed by the outward-opening injector is another kind of hollow-cone spray. Spray break-up process of this injector also is similar to that of swirl injector. However, the fuel liquid injected from the nozzle directly forms a free cone-shaped liquid sheet without the pre-spray of liquid fuel (sac spray) since the outward-opening injector does not need any rotation motion inside the nozzle hole. Hence no such accelerated gas occurs inside the hollow-cone spray in contrast to the swirl injector, thereby the level of secondary flow is decreased which helps the spray of outward-opening injector keep its spray shape without the collapse. Similarly to the swirl injector, few studies were found to report the detail spray parameters of this kind injector. However, numerous works have been carried out to develop the valuable mathematic models to predict the evolution of hollow-cone spray, which could help to improve the calculation fluid dynamic (CFD) model and the design of fuel injection system in GDI engines. More detail about the simulation model can be found in elsewhere [93-99].

1.4.1.2 Wall-impinging Spray

Whether the swirl injector used in GDI engines or hole-type nozzle and outwardly opening nozzle applied in SG-DISI engines, the spray-wall interaction plays a pivotal role on the engine performance and emission. For the wall-controlled stratified GDI engines, the spray is targeted directly towards the piston wall which is inevitable to cause a sever fuel film formation. While for the SG-DISI engines, the spray penetration is more sustainable propagation by hole-type nozzle or outwardly opening nozzle, and the injection usually takes place at the later stage of compression stroke under stratified operating. Therefore, fuel film is accessible to be generated because of the rebound of droplets. If using the alternative fuels, such as ethanol, the spray impingement may become more sever due to a larger injected fuel mass needed to maintain the same stoichiometric condition to the use of gasoline. The formation of fuel film on the piston can result in a region where the fuel-air mixture is too rich for combustion, hence leading to a high hydrocarbon and soot emissions. Consequently, numerous researches on the spray–wall impingement have been performed by the experimental and numerical methods.
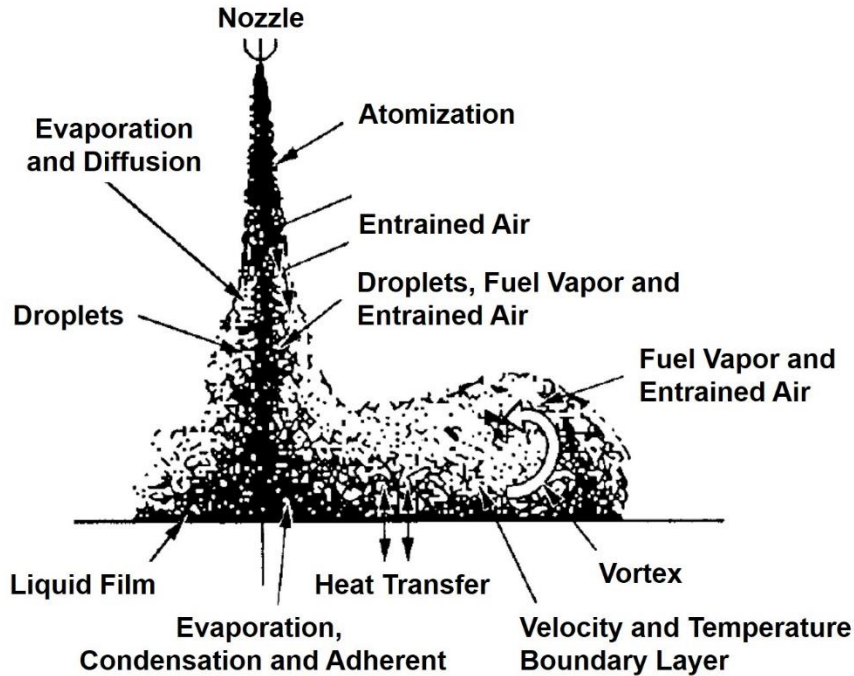
24

Figure 1.18 Model of Evaporating Spray Impingement

Senda et al. [100-102] proposed two ways of modeling spray impingement in which divided the fuel impact into two cases based on the wall temperature and impact energy as shown in Fig. 1.18. It is observed that in an evaporating spray, after impinging on the wall the fuel droplets with momentum move radially along the wall. At the center of impinge wall, fuel evaporation, condensation and liquid adherent are co-corporation due to the difference between spray and wall which leads to an interaction of heat transfer between the droplet and wall surface. While the fuel vapor and a fraction of droplet are induced to form a vortex near the spray tip due to the effects of both air entrainment and the resistance of ambient gas. One of impinge transition value according to the temperature criterion was the liquid boiling point (critical temperature). By this method, different impinged regimes could be distinguished coupling with the break-up parameter of weber number. Another impinge transition is based on the impact energy which used the weber number (We = 300) as the limit between the cases. Bai and Gosman [103] also developed a spray-wall model based on various experimental results using diesel and water droplet. They took the dry and the wet wall into account and divided the impingement into 10 regimes by different conditions of impinging droplet as shown in Fig.1.19. While Lindgren and Denbratt [104] investigated the prediction capability of spray-wall impinge models, such as the Watkins model [105], the Gosman model [103], and the Senda model [100-102]. They found that those models based on the impingement theory of single droplet are insufficient to evaluate the spray-wall process. Also, those models were primary established by using the

water and diesel, relatively large droplets compared with gasoline. Therefore, more experiments with gasoline sprays interacting with wall are need to improve the impingement model for gasoline engines.
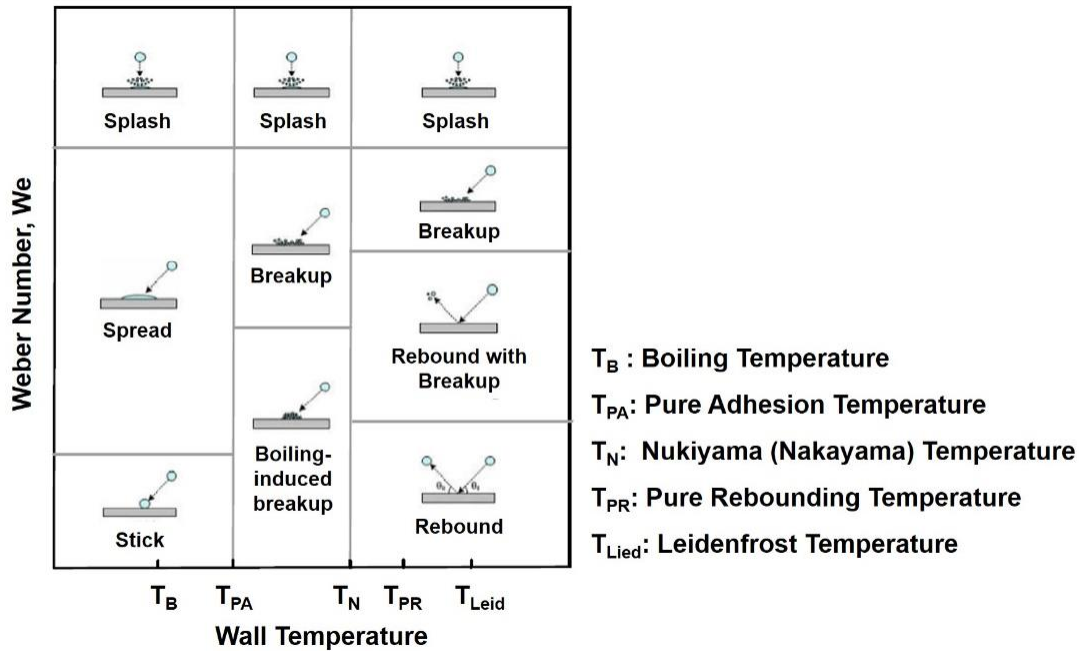

Figure 1.19 Overview of droplet impingement regimes and transition conditions for a dry wall

Due to the droplet size formed by the gasoline PFI injector (around 100µm) is much larger than that of diesel (about 20µm) in high-speed direct diesel engine, the previous models does not be employed in the PFI injector directly. Bai and Gosman [106] developed a new gasoline impingement model based on two simplified hypothesis of (1) a parcel of spherical droplets are used to represent the continuous liquid sheet emerging from the injector, and (2) droplet aerodynamic breakup, collision/coalescence and evaporation were all ignored and performed at normal ambient pressure and temperature. They showed a general agreement results between the simulation and measurement data, but should be a further validate in the aspects of regime transition correlations. Also, Senda et al [107] using low-pressure gasoline PFI injector proposed a spray-wall sub-model, in which the interaction in both droplets and droplet-wall, and velocity/direction of dispersing/splashing droplets were considered based on experimental results. They showed a well prediction sensitivity to the fuel impingement on the wall when gasoline was following into the cylinder from the intake manifold.

In DISI engines, spray-wall interaction from hollow-cone spray also were investigated at various ambient conditions due to the size of droplet formed by swirl injector is smaller than that of diesel. Effect of wall temperature on the spray-wall impingement was clarified by Park et al. [108], and showed that upward spray vortex inside the spray can be observed more clearly with increase of wall temperature. In

addition, the vapor phase occurred at not only the normal ambient but also the elevated temperature conditions, especially in the toroidal vortex and impinging plume. Also, Habchi et al. [109] found that no significant liquid film remains on the piston when the wall temperature exceeded the mean of the boiling and Leidenfrost temperature. According to the numerical and experimental result conducted under various ambient pressure, Shim et al [110] reported that the spray and vortex were limited at inner area of cavity and more fuel film was observed at this condition. A fan-shaped DI gasoline spray also was examined to clarify the wall impingement effect. The results showed that the droplet size near the wall would increase with reducing the distance between the nozzle tip and wall [111].

Recently, some studies have focused on the spray-wall of gasoline spray injected by hole-type nozzle in DISI engines. Lindgren and Denbratt [112] used a multi-hole nozzle in a stratified-charge DISI engine to investigate the spray-wall effect, and showed that few droplets bounced away from the wall with a large reflection angle. Moreover, no significant changes were found with varying of wall temperature and surface roughness. An asymmetrical six-hole nozzle centrally mounted in the chamber of an optical engine at real engine operating conditions, was used to study the spray-wall impingement of different fuels (e.g. gasoline, iso-octane, ethanol and butanol) by Serras-Pereira and Aleiferis [113-114]. They also applied a heat flux sensor installed in the top of optical piston to measure the heat transfer process during droplet impingement. The experimental results showed that the liquid break up process and flow interaction induced from the in-cylinder bulk/intake valve flows, were mainly relative to the impingement variability. Analysis of the signal characteristics indicated that the peak heat flux temperature owing to the impingement was linked to the fuel impact temperature, which was considered as the evidence of liquid droplets reaching their steady-state evaporation period at impingement. Also the liquid temperature was well in consistent with the wet-bulb temperature of the droplet model. Furthermore, contributing to heat flux in spite of more mass needed, such the high latten heat of evaporation should be considered to account for the higher peak heat fluxes for alcohols compared with the hydrocarbon fuels.

However, there are only few reports in the literature on the study and measurement of impinged spray for DISI engines. More to the point, primary of those researches above were conducted in the normal atmosphere but not the DISI-like conditions. Especially for late injection at the near TDC condition with higher temperature and pressure, the evaporation process of before/after interaction with piston wall becomes considerably intense and may greatly differ from that in atmosphere condition. Therefore, in order to provide the optimization of fuel-air mixing at late injection, it is worth to understand the spray-wall interaction under the DISI-like condition by using the sprays of gasoline and the other future commercial fuels that can contain significant quantities of bio-components with very different chemical and physical properties to those of typical hydrocarbon fuels.

1.4.2 Combustion Concepts in DISI Engines

In the modern gasoline engine, the two combustion technologies which can overcome the limitations of PFI gasoline engine and have great potential to the use of passenger car, are the stratified-combustion direct-injection spark ignition (SC-DISI) engine and the homogeneous-charge compression ignition (HCCI) engine. All of the concepts in DISI engines, namely the wall-guided, air-guided and spray-guided (in section 1.1) are aimed to realize the stratified mixture formation in cylinder at the combustion. Both of SC-DISI and HCCI employ overall lean combustion under highly diluted and unthrottled operation. In comparison to the traditional PFI engine, the former offers a significantly higher fuel economy and reduced engine-out emissions. While the same magnitude of fuel consumption to SC-DISI and dramatic reduction of NO emissions (>90%) can be produced by the HCCI which indicates that it is possible to remove the NO-exhaust after-treatment.
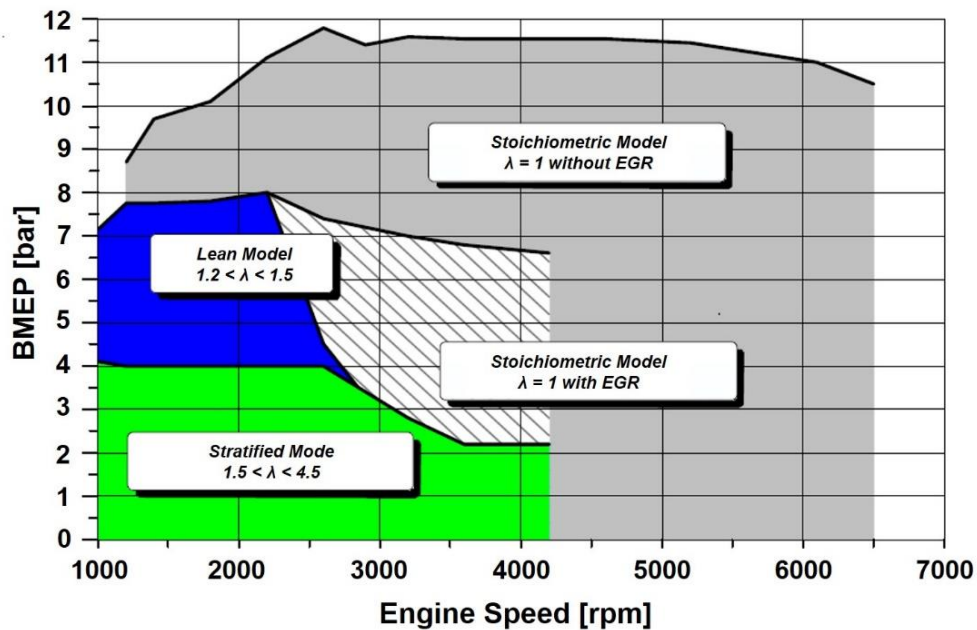
Figure 1.20 Typical Operation Model of DISI Engines

Figure 1.20 [115] shows an ample of the operation models of a DISI engine. During the low load and speed operation, engines is worked in the stratified model in the range of (1.5<λ<4.5), even in the ultra-lean mixing with the excess air ratio at between 1.2 to 1.5 in order to approach an minimal fuel consumption. When the engine runs with a "homogenous" charge at high load and speed, in-cylinder mixture should be controlled in stoichiometric condition to ensure the sufficient output power. In some cases, the homogeneous model could be separated into medium load region where the charge is overall lean, or highly diluted stoichiometric, and higher load regions where the charge is stoichiometric or even rich. Because an increase of NO_x emission can be produced at the highest load/speed. Exhaust gas recirculation (EGR) is

required to employ extensively to control the NO$_x$ emission. Furthermore, the co-operation level of excess-air and EGR dilution used is primarily dependent on the need to maximize fuel economy, yet maintaining emissions and combustion stability at acceptable levels.
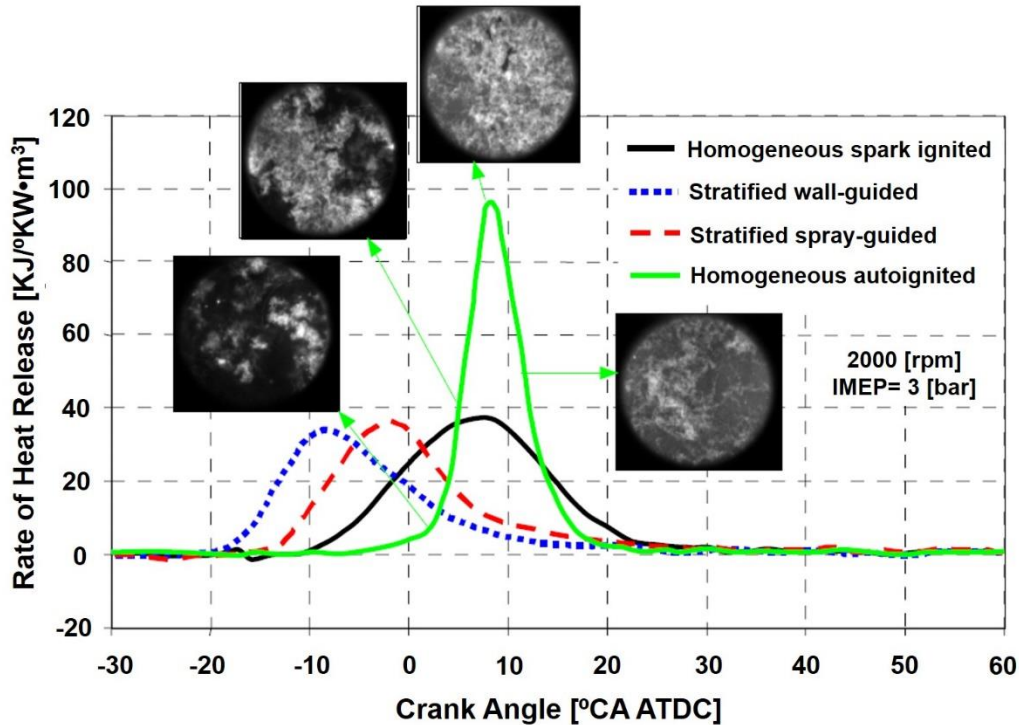

Figure 1.21 Typical Hear Release Histories of Stratified and Homogeneous Combustion System

Numerous studies have been carried out to focus on the different combustion behaviors for the SC-DISI engine among the three mixing-controlled concept as discussed previously. A typical sub-optimal phasing of SC-DISI combustion is illustrated clearly in Fig.1.21, in which shows a comparison of heat release histories of various stratified- and homogeneous- combustion system [116-119]. In contrast to the homogeneous spark ignited combustion (optimum phasing), although the stratified model has an advantage of fuel economy, the combustion for both stratified combustion systems, is advanced which will result in an increase of negative work, leading to a reduction in the efficiency of engines. In addition, Figure 1.20 shows the phasing advantage of the spray-guided system respect to the wall-guided system, which indicates that both combustion efficiency losses and combustion phasing loess are lower than latter, as a result of a better fuel economy of spray-guided over that of the wall-guided system. Also, since the combustion phase is optimized close to the TDC according to the narrow placement between the injector and spark plug, the spray-guided has better containment of fuels in the piston bowl, leading a result of lower hydrocarbon emission. It does only require a simpler design of piston crown which can reduce a lower surface area and heat losses, and also require little or no in-cylinder air motion. The results of Frohlich and Borgmann [120]

29

revealed the enhanced fuel economy potential of more than 20% and higher specific power of up to 60 kW/L in spray-guided system compared to that in a PFI engine. Also, the fact that a decreased fuel consumption in spray guided concept of at least 3 times over PFI and 1.5 times over wall-guided system, was proven by Wirth et al. [121] by performing test on a 2L, I4, spray-guided engine. Van Der Wege et al. [18] developed a new system of spray-guided and suggested that the combustion stability could be improved when the in-cylinder swirl ratio was up to 1.5, and the net specific fuel consumption (NSFC) and UHC also were able to be reduced 11.2% and 60% respectively.

Although the spray-guided concept has a fuel-economy advantage over the corresponding wall-guided and air-guided combustion systems, it also has somewhat inferior aspects of cycle-to-cycle variability and engine-out HC emissions than PFI engines. A significant reasons for the problem above is that the ignition timing range for robust combustion is relatively narrow as reported in the literature [122], where showed the only 4º CA from a given end-of-injection timing to the start-of-ignition timing for the acceptable combustion stability level (CoV of IMEP < 5%). A few degrees away from the optimum ignition timing can induce a dramatic rise in CoV of combustion stability, even results in a misfire of which frequency increases rapidly in the over advanced ignition.

The advanced combustion system, HCCI combustion, has been ongoing interest for over 25 years. While the recent growth attention on the gasoline HCCI combustion began in the late 1990's [123]. The overall configuration for gasoline HCCI combustion is similar to the spray-guided. Whereas, some of the processes are considerably different. In HCCI, homogeneous mixture is formed according to the early injection and the ignition occurs by compression ignition. Typically, the mixture is very lean ($\Phi \sim 0.2$-0.4) or heavily diluted with EGR so that flame propagation does not appear and emissions are low. In comparison to the PFI and SC-DISI, HCCI combustion has a steep increase of heat release rate (see Fig.1.21) with better phasing at 8-12° CA ATDC for improved combustion efficiency [124-125]. Also, the fuel economy for HCCI engines is similar to that of SG-DISI engines at a fixed operating conditions. The main advantage of HCCI is attributed to the ultra-low engine-out emissions. The optimum combustion temperature range for HCCI is about 1500-1800K, which indicates that the CO can be converted to CO2 completely above 1500K and that the NO_x can be neglected below 1800K [126]. And soot emissions are negligible due to the lack of rich zone. However, high UHC and CO emissions results from incomplete reactions at near cool wall boundary and fuel trapped in piston ring crevices. These may become more important than in SI engines due to the much lower combustion temperature.

The two major disadvantages of HCCI are difficult in controlling ignition timing (combustion phasing) and in operating over a wide speed-load range for maximum fuel economy.

1. Unlike diesel where autoignition and combustion phasing can be governed by injection timing, gasoline HCCI combustion is mainly controlled by in-cylinder temperature and temperature distributions due to the burning temperature of gasoline is much lower than diesel.

2. For cold start and light load, the lower in-cylinder temperature will result in unstable combustion, even misfires, as well as poor combustion efficiency.

3. At high load, the maximum rate of pressure rise probably become unacceptable, such as knock. Under the maximum power at full load, HCCI engines operates as stoichiometric DISI engines, limiting the maximum compression ratio below 15:1. Furthermore, owing to the thermal lag, smooth transitions from HCCI to DISI can be a problem to commercialize HCCI engines.

Some methods considered as the effective ways to solve those issues above are listed as follows.

1. For combustion phasing controlling, the variable EGR rates, sophisticated variable-valve actuation and intentional stratification can be used to realize the in-cylinder temperature controlling.

2. The narrow stable combustion range of HCCI can be alleviated by maximizing EGR temperature [127-128], preheating of intake charge [129-132] or spark-assisted ignition [132-134].

3. More precise numerical models for spray and combustion are needed to control HCCI combustion and the model transition of different combustion type.

Generally, the injection and ignition controlling are the key factors for the advanced combustion concept. Fuel/air mixing with the help of EGR determined the in-cylinder temperature distribution. The advanced control strategy of mixture formation is more important than simple" homogeneous charge" in the HCCI combustion process. In addition, under an optimum ignition strategy, the spontaneous ignition (multipoint ignition) can be realized with less flame propagation, in order to obtain the ultra-low emission and maximum fuel economy. Combing these aspects, the HCCI operating range is able to be extended at high load without the knock occurrence and light load without difficulty of compression ignition.

1.4.3 Optical Diagnostics in DISI Engines/DISI-like Conditions

The complexity of the physical and chemical processes and their interaction ensure internal combustion engines to convert chemical energy of fuel into mechanical work. Level of fuel use for transportation and applications of IC engines makes performance improvements to higher fuel economy and lower emissions. With an aid of the information which can obtained from the "optical engines" or steady-state "bomb", much insight can be gained to improve existing technology or even develop completely new combustion concept.

This section will introduce the typical well-known/new developed technologies of high-speed visualization and laser diagnostics measurement used in the real DISI engines or DISI-like quiescent-steady conditions.

1.4.3.1 Diagnostics Techniques of In-cylinder Flow, Spray Mixing and Ignition Process

It is well-known that the gas motion plays a significant role on not only initialing the in-cylinder turbulent levels and bulk flow motion during suction stroke, but also determining the fuel/air mixing for the stratified mixture preparation during compression stroke, especially near TDC. The former is critical to the variability in flow pattern affecting fuel injection and ignition, while the latter is important to the mixture distribution and flame development greatly depended on the large-scale turbulent. Traditional detection of airflow is limited by the technology of laser and camera which only allows to capture a few images per data set in optical engines. A traditional high-speed particle image velocimetry (PIV) was considered as an effective way to solve the above issue and employed with one laser to measure the flow in cylinder was took by stolz et al. [135]. Müller et al. [136] used the improved all-solid-state diode-pumped frequency-double Nd:YAG or Nd:YLF lasers combining with CMOS cameras to investigate the temporal evolution of large-scale flow structure in SG-DISI engine, revealing the possibility to quantitatively analysis on the cyclic variation by using kinetic energy which did not show a strong variation of individual cycles to the mean. Furthermore, a new developed method of ultraviolet (UV) lasers operated at 355nm and a CMOS camera was implemented by Fajardo and Sick [137-139] to reach the purposes of simplified simultaneous laser induced fluorescence (LIF) measurements and suppressing the flame luminosity in the visible spectral range. They used silicon oil as tracer to detect the flow near spark plug and suggested that the increased shear strain in the periphery of spark plug could prevent flame kernel development. The schematic setup was shown in Fig.1.22. A broad width of visualized window was formed by combining the beams of horizontal and vertical direction. Therefore, the distribution of flow velocity in cylinder can be assessed in X and Y direction. Also coupled with Mie scattering [137] or PLIF technique [140-141], the integrated information of spray, mixing and flow near spark plug was possible to be measured. 355nm narrow interference filter enabled the tracer light to prevent from the flame luminosity, hence the flow flied was able to be continuously measured during ignition and combustion process.
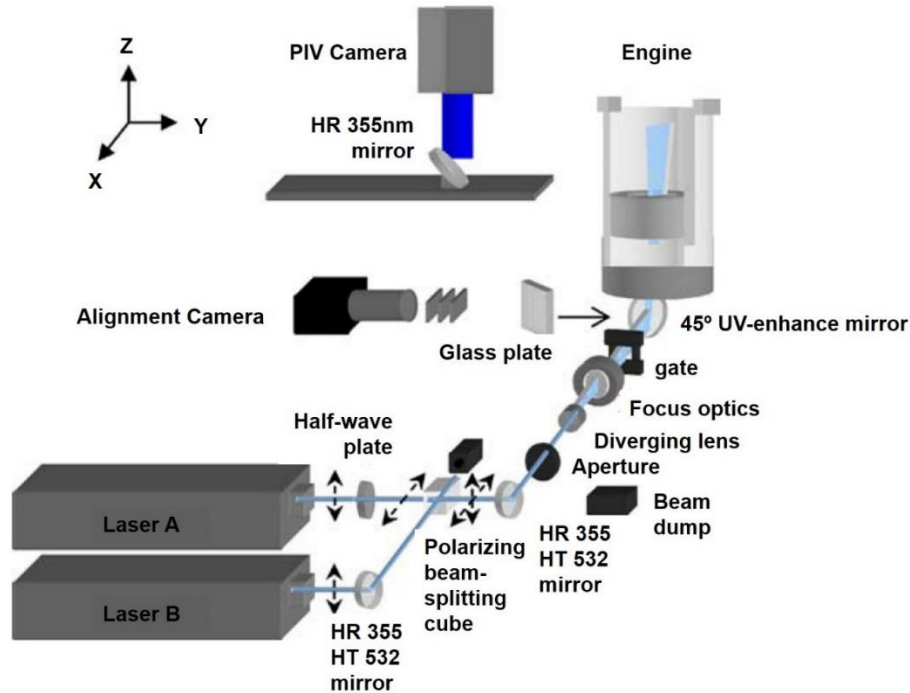
Figure 1.22 Overall View of Dual-laser UV-PIV System

The optical techniques also have been widely used to identify the macroscopic and microscopic characteristics of spray evolution. New SAE standard (J2715) [142] was proposed in 2008 to achieve significant reductions in spray data between companies and laboratories, and recommended the backlit illumination as the preferred choice to characterize the spray parameter and boundary in automobile industry. However, in order to understand more detail in the mechanism of fuel spray, more optical measurements are used and developed in laboratory. Mie scattering [143-144], Schlieren and Shadowgraph techniques are maturely and used to provide the qualitative information of liquid and vapor phases of fuel spray and droplets distribution in quiescent steady-state, which have been summarized and published in elsewhere [145-148]. The movement of internal spray and surrounding gas can be simultaneously measured by the measurement of LIF-PIV, which also were popularly introduced into the diesel spray [149-150]. Rottenkolber et al. measured the two phased of movement about spray and ambient gas for a hollow-cone spray. They used the aerosol of droplets as the tracer to seed the surrounding gas, while the inner spray flow was obtained by a narrow bandpass filter [151].

In order to get detail information of mixture formation, such as fuel concentration, liquid and vapor phase distributions et al., the diagnostics of spray mixing process have been developed greatly for many years, especially the planar laser-induced fluorescence (PLIF), laser-induced exciplex fluorescence (LIEF) and laser extinction/absorption (LEA) technique.

33

The principle of LIF is that the electronic absorption/emission process of the certain species is excited by the incident laser power, then the intensity of emitted fluorescence light is proportional to the mole fraction of the certain species of interest [152-153]. Sick et al [154-156] developed a new PLIF method, enabling to produce a high temporal resolution in 355nm excited wavelength, in order to quantitatively measure fuel distribution near spark plug in SG-DISI engine. The biacetyl was applied as the tracer in iso-octane, to overcome the problem of low pulse repetition rate as the conventional tracers like acetone, 3-pentanon or toluene were used in the 280nm excited wavelength. If combining the PIV technique as mentioned above, it provides a powerful way to understand the in-cylinder conditions that exist in the vicinity of the spark plug during ignition [157]. By this method, the interaction of fuel spray plume and the spark plug can be observed. In short, this measurement visualizes instantaneously the distribution of fuel concentration, velocity magnitude, shear strain rate, and vorticity values which varies substantially from cycle-to-cycle during the spray event, as shown in Fig.1.23 [158-159]. Also the ignition process (successful, partial and misfire) can be examined by the effect of the gradient of fuel/air ratio and velocity distribution [160-161]. However, the stray-light problem and interference by the electrodes create difficulty for baicetyl-PLIF measurement right at the spark gap [162]. The CN* chemiluminescence during spark charge was found proportional to the local fuel concentration for fixed operating conditions, and calibrated on homogeneous fuel-air mixtures. Therefore, under fixed fuel concentration, the spark energy during the measurement interval was strongly corrected with CN* emission intensity, hence the local fuel concentration diagnostic based on the spark-emission spectroscopy was developed [163]. According to the analysis of CN* chemiluminescence, Dahms et al. [164] revealed the fact that strong fuel concentration gradients along the stretched plasma channel in a spray-guided SC-DISI engine. Also due to the spark charge channel influenced by the intensity and variation of local turbulence and fuel concentration, a physically-based spark channel ignition model of SparkCIMM was built and enhanced to bridge the gap between a detail spray/vaporization model and a model for fully developed turbulent flame front propagation [165-166].
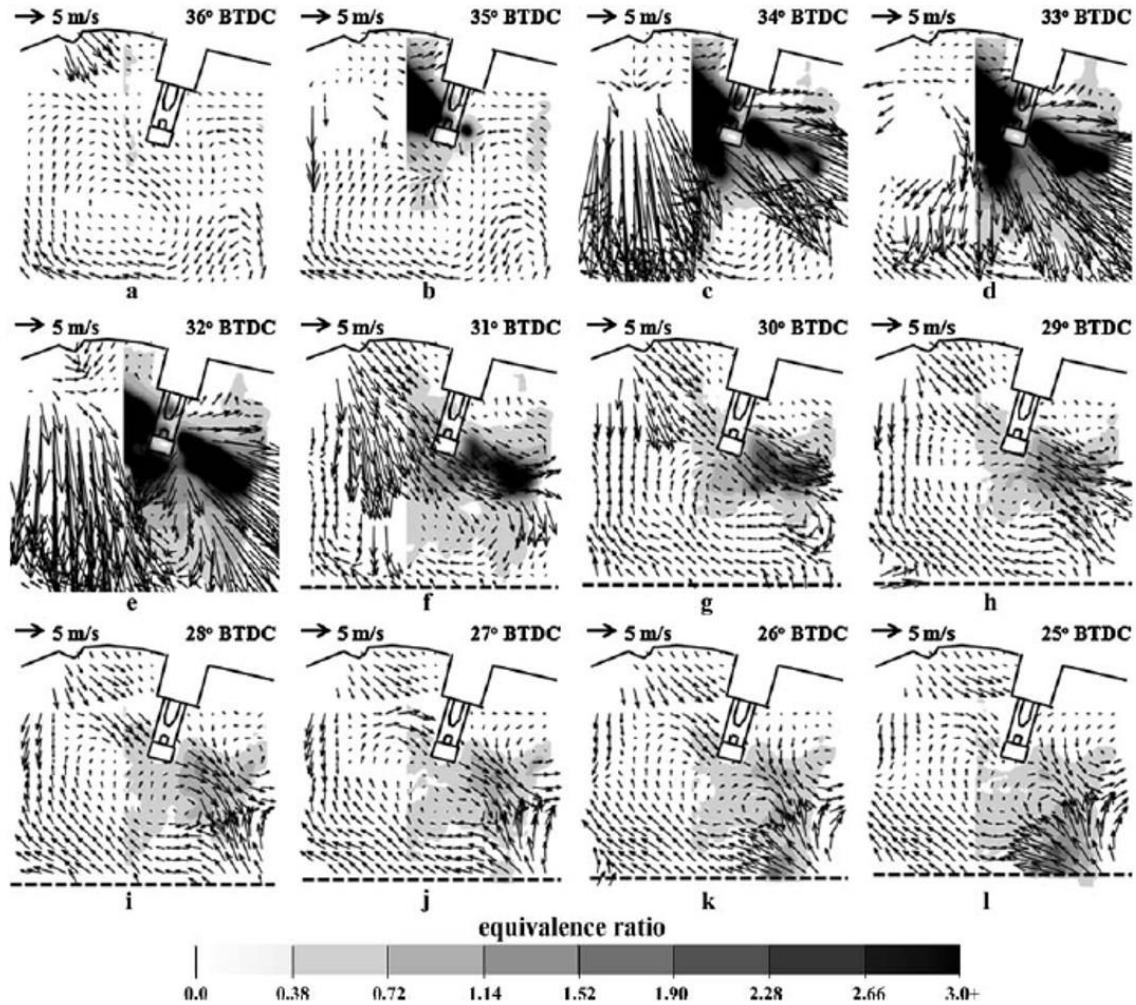
Figure 1.23 Simultaneously Recorded High-speed Flow (PIV) and Fuel (PLIF) Images at Spark

The distribution of liquid and vapor concentration, which usually measured by the LIEF or LEA, is another key issue to understand the mixture formation in cylinder. In the case of LIEF, the fluorescence molecular at the exited state called monomer reacts with another molecular at ground state, hence the second fluorescent molecular namely exciplex is formed. The concentration of monomer is dominant by the gas phase while the exciplex is determined by the liquid phase. As a result, the fluorescent intensity is directly proportional to the fuel concentration. This technique was originally developed by Melton et al [167], and was applied in numerous studies [168-171]. However, LIEF only gives right results in the totally vaporized zone of the spray rather than the place where liquid and vapor coexist, and is greatly dependent on the fuel and dopants used due to different evaporation behavior [172]. LEA, also namely laser absorption scattering (LAS), carried out a transmission measurement at a visible wavelength to determine the optical thickness of liquid droplet due to the scattering, and a transmission measurement at an absorption wavelength to determine the optical thickness of vapor and liquid phase due to the absorption and scattering, respectively.

35

Thereby, based on this theory, the simultaneously imaging of liquid and vapor concentration can be realized. This measurement was firstly introduced by Chraplyve [173] in 1981 to measure the vapor concentration in an axisymmetric n-heptane spray by using two He-Ne lasers at the wavelength of 3.39 and 0.6328 μm respectively. Thereafter, a similar infrared light extinction method was used to determine the liquid and vapor distribution in a pressure-atomized steady spray [174-175]. Moreover recently, using ultraviolet and visible light, a new LAS technique was developed to quantitatively measure the liquid and vapor phase distributions in gasoline spray [176-177].
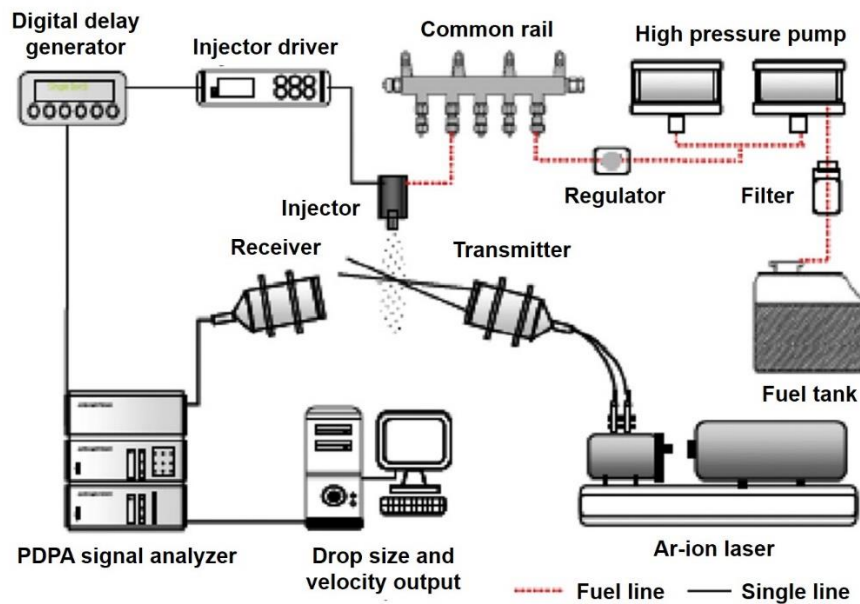

Figure 1.24 Schematic of PDPA System Set-up

Another significant characteristics of spray atomization is the size of liquid droplet. Phase Doppler particle anemometer (PDPA) or laser doppler anemometer (LDA) has been widely used to measure the size and velocity of spray. A typical schematic of PDPA system set-up by Sun et al. [178] is shown in Fig.1.24. When the transient spray passes through a measurement volume in the path of the laser beam, the dispersed beam signal can be obtained by the receiver. The velocity of the droplets will be related to the temporal modulation, while the droplet size will be related to the spatial frequency. Since a large amount of droplets can be detected in the measurement volume, the representative SMD can be obtained by averaging the captured droplets over the all measuring area. Although numerous studies have been carried out to investigate the spray droplet size of different gasoline spray based on the PDPA technique [179-180], it is limited to the spray density and provide size distribution in a single transient injection [181]. Recently, another method of using LIEF/Mie to measure the liquid droplet in evaporating spray also has been developed, according to the theory of the assumption that the fluorescence intensity emitted by the

fluorescent dye is proportional to the volume (d^3) of the droplet and that the scatted intensity is proportional to its surface area (d^2). Hence, the ratio of these two intensity on an illuminated plane of a spray is proportional to the SMD [182]. Their result showed that a good agreement with a standard measurement of PDA. For the dense spray field, especially near nozzle tip, it is difficult to measure the microscopy spray structure by using the PLIF, PIV or laser sheet dropsizing systems, due to the complexity in the mechanism of multiple scattering at those places. The X-ray imaging, as an effective way of light-of-sight visualization, was considered as one of the most significant measurement to detect the dense liquid area, and some of valuable results of spray microscope structure injected from a GDI injector was reported in elsewhere [183-184]. However, all of those experiments were conducted in the normal atmosphere which is need to be further improved to enable the X-ray imaging to be employed under the high- temperature and pressure conditions [185].

1.4.3.2 Diagnostics Techniques of Combustion Characteristics

The optical diagnostics measurement on combustion is considerably necessary for the optimization engine performance or development of new combustion concept in DISI engines. Natural luminosity of flame is mainly dominant from soot incandescence, hence the soot formation can be qualitatively analyzed by the line-of-sight flame luminosity. Oh and Bae [186] studied the effect of injection timing on the combustion performance in a SG-DISI engine by imaging of natural luminosity, and suggested that the luminous and non-luminous flame can be successfully distinguished according to a proper threshold of R channel in the color imaging due to the color characteristics of different flame type (pre-mixed flame and diffusion flame). Also, they proposed a ratio of diffusion flame to the total flame, to describe the soot formation and diffusion flame development.

Another well-used method to measure the flame development is the hydroxyl radical chemiluminescence or fluorescence. Chemiluminescence emissions occur when the excited radicals, such as OH*, CH*, and C_2*, formed within the flame front, return from an excited energy state to a lower energy state by emitting light at a characteristic wavelength. This natural emission is non-thermal radiation of relatively narrow spectral ranges emitted from combustion intermediate species. In hydrocarbon-air flames, the strongest chemiluminescence intensity peaks are produced by the excited OH radical at 280-310nm, CH radical at 431nm and C_2* at 516/563/619nm. The primary path for emission of CH* is dominant by the reaction $C2+OH \rightarrow CH*+CO$. Flowing this process, OH* is produced by the reaction $CH+O_2 \rightarrow CO+OH*$ [187]. Since the chemiluminescence marks the location of the initial reactions during the combustions, thereby this natural emission of radicals have been widely accepted to the flame diagnostics. The OH* and CH* emission were considered as the excellent flame markers to study the combustion process, especially

37

in the flame front location [188-189]. In addition, the OH* maximum peak value was found to be in consistent with the peak of heat release rate (RoHR) [190]. Also, both the OH* and CH* chemiluminescnece has been proven that they are able to be the good marker of RoHR [191], and the ratio of OH* to CH* can be used to characterize the equivalence ratio in flame [191-193].   Although the chemiluminescence is able to provide the global information of flame evolution, it is difficult to describe the local characteristics of flame during the combustion. The OH emitted fluorescence induced by the laser, namely OH-PIFL technique, was adopted in some studies [194-197] to enable the investigation of spatial resolvedly imaging on the local or microscope structure of flame, which showed a great different flame profile compared to the light-of-sight chemiluminescence.
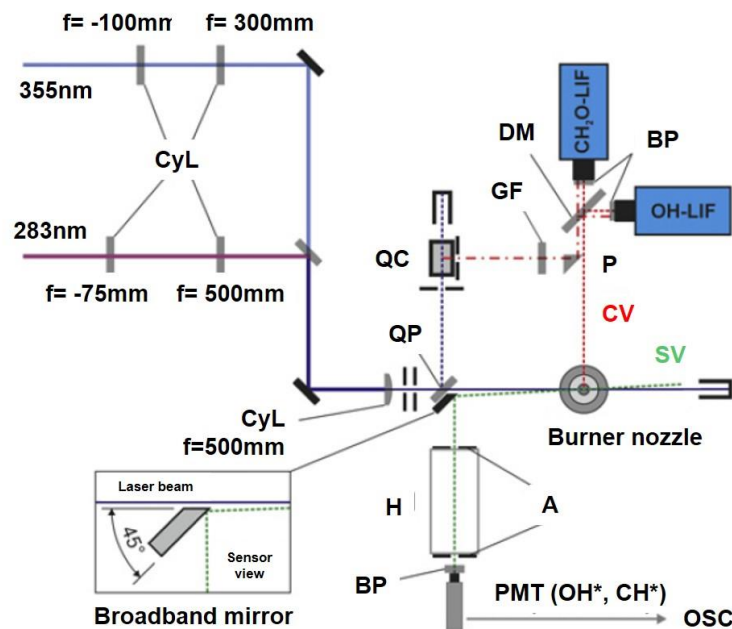

Figure 1.25 Typical Schematic Setup of Simultaneous RoHR Imaging via OH and CH_2O-LIF

For the RoHR measurement, the drawbacks of chemuluminescnece are that it does not provide a straightforward interpretation of from what spatial region the signal originates, and that the signal of OH* can be trapped and attenuated by ground-state OH in the hot burnt gas [198]. Recently, more attention has been drawn to the simultaneously PLIF imaging of hydroxyl (OH) and formaldehyde (CH_2O). Najm et al. [199-200] firstly proposed that these productions showed a good proportional relation to the forward reaction rate of the $CH_2O+OH{\rightarrow}HCO+H_2O$. Based on this reaction theory, the formation of HCO radical, which was found more suitable to represent the local RoHR because they are associated with the main reaction path of fuel [201], was probably denoted by the fluorescence signal multiplication of OH and CH_2O. Therefore, the local RoHR can be measured by the OH/CH_2O-LIF instead of the directly imaging of HCO,

whose life time is so short that it is difficult to be recorded [202-203]. A typical novel OH/CH_2O-LIF technique was showed as in Fig.1.25 [203]. OH was excited via the Q_1 (6) transition in the A-X (1,0) electronic band at 282.927nm by a frequency-doubled dye laser, while the CH_2O was excited within the A-X 4_1^0 electronic band near 355nm by a frequency-tripled Nd: YAG laser. Based on this technique, the local HoRR can be obtained by the pixel-by-pixel multiplication of the signal counts from OH and CH_2O fluorescence.

Two color pyrometry is the well-known technique to measure the soot formation in combustion. This method uses the thermal radiation from soot particles to obtain the line-of-sight information of soot concentration (KL factor, which is proportional to the soot concentration). As contrast to the mostly utility in diesel combustion [204-206], few studies [68,189] of DISI gasoline engine were found to apply this method to be an optical diagnostic for soot formation, due to the considerably less soot formation of gasoline or alternative fuels in DISI engines compared with that of diesel engines. Laser induced incandescence (LII) is one of the other popular method to detect the soot formation, especially the planar soot distribution by inducing a laser sheet across the flame. The soot particles are heated to a temperature well above the surrounding gas temperature due to the absorption of laser energy, then subsequently emit black body radiation corresponding to the elevate soot particle temperature. Numerous works have been conducted by LII to investigate the soot formation in diesel flame and proposed the conceptual model of soot formation and oxidization process. [207-209]. However, LII technique mostly was used at atmospheric pressure and steady condition due to the uncertainty of soot refractive index under high pressure in the case of the large soot measurement. Moreover, measuring soot concentration in engines using 2-D PLII does not allow the high time resolved recording because of the lower repetition of laser pulse. Also, another weakness of LII is the laser attenuation would occur when soot concentration is sufficient high, probably accompanied by signal trapping, then leading to an inevitable error in the measurement system. In order to overcome the issues discussed above, a new soot measurement, namely two-color diffused back-illumination imaging, has been presented as a diagnostic for the high time-resolved recording [210]. They suggested that the shorter visible wavelengths are more preferred to measure soot concentration. Moreover, the soot refractive index should be carefully considered due to its significantly dependent on the wavelength.

1.5 SUMMARY

In order to moderate the dependency of conventional petroleum-derived fuels, such as gasoline and diesel, and reduce the greenhouse-effect and engine-out emission (HC, NO_x, CO_2, et al.), it is necessary to use the ethanol-gasoline blends to replace of the gasoline in DISI engines. Therefore, the validation of

whether this alternative fuels is suitable for that state-of-the-art gasoline injection concept, becomes more emergent nowadays. In this chapter, the purpose of this study was presented to investigate the characteristics of mixture formation process and combustion of ethanol-gasoline blends, and the comparison of those and pure gasoline.

Firstly, the development of direct-injection spark ignition (DISI) engine and its corresponding injectors were introduced. Also, the review of the ethanol used in DISI engines also was presented. Thereafter, the objective of this study and approaches were introduced. Subsequently, the main fruits of the previous studies on the spray and combustion in DISI engines were described, including the typically classic models and empirical equations. Finally, the introduction of mature/novel diagnostics of spray and combustion for gasoline in D.I. engine also were presented.

CHAPTER 2 EXPERIMENTAL APPARATUS AND MEASUREMENT TECHNIQUE

2.1 CONSTANT VOLUME VESSEL

The investigations of spray and combustion process were conducted under the quiescent condition in the constant volume vessels. Figure.2.1 shows a schematic cross-section diagram of the structure of the combustion bomb. The internal height of the chamber is about 287mm and has a diameter of 208 mm. The sufficient volume of 9.75L can ensure the spray and combustion develops in the nearly quiescent condition. A kanthal alloy electrical heating unit (single-phase voltage of 200V, 1.5kW) was installed under the chamber to produce the elevated temperature up to a maximum 700K. The thermal insulator with a thickness of 25 mm at the inner surface to avoid the direct heat conduction. Compressed N_2 or air can be introduced into the chamber by the gas passage to produce the in-chamber pressure up to 1.3MPa.Two thermal couple antennas (OKAZAKI MFG Co., K type) were inserted into the chamber to measure the temperature of ambient and heater at different position without interference with the spray. In the experiment, the spray was injected into the chamber after the temperature reaching a sable value and maintaining for about 30 minutes, thereby the ambient environment can be regarded as the homogenous thermodynamic condition. For this constant volume vessel, it is a flexibility for the window arrangement at the light path.
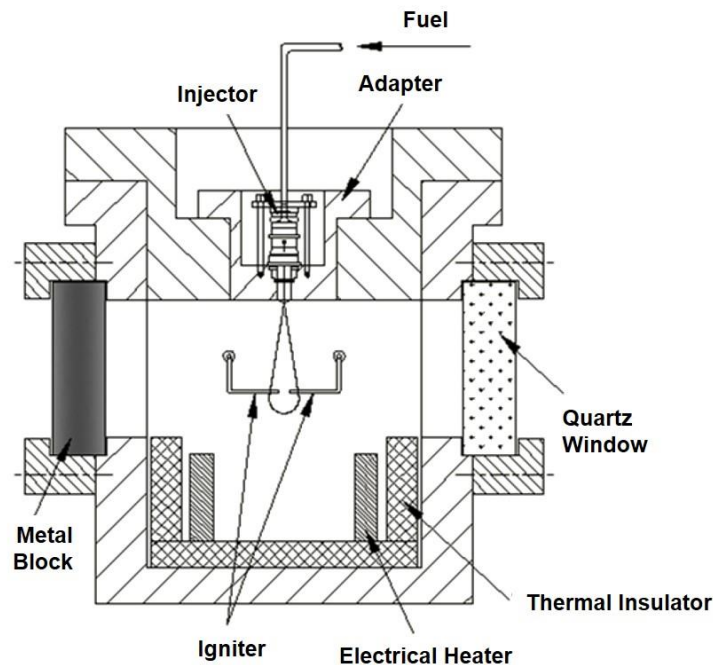

Figure 2.1 Schematic of Cross-section Structure of Constant Volume Vessel for Combustion

41

As Fig.2.1 shown, a quartz window was installed in one side of the vessel providing the optical access, while a metal block was at the opposite side in order to reduce the background noise from the ambient environment, which was demanded for the experiments with only one side needed. However, if necessary, the metal block can be replaced by a quartz window for the optical visualization (diameter of 100mm). Injector adapter was equipped with a cooling water jacket, in order to maintain the fuel in the nozzle at a normal temperature.

2.2 HIGH INJECTION PRESSURE SYSTEM

During the spray and combustion experiments, a single electrical controlled solenoid valve-covered-orifice (VCO) injector was centrally mounted in the top of the vessel as shown in Fig.2.2 (a). The inserted angle was set to 25°, in order to vertically inject the fuel into the chamber because of the same angle between the hole axis and nozzle axis as presented in Fig.2.2 (b). The hole diameter of this single VCO nozzle is 0.15mm, and its L/D is 2.0. The injection pressure was fed by a special high-pressure accumulator which could be pressurized by the nitrogen up to 20MPa. Injection signal was controlled by a delay plus generator (Stanford Inc., DG535), which also was used to synchronize the ignition and imaging recording. Then this single was converted to a special electrical signal to the solenoid coil in the injector, thus drove the nozzle needle to injection.
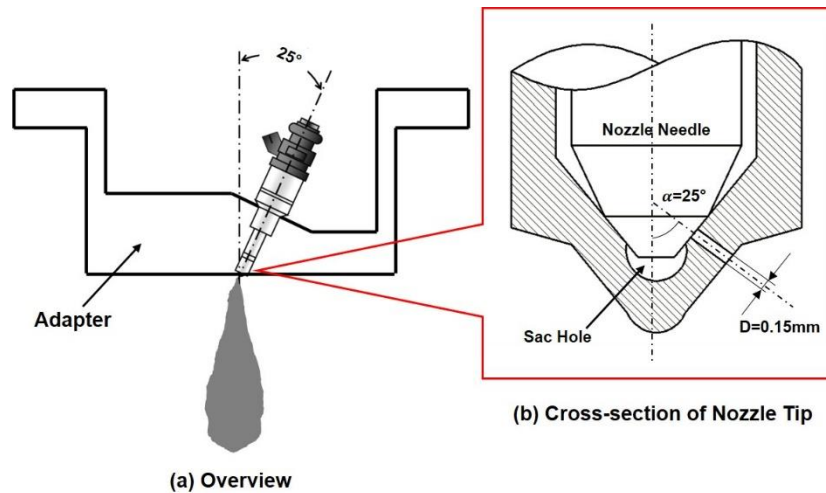

(a) Overview

(b) Cross-section of Nozzle Tip

Figure 2.2 Schematic Setup of Injector and Its Cross-section Structure

In this work, the injection pressures of 10, 15 and 20MPa were used in different experiments for gasoline and its ethanol blended fuels. The injection pulse of E0 as an example was defined as 1.51, 1.34 and 1.1ms for 10, 15 and 20MPa respectively as shown in Fig.2.3. This solenoid injector produced a square-like shape

of injection rate. The duration from the start of injection to quasi-steady state and the ramp-down were approximately 0.2ms respectively.
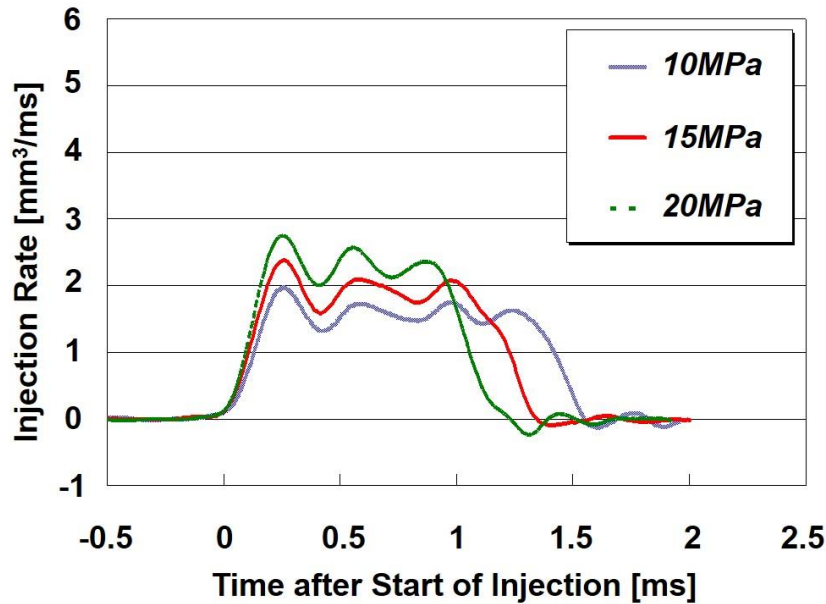

Figure 2.3 Fuel Injection Rate for E0

2.3 IGNITION SYSTEM

In the combustion experiment, a special manufactured igniter was installed in perpendicular to the light path. Figure 2.4 (a) shows the schematic of the igniter. Two independent stainless steel electrodes with a diameter of 1mm were mounted on the stainless steel robs with the sealing ground (Conax Co. EGT Ground). The electrodes were flexible for the position setting. Because of the small scale and the arrangement of surrounding into the spray, these electrodes had less effects on the spray propagation and mixture formation. A transistor controlled ignition (TCI) system was used to provide spark. The ignition coil (Mitusbishi Co. B6S718100) was charged by a power source (12V). When the signal from the delay pulse generator forms, the transistor (Mitusbishi Co. J121 Power unit) will breakdown the closed-circuit if the falling edge in signal is detected. Thus a high voltage (~25kV) can be produced from the ignition coil due to the electromagnetic induction. An example of ignition current and voltage under normal atmosphere is shown in Fig.2.4 (b) in the case of the dwell time (ignition coli charge time) at 6ms. The ignition duration (3.189ms) is dependent on the glow and arc phases, which also mainly determines the total ignition energy of 34.16mJ.
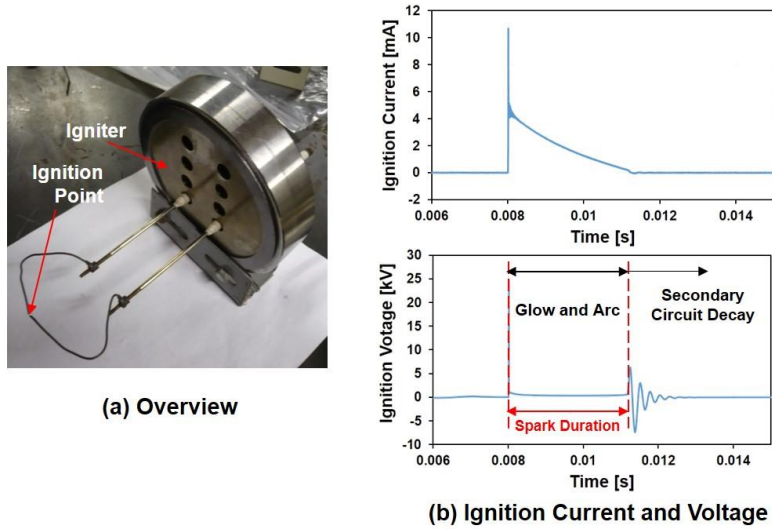
Figure 2.4 Overview of Igniter and Ignition Current and Voltage at Dwell Time of 6ms under Normal Atmosphere Condition

2.4 ELECTIRCAL CONTROLLING SYSTEM

A delay pulse generator was used to synchronize the injection, ignition and camera. Figure 2.5 shows the example map of injection and ignition timing for E0 under P_{inj}=20MPa. In the case of laser-based spray imaging, the Injection timings are set to the places where the blue triangles present due to the laser pump shot. While for the experiments using high-speed camera, the injection even is consecutive in contrast to the laser shot. Yellow triangles denote the ignition timing during the combustion experiments. All of the timing points characterized by the time after end of injection (AEOI). Different injection pulses were set to different types of fuels due to different injection mass.
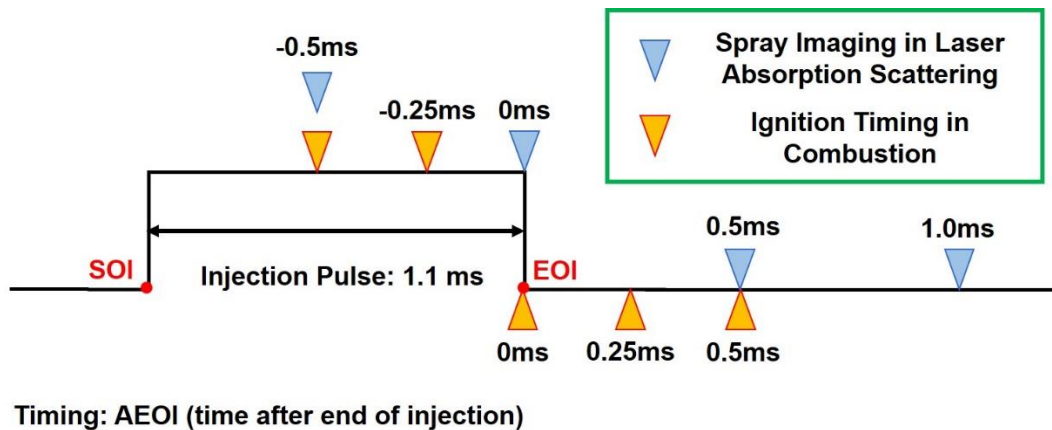

Figure 2.5 Timing Chart of Injection and Ignition for E0 under P_{inj}=20MPa

2.5 OBSERVATION TECHINIQUES

2.5.1 Laser Absorption Scattering (LAS) Technique

2.5.1.1 Principle of LAS Technique

The dual-wavelength laser absorption scattering technique has the advantages of less sensitive to the ambient temperature in the heated-state constant volume vessel, and none influence by either the water vapor or oxygen quenching. Figure 2.6 shows the principle of the LAS.
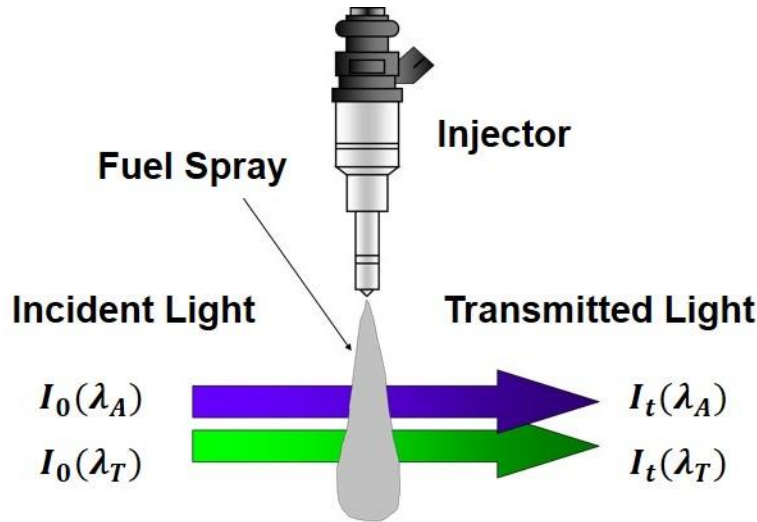

Figure 2.6 Principle of LAS Technique

The two wavelengths of absorption and transparent light (λ_A and λ_T) with the intensity of I_o pass through the spray area. Due to the extinction of the liquid droplet and vapor, the intensity of those two bands become the transmitted intensity, denoted by I_t. The extinction of the absorption wavelength, represented by $\log(I_0/I_t)_{\lambda_A}$, as described in Eq. (2.1), is attributed to the absorption of vapor ($\log(I_0/I_t)_{V_{abs}}$) and liquid droplet ($\log(I_0/I_t)_{L_{abs}}$), as well as the scattering of liquid droplet ($\log(I_0/I_t)_{L_{sca}}$). Likewise, the extinction of the visible wavelength, denoted by $\log(I_0/I_t)_{\lambda_T}$, only involves the scattering of liquid droplet ($\log(I_0/I_t)_{L_{abs}}$), as expressed in Eq. (2.2).

$$\log(\frac{I_o}{I_t})_{\lambda_A} = \log(\frac{I_o}{I_t})_{L_{sca}} + \log(\frac{I_o}{I_t})_{L_{abs}} + \log(\frac{I_o}{I_t})_{V_{abs}} \qquad (2.1)$$

$$\log(\frac{I_o}{I_t})_{\lambda_T} = \log(\frac{I_o}{I_t})_{L_{sca}} \qquad (2.2)$$

Due to the high-pressure direct injection, the liquid absorption of droplets is seem so small that the second right item in Eq. (2.1) can be neglected. In consideration of the theory from Bohren [211], the limiting value of efficiency for extinction approaches to 2 if the droplet size parameter is sufficient large, hence the scattering extinction from liquid droplet in both the absorption and visible wavelength are the same. To verify the deductions above, the previous study using swirl injector showed the imaging results of absorption and visible wavelength under non-evaporating spray of p-xylene as shown in Fig. 2.7. Non-evaporating spray only includes the liquid droplets. At both Z=10mm and 30mm, the extinction at the visible and absorption wavelengths (λ_T=532nm and λ_A=266nm, which also were used in this study and would discussed in section 2.5.1.6) shows the nearly same distribution and value, which means two significant facts that it is reasonable to neglect the absorption of liquid droplets in 266nm wavelength, and that the droplets scattering in both two wavelengths are nearly the same.
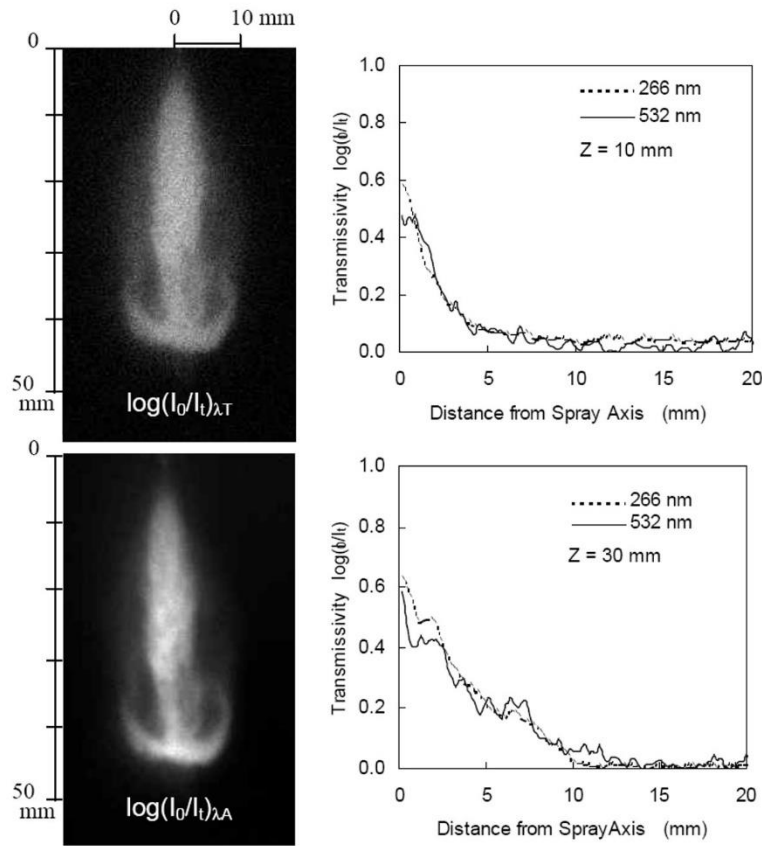

Figure 2.7 Extinction Images of p-Xylene Non-Evaporating Spray at Two Wavelengths λ_T: =532nm and λ_A=266nm. (Z is the axial distance from the nozzle tip) [212]

Therefore, by substituting Eq. (2.2) into Eq. (2.1), the equations express the extinction of vapor and the droplet can be shown as follow respectively.

46

$$\log(\frac{I_o}{I_t})_{V_{abs}} = \log(\frac{I_o}{I_t})_{\lambda_A} - \log(\frac{I_o}{I_t})_{\lambda_T} \tag{2.3}$$

$$\log(\frac{I_o}{I_t})_{L_{sca}} = \log(\frac{I_o}{I_t})_{\lambda_T} \tag{2.4}$$

The extinction of vapor ($\log(I_0/I_t)_{V_{abs}}$) is corresponded to the light absorption theory (Lamber-Beer Law). While the extinction of liquid droplet is based on the light scattering theory (Bouguer-Lamber-Beer Law). Consequently, the fuel vapor concentration can be quantitatively calculated by this way that the extinction of the absorption wavelength removes that of the visible wavelength. In this study, a second harmonic wavelength of 532nm (visible wavelength) and fourth harmonic wavelength of 266nm (absorption wavelength) were used as the source of the incident light to illuminate the spray in LAS experiment.

2.5.1.2 Light Absorption Theory of Vapor

Based on the Law of Lambert-Beer, the extinction of vapor ($\log(I_0/I_t)_{V_{abs}}$) can be used to calculate the vapor concentration distribution. Figure 2.8 shows an introduction of the Lamber-Beer Law. Provided the incident light with intensity of I_o passes through a field of homogenous concentration C_V [kg/m³] with a light path of l [m], the light intensity becomes a transmitted light with the intensity of I_t. The correlation of vapor extinction and concentration can be described as:

$$\log(\frac{I}{I + dl})_{V_{abs}} = \frac{\varepsilon}{MW} \cdot C_V \times 10^2 dl \tag{2.5}$$

Where ε is the molar absorption coefficient [litter/(mol•cm)], MW is the molar weight [kg/kmol]. Therefore, if the vapor extinction and absorption coefficient can be measured, the vapor concentration is able to be acquired based on the given molar weight and light path, also is expressed as follows.

$$C_V = \frac{MW \cdot \log(\frac{I_o}{I_t})_{V_{abs}}}{\varepsilon \cdot l \times 10^2} \tag{2.6}$$

In the practical application in IC engine, the equivalence ratio is usually used by automobie engineers and researchers. The equivalence ratio of vapor phase is defined as the ratio of the stoichiometric air/fuel (AF_{stoich}) to the local air/fuel (AF_V), and can be described by:

$$\phi_V = \frac{AF_{stoich}}{AF_V} = \frac{AF_{stoich}}{(C_{amb}/C_V)} \tag{2.7}$$

Where C_{amb} is the ambient gas concentration without the fuel vapor and liquid droplet. The stoichiometric air/fuel of hydrocarbons are derived from the chemical reaction equation under the complete combustion condition. The chemical reaction equation and the AF_{stoich} are shown following:

$$C_nH_m + \left(n + \frac{m}{4}\right)O_2 + 3.76\left(n + \frac{m}{4}\right)N_2 \rightarrow nCO_2 + \frac{m}{2}H_2O + 3.76(n + \frac{m}{4})N_2$$
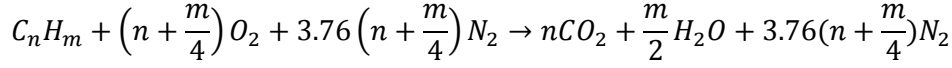
$$AF_{stoich} = \frac{137.3\left(n + \frac{m}{4}\right)}{12n + m} \tag{2.8}$$
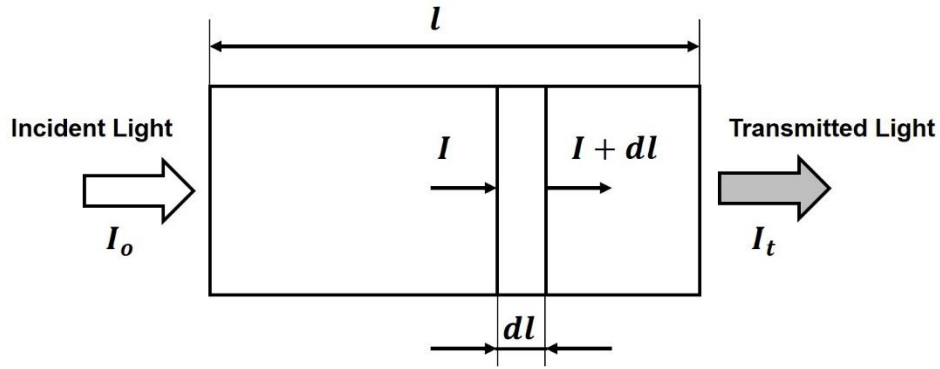

Figure 2.8 Lamber-Beer's Law

2.5.1.3 Light Scattering Theory of Liquid Droplet

The acquisition of liquid concentration is dependent on the Law of Bouguer-Lambert-Beer. As Fig.2.9 shown, when the incident light traverses thought the field with homogenous liquid particles, the light extinction of the light path element dl can be expressed as follows.

$$\frac{dI}{I} = -\beta \cdot dl \tag{2.9}$$

Therefore, the initial intensity of incident light becomes the transmitted light with the intensity of I_t, as the light passes thought the whole length l. The total extinction is described as:

$$\frac{I_t}{I_0} = \exp\left(-\int_0^\infty \beta \cdot dl\right) \tag{2.10}$$

$$\beta = \int_0^\infty R(m, D, \lambda, \theta) \cdot Q_{ext}(m, D, \lambda) \cdot \frac{\pi}{4} D^2 \cdot n \cdot f(D) \cdot dD \tag{2.11}$$

Where R is the ratio of the droplet optical thickness at the two wavelengths, θ is the half-angle corrected by the droplets scattering direction. Q_{ext} is the extinction efficiency, which is greatly dependent on the

48

refractive index and size parameter. m and D are the refraction rate and diameter of droplet respectively. λ is the incident wavelength. n is the droplet number. And the $f(D)$ is a distribution function of liquid droplet.
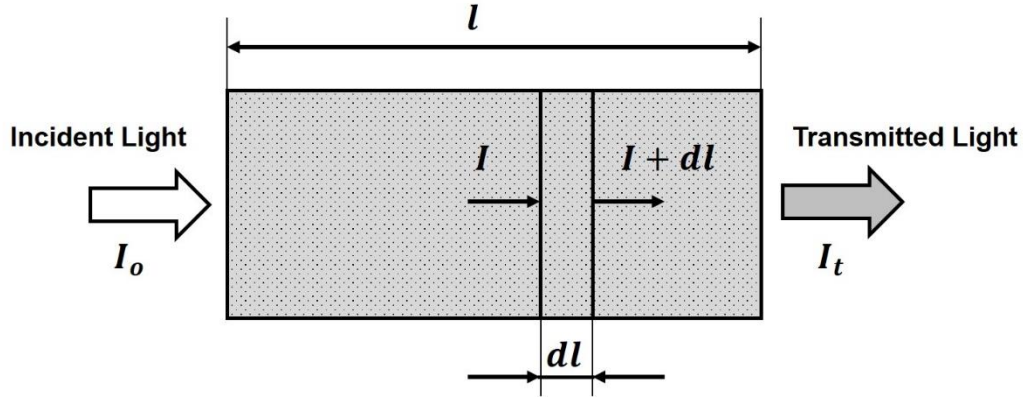

Figure 2.9 Bouguer-Lambert-Beer's Law

For the optical coefficient of liquid scattering R, it is determined by the correlation of the scattering light collection and optical lens. In this study, because the distance between the lens and spray was over 2m, which is much larger than the field depth of droplet, thereby the R was defined as 0.6 [213]. It is well known that given the refractive index of a spherical particle, the extinction efficiency Q_{ext} can be calculated with Mie theory. Previous study have proven that the regardless of the absorption, the total extinction of a cloud of particles approaches the limiting value 2 if the particles is sufficiently large [211]. Also, the fuel similar to gasoline properties, such as p-Xylene, was verified that the Q_{ext} reached 2 with the droplet size over 5μm at 266 and 532nm wavelengths [214]. For gasoline direct injection, the size of liquid droplet mostly falls into the range of 5~100μm, which is in agreement with the total extinction Q_{ext}=2. Therefore, the effect of the extinction error of visible and absorption wavelength on the vapor concentration measurement is limited. According to the Eqs. (2.10) and (2.11), the total extinction of scattering can be simplified as:

$$\frac{I_t}{I_0} = \exp[-R \cdot Q_{ext} \int_0^l \int_0^\infty \frac{\pi}{4} D^2 \cdot n \cdot f(D) \cdot dD \cdot dl] \qquad (2.12)$$

Also, the definition of the surface area of liquid droplet A_f [m^{-1}] can be described as Eq. (2.15).

$$A_f = \int_0^\infty \frac{\pi}{4} \cdot n \cdot f(D) \cdot dD \qquad (2.13)$$

If combining the Eq. (2.12), the A_f can be expressed related with the total extinction as:

$$A_f = \frac{2.303 \cdot \log(I_o/I_t)_{L_{sca}}}{R \cdot Q_{ext} \cdot l} \tag{2.14}$$

In consideration of sauter mean diameter D_{32} [m], the liquid concentration C_l [kg/m³] can be described by using A_f and D_{32} as follows.

$$C_l = \frac{2}{3} \cdot \rho_f \cdot D_{32} \cdot \frac{2.303 \cdot \log(I_o/I_t)_{L_{sca}}}{R \cdot Q_{ext} \cdot l} \tag{2.15}$$

$$D_{32} = \frac{0.63 \cdot R \cdot Q_{ext} \cdot M_f}{\rho_f \cdot \Sigma\{\log(I_o/I_t)_{L_{sca}} \cdot \Delta S\}} \tag{2.16}$$

$$M_f = \int_0^S \int_0^l \int_0^\infty \rho_f \cdot \frac{\pi}{6} \cdot D^3 \cdot n \cdot f(D) \cdot dD \cdot dl \cdot dS \tag{2.17}$$

Where S is the projected area [m²] of spray, and the M_f is the liquid mass which is derived from the total injected mass subtract the vapor mass. Therefore, the equivalence ratio of liquid phase can be obtained based on the liquid concentration C_l and ambient density C_a [kg/m³] .

$$AF_{stoich} = \frac{AF_{stoich}}{AF_l} = \frac{AF_{stoich}}{(1 - \frac{C_l}{\rho_f}) \cdot \frac{\rho_a}{C_l}} \tag{2.18}$$

2.5.1.4 Quantitative Analysis of Vapor and Liquid Phases

In order to calculate the spatial distribution of the liquid and vapor phase concentrations from the light-of-sight LAS images, the onion-peeling model [215] was adopted. The spray is assumed as an axisymmetric spray structure in this model. Then the traverse cross section of the spray is considered as be comprised of a number of concentric rings as shown in Fig.2.10, if the area of each ring can be regarded as homogenous. Based on the Eq. (2.5), the extinction by the vapor phase absorption in the first ring is written as Eq. (2.19).

$$\log(\frac{I_o}{I_t})_{\lambda_A} = \frac{\varepsilon}{M} \cdot C_V(1) \cdot l_{1,1} \times 10^2 \tag{2.19}$$

In the second ring, the extinction by the vapor phase absorption is written as Eq. (2.20).

$$\log(\frac{I_o}{I_t})_{\lambda_A} = \frac{\varepsilon}{M} \cdot [C_V(1) \cdot l_{2,1} + C_V(2) \cdot l_{2,2}] \times 10^2 \tag{2.20}$$

Following the same manner, the extinction by the vapor absorption in the number i ring can be acquired. Thereby, the vapor phase concentration in the i ring can be described as Eq. (2.21).

$$C_V(i) = \frac{1}{l_{i,i}} \cdot [\frac{1}{\varepsilon} \cdot \frac{M}{10^2} \left\{ \log\left(\frac{I_0}{I_t}\right)_{\lambda_A} - R\log\left(\frac{I_0}{I_t}\right)_{\lambda_T} \right\} - \sum_{k}^{i-1} (C_V(k) \cdot l_{i,k}) \qquad (2.21)$$

The local droplets density also can be devonvoluted in the similar way and derived as follows.

$$C_d(i) = \frac{1}{l_{i,i}} \cdot [\frac{2\rho_f D_{32}}{3Q_m} \cdot 2.303 \cdot \log\left(\frac{I_0}{I_t}\right)_{\lambda_T} - \sum_{k}^{i-1} (C_d(k) \cdot l_{i,k}) \qquad (2.22)$$
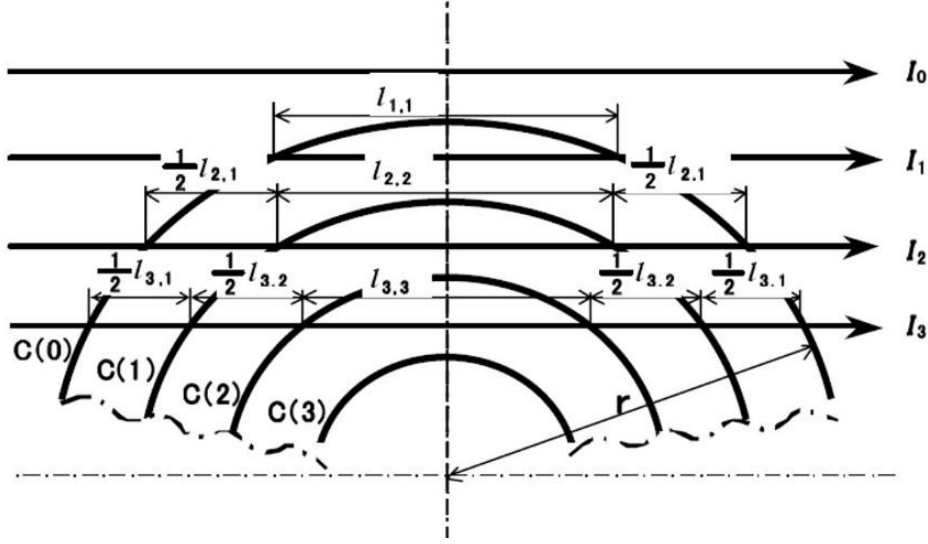

Figure 2.10 Onion-Peeling Model of Cross-Section

The flow chart of the LAS image processing in an axisymmetric spray is illustrated in Fig.2.11. First, the images with and without spray at both wavelengths are taken. Hence the extinction images in visible and absorption wavelengths can be obtained and the injection angle is corrected to ensure the vertical spray. Thereafter, according to the Eq. (2.3), extinction by vapor phase is gained by removing the extinction image of transparent wavelength from that of absorption wavelength. While the extinction by liquid phase is attributed to the extinction image of visible wavelength. Based on Lambert-Beer's Law and the onion-peeling model, the concentration distribution of vapor phase can be obtained. By summing up the vapor mass over the whole spray, thus the total vapor mass in the spray with time escape is known. Therefore, the liquid mass is derived from the difference between the total mass of injected fuel and the vapor mass. Consequently, using the onion-peeling model and Bourguer-Lamber-Beer's Law, the concentration of liquid droplets can be calculated.
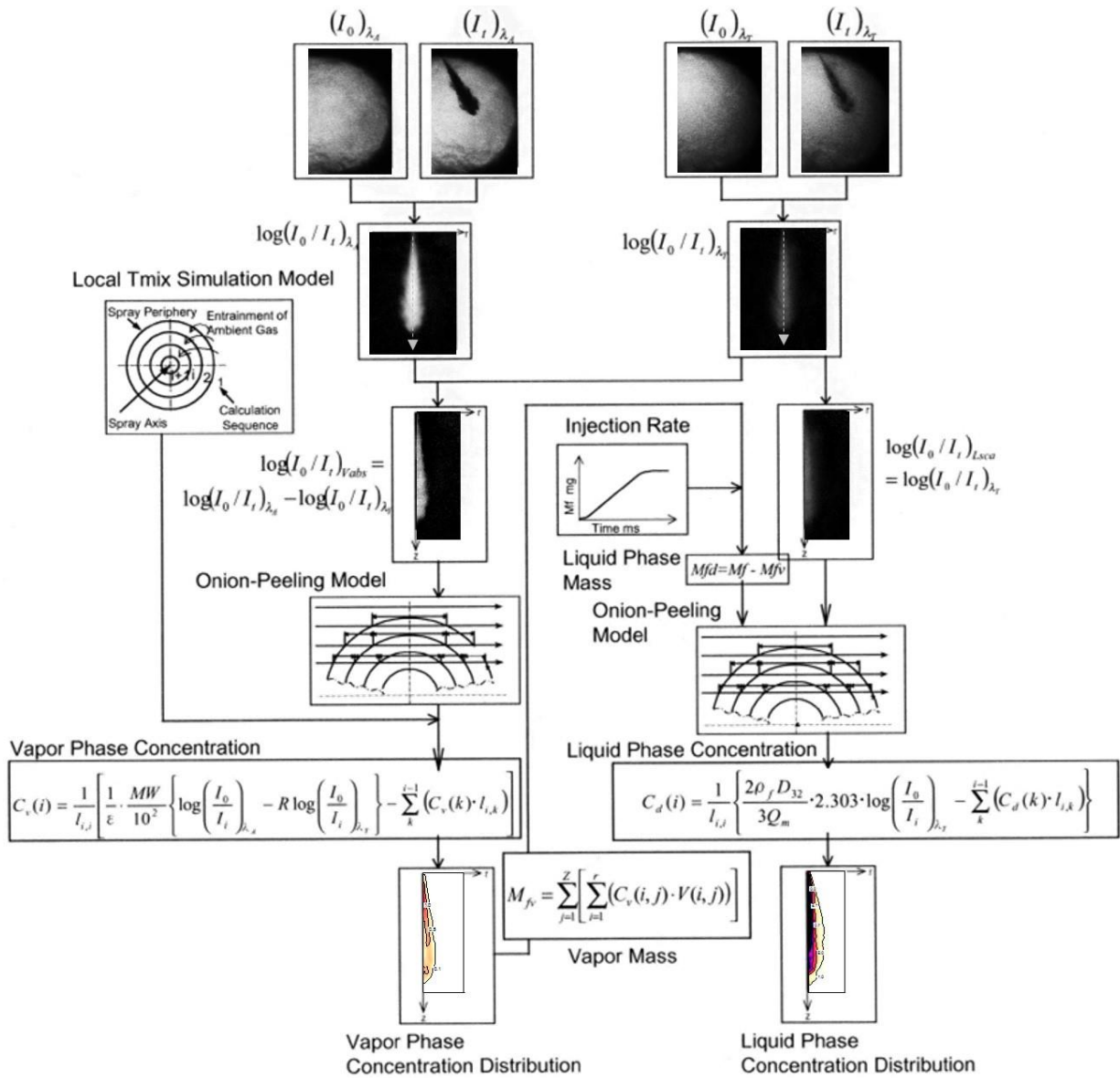
Figure 2.11 Flow Chart of LAS Axisymmetric Spray Measurement

2.5.1.5 Quantitative Analysis of Non-asymmetrical Spray

If using the LAS technique on the non-axisymmetric spray [216], such as the multi-hole injection or impinged spray, the preceding onion-peeling deconvolution method cannot be employed to calculate the vapor concentration. Therefore, an extended LAS data processing method for non-axisymmetric sprays was proposed by Gao et al. [217] and Zhang et al. [218], which suggested that the vapor mass in a light path was probably obtained by the integrating light extinction rate from the absorption wavelength at per unit area along the light direction.

Based on the Eq. (2.5), the integrated value of vapor phase mass $\overline{C_V}$ in the light path at per unit cross-sectional area can be expressed in Eq. (2.23).

$$\overline{C_V} = \int C_V dl = \frac{MW \cdot \log(I_o/I_t)_{V_{abs}}}{\varepsilon} \tag{2.23}$$

In this case, provided that the molar absorption coefficient is a constant in the direction of light path, the vapor mass M_V [kg] in the fuel spray can be obtained by integrating the average vapor concentration in whole spray area , and as shown in following.

$$M_V = \int \overline{C_V} \, dS = \int \frac{MW \cdot \log(I_o/I_t)}{\varepsilon} \times 10^2 \tag{2.24}$$

So far, by means of the extended LAS analysis, the accumulative mass of vapor and its distribution, as well as liquid phase, are able to be quantitatively measured in an non-axisymmetric spray. The flow chart of the extended LAS image processing is illustrated in Fig.2.12.
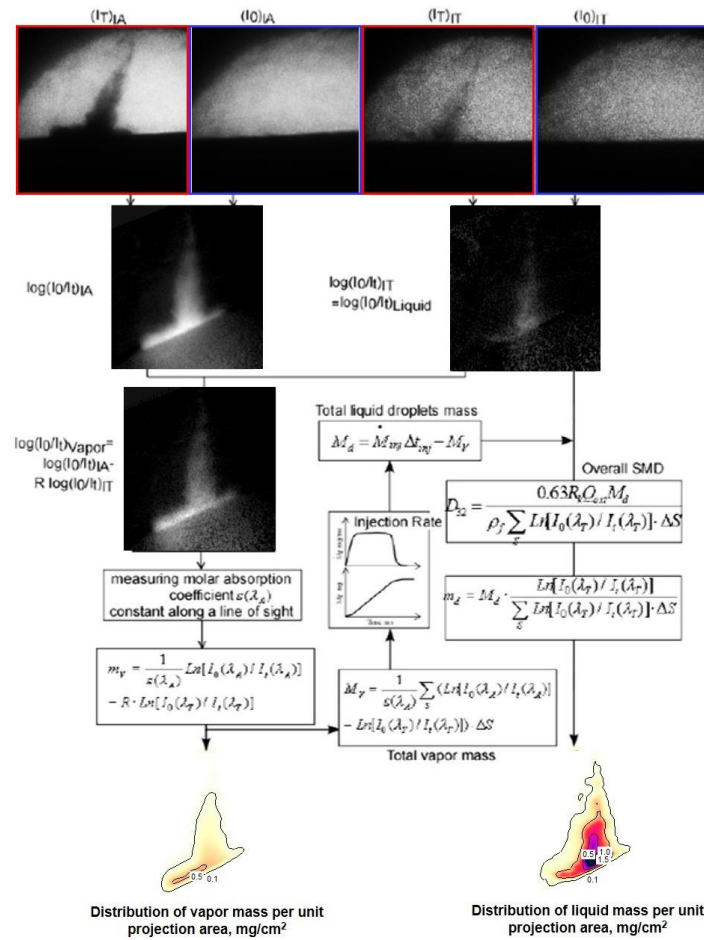

Figure 2.12 Flow Chart of LAS Non-Axisymmetric Spray Measurement

2.5.1.6 Test Fuels in LAS Experiment

For the hydrocarbon fuels, most of them have absorption band in ultraviolet and infrared region, but not in visible spectrum. It is evitable that the absorption is greatly dependent on the temperature in the infrared extinction technique. Moreover, this technique also tends to be influenced by radiation from heating system and interfered by existing water vapor in the measurement system. In contrast to it, the ultraviolet-visible laser extinction shows its great advantages to overcome the problems of infrared extinction, because the temperature tends to affect more strongly on low-frequency (infrared and far infrared) than high-frequency (visible and ultraviolet) absorption mechanisms. However, the disadvantage of ultraviolet-visible extinction is that many of hydrocarbon fuels have no sufficiently strong absorption band. Therefore, based on the theory of LAS, it is vital to find the suitable test fuel and exam its optical property, especially the absorption characteristics.

In this study, the ultraviolet-visible dual-wavelength laser absorption scattering technique was employed to detect the liquid and vapor phase distributions of gasoline and ethanol-gasoline blends. Therefore, two kinds of fuel, which simulates gasoline and ethanol respectively, should be considered in the fuel selection. The critical criterion of test fuel in LAS can be summarized as:

- The test fuels have similar physical properties, especially the atomization and vaporization properties, to the gasoline and ethanol respectively.
- High absorption for ultraviolet light and hardly sensitive to the visible light are required to the test fuels.
- Less temperature-dependence of absorption coefficient is another important requirement for the test fuels, which also should follow the Lamber-Beer's Law.

According to these factors, the spectrum characteristics of some candidate test fuels were examined, due to the much poor absorption of iso-octane (typically represents to gasoline) and ethanol at ultraviolet band. Some representative physical properties of candidate fuels were listed in Table 2.1.Firstly, we focuses on the gasoline surrogate fuels, thereafter, the discussion of ethanol test fuel will be followed. Such as benzene, toluene and p-Xylene, they have physical properties similar to those of gasoline in terms of evaporation (boiling point, latten heat and vapor pressure) and atomization (density, kinetic viscosity and surface tension). The previous study [212] using a normalized method of droplet size demonstrated that the p-Xylene and benzene shared almost the same evaporation history to the gasoline, instead of the toluene has a slightly faster evaporation rate. However, the calculation of gasoline was based on the iso-octane. If considering the multicomponent of gasoline, the evaporation of gasoline would probably become to follow the tendency of toluene, which also is implied at both the boiling point and vapor pressure in Table 2.1. Moreover, the evaporation of blended fuel also is greatly dependent on the boiling point of individual components under high temperature conditions. Taken into account the above issues, compared with the

higher boiling point of p-Xylene, the toluene seems more suitable to be the test fuel representing the gasoline. While the absorption of toluene should be carefully examined at the ultraviolet band.

Table 2.1 Physical Properties of Test Fuels for Gasoline and Ethanol (P_a=0.1MPa, T_a=298K)

Fuel	Boiling Point [K]	Density [kg/m^3]	Kinetic Viscosity[1] [mm^2/s]	Surface Tension[2] [mN/m]	Lower Heat Value [MJ/kg]	Enthalpy of Vaporization[3] [kJ/kg]	Vapor Pressure[4] [kPa]
Gasoline	T_{10}<343[5] T_{90}<453[5]	<783[6]	0.68[6]	20.8[6]	44.4	269.9[6]	6.3[6]
Benzene	353.4	874	0.69	28.2	40.2	394.9	12.73
Toluene	383.8	862	0.64	27.3	40.6	363.6	3.66
p-xylene	411.5	857	0.71	27.8	40.8	339.7	1.1
Ethanol	352	796	1.37	22.2	27	875.3	7.3
MEK	353	810	0.49	24.6	26.7	443.7	11.7

[1] The kinetic viscosity of mixture was based on the Lobe method.

[2] The surface tension of mixture was based on the Goldsack and Sarvas Model.

[3] The enthalpy of vaporization was based on the Riedel Empirical Method.

[4] The vapor pressure at 25°C was based on the Riedel Equation.

[5] JIS K 2202 T_{10}: Distillation temperature of 10% mass. T_{90}: Distillation temperature of 90% mass.
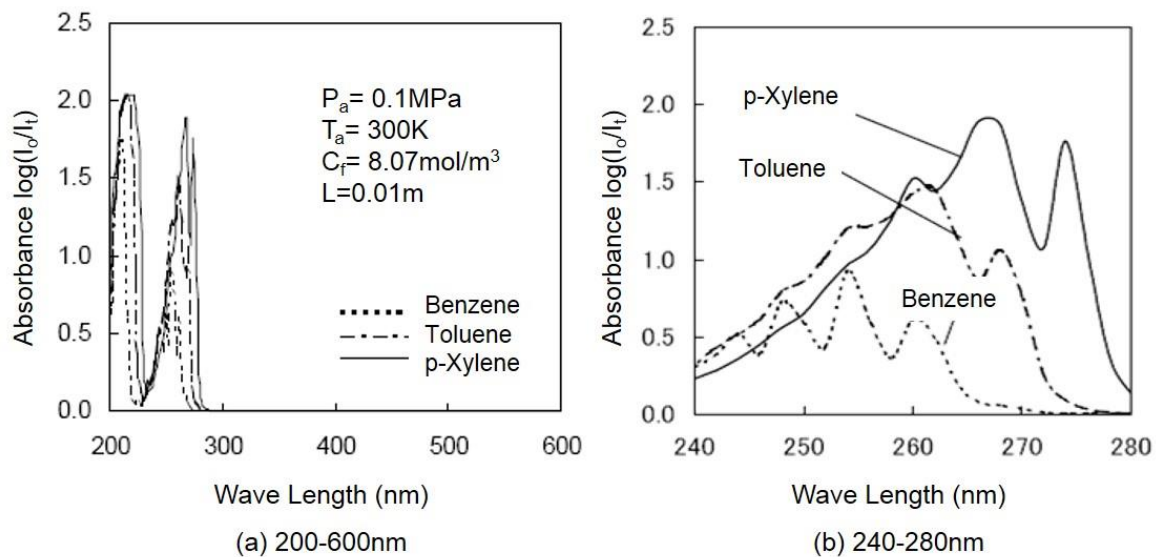
[6] iso-octane

(a) 200-600nm (b) 240-280nm

Figure 2.13 Absorption Spectra of Liquid Phase Candidate Fuels [212]

The absorption spectrum of the liquid phase of those candidate fuels were also studied by a UV-Vis spectrophotometer (Shimazu Co. UV-3000) with a bandwidth of 190-1200nm. All of those fuels have high absorption on the ultraviolet band of 200-300nm, but transparent for the visible band at 400-600nm as shown in Fig. 2.13 (a). In addition, the absorption band of toluene and p-xylene are sufficient large at the 266nm wavelength (see Fig. 2.13 (b)), in contrast to the benzene which shows a smaller absorbance, probably leading to a difficulty on the UV-Vis measurement.
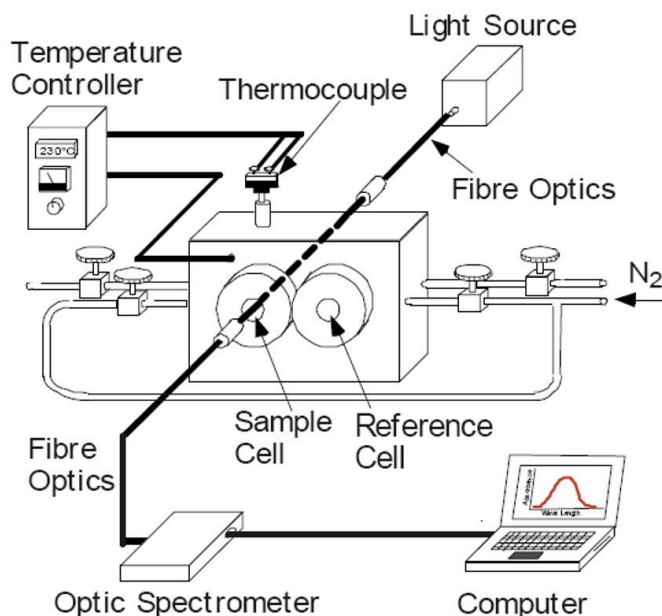

Figure 2.14 Experimental Setup of Molar Absorption Coefficient Measurement

Moreover, the absorption spectrum of the vapor phase toluene-nitrogen mixture under various temperature and pressure were measured by using a spectrometer (Ocean Optics, S-2000) and a high-temperature and pressure cell, in order to examine the dependence of temperature and pressure. The schematic of the molar absorption measurement is shown in Fig.2.14. The inner diameter of the visualized window was 15mm, and a 25W deuterium lamp (Ocean Optics, D-1000) of 190-410nm bandwidth was used as a light source. The light path was set to 100mm. the temperature and pressure of this cell can be elevated up to 900K and 5MPa respectively. The experimental conditions were determined by the engine operation at the compression stoke from -60°CA ~ -15°CA, corresponding to the temperature and pressure variation of 0.5MPa~1.5MPa and 425K~600K respectively based on the thermodynamic simulation in cylinder. The molar absorption coefficient can be calculated based on the Lamber-Beer's Law as mentioned in section 2.5.1.1 and expressed as follows.

56

$$\log(\frac{I_o}{I_t})_{V_{abs}} = -\varepsilon \cdot C_{v,mol} \cdot l \times 10^{-1} \tag{2.25}$$

$$\varepsilon = 10 \cdot \frac{\log(\frac{I_o}{I_t})_{V_{abs}}}{C_{v,mol}} \cdot \frac{1}{l} \tag{2.26}$$

Where $C_{v,mol}$ is the molar concentration, [mol/m^3]. Therefore, in terms of Eq. (2.6), the vapor concentration can be obtained in the LAS measurement. More detail of the vapor absorption measurement can be found in elsewhere [214, 219].
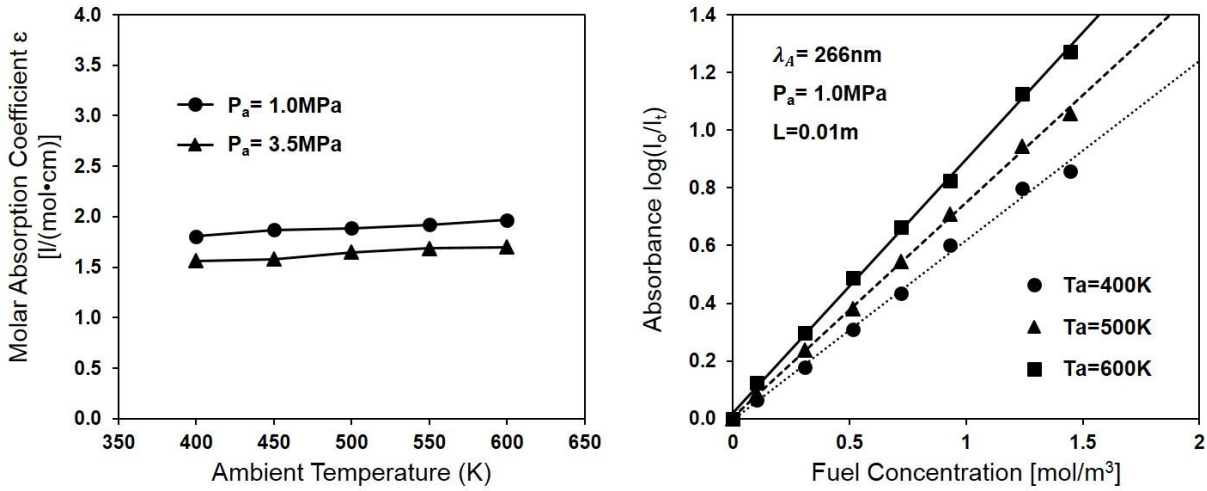

Figure 2.15 Absorption Characteristics of Pressure and Temperature Dependence for Toluene

Figure 2.15 shows the results of the absorption of toluene determined by the pressure and temperature. The molar absorption coefficient decreases with the increased of ambient pressure from 1.0MPa to 3.5MPa. While this coefficient slightly increases as the temperature is elevated from 400K to 600K. The tendency of the molar absorption coefficient varying with temperature suggests the favorable independence of the absorption of toluene on the ambient temperature. In addition, the relation between the absorbance and the toluene vapor concentration at different temperature under 1.0MPa demonstrates an excellent agreement with the Lambert-Beer's Law for the toluene absorption characteristics is validated. Figure 2.16 furthermore illustrates the comparison of spray structure for gasoline and toluene under the same ambient condition in LAS images. It can be seem that the spray structure shows a desirable consistency with gasoline and toluene, especially the spray tip penetration and spray angle. Therefore, according to the analysis of the gasoline surrogate fuels, the toluene was selected as the test fuel to represent the gasoline in LAS experiment.
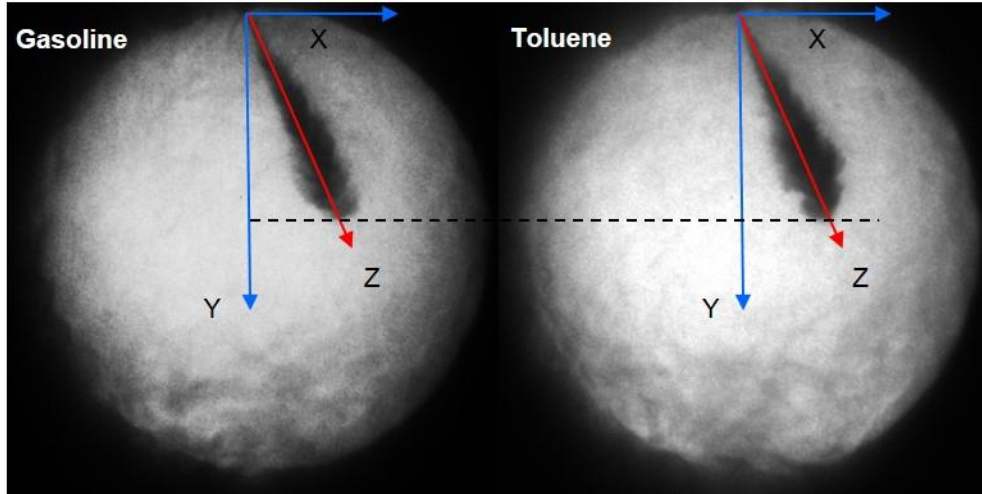
Figure 2.16 Comparison of Spray Structure for Gasoline and Toluene in LAS (P_a=1.0MPa, T_a=500K, P_{inj}=20MPa, t_{inj}=1.1ms, t_{AEOI}=0ms)
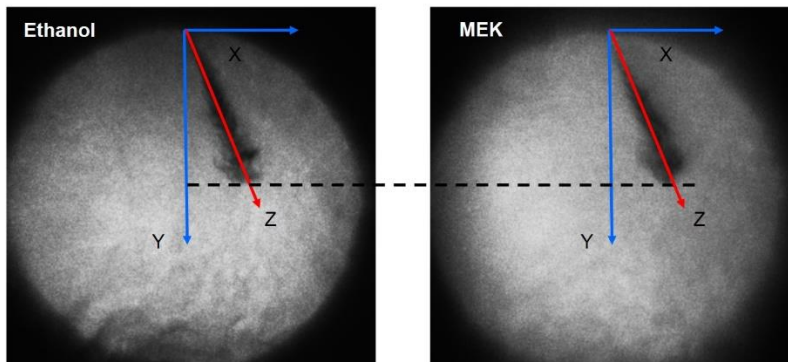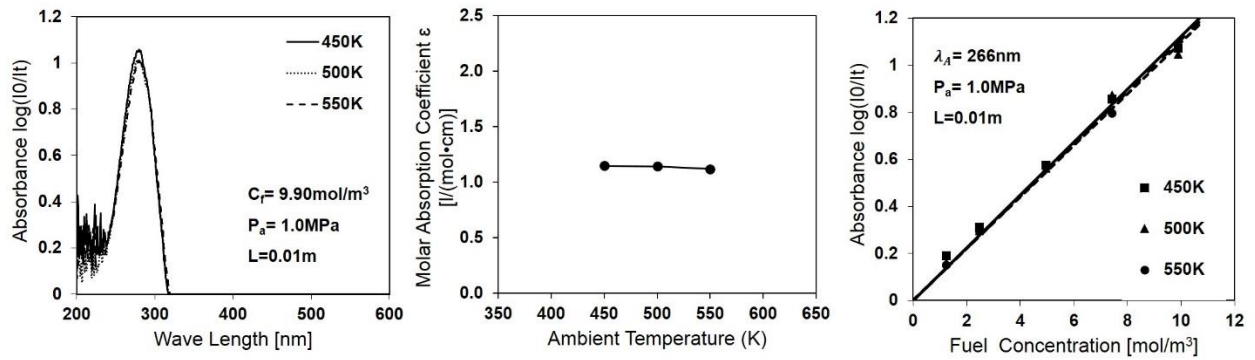

Figure 2.17 Absorption Characteristics of MEK and Comparison of Spray Structure of Ethanol and MEK (P_a=1.0MPa, T_a=500K, P_{inj}=10MPa, t_{inj}=1.51ms, t_{AEOI}=0ms)

For the test fuel of ethanol, the methyl ethyl ketone (MEK) shares the similar physical properties to the ethanol in Table 2.1, especially nearly the same boiling point and density. Figure 2.17 shows the absorption characteristics of MEK. It is obviously that the MEK has the high absorption at 266nm wavelength, but nearly none sensitive to the visible band. Also, it has a great temperature-independence on measurement and follow the tendency with Lambert-Beer's Law, which indicates that the MEK is competent to simulate the ethanol in LAS. Although the less difference of spray structure exists between the MEK and ethanol, it should be noticed that the kinetic viscosity of MEK is not half to that of ethanol. The effect of this difference on the spray atomization of test fuels simulating ethanol-gasoline blend will be discussed following.

Table 2.2 Physical Properties of Test Fuels for E85 (P_a=0.1MPa, T_a=298K)

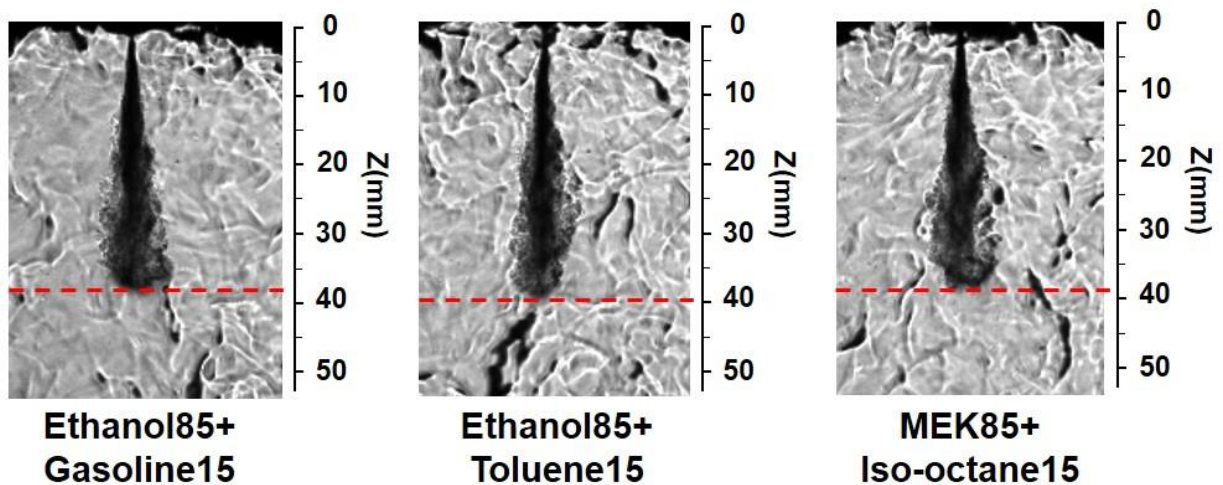| Fuel	Boiling Point [K]	Enthalpy of Vaporization [kJ/kg]	Vapor Pressure [kPa]	Density [kg/m^3]	Kinetic Viscosity [mm^2/S]	Surface Tension [mN/m]	Lower Heat Value [MJ/kg]
Ethanol85/ gasoline15	358	850.1	–	784	1.22	22.0	29.7
MEK85/ isoocatne15	356	417.6	11.1	792	0.56	23.8	29.3
Ethanol85/ toluene15	356	837.62	6.63	808	1.14	22.9	29.0

Figure 2.18 Comparison on Spray Structure of E85 and Its Surrogate Fuels in Shadowgraph (P_a=1.0MPa, T_a=500K, P_{inj}=20MPa, t_{inj}=1.1ms, t_{AEOI}=0ms)

The outline in Chapter 1 has demonstrated this study's purpose focused on the spray and combustion characteristics of different ethanol-gasoline blend fuels, including E0, E85 and E100. As mentioned above, the vapor distribution of E0 can be determined by pure toluene (denoted by toluene100) in LAS. Likewise, the vapor behavior of E100 can be determined by pure MEK (denoted by MEK100). While for the E85, the original representative group is the MEK85/toluene15. The previous study, however, revealed the difficulty of analyzing the vapor and liquid phases quantitatively for a binary spray if simultaneously using two fuels which were highly sensitive to the UV beam [220]. Consequently, the two groups of fuels, namely the Ethanol85/toluene15 and MEK85/iso-octane15, were selected as the candidates to determine the individual evaporation of gasoline and ethanol respectively in the E85 spray. While the kinetic viscosity of the surrogate fuels of E85 are different with each other, especially for those containing the MEK as shown in Table 2.2. Therefore, their spray atomization should be carefully examined in this study. The sauter mean diameter (SMD) of MEK85/iso-octane15 was approximately 72% to that of the Ethanol85/gasoline15 ($\approx$ 17μm) which was evaluated by the Hiroyasu's empirical equation [221]. While the SMD of Ethanol85/toluene15 was closed to the real fuel. Furthermore, the ambient condition with a high temperature tends to decrease the effect of the viscosity on the atomization. As shown in Fig. 2.18, the shadowgraph images are used as the benchmarking to make a comparison between the real E85 and its surrogate fuels. It can be seen that the spray structures of real E85 and its surrogate fuels are almost the same, and the relative error of the spray tip penetration is only approximate 4.5%. Consequently, these substitute fuel groups of Ethanol85/toluene15 and MEK85/iso-octane15, are convinced to simulate the E85 spray reliably in LAS experiment. The schematic of test fuels for E0, E85 and E100 respectively and the expect result acquisitions are illustrated in Fig.2.19.
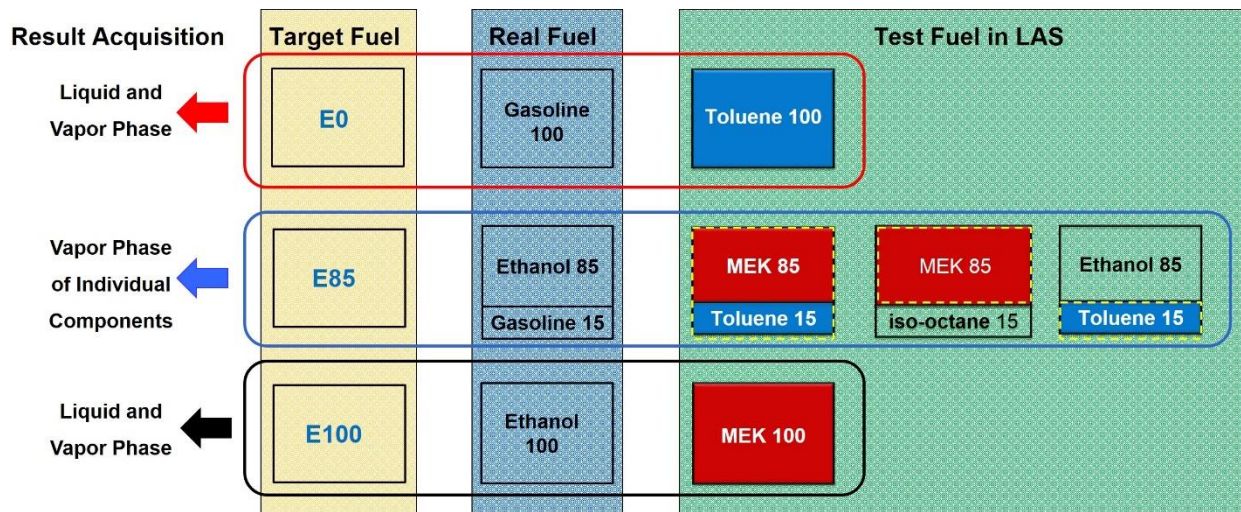

Figure 2.19 Expect Result Acquisitions of Test Fuels for E0, E85 and E100 in LAS

2.5.1.7 Experimental Setup of LAS Technique

In order to simultaneously measure the vapor concentration and droplets density in a fuel spray, a basic dual-wavelength laser imaging system is established by using toluene/MEK as the test fuels and the second (visible 532 nm) and the fourth harmonic (ultraviolet 266 nm) of a pulsed Nd:YAG laser. The imaging system mainly included the laser power unit for providing a radiation of two wavelengths, an optical system for expanding, collimating, and focusing the laser beam, CCD imaging system for concurrently recording and acquiring both attenuated and non-attenuated spray image at the two wavelengths respectively. The high-temperature and high-pressure constant vessel was used to provide an environment similar to that in an actual gasoline engine at near TDC condition, into which the fuel was injected at high pressures. Also, the homogeous temperature field in the constant veolume vessel was assuemed if maining the heating for 30 mintus after the expected temperature was reached.
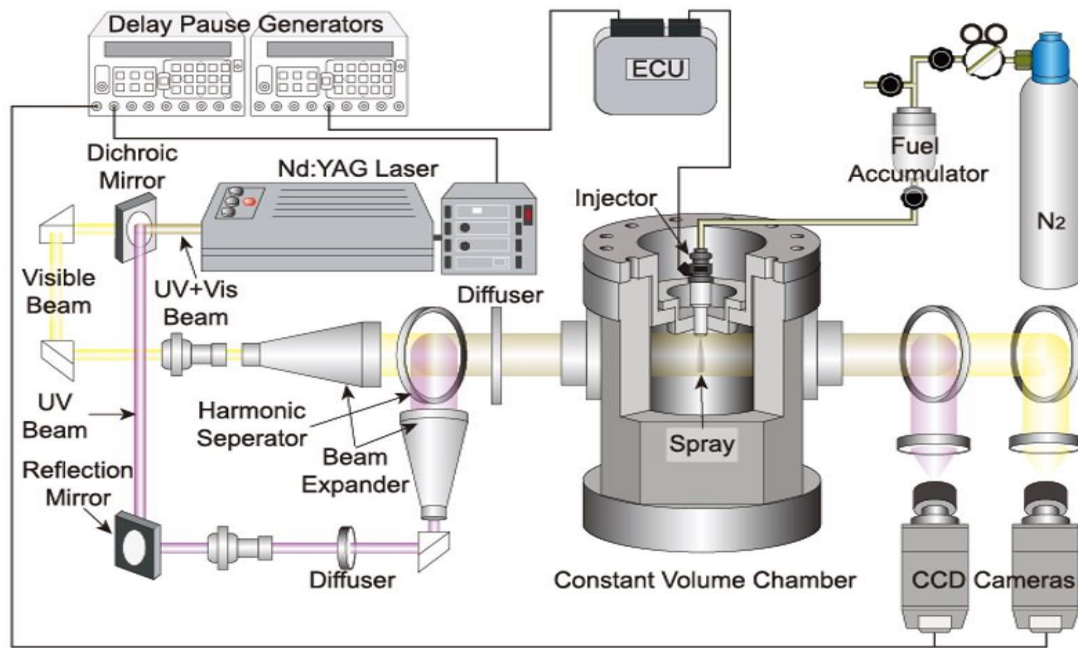

Figure 2.20 Experimental Setup of LAS Measurement

Figure 2.20 shows the optical setup of the ultraviolet-visible LAS imaging system and a high-temperature and high-pressure constant vessel associated with a fuel injection system. A pulsed Nd: YAG laser (Continuum, NY 61-10) emitted the coaxial laser beam consisting of the ultraviolet (UV) band (absorption wavelength, λ_A=266nm, 50mJ) and visible band (transparent wavelength, λ_T=532nm, 300mJ). A dichroic mirror separated the coaxial beams into two, an ultraviolet one and a visible one. The ultraviolet and the visible beam were then directed to the respective beam-expander and thereby were magnified into a diameter of 100mm. Thereafter, with an aid of the harmonic separator, the UV and visible beams were

combined together again and passed through the spray area in the chamber. Before the laser beam entered into the chamber, a diffusion sheet (Mitsubishi Rayon Co., thickness of the film: 18μm) was used to cut off the schlieren-like and light noises resulted from the heterogeneity of ambient gas density in the high-pressue and temperature volume vessel. Because of the absorption and scattering, the intensitys of the incident light, i.e., $I_0 (\lambda_A)$ and $I_0 (\lambda_T)$, were attenuated into $I_t (\lambda_A)$ and $I_t (\lambda_T)$ when transmitted by the fuel vaopr and droplets. After this light extinction, the two transmitted beams were re-separated into two, a visible beam and UV beam again, by a dichroic mirror. Then the collimating lenses focused these two beams into the CCD cameras (Hamamatsu Co., C4880)repectively, thereby the light extinction images of spray were recorded. The bandpass filters in front of CCD camears were used to cut off the noise cuased by the wavelength of light beyond that of the incident light. And the scattering light intensity was adjusted by the special apertures availuable for detecting half angles. Image acquired by CCD cameras were 16-bit digital data, from which the optical thicknesses at the two wavelengths were able to be obtained through some arithmetic processing. The Table 2.3 shows the detail information about the specification of optical systems.

Table 2.3 Specification of Optical System in LAS Measurment

|	Type	Continuum, NY61-10	
	Wavelength	532nm	266nm
Nd: YAG Laser	Energy	300mJ	50mJ
	Energy Stability	±3.5%	±10.0%
	Pulse Width	4~6nm	3~5nm
	Type	Hamamatsu Photonics C4880-21-24A	
	Effective Number of Pixels	512×512	
CCD Camera	Cell Size	24×24μm	
	Exposure Time	20ms or more	
	A/D Converter	12/14/16 bit Grayscale	
Spectral Filter	Transmittance	λ=532nm:80%	λ=266nm:15%
Aperture	Diameter of Hole	λ=532nm: 16mm	λ=266nm: 8mm
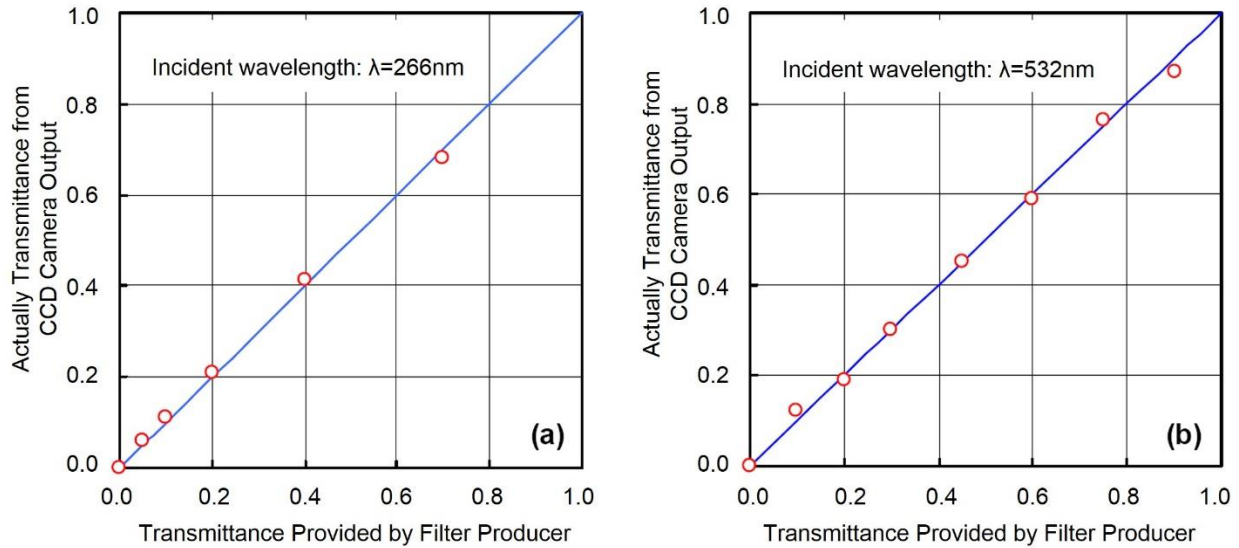
Figure 2.21 Calibration of Imaging System by Standard Optical Filters (a) λ=266nm (b) λ=532nm

For each standard neutral density (ND) filter with known transmittance, which was provided by the filter producer, two transmission measurements were made to record both the light intensity with the absence of the filter, and the intensity transmitted through the filter. Figure 2.21 shows the measurement resutls of actually transimittance obtained from CCD camera output at UV and visible wavelengh. The linear distribution of the actual transmittance ensures the reliable light intensity and releases the fatct that the relative error in optical thickness is proved approximately 3.2% by ultraviolet measurements and approximately 4.0% by the visible measurements.

In order to eliminate the impact induced by the jet-to-jet variation, per 4 laser shots for each spray at specific injection timing was required to obtain the reliable image. A single valve-cover-orifice (VCO) hole-type nozzle was pressurized by the high-pressure accumulator and controlled by an ECU unit. The electrical triggering signal generated by the delay pulse generators (Stanford Inc., DG535 and 645) were sent to synchronize the pulse of laser, CCD shutter and the injection.

The accuracy of the extinction correlation of UV and visible light has been discussed in section 2.5.1.1. However, the overall measurement accuracy of LAS technique should be evaluated carefully. Based on the arithmetic of LAS, the mass of vapor is firstly to be calculated, thus the mass of liquid phase is obtained by the total injected fuel subtracts that of vapor. In order to verify the accuracy of the result of vapor mass, it is necessary to use the fuel evaporating spray under a high temperature condition. The completely evaporating spray is considered as an effective way to evaluate the accuracy of vapor mass, since the calculated vapor mass should equal to the total injected mass without any liquid droplets. The experimental condition is shown in Table 2.4.

Table 2.4 Experimental Conditions

Ambient Condition	Gas	Nitrogen	
	Temperature (K)	500	
	Pressure (MPa)	1.0	
Injection Condition	Injector	Single VCO Hole-type	
	Injection Pressure (MPa)	20	
	Fuel	Toluene	MKE
	Injection Pulse (ms)	1.1	
	Injection Mass (mg)	1.67	1.66
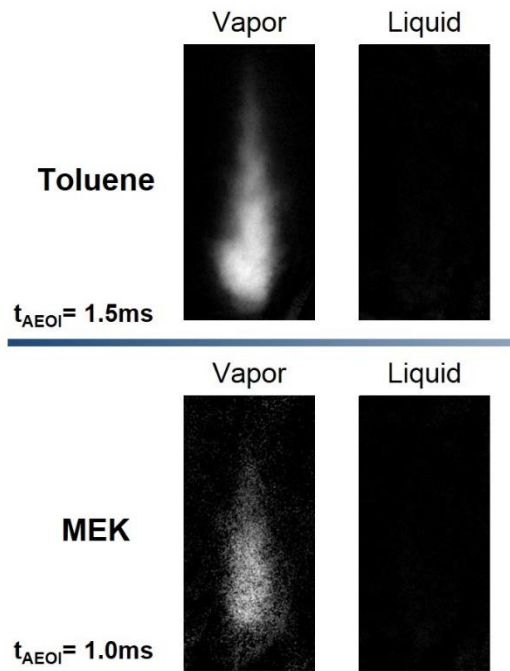
(a) Optical Thickness Images of Vapor and Liquid Phase at Completely Evaporating Spray
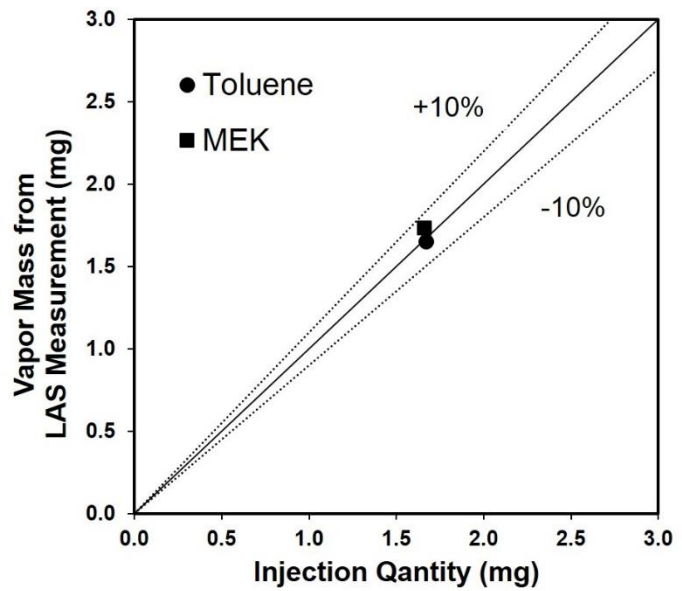
(b) Correlation of Vapor Mass Measured from LAS and Total Injected Fuel Mass

Figure 2.22 Accuracy Evaluation of Vapor Measurement for Toluene and MEK under Axisymmetric Completely Evaporating Spray (P_a=1.0MPa, T_a=500K, P_{inj}=20MPa, t_{inj}=1.1ms)

The light attenuated image in Fig. 2.22 (a) shows that it is hard to find any liquid droplets under the complete evaporation condition either for toluene at t_{AEOI}=1.5ms, or for MEK at t_{AEOI}=1.0ms. The toluene takes more time to approach totally evaporation than MEK due to its higher boiling point. The right column

of Fig. 2.22 also suggests the result of measured vapor mass in consistent to the total injected mass within the 10% error. Beside the axisymmetric spray, the overall accuracy of LAS measurement also should be considered in the non-axisymmetric spray. Previous study [214] using p-xylene as the test fuel under the same ambient environment, has proven the measurement error of vapor mass in the range within ±13% at the impinged spray. However, with introducing the binary spray, such as MEK85/iso-octane15 and Ethanol85/toluene15 employed to represent the E85, the verification of the interference on the vapor mass measurement should be considered in this study. The Ethanol85/toluene15 was selected to measure the vapor mass of toluene component under completely evaporating-impinged spray as shown in Fig. 2.23. The result demonstrates that the measured error of vapor phase of individual component in impinged binary spray locates at the acceptable level within ±15%, a slightly higher than impinged spray of pure fuel.
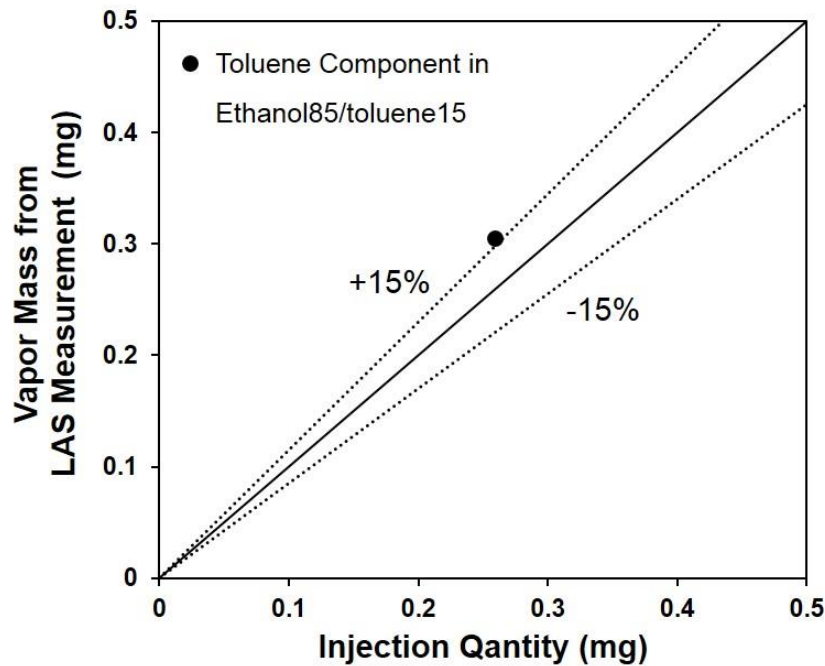
Figure 2.23 Correlation of Vapor Mass Measured from LAS and Total Injected Fuel Mass in Impinged Spray under Non-axisymmetric Completely Evaporating (P_a=1.0MPa, T_a=500K, P_{inj}=15MPa, θ_w=65deg, T_w=298K, t_{inj}=1.3ms, M_f=0.259mg)

2.5.2 Schlieren/Shadowgraph

Schlieren/shadowgraph imaging have been used for many years as a fundamental and powerful tool to identify refractive index gradients in various applications, such as turbulent multi-phases flow and flame propagation. Despite this light-of-sight technique is limited to obtain quantitative results, schlieren imaging

can visualize the internal structures of the gas-liquid coexisting fluid flow. For evaporating fuel sprays, the schlieren/shadowgraph was widely used to detect the boundary between vaporized fuel and the background ambient gas due to (1) a different refractive index at the interface between the ambient gas and fuel, and (2) the dramatic density gradient forming as the evaporating fuel cools down the ambient gas [222]. So far, numerous studies have been conducted in automobile application on either the fuel sprays [222-225] or gaseous fuel jets in engine-like condition [226]. The detail theory and diagnostic considerations of schlieren technique are available in many textbooks [145]. Also, its application in gasoline sprays also have been summarized in elsewhere [146].

Schlieren signal is proportional to the first derivative of the refractive index, which means that it can visualize flows as a uniform refractive index gradient exists at the ambient and be higher sensitive than shadowgraph. For the high temperature and pressure conditions, however, shadowgraph shows its great advantage to eliminate a background variation because of the naturally great density gradient at the ambient gas, and falls within the photo post-processing since the shadowgraph without any schlieren stops, namely "focused shadowgraph", can collect more light which allows decreased exposure time and increased frame rates. That is to say, the "focused shadowgraph" has enough sensitive to detect the boundary of a spray in this high temperature and pressure environment [227].
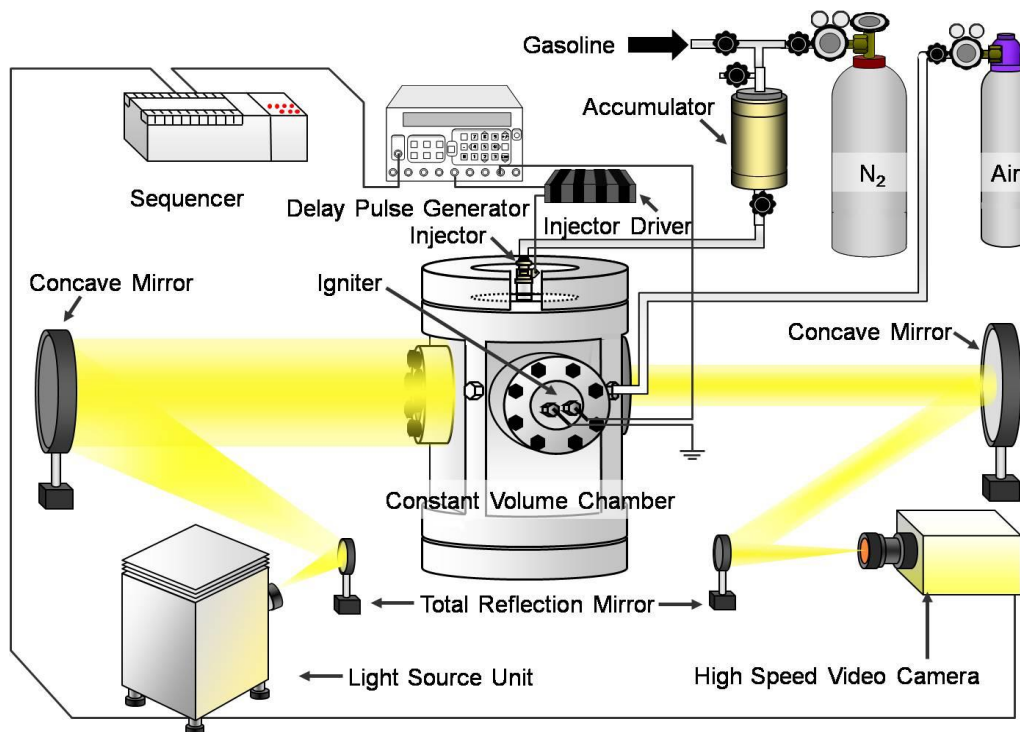

Figure 2.24 Experimental Setup of Z-type Shadowgraph

Therefore, the experimental setup of the "focused shadowgraph" was employed in this study as shown in Fig. 2.24, to investigate the spray evolution interacted with flame development, and the ignition probability for fuels under various spark timings and locations. A xenon flash lamp (Mizojini Optical Co., 1kW) with adjustable aperture was used as a continuous white light source. A white light source is convenient, and in fact, preferred in schlieren imaging over a laser since it avoids diffraction (or speckle) effects that occur with coherent light source. The reflection mirrors were used to form into the Z-shape light path that can take full advantage of the room space. The light was passed through a 1mm aperture to forma a high quality point-like source, which was collimated by a 200-mm diameter concave schlieren mirror (f=2000mm). This parallel light passed through the combustion vessel, enabling the visualization of the spray and combustion. Then the collimated beam was re-focused by a second 200-mm concave mirror (positioned 1790mm from the combustion vessel center), and finally collected by the color/black-white high-speed camera equipped with several different Nikkor lenses. The image acquisition was operated at the 10000 frame per second (FPS), resolution of 512×512 mm and a fully open shutter. Special apertures were used for different type of fuels in order to ensure the sufficient light intensity for capturing the ignition and flame.

However, the quantitative analysis of flame development is difficult to be obtained from shadowgraph in the spray combustion condition, regardless of many literatures reporting the utility of schlieren/shadowgraph in premixed mixture to study laminar or turbulent flame [228-231]. Because the edge of thin/thick flame can be quantitatively identified in accordance to the schlieren theory under the premixed condition [232-233]. While the spray-combustion process in this study tends to cause a stratified mixture, thus leading to a premixed-diffusion combustion. Because of the high level of mixture fluctuation, in some rich zone the appearance of high soot luminosity from hydrocarbon fuels, such as gasoline or diesel, probably disturbs the observation of flame front. In contrast, some intermediate species in chemical reaction, i.e., OH and CH during combustion process, can be regarded as the "marker" to characterize the flame front, thus more suitable to be used for the quantitatively analysis of flame which will be discussed in the following section.

2.5.3 Simultaneously Imaging of Natural Flame Luminosity and OH* Chemiluminescence

The natural luminosity (NL) of the flame is usually used as an intuitively way to analyze flame structure in diesel flame [234] due to its considerably high luminous level. Also, there are two main components included in flame natural emission: soot incandescence and chemiluminescence [235]. Soot incandescence is a broadband thermal radiation from hot soot particles while the chemiluminescence is non-thermal radiation with relatively narrow spectral ranges emitted from some combustion intermediate species. Since

different types of flame are relative to the corresponding colors (i.e., blue for non-luminous flame, yellow/orange for luminous flame), the combusting flame can be characterized by the flame color in a red-green-blue (RGB) image recorded by a color high-speed camera. In addition, the luminous flame signal in fuel combustion is known to be dominated by soot incandescence. Therefore, the characteristics of flame visualization and soot formation can be qualitatively analyzed by the natural luminosity. Also, the direct imaging was used to detect a spray movement based on the Mie scattering, in order to investigate the spray evolution under different ambient environment. In this case, a xenon lamp (Ushio Inc, SX-UID 510XAMQ) was used to illuminate the spray droplet at the right angle direction with the camera.
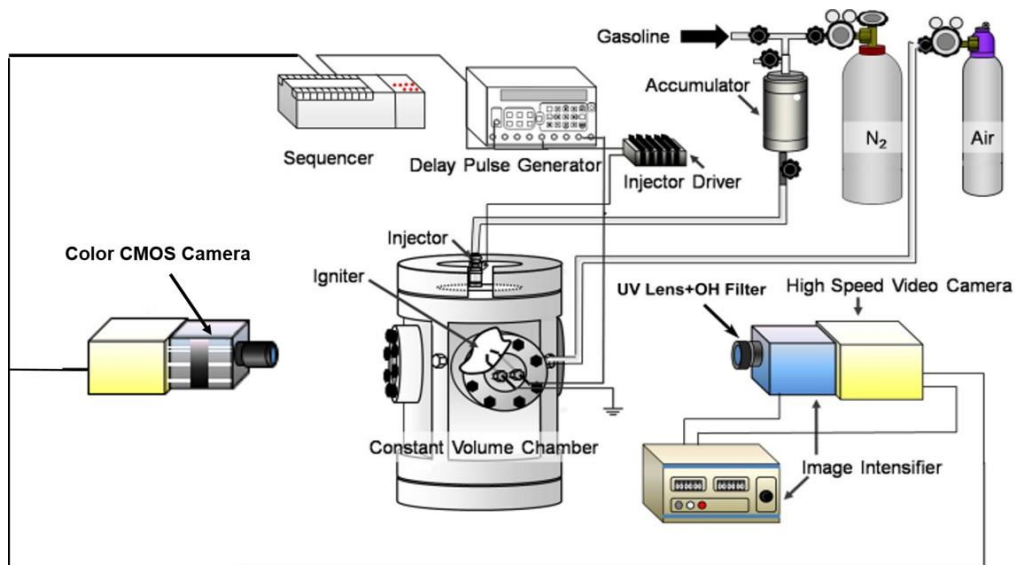

Figure 2.25 Experimental Setup of Simultaneous Imaging of Natural Luminosity and OH* Chemiluminescence

The signal of OH* chemiluminescence is recorded and showed the shape of flame only because of forming in the flame front region, so that possible to extract the information of the flame morphology. Also, OH* emission is accepted to the application of an excellent marker of combustion activity and predicting alternation of in-cylinder temperature and pressure since it yields in the chemical reaction at the near-stoichiometric and high heat release region as discussed in section 1.4.3.2. Although this light-of-sight technique prevents a straightforward interpretation on the local flame as opposed to the spatially resolved imaging, the integrated distribution of the OH* intensity also provides a useful information on the combustion behavior, especially for the global burning performance.

In this study, in order to analyze the flame characteristics and combustion performance, the flame natural luminosity and OH* chemiluminescence were captured simultaneously to the convenience

discussion of flame development and soot formation for ethanol-gasoline blends. Figure 2.25 shows the schematic of experimental setup.

The constant volume vessel is the same with the shadowgraph experiment. Due to the weak signal of the OH* natural emission, the visualization of the OH* chemiluminescence necessitated the image intensifier (HS-IRO, LaVision Inc) with a carefully chosen gain value of 85µs for the reliable image acquisition without saturation. Because of no need for the color imaging, the black-white camera (FASTCAM-APX RS, Photron Co.) was used to capture the OH* emission with a resolution of 512×512 pixels. To avoid the interference from soot luminosity, a special narrow filter for OH* detection is needed. One of the strongest bands of OH* emission occurs near 310nm. Furthermore, Siebers et al. [236] reported that the light at near 310nm is dominated by OH* chemiluminescence rather than soot emission, while the impact of soot luminosity becomes the primary emission at over 340nm. Therefore, a bandpass filter of 313nm (10nm full width at half-maximum (FWHM)), coupled with a UV lens (Nikon, F=105mm, f/5.6), was used to detect the electronically excited $A^2 \Sigma$ wavelength from the OH* emission. In order to characterize the NL signal, a high-speed color video camera (MEMRECAM GX-1, Nac Co.) with high sensitivity was used at the oppose side of the OH* camera. A short focus lens (Nikon, F=50mm, f/2.0) was use to allow a high spatial-resolution NL image of 468×468 pixels. A frame rate of 10000/s was set for these two cameras to obtain the temporally resolved scale as the 0.1ms per image.

2.6 SUMMARY

In this chapter, the specific experimental apparatus, consisting of constant volume vessel, injection system, ignition system and electrical controlling were introduced in detail. In order to investigate the spray and combustion of ethanol-gasoline blends, some main measurement techniques also were presented. Summaries are shown as follows.

1. High temperature and high pressure constant volume vessel with 500K and 1.0MPa respectively was used to provide the similar thermodynamic environment to the near TDC in DISI engine. A valve-cover-orifice (VCO) single hole nozzle, pressurized by an high-pressure accumulator, was employed to make the fundamental study of spray and combustion. The injection pressure was set to 10MPa, 15MPa and 20MPa respectively in different experiments. A special designed igniter was installed in the perpendicular direction to the light path, with less interference with the spray. The synchronization process of injection, ignition and imaging was controlled by a delay pulse generator.

2. A dual-wavelength ultraviolet-visible laser absorption scattering (LAS) technique was used to differential the vapor distribution from the liquid fuel. The most significant factor is to find the suitable test fuels to represent the real fuel. After being examined the absorption characteristics, the surrogate fuels, toluene and methyl ethyl ketone (MEK), were believed as the favorable test fuels to represent the gasoline and ethanol in LAS experiment, due to those sharing the similar physical properties to the real fuels and high absorbing for ultraviolet light, as well as less temperature-dependence in absorbance. Also, based on the empirical equation of spray atomization, the spray of E85 was proven that it can be characterized by the surrogated fuels, namely Ethanol85/toluene15 and MEK85/iso-octane in which the individual vapor phase in E85 was able to be acquired.

3. Shadowgraph was used to study the interaction of spray and flame development due to its high sensitive to the density gradient in the high-temperature and pressure condition. Also, the ignition probability was verified based on this technique. Mie scattering also was employed to study the spray evolution under various ambient condition, in order to provide a deep information of the spray characteristics for ethanol-gasoline blends.

4. Direct photography using the color high-speed video camera was used to image the flame natural luminosity, in the purpose of characterization of the flame visualization and soot formation. In order to quantitatively analyze flame development, the OH* chemiluminescence was employed to investigate the combustion behavior for different fuels. Combining the natural luminosity, the correlation of soot formation and flame development was able to be studied.

CHAPTER 3 ANLYSIS OF SPRAY EVOLUTION FOR ETHANOL-GASOLINE BLEND VIA HIGH-SPEED IMAGING

3.1 VISUALIZATION OF E85 SPRAY BY MIE SCATTERING

In direct-injection spark ignition (DISI) engines, the spray evolution is a key factor for the in-cylinder mixture formation, especially the wall impingement easily causing a fuel film on the piston. Hence a pool fire may occur when the flame propagates towards the cavity wall that results in a high-level emission of unburned hydrocarbon (UHC) and particulate matter (PM). In addition, a more sever spray-wall interaction if using ethanol-gasoline blend as fuel, may occur at the near TDC as a result of a longer spray tip penetration due to more injected mass required to maintain the same air/fuel ratio to gasoline as shown in Fig. 3.1. Therefore, the study of spray characteristics of ethanol-gasoline spray injected by hole-type nozzle becomes more significant. In this chapter, the visualizations of ethanol-gasoline blend spray (E85) under various injection pressure, ambient density and temperature were conducted to make the characterization of spray evolution.
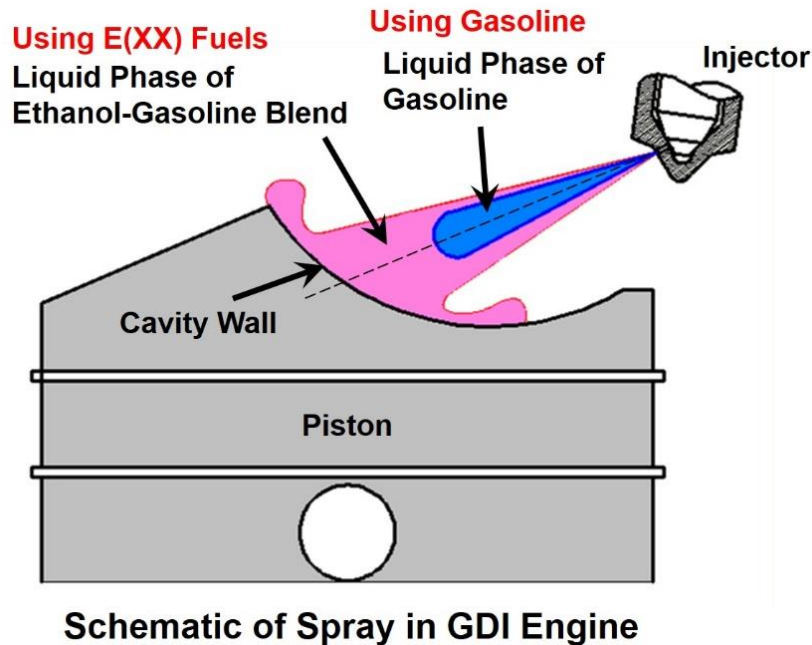
Figure 3.1 Spray Schematic of Using Ethanol-Gasoline in GDI Gasoline Engine

3.1.1 Experimental Condition

Mie scattering was employed in this chapter to measure the spray characteristics for ethanol-gasoline blends. The optical setup was discussed in Chapter 2 and as shown in Fig. 3.2. A Nikkon lens with F/105mm, f/2.0 was used to detect the spray. Detail experimental conditions were shown in Table 3.1. Experiments were conducted in various injection pressure, ambient temperature and density based on the ideal gas equation. The wide-range typical ambient temperature and gas density were selected to simulate the DISI engine operations from suction stroke to near TDC. In this study, because the backpressure was set to the range from 0.18MPa to 1.0MPa which was lower than that in diesel spray condition, a 1.2mg injection mass was carefully chosen in order to avoid the spray tip beyond the visualization window within a short time interval by using high injection pressure, i.e., 16/20MPa, under a low ambient density, i.e., 2/4 kg/m^3. Different injection pulses were also determined by the total injected mass for the corresponding injection pressures, from 1.44ms for 4MPa to 0.75ms for 20MPa. The image pixel resolution was determined to 512×512, and a 10000/s shutter was set to ensure a high temporal resolvedly image.
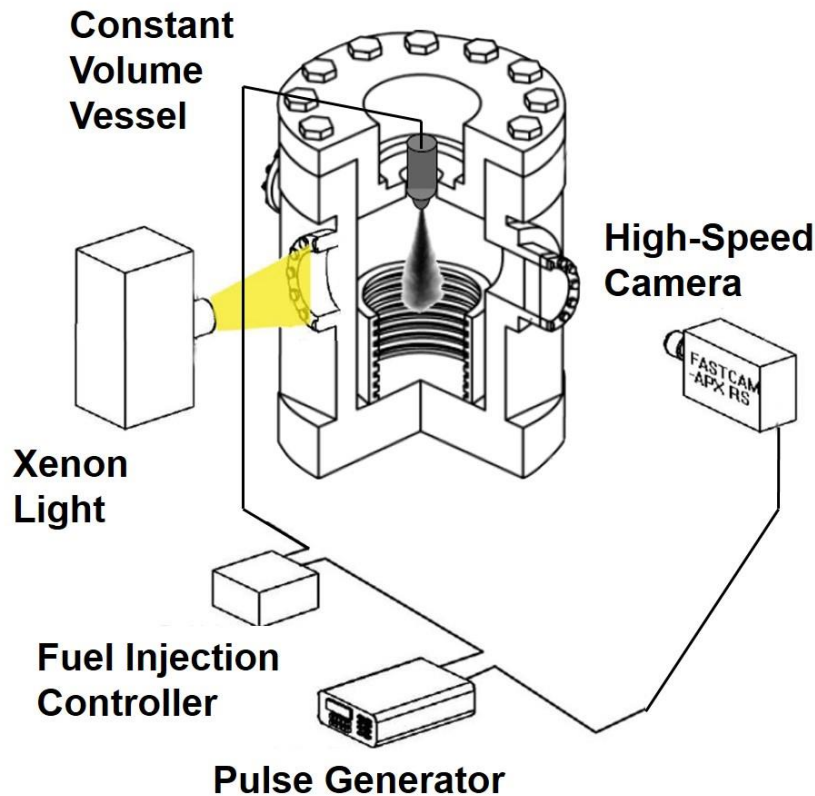

Figure 3.2 Experimental Setup of Mie Scattering

Table 3.1 Experimental Conditions for Mie Scattering

Ambient Condition	
Ambient Gas	Nitrogen
Ambient Temperature, T_a (K)	300, 350, 400, 450, 500
Ambient Density, ρ_a (kg/m^3)	2, 4, 6, 8, 10
Fuel	
Type	E85 (85% ethanol+15% gasoline)
Density, ρ_f (kg/m^3, 298K)	796
Kinematic Viscosity, ν (mm^2/s, 298K)	1.37
Surface Tension, σ (mN/m, 298K)	22.2
Injection Condition	
Injector Type	VCO single hole type
Hole Diameter, D (mm)	0.15
L/D	2.0
Injection Pressure, P_{inj}, (MPa)	4, 8, 12, 16, 20
Injection Mass, M_{inj}, (mg)	1.2
Injection Duration, t_{inj} (ms)	1.44, 1.08, 0.93, 0.82, 0.75

3.1.2 Image Processing and Analysis Method

In order to quantitatively analyze the spray characteristics, the proper post-processing of image is required. Figure 3.1 shows the flow chart of the image processing. Firstly, the background cut-off image is made to eliminate the background noise from ambient and light interference. Then a binarized image is produced by choosing a proper threshold value to further identify the spray region. It should be mentioned that the spray structure and penetration length does not be changed too much based on the chosen threshold value. In this study, a threshold of 10 (4% of the maximum intensity of 255) was selected to distinguish the spray edge. Thereafter, a clear spray image is produced and the specific algorithm should be employed to analyze the spray characteristics. As shown in Fig. 3.3, the liquid penetration length S_L is determined by the distance from the nozzle tip to the farthest axial location of the spray boundary in the binarizaiton image. And the angle of liquid-containing core θ_L is dependent on the radial distance at the axial location of the half length of spray tip penetration. The spray volume was considered as an important factor to investigate

the spray evolution. According to the detection algorithm on spray edge developed by Excel Micro, the total volume V_L of spray can be gained by the integration of individual volume element in pixel scale along the spray axis. Every case of spray even was imaged 5 times to get the reliable data.
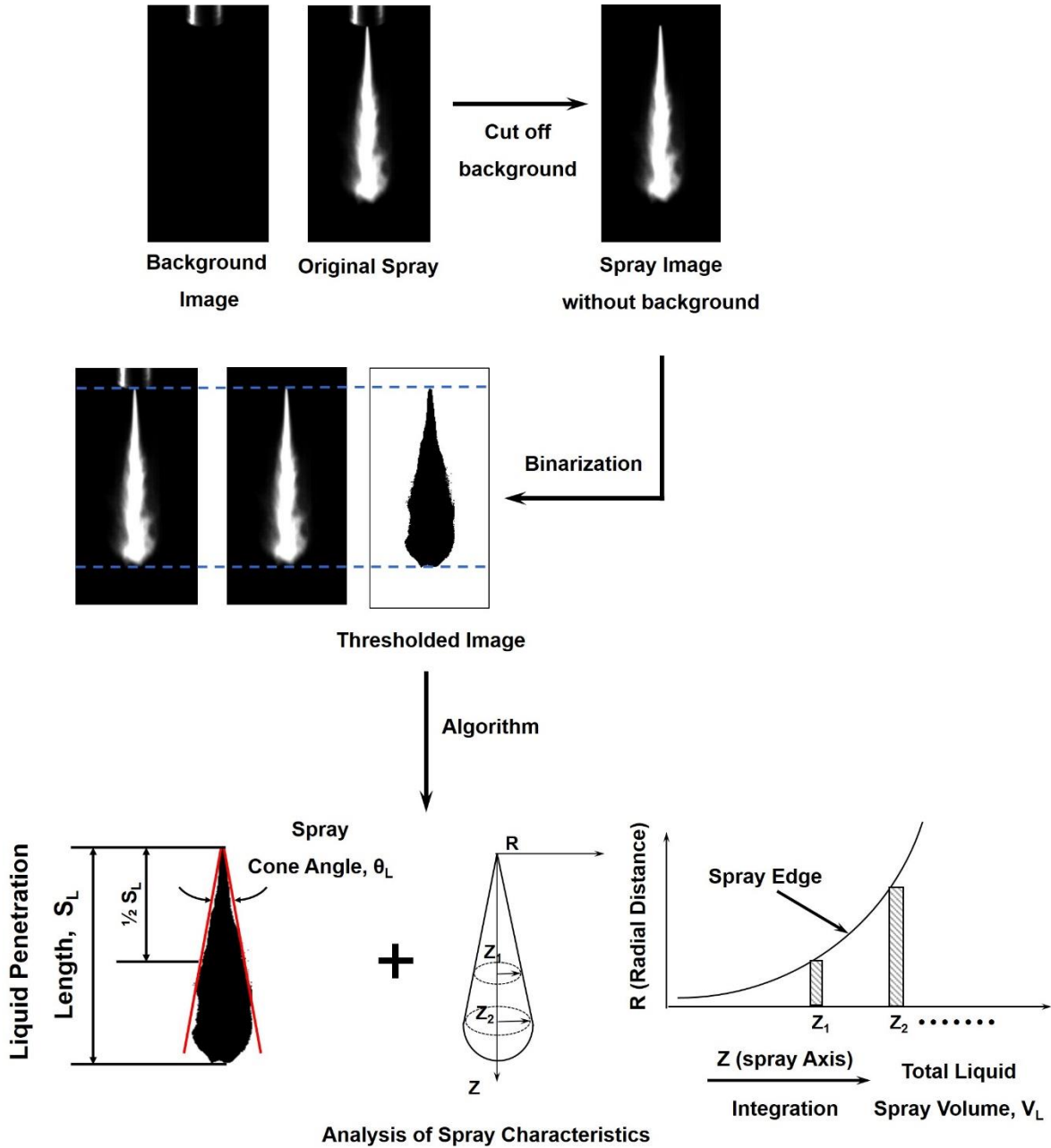

Figure 3.3 Flow Chart of Post-Processing for Mie Scattering Spray Image

3.2 SPRAY BEHAVIOR OF E85

3.2.1 Effect of Injection Pressure on E85 Spray
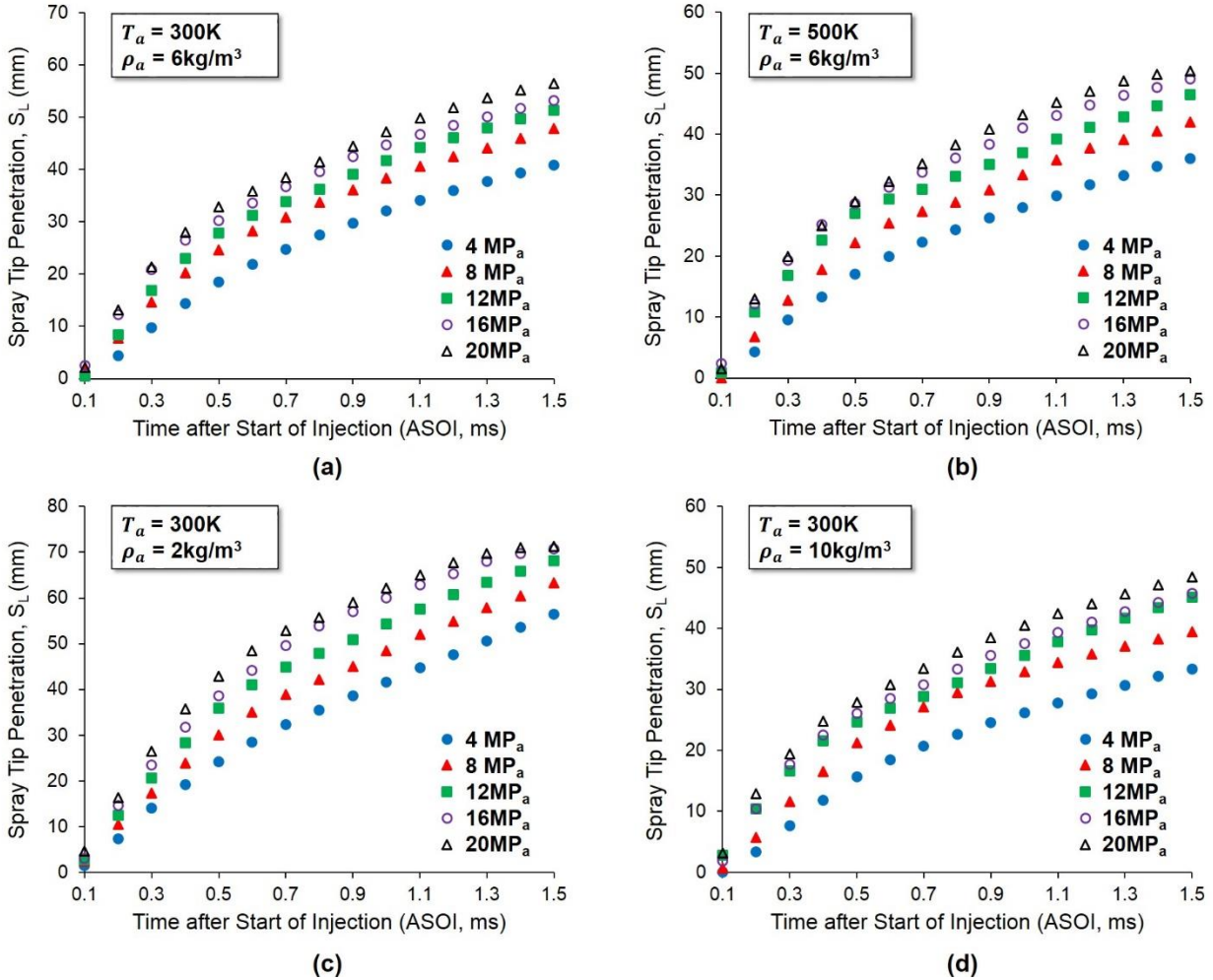
3.2.1.1 Spray Tip Penetration

Figure 3.4 Spray Tip Penetration under Different Injection Pressure

Figure 3.4 shows the Mie scattering results of spray tip penetration varying with injection pressure, whose effects on the spray characteristics are separated into two conditions: ambient temperature and surrounding gas density. From Fig. 3.14 (a)~(d), as expected, higher injection pressure produces a longer penetration, while this tendency has a significant difference when the fuel is low pressurized into the chamber. It seems that a pronounced shorter penetration occurs under the low injection pressure (P_{inj}<5MP$_a$), implying that the spray tip penetration is not quite gradually influenced by injection pressure. Especially under the high gas density condition, the liquid spray tip penetration is much shorten in the case of low

injection pressure, probably as a result of a greater effect of air resistance on reducing the liquid momentum than that in the high injection pressure.

The difference in spray tip penetration, however, becomes smaller at high injection pressure over 12MPa. Even in evaporating spray as shown in Fig. 3.5, it shows only a slight increase on liquid spray propagating length under high pressure drop (between fuel pressure and chamber pressure) at fully spray development. The possible reason can be explained as follow. The slow liquid droplets are not sufficient to compensate the momentum loss at spray tip. As a result, a short penetration length is formed. While in the case of high injection pressure, the speedy droplets follow faster, and collide the other smaller droplets at spray tip. The droplet coalescence forms a larger one and sustains a longer penetration. However, this effect becomes weak since the higher spray velocity enhances the aerodynamic force and heat transfer, which lead to a droplets deceleration and faster evaporation. Also, recent study [237] reported a limitation to reduce the SMD when the fuel was pressurized over 20MPa using GDI injector. It means the coalescence effect becomes decreased under high injection pressure. Therefore, the result of Fig. 3.5 indicates the usage of high injection system in DISI-like condition may slightly influence on the spray penetration, and the further fact that spray can be atomized well by high injection pressure and also avoided the increased risk of impinging wall.
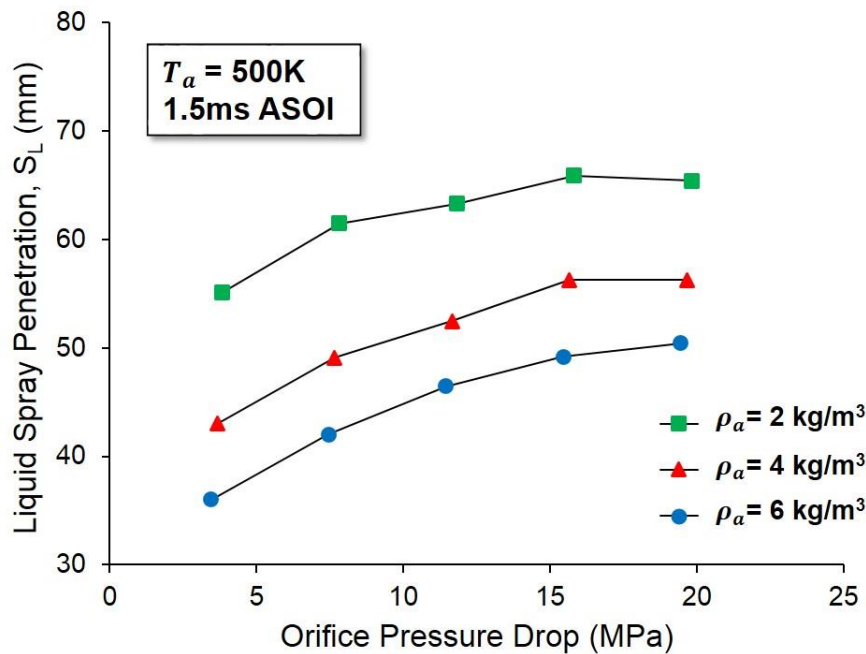

Figure 3.5 Liquid Spray Penetration versus Pressure Drop at Fully Development

1.2.1.2 Spray angle

An anther important spray characteristic is the spray angle, which is measured in a quasi-steady, constant angle region of a spray. Figure 3.6 (a) shows the typical measured average result of spray angle under P_{inj}=4 to 20MPa. Generally, the spray angle has an increase tendency with fuel injected by an elevated injection pressure for all cases. When the injection pressure increases from low level (4MPa), the injection velocity becomes speedy, in turn enhancing the secondary breakup process and dispersing the spray wider, hence increases the spray angle. Also, Fig. 3.6 (b) presents an increase of spray volume with improved injection pressure. This tendency, however, tends to weak under high injection pressure, possibly as a result of only slightly increase of spray velocity which also is demonstrated in no significant differences on spray tip penetration under high injection pressure as shown in Fig. 3.4 (a).
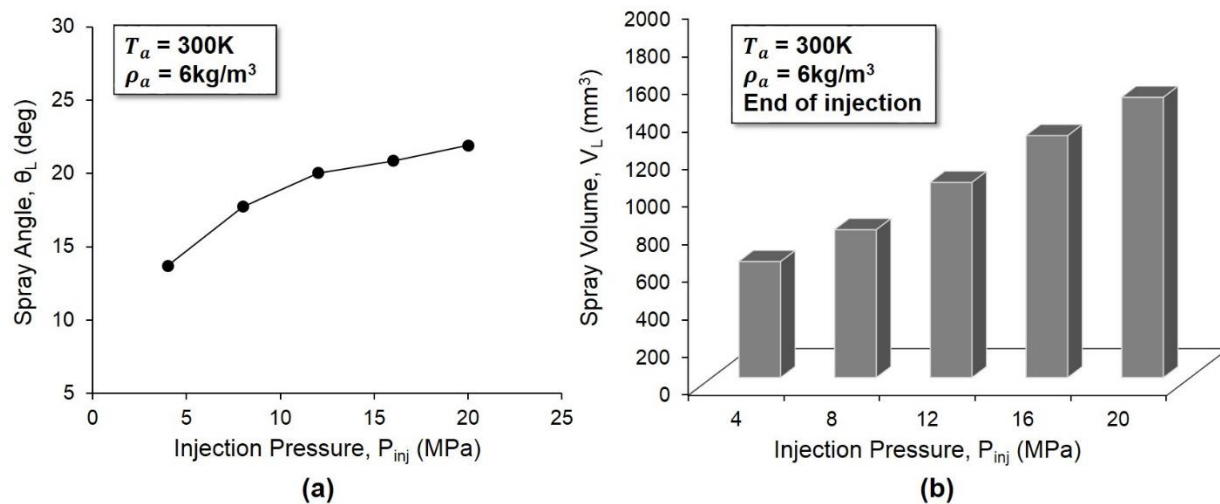

Figure 3.6 Effect of Injection Pressure on (1) Spray angle and (2) Spray Volume

3.2.2 Effect of Ambient Gas Density on E85 Spray

3.2.2.1 Spray Tip Penetration

Figure 3.7 shows the typical results of effect of ambient gas density on the spray characteristics of E85. Not only for the evaporating spray but also the high injection cases, the tendency in those is similar to the typical cases of P_{inj}=4MPa in atmosphere temperature. The most noticeable trend shown by the penetration data in Fig. 3.7 (a) is the decrease in spray tip penetration with an increase in ambient gas density decreasing rate of penetration with time escape. This trend was observed by many others researchers using diesel. Most significant reason for this result is that the improvement of mixing process. As the introduction in Chapter

77

1, the secondary disintegration of liquid droplets is dominant by the aerodynamic force and surface tension. Based on the Gas Weber number, the aerodynamic fore will increase according to the increase of ambient gas density. In addition, the local air entrainment rate along a spray will be proportional to the surrounding gas density [79]. Both of these effects accelerates the breakup process of liquid droplet, especially in the spray tip, and then decrease the penetration length. It also should be noticed that the difference in penetration turns to small under higher gas density.
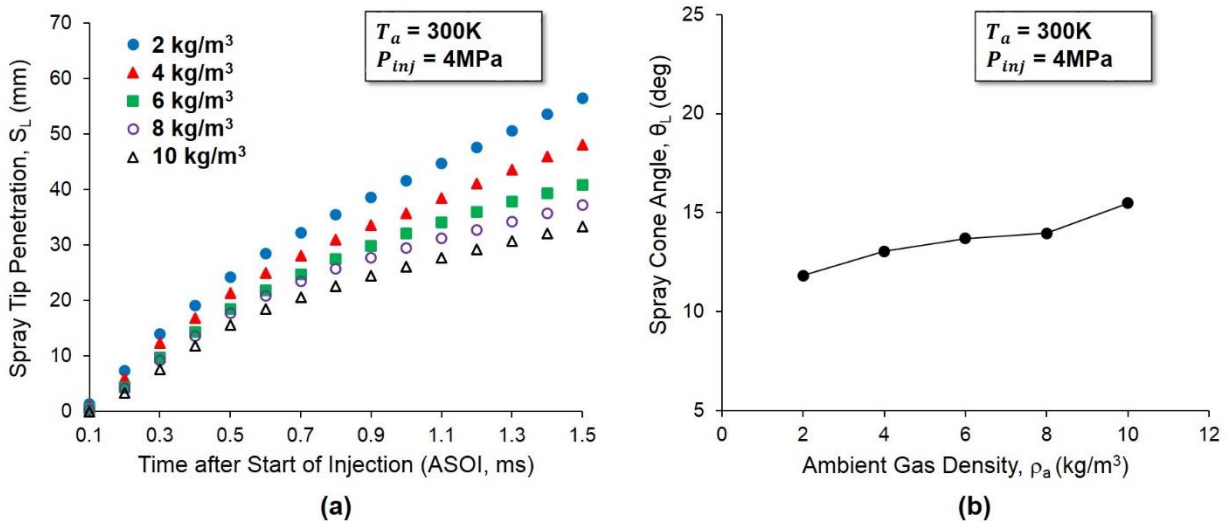

Figure. 3.7 Effect of Ambient Gas Density on (1) Spray Tip Penetration and (2) Spray angle

1.2.2.2 Spray angle

The variation of spray angle in different ambient gas density is plotted in Fig. 3.7 (b). The obvious result shows that the spray angle increases with increasing the ambient gas density. If coupled with different cases of injection pressure, the logarithm map of the tangent of half spray angle versus the ratio of ambient gas density and injected fuel density for non-evaporating, is shown in Fig. 3.8. The least square fits of data for different injection pressures to a power relationship are plotted. The dot lines on either side of each fit give a ±10% repeatability noted for the average angles listed. The typical thermodynamic environment of spray injection in DISI engine with the gas density, from 2 to 10kg/m^3 were used in the least square fits. The exponent in the fits at upstream of the figure is the average of three exponents that extracting from the data for each injection pressure individually (consisting of 12, 16 and 20MPa) with the power law relationship.
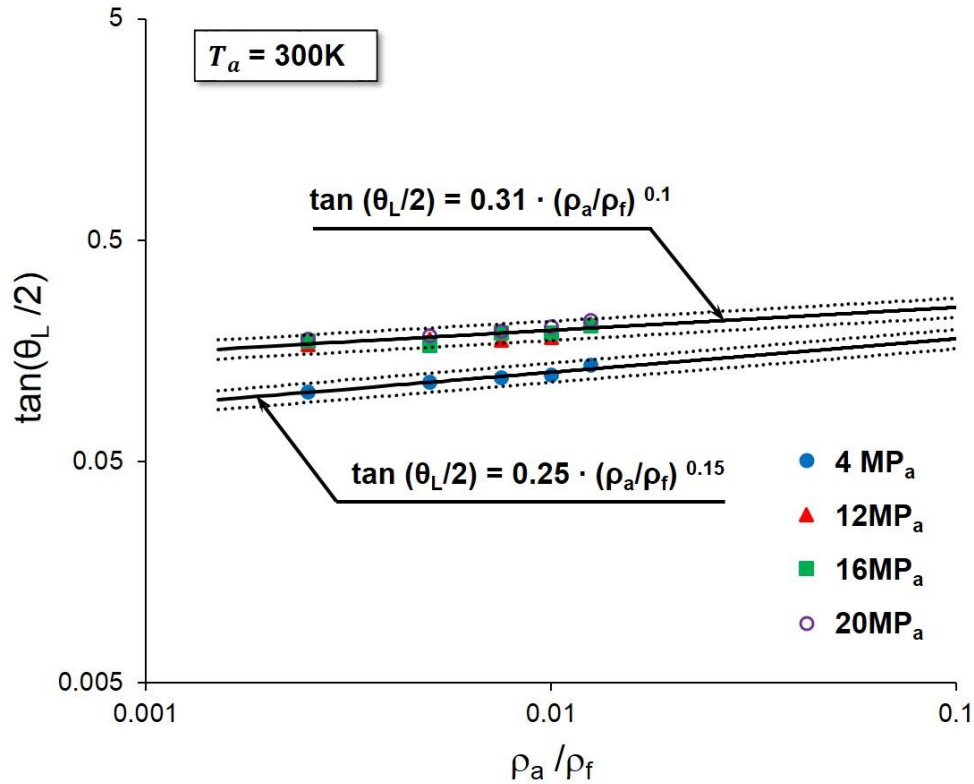
Figure 3.8 Spray angle versus Ratio of Ambient Gas Density to Fuel Density for All Non-Evaporating Conditions

Since no major reports were found relative to the strong correlation of spray angle and ambient gas density for DISI system. The discussion on this tendency shown in the figure should be made to compare with diesel spray in high gas density and high injection pressure proposed by Naber and Siebers [79]. First, for all cases, the increase of ambient gas density (ρ_a/ρ_f) will lead to a more dispersion spray as discussed in Fig. 3.7 (b). Also, the dependent of the tangent of the spray half angle on the density ratio shows a great fit within the density ratio less than 0.1, which is well in consistent with the diesel results. However, different sensitive to the surrounding gas density for E85 spray is found in this study, showing an exponent dependence of 0.1 to density ratio for high injection pressure (>10MPa) and 0.15 for low injection pressure respectively. This result is considerably different from the diesel spray which suggested a same power dependence of 0.19 to ambient gas density for not only different nozzle tip but also different injection pressure (80MPa~140MPa). It is not clearly that whether the fuel properties results in this difference, since no results are found for diesel spray injected by such lower injection pressure and lower ambient gas density. In addition, the structure of nozzle tip may have a significant effect on this result since Naber and Siebers found that their results showed an inferior agreement with that from other researchers, i.e., Hiroyasu and Arai [77], Wakuri et al. [78] and Varde et al. [238]. However, one should be mentioned that in Naber and

Siebers's result, they showed no significant effect of injection pressure on the spray dispersion angle for the range of injection pressure examined (75~160MPa). While the result shown in Fig. 3.6 (a) reveals that increased tendency of spray angle with increasing injection pressure, becomes weak when the injection pressure excesses 10MPa. Therefore, the fact in Fig. 3.8 can be summarized as follow. In the case of low injection pressure for DISI system ($<P_{inj}$=5MPa), the spray angle shows a relatively high sensitive to the ambient gas density. While under high injection pressure ($>Pinj$=10MPa), the effect of ambient gas density on spray angle is almost not influenced with further increasing injection pressure.

3.2.3 Effect of Ambient Temperature on E85 Spray
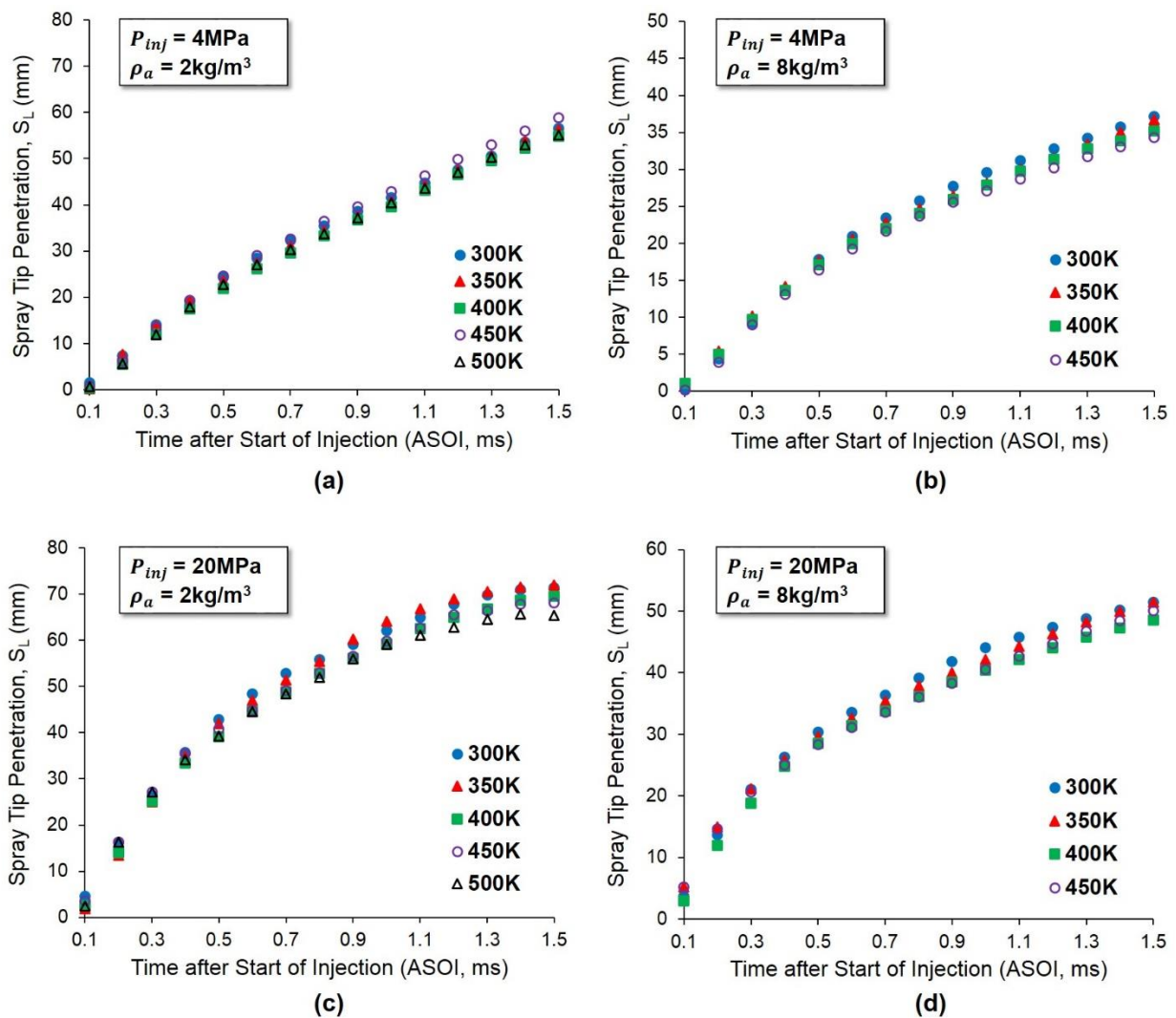
3.2.3.1 Spray Tip Penetration

Figure 3.9 Effect of Ambient Temperature on Spray Tip Penetration

80

The effect of ambient temperature on spray tip penetration is presented in Fig. 3.9 (a)~(d) under different injection pressure and surrounding gas density. The comparison shows even if the boiling point of E85 is generally lower than hydrocarbon fuels, such as gasoline and diesel, it only presents a limited effect of vaporization on reducing the spray tip penetration in around 1.8% to 8%. This result is greatly different from that obtain by diesel spray (almost 20% reduction in penetration under low ambient gas density), which also indicates that the E85 has a good temperature-independence on surrounding gas density. In the case of DISI engine condition, the in-cylinder temperature and pressure at end of compression stroke are at the range of 600~750K and 0.8~2.0MPa respectively, meaning the maximum ambient gas density only closed to 10kg/m^3 which is in consistent with the experimental condition in this study. Therefore, the effect of temperature on penetration length in the figure suggests that the usage of spray prediction on penetration from non-evaporating sprays to represent vaporizing sprays is considerably reasonable at both low- and high- density conditions for E85 spray.

1.2.3.2 Spray angle

Figure 3.10 shows the effects of vaporization on spray angle in a plot similar to Fig. 3.8. The fitting manner for evaporating data was under the same way for non-evaporating sprays. The solid lines through the vaporizing data indicates the observed trend. In addition, the trend lines (dash line) of non-evaporating data in Fig. 3.8 under low- and high- injection pressure conditions also were plotted to make a comparison in Fig. 3.10. The boiling point of E85 used in this experiment is about 358K as listed in Table 2.2. Moreover, the distillation curves of E85 suggested that the fuel volume was evaporated completely when the temperature was up to its boiling point [55]. Therefore, the ambient temperature of 450K can be considered as the evaporating condition for E85 spray, allowing to adopt more measured points for the analysis than those in 500K condition.

Comparison of the vaporizing data to the fits for the non-vaporizing data demonstrates that the vaporization reduces the spray angle, while this reduction decreases with increasing the density ratio (ρ_a/ρ_f). The reduction at the lowest density ratio is about 20% for both high- (upstream solid line) and low- (downstream solid line) injection pressure, but by a gas density of 8kg/m^3 (density ratio is ρ_a/ρ_f =8/796 =0.0101) the difference becomes small. Also, the figure shows the effects of injection pressure and gas density on the spray angle are the same with non-evaporating spray. It should be noticed that the temperature will have no significant effect at the high surrounding gas density conditions.
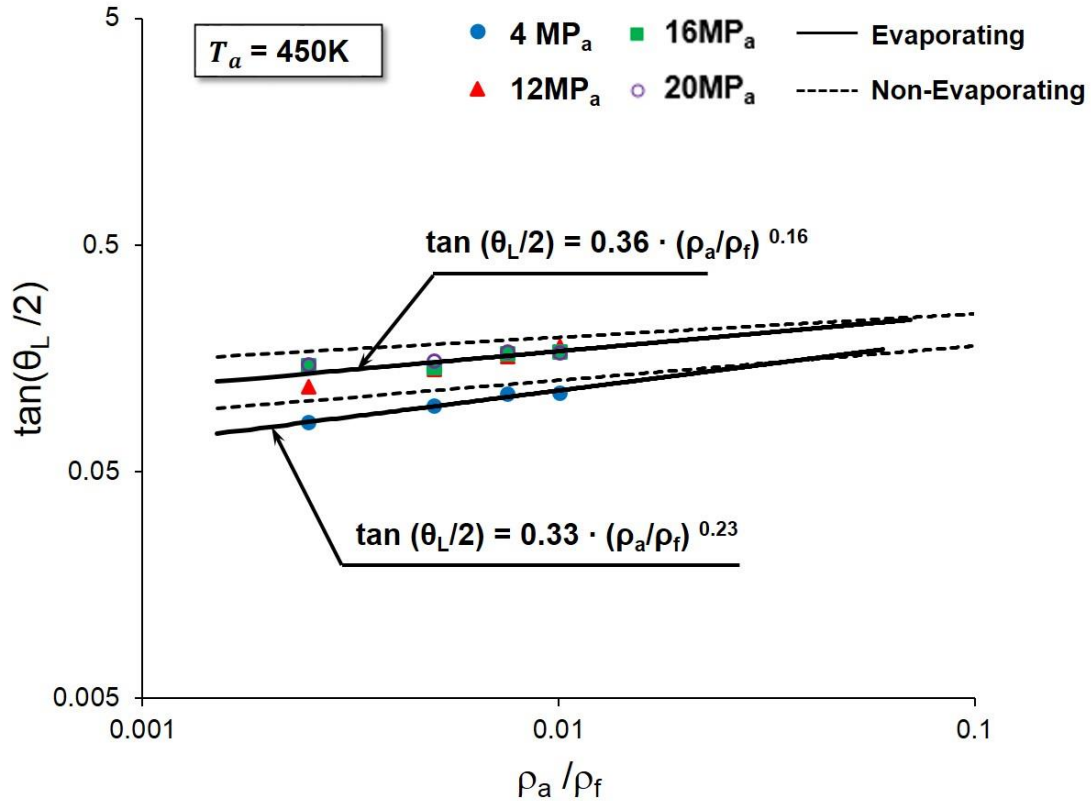
81

Figure 3.10 Spray angle versus Ratio of Ambient Gas Density to Fuel Density for All Evaporating Conditions. The solid lines represent the measured trends in the vaporizing data. The dash lines are fits to non-evaporating spray data from Fig. 3.8.

Narber and Siebers [79] considered that the main reason of reduction spray angle under vaporization was attributed to the contraction of the evaporating spray when it cooled down the entrained hot gas by fuel evaporation. They estimated the 40% of spray contraction of the cooled air and expansion of the vaporized fuel. And the corresponded reduction of spray width was about 25% under the 6.5kg/m^3 gas density, which was similar to their practical reduced spray angle of 15%. Their result reveals a slightly disagreement with the data in Fig. 3.10, where gives an 11% reduction of spray angle under 6kg/m^3 gas density (0.0075 for density ratio). The biggest potential factor contributes this difference is the ambient temperature in experiment. A great difference of ambient temperature (1000K) and 100% evaporation point of diesel (604K) in comparison to the condition in this study (500K in ambient and 358K at 100% distillation point for E85), will lead to a more heat transfer in spray, hence enhances the species transport inside the fuel and reduces more spray width.

The results, in general, indicates that for a density ratio range denoting the typical DISI condition where the E85 is introduced, spray angle under vaporization will reduce from 20% at low gas density to a few percent at the high ambient density. In addition, this impact is independence on the injection pressure.

1.2.3.3 Spray Volume

Figure 3.11 shows the effects of temperature on the spray evolution under different injection pressure and ambient gas density. For all of the cases, elevated temperature suggests its efficient reduction of spray liquid volume due to the vaporization. It is noticeable that the spray volume has no obvious decrease in vaporizing sprays compared with the non-evaporating ones during the early spray evolution (before 0.5ms ASOI) . An explanation for this is that not sufficient time for the ambient temperature enable the influence on the vaporization of large liquid droplet. However, this trend is improved after 0.9ms ASOI in which the temperature becomes dominant factor to decrease spray volume, i.e., 65% reduction of spray volume from the temperature of 300K to 500K in the present injection range (4MPa~20MPa).

Several observations of interest are found in the figure and should be discussed as follow. Firstly, the injection pressure plays a pivotal role on the increase of spray volume since the well atomization is achieved under high injection pressure. In this study, the increased P_{inj} ratio of 5.0 (20MPa/4MPa) leads to an expansion of spray volume at least 3.6 times.

Second observation is based on the ambient gas density. Under the low gas density, as shown in Fig. 3.11 (a) and (c), the decreased tendency of spray volume at elevated temperature is similar between P_{inj}=4MPa and 20MPa. However, more reduction of liquid volume can be found under the high gas density as illustrated in Fig. 3.11 (b) and (d). It seems that the evaporation can be well improved for E85 spray if combing the high gas density and high injection pressure.

The third observation is less significant but wroth being discussed. Under non-evaporating spray, effect of increasing ambient gas density (i.e., from 2~8kg/m³) on the reducing liquid volume is only about 10% at P_{inj}=20MPa, which is much less than that of 26% at P_{inj}=4MPa. While this effect, with about 25%~30% reduction of spray volume, are almost the same to both injection pressure under vaporizing condition. The result indicates that the atomization improvement under high injection pressure is less significant than the low one with increasing ambient gas density, due to the better breakup process of liquid droplet already induced by high-pressure injection.

However, under vaporizing condition, increased gas density becomes an efficient way to enhance the evaporation for both high- and low- pressure injection.
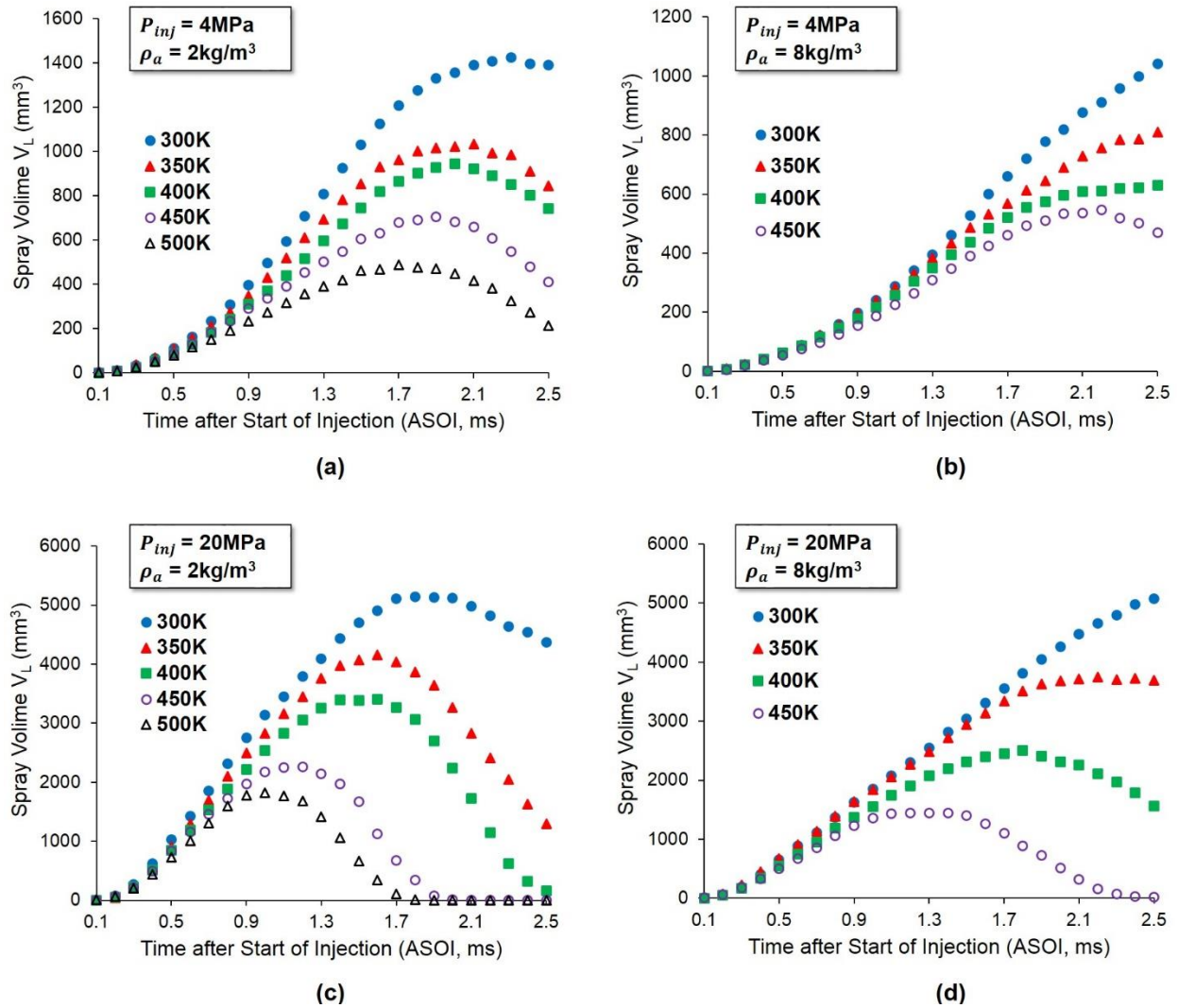

Figure 3.11 Effect of Ambient Temperature on Spray Volume

3.3 CORRELATION OF EXPERIMENTAL DATA AND PREDICTED MODEL FOR SPRAY TIP PENETRATION

3.3.1 Comparison of Experimental Data to Classic Predicted Model

In this section, the breakup process and penetration length that describes the E85 spray injected by hole-type nozzle under DISI-like condition is introduced. As mentioned about the literature reviews in Chapter 1, previous studies have reported many empirical equations or scaling models for penetration length

prediction. However, it is difficult to make all the correlations between this study data to those. Here only several classic models were used to directly compare to the result of E85 spray.

Figure 3.12 plots the results of the typical spray data of E85 and the corresponding correlation equations proposed by Hiryasu-Arai [77], Naber-Siebers [79], Wakuri [78] and Dent [239] respectively. All of those models show a remarkable agreement with the experimental data in fully developed spray region, except the Naber-Siebers's equation whose prediction suggested more well in consistent with the diesel sprays under high injection pressure (>80MPa) [240]. It should be noticed that all the correlation equations suffer from the disadvantage of over prediction of the initial liquid phase of the spray, which also was mentioned by other researcher like Dent, et al. Several physical properties of fuel, such as density, viscosity and surface tension, will influence the early breakup of liquid. This implies that the spray tip penetration at the early injection period, should be examined in the case of using ethanol-gasoline blend.
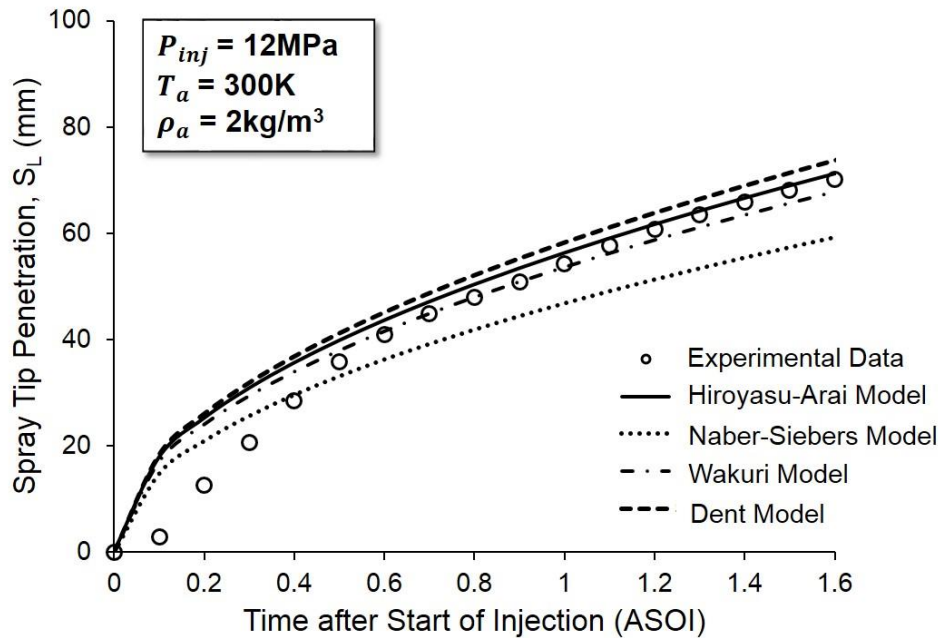

Figure 3.12 Comparisons of Experimental Data to Several Classic Predicted Model on Spray Penetration Length

3.3.2 Correction of Spray Tip Penetration

As discussed in last section, the prediction of spray tip penetration almost developed by diesel sprays under high injection pressure and high gas density (i.e., in cylinder TDC gas density greater than 25kg/m^3 at temperature of 1000K and injection pressure in excess of 100MPa). The research of gasoline or gasoline alternatives, however, does not play attention to the prediction of their penetration lengths since PFI system

in gasoline engine is operated by the introduction of a well-premixed mixture for a long time, even for the wall-guided DISI system with an air-motion induced mixing process. No major reports with empirical correlations were found that could be applied to DISI systems, especially obtained with fuel as the real fluid instead of water. In this section, an effort was made to correct the difference at the early breakup for E85 spray and predicted model.

Based on the result from Fig. 3.12, one of the models useful to fit the experimental data is the Hiroyasu-Arai's equation because (1) the prediction in far field of spray shows a well agreement, and (2) the equation is separated into two aspects to descript the different disintegration processes of liquid fuel, which gives an efficient way to correct the initial spray region directly instead of the analyzing the mass momentum in detail, such as Wakuri's model. Furthermore, the spray in experimental conditions examined by Hiroyasu and Arai were in the injection pressure of less than 75MPa and the ambient gas density range from 10 to 33kg/m^3 which had been found as the most similar data to DISI-like condition so far. Also, the section 1.2.3 has provided the fact of no significant effect of ambient temperature on E85's penetration length under the range from 300K to 500K. Therefore, the temperature term in the empirical equation, such as Dent's model can be ignored in this study.

In Hiroyasu-Aari's theory, they proposed a transition time (also called break-up time), denoted as t_{break}, to characterize the spray from a liner dependence of penetration on time to a square root dependence. Also, it corresponds to the ended breakup length L_b.

$$L_b = 15.8 \cdot \left(\frac{\rho_f}{\rho_a}\right)^{0.5} \cdot D \qquad\qquad (3.1)$$

The magnitude of the breakup length decreases with the increase of ambient gas density, i.e., the breakup length will shorten to around 10-20mm when the ambient gas is pressurized over 1.0MPa. While it tends to over 40mm under the atmosphere. This trends was examined for diesel spray in which usually using the high injection pressure (>40MPa). However, when the relative lower injection pressure (<20MPa) for gasoline or ethanol used in lower ambient gas density condition, such as 2kg/m^3 in this study, it is inevitable to cause an over prediction of breakup length, and also the reason of the disagreement as shown in Fig. 3.12 at the early injection.

In order to correct the spray evolution at that period, the break-up time should be considered as the key factor to re-separate the proper region of E85 spray. However, it is difficult to directly measure the breakup length (corresponding to breakup time) since recent study shows a limitation to detect the liquid core length by photography, i.e., shadowgraphs or optical connectivity, i.e., laser illumination/Mie scattering [241]. Although some reports have tried to relate features of spray penetration curves to break-up lengths and time

usually by analyzing the change in gradient indicating the time when aerodynamic drag begins to affect the penetration velocity significantly [242-244]. No any significant researches with empirical correlations were found that could be employed in DISI systems. Furthermore, for the first stage of injection, the spray penetration has been expressed in Eq. 1.3. A constant of 3.9 was proposed as the velocity coefficient C_v for diesel spray, which was gained from experiments at higher surrounding gas density from 10 to 33kg/m³ by Hiroyasu and Arai. However, in the case of DISI engine, the surrounding gas density at injection timing is usually lower than that in diesel engine, i.e., atmospheric condition at suction stroke or near 10kg/m³ at TDC. Therefore, the relation between the velocity coefficient C_v and ambient gas density was evaluated in this study. The modified equation is proposed as:

$$S = C_v \cdot \left(\frac{2\Delta P}{\rho_f}\right)^{0.5} \cdot t \qquad (t < t_{break}) \qquad (3.2)$$

$$C_v = C_d \cdot \left(\frac{\rho_a}{\rho_0}\right)^{-0.2} \qquad (3.3)$$

Where C_d is the discharge coefficient of nozzle in a typical range from 0.6~0.7, hence a value of 0.65 is selected as C_d in this study. An impact index of ρ_a/ρ_0 is introduced in order to correct the effect of ambient gas density on E85 spray. ρ_0 is the air density in standard condition, 1.293kg/m³. The negative exponent value of 0.2 is the dependence coefficient determined by the ambient gas density which will be discussed as follow.
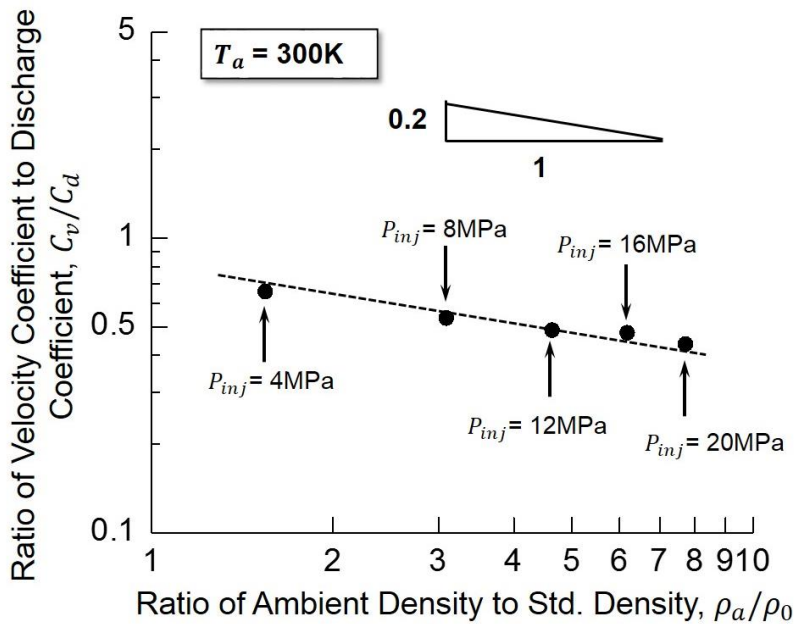

Figure 3.13 Correlation of Velocity Coefficient and Surrounding Gas Density

It is found from the evaluation that the coefficient decreases with increasing the surrounding gas density as shown in Fig. 3.13 and the correlation of power dependence is $(\rho_a/\rho_0)^{-0.2}$. Therefore, the velocity coefficient in Eq. 3.2 for different ambient gas density can be calculated in Table 3.2. On the other hand, the spray tip penetration after the first injection stage was determined by the Hiroyasu-Arai's equation again as shown in 3.4, since that empirical equation has showed a sufficient accuracy for the secondary breakup evolution of E85 spray. And the breakup point of intersection of Eqs. (3.2) and (3.4), also namely breakup time t_{break}, is expressed in Eq. (3.5)

Table 3.2 Velocity Coefficient varied with Ambient Gas Density

Ambient Gas Density, ρ_a (kg/m³)	2	4	6	8	10
Velocity Coefficient, C_v	0.41	0.36	0.33	0.31	0.30

$$S = 2.95 \cdot \left(\frac{\Delta P}{\rho_a}\right)^{0.25} \cdot (D \cdot t)^{0.5} \qquad (t > t_{break}) \tag{3.4}$$

$$t_{break} = \frac{4.35 \cdot \rho_f \cdot D}{C_v^2 \cdot (\rho_a \cdot \Delta P)^{0.5}} \tag{3.5}$$

Figure 3.14 shows a comparison result of experimental data and revised equation on spray tip penetration. It can be seen that the above-mentioned Eqs. (3.2) to (3.5) are suitable to predict the spray tip penetration.
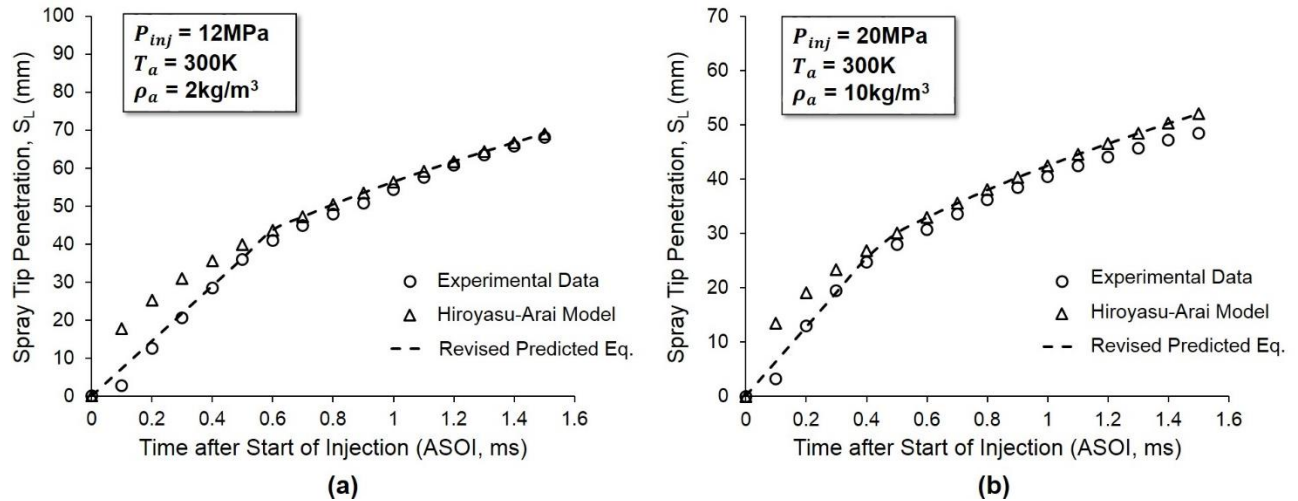

Figure 3.14 Comparison of Measured and Calculated Results in Spray Tip Penetration

Based on the Eq. (3.5), the breakup time have been calculated and analyzed in a consecutive curve of spray penetration length. Although this is a rather gradual transition without clear break point, it provides an interesting information on the spray tip penetration of E85 at early injection. The log/log plot in Fig. 3.15 shows a typical penetration rate measurement, and suggests the fact that indeed a transition time from the linear to power trend. The dependence of downstream development for E85 spray seems similar to diesel with a about $t^{0.5}$ power correlation, but distinguished by approximately $t^{1.5}$ dependence different from the diesel with $t^{1.0}$ at the first stage of injection. The physical property can be considered as the main reason to result in this difference at near nozzle, yet the effect tends to weak with the spray further propagating towards downstream.
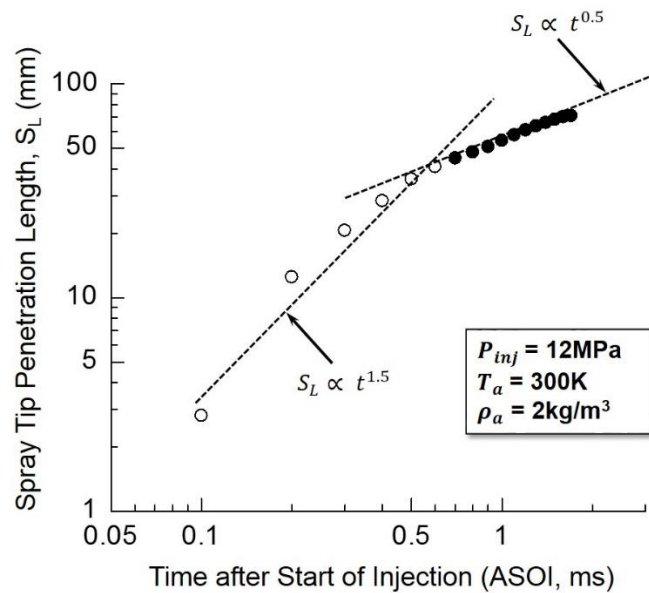

Figure 3.15 Comparison of Penetration History with Expected Proportionalities in Near Nozzle and Downstream Zone

3.4 SUMMARY

The spray evolution of E85 was characterized by Mie scattering directly. Various conditions, such as injection pressure, ambient temperature and surrounding gas density were carefully selected as the experimental conditions to simulate the typical injection environment for DISI engines. By means of the thresholding method, the spray characteristics can be quantitatively analyzed.

Several significant factors of spray development were played attention in this chapter, especially the spray tip penetration, spray angle and liquid volume. The main conclusions are summarized as follow.

1. Liquid spray tip penetration S_L is mainly controlled by injection pressure and ambient gas density. In detail, S_L tends to propagate more sustainably with the increase of injection pressure due to the high momentum. However, with increasing ambient gas density, the penetration length is shorten. It is worth noticing that those trends of spray tip penetration length become no more significant at high injection pressure and high ambient gas density. Under given surrounding gas density, the liquid penetration length of E85 will not greatly affected by the increase of injection pressure (>15MPa) that means the spray atomization could be well improved by high injection pressure in DISI system with the usage of E85 fuel, but not worry about the wall-impingement impact.

2. In this chapter, the correlation of liquid spray angle of E85 and ambient gas density, as well as injection pressure were proposed. In contrast to the diesel with a 0.19 power dependence on ambient gas density under non-vaporizing condition, the relation between spray angle of E85 and ambient gas density shows a distinguishable trends under different injection pressure that can be summarized as follow.

   Non − Vaporizing Condition:

   $$\tan(\theta_L/2) \propto \left(\rho_a/\rho_f\right)^{0.1} \qquad High\ Injection\ Pressure:\ P_{inj} > 10MPa$$

   $$\tan(\theta_L/2) \propto \left(\rho_a/\rho_f\right)^{0.15} \qquad Low\ Injection\ Pressure:\ \ P_{inj} < 5MPa$$

   Under vaporizing condition, liquid spray angle is reduced with elevated ambient temperature, especially would cause a maximum approximately 20% reduction under low ambient gas density. However, the reduction turns so small that can be ignored under high surrounding ambient gas density. The correlation of them is also described as follow.

   Vaporizing Condition:

   $$\tan(\theta_L/2) \propto \left(\rho_a/\rho_f\right)^{0.16} \qquad High\ Injection\ Pressure:\ P_{inj} > 10MPa$$

   $$\tan(\theta_L/2) \propto \left(\rho_a/\rho_f\right)^{0.23} \qquad Low\ Injection\ Pressure:\ P_{inj} < 5MPa$$

   For both non-vaporization and vaporizing conditions, the variation of spray angle of E85 indicates a stronger dependence of ambient gas density occurs under the low injection pressure less than 5MPa, yet becoming weaker under high injection pressure over 10MPa.

3. Spray volume is dominated by injection pressure and ambient temperature. It will grows with the increase of injection pressure, for example, at least 3.6 times of volume expansion is found as the fuel injection is increased from 4MPa to 20MPa. On the other hand, surrounding temperature will lead an opposite effect on the spray volume. It should be pointed out that the ambient temperature has no significant effect on spray volume at the early injection period due to the present of liquid ligament/large droplet under primary breakup. The result also demonstrates that the evaporation of E85 may greatly improve under high temperature condition with increasing injection pressure and ambient gas density.

4. The Hiroyasu-Arai empirical equation has been improved to fit the results of E85 spray under various DISI-like conditions. An impact index of ambient gas factor is introduced to describe the effect of ambient gas on the spray tip penetration at early stage of injection. Hence the new empirical equations of spray penetration length ($t < t_{break}$) and breakup time have been proposed. The result shows a good agreement to experimental data and is useful to improve the predict model in numerical simulation. One should be mentioned that E85 spray reveals a power dependence of $t^{1.5}$ at the first stage of injection that differs from the traditional diesel spray with $t^{1.0}$.

CHAPTER 4 MIXTURE FORAMTION AND FUEL DISTRIBUTION OF ETHANOL-GASOLINE BLENDS

4.1 Experimental Condition

The mixture formation and fuel distribution of liquid and vapor phases were quantitatively measured by the ultra-visible laser absorption scattering (LAS) technique whose principle and experimental setup have been in detail introduced in Chapter 2. Tables 4.1 shows the experimental conditions and the test fuels in LAS under free spray and impinged spray respectively. The constant volume vessel was charged with nitrogen gas in 1.0MPa and elevated to 500K in temperature, in order to simulate the typical thermodynamic environment near TDC under DISI-like condition. In this study, the same valve-covered-orifice (VCO) injector coupled with the injection pressure of 20 and 15MPa was selected to investigate the free spray and impinging spray respectively, and the corresponded injection pluses were setup. Several capturing timings were selected for free spray during fuel injection and after the end of injection (EOI), for example, 0.6, 1.1, 1.5 and 2.1ms time after start of injection (ASOI).
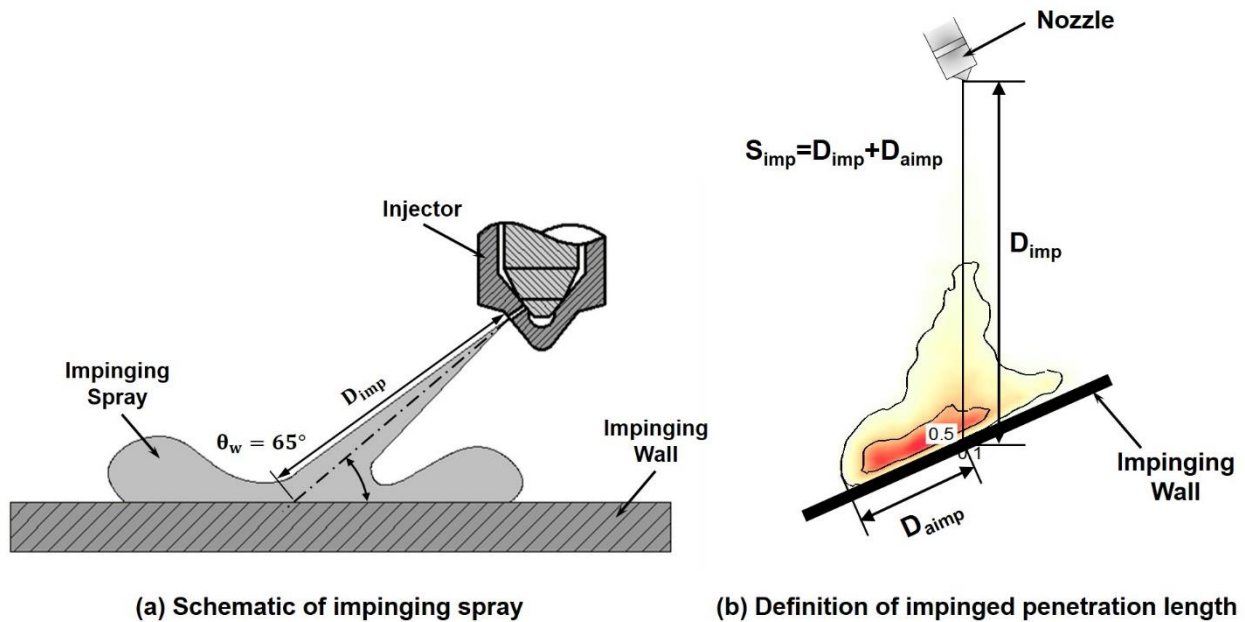

(a) Schematic of impinging spray   (b) Definition of impinged penetration length

Figure 4.1 Schematic of Impinging Spray and Definition of Spray Tip Penetration

Table 4.1 Experimental Conditions in LAS

LAS Experiment						
Specific Items	Free Spray			Impinging Spray		
Ambient Condition						
Ambient Gas and Density, ρ_a	Nitrogen, Density (6.85 kg/m^3)					
Ambient Temperature, T_a (K)	500			500		
Ambient Pressure, P_a (MPa)	1.0			1.0		
Injection Condition						
Hole Diameter, D (mm)	0.15			0.15		
Injection Pressure, P_{inj} (MPa)	20			15		
Injection Duration, t_{inj} (ms)	E0	E85	E100	E0	E85	E100
	1.1			1.3		
Timing Shot, t_{AEOI} (AEOI, ms)	-0.5, 0, 0.5, 1.0			-0.7, -0.3, 0.2, 0.7, 1.7		
Test Fuel						
E0	Toluene 100 (100% toluene)					
E85	MEK 85 (85% MEK) + iso-octane 15 (15% iso-octane)					
	Ethanol 85 (85% ethanol) + Toluene 15 (15% toluene)					
E100	MEK 100 (100% methyl ethyl ketone)					
Impingement Condition						
Impinged Distance, D_{imp} (mm)				30		45
Impinged Angle, θ_w (deg)				65		
Wall Temperature, T_w (K)				273		298

For using ethanol-gasoline blend in DISI engine, the difficult ignition and poor emission are considered as the significant problems in practical operation due to the ethanol cooling down more ambient temperature and excess of liquid impingement. Therefore, the investigation of impinging spray under cold start condition was conducted in this study by LAS. Figure 4.1 (a) shows the schematic setup of impinging spray in detail. The impinge distance was defined as the length from the nozzle tip to the place where the fuel impacts the wall, denoted as D_{imp}. This distance was selected as 30 and 45mm simulating the two typical

injection conditions near TDC. Therefore, the impinge angle of 65° was determined based on a 25° angle between the hole axis and nozzle axis. Two wall temperatures, controlled at 273 and 298K by a neo cool circulator (Yamato Co., CF701 600W, -20°C~room temperature) which uses R404A as the cooling media and can provide a constant temperature for the impinging wall, were chosen to produce a similar wall condition for the normal and ultra-low cold start.

The toluene and methyl ethyl ketone (MEK) were used to represent the mixture formation of gasoline and ethanol in LAS respectively. Also the spray behavior of E85 was determined by MEK85/iso-octane15 and Ethanol85/toluene15. Meanwhile, the individual vapor phase of different components in E85 can be quantitatively measured as discussed in Chapter 2. The imaging timings were selected to detect the mixture formation before/at/after wall impingement. In this study, the penetration length of impinging spray, denoted by S_{imp}, was defined as summing the length of impinging and impinged distances along the spray moving direction as illustrated in Fig.4.1 (b). Every case was recorded in four times and the averaged image can be obtain to eliminate the shot-to-shot variation. Thereafter, the quantitative result of equivalence ratio distribution is able to be acquired in accordance to the onion-peeling deconvolution as described in Chapter 2.

4.2 Fuel Distribution and Mixture Formation in Free Spray

4.2.1 Time-Resolve Image of Free Spray

As the previous introduction of LAS principle in Eqs. (2.3) and (2.4), the line-of-sight vapor extinction in a spray with present of liquid droplet, is derived from the ultraviolet extinction imaging and the knowledge of droplet extinction in visible wavelength. On the other hand, the light-of-sight liquid extinction is only dominant by the visible extinction imaging. For examining the spray evolution of fuel vapor and liquid droplets in ethanol-gasoline blends at different timing before/at/after EOI, the raw optical thickness images of their sprays are shown in Fig.4.2. In every shot time, the left column was the visible (Vis) image that characterize the liquid droplets. While the integrated vapor and liquid phases were shown by ultraviolet (UV) image at the right column. The distances along the spray axis of 10, 30 and 50mm away from the nozzle tip, were marked by the white dot lines.

The optical thickness of Vis image is much smaller than that of UV image in almost spray area after EOI, except in the liquid core region before injection. The similar shape between the liquid and vapor phase can be found in t_{ASOI}=0.6ms, also suggesting the present of a large amount of liquid droplets at the early stage of injection. After EOI, especially from t_{ASOI}=1.6ms to 1.0ms, a fact of the increased brightness of

optical thickness in UV image and reduced extinction in Vis image implies a fully vaporizing process during spray downstream propagation.
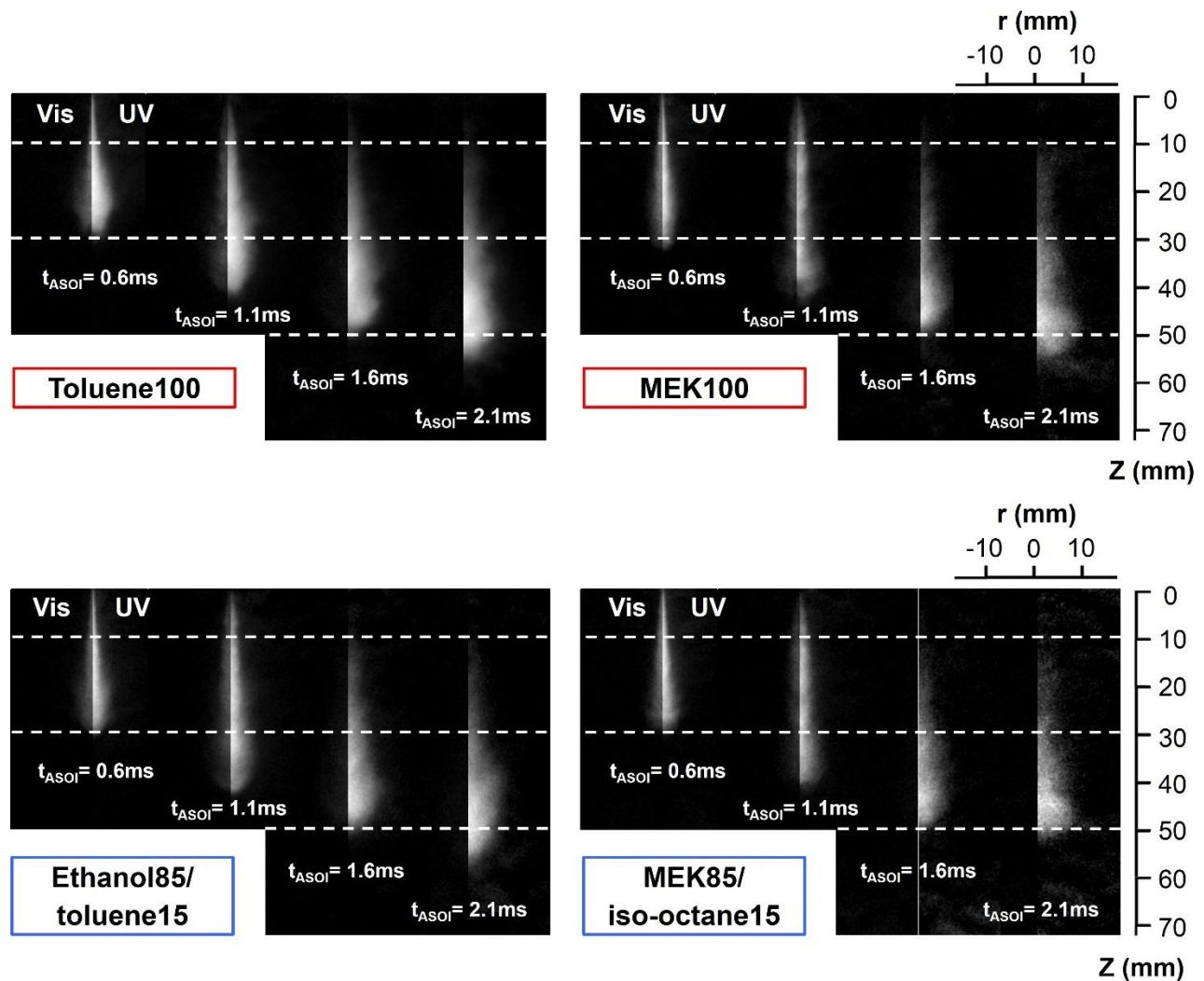

Figure 4.2 Time-Resolved Image of Spray in Optical Thickness (P_a=1.0MPa, T_a=500K, P_{inj}=20MPa, t_{inj}=1.1.ms)

One of interest should be pointed out that the vapor tip of Ethanol85/toluene15 in t_{ASOI}=2.1ms where shows a length closed to 60mm at downstream, has a more sustainable approach than that of MEK/iso-octane15 with a penetration length slightly over 50mm at spray direction. Because the vapor in the UV image of Ethanol85/toluene15 represents the toluene component only. Likewise, the vapor of MEK component in E85 spray was denoted by MEK85/iso-octane15's UV image. Therefore, the result mentioned above tends to cause a significant stratified mixture formation in E85 spray which will be discussed more in detail latter.

95

4.2.2 Spray Tip Penetration and Spray angle

In this section, two significant factors of spray, such as spray tip penetration length and spray angle were extracted from the LAS images to make the comparison in different fuels. The reliable images were obtain by the proper threshold value to cut off the background noise. The spray tip penetration was defined as the distance from the nozzle tip to the farthest downstream spray. Two typical penetration lengths, namely the liquid core penetration length S_L as mentioned in Chapter 3, and the total penetration length S (means vapor penetration length under vaporizing condition) were investigated and measured from the Vis and UV images respectively. Meanwhile, the spray angle was calculated as the angle formed by the two lines crossing with the half of penetration length in UV image for every recorded timing. The detail definitions of spray tip penetration and cone angle are illustrated in Fig.4.3.
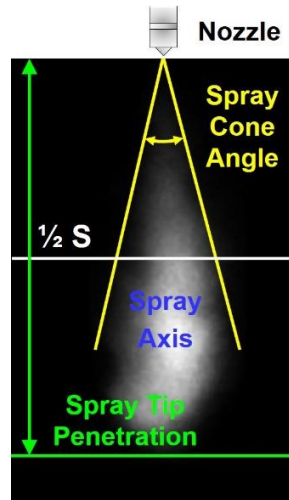

Figure 4.3 Definition of Spray Tip Penetration Length and Cone Angle

Figure 4.4 shows the result of total penetration length of different ethanol-gasoline blends. Because the individual vapor extinction can be gained from the E85 substitute fuels in LAS. The result of MEK85/toluene15 was determined by the maximum length from the UV images of MEK85/iso-octane15 and Ethanol85/toluene15 removing the corresponded Vis images. Also, the semi-equation of Hiroyasu-Arai's model was used as the comparison. In the figure, MEK100 shows its substantially longer spray penetration than the other fuels. Also, the E85 represented by MEK85/toluene15 propagates farer than E0 represented by toluene100. This result reasonably implies a fact that more vapor quantity produced at the spray tip for ethanol-gasoline blends than gasoline. The low boiling point of MEK, make it possible to faster evaporate when the fuel is injected into a high temperature condition. This longer propagation, however, tends to almost unconspicuous at fully development after EOI due to the momentum losses, for example at 1.0ms after end of injection (AEOI) as shown in the figure. In addition, the results of penetration

length show a well fit to the Hiroyasu-Arai's model during the injection for all fuels, also again confirm that this semi-equation can be used to predict the spray penetration at the secondary breakup of liquid droplets not only for diesel but also for ethanol-gasoline blends.
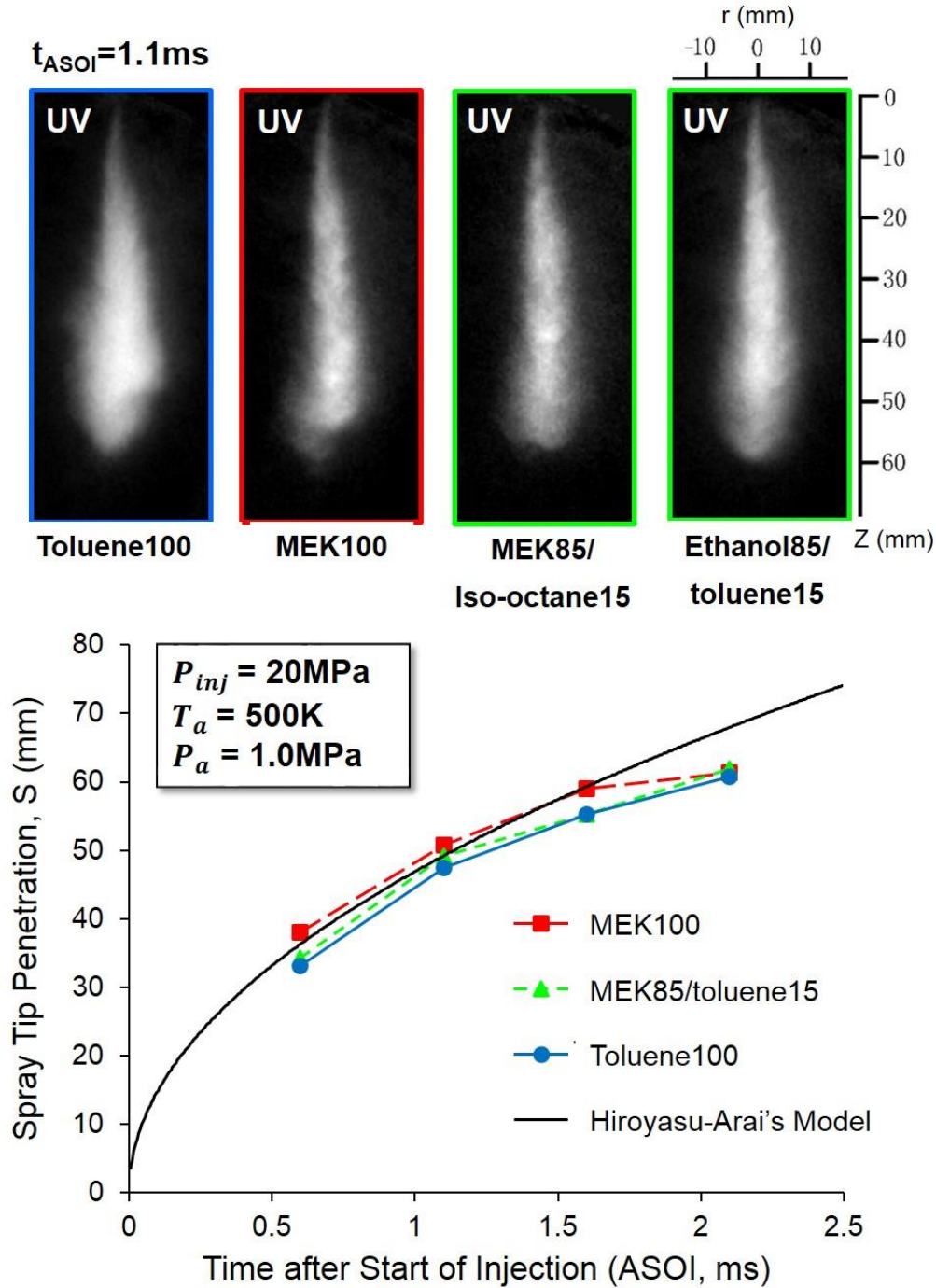

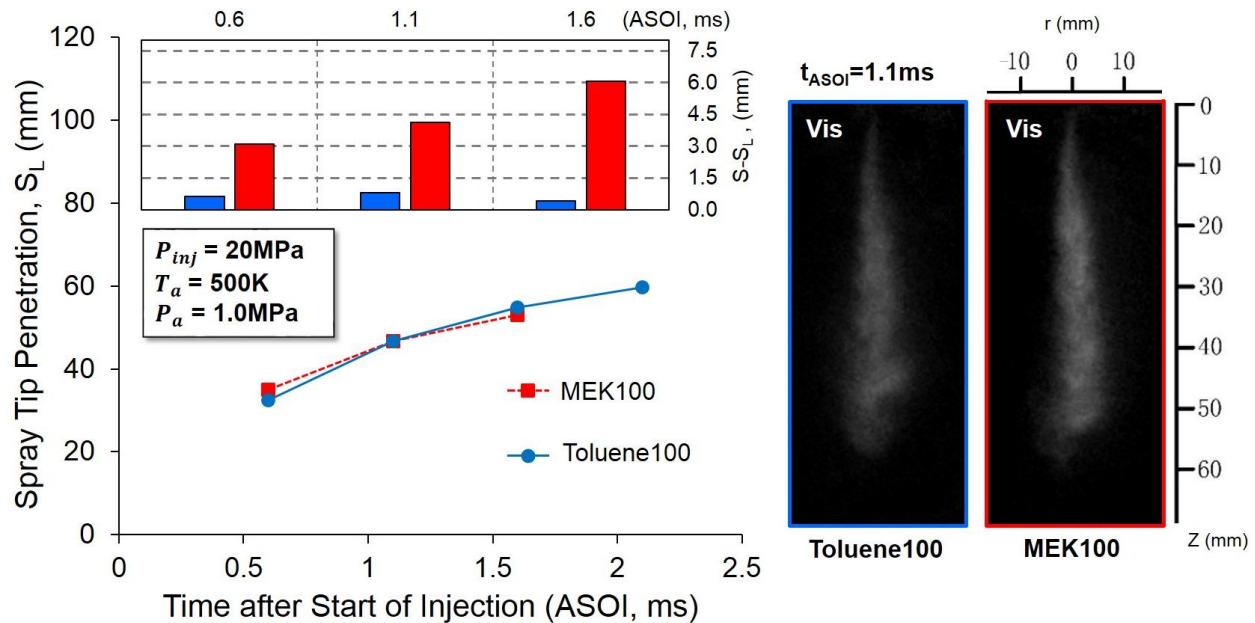**Figure 4.4** Total Spray Tip Penetration Length

Figure 4.5 Comparison of Liquid Penetration Length for E0 and E100

In order to clarify more detail about the evaporation process at spray tip, a liquid penetration length and its comparison to vapor penetration length are presented in Fig.4.5. Because it is hard to separate the actual liquid phase of toluene and MEK component in their binary sprays due to the light interference between components in Vis image. Here, only the MEK100 and toluene100 was made in the comparison and the tendency can be addressed. A similar temporal variation and level of liquid penetration length is found in both MEK100 and toluene100. Coupled with the result in Fig.4.4, a comparison of vapor formation at spray tip can be obtained and presented in the left-top of Fig.4.5. The vapor of MEK100 formed at spray tip, calculated from $S-S_L$, shows much larger than that of toluene100, from 5 times before EOI to about 15 times after EOI. This result is well account for the faster evaporation for MEK100 at spray tip.

One should be mentioned that the trends of $S-S_L$ are different from those two fuels each other. At t_{ASOI}=1.6ms, the error of vapor and liquid penetration length in toluene100 decreases that indicates the still larger amount of toluene liquid remains in spray and low evaporation speed under the continuous downstream propagation. Whereas in the case of MEK100, the increase of $S-S_L$ makes it clearly that the MEK liquid at spray tip evaporates faster and much expands towards downstream due to its lower boiling point. According to this result, a conclusion can be addressed that a faster evaporation occurs at spray tip by using ethanol-gasoline blends compared to gasoline fuel. Also, this tendency will enhance with the increase of ethanol ratio since additional ethanol helps to reduce the boiling point of blended fuel.
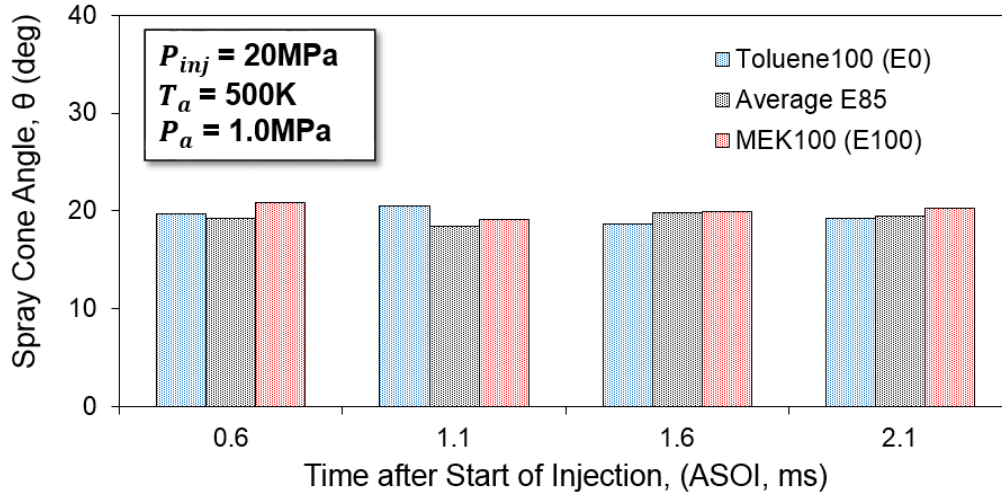
98

Figure 4.6 Comparison of Spray angle for Ethanol-Gasoline Blends

Figure 4.6 shows the result of spray angle of different ethanol-gasoline blends. The E85 data was determined by the averaged data from Ethanol85/toluene15 and MEK85/iso-octane15 in Vis images. The spray angle does not changes with fuel types so much that indicates the high temperature condition reduces the effect of physical properties on spray dispersion. In addition, during the quasi-steady injection, for example at t_{ASOI}=0.6ms, the E85 spray has a spray angle of θ=19.28° that is almost the same with the result of Mie scattering with a θ=19.16° under 450K temperature. This result again confirms the temperature effect on the early stage of spray is less significant for the spray expansion.

4.2.3 Liquid and Vapor Phase Distribution

Figure 4.7 shows the quantitative results of the liquid and vapor distributions for E0, E85 and E100, and demonstrates the differentiable mixture formation of the ethanol-gasoline blends under various blending ratios. For toluene100 and MEK100, the liuqid phase was presented in the left column, while the right one shows the vapor phase distribution. In the case of blended gourps, only the vapor phases of differnet components in E85 spray was given. Based on these data, the calcualted vapor distribution of MEK85/toluene15 can be obtained and illustrated in the righest column. The lower limit of the observable equivalence ratio was defined as Φ_V=0.1.
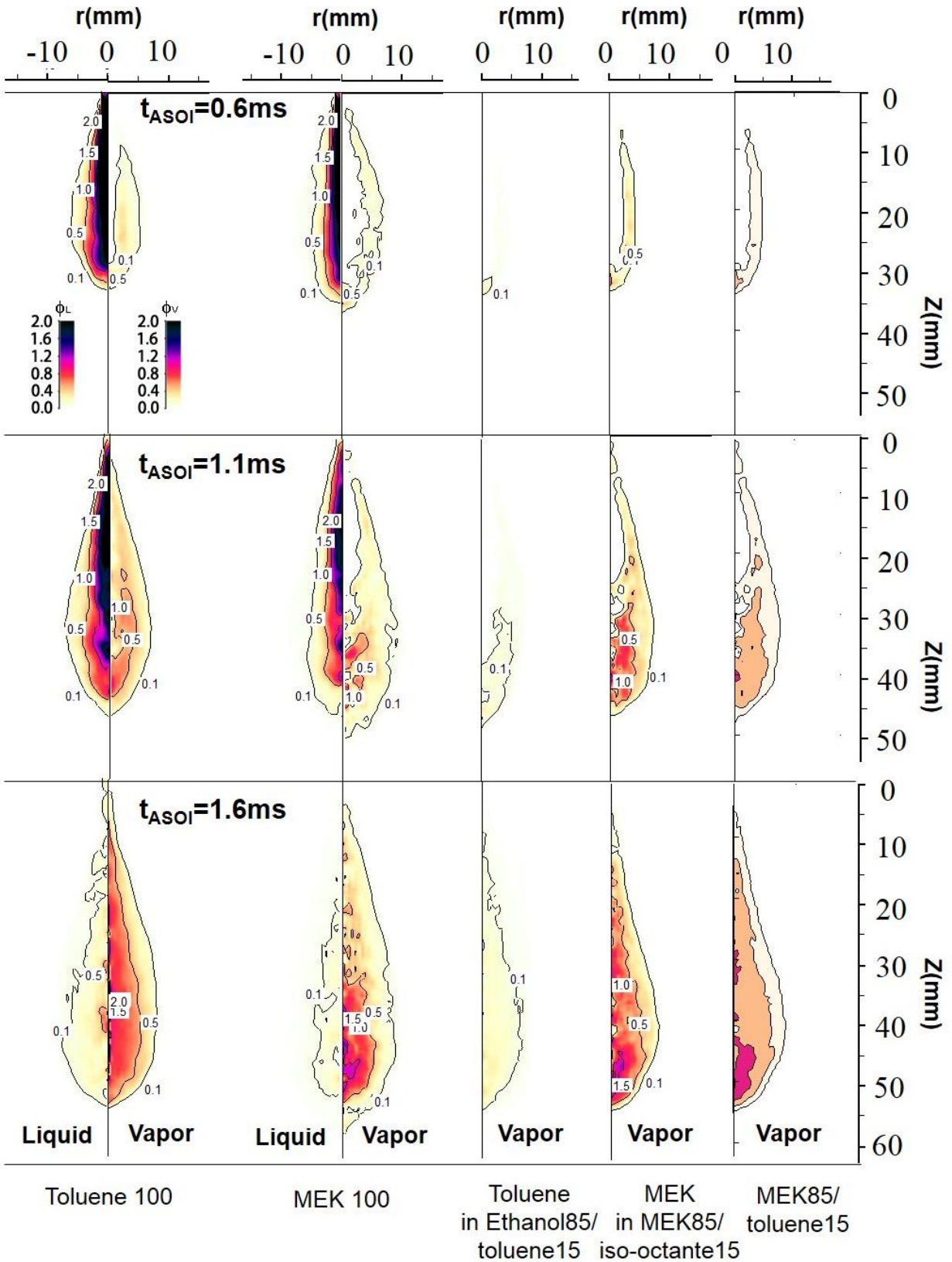
Figure 4.7 Liquid and Vapor Phase Distribution of Different Fuels

100

The result of the spray mixture suggests that both toluene100 and MEK100 present a dense liquid phase along the spray axis and the similar less vapor concentration at early injection (t_{ASOI}=0.6ms), due to the limited effect of temperature on the vaporization. However, this trend becomes changed with spray evlution. A larger amount of liquid droplets in the upstream of the toluene100 spray than MEK100 at the EOI, even more liquid fuel still remains at t_{ASOI}=1.6ms. While the vapor phase of MEK100 shows a richer concentration along the spray axis, and the shorter liquid penetration length compared with the toluene100. Obviously, the result implies that ethanol evaporates faster than gasoline. However, a similar research of spray and combustion conducted by Chen et al [61] using a multi-hole injector in a SG-DISI engine provided a contrast. In their experiment, the fuel was targeted into the chamber during the suction stroke where the ambient temperature was believed to be lower than that of near TDC condition. The effect of the physical properties of ethanol, such as the high viscosity and surface tension, on the spray atomization may decrease under the high temperature environment. Recent work conducted by Oh and Bae [57] demonstrated the vaporization pressure of ethanol become much higher than that of gasoline when the ambient temperature was over 410K, which also indicated the ethanol would evaporate faster than the gasoline under the high temperature condition.

Since the ethanol and iso-octane are transparent for the UV light, only the toluene and MEK components could be observed in their corresponding E85 groups. The evaporation of different components in a binary spray, therefore, could be intuitively investigated as shown in Fig.4.7. From the early injection to the EOI, the toluene component only locates at the middle region to downstream of the spray, and it becomes a large vapor distribution after EOI. Whereas the MEK component presents a homogenous vapor distribution along the spray axis and wider spray dispersion at before/after the EOI. The result suggests that the evaporation of toluene component is impeded due to its higher boiling point (HBP), which accounts for the poor vaporization near the nozzle tip at the early injection (before the EOI). This result is possibly attributed to, first, that owing to the higher enthalpy of vaporization, the faster and earlier evaporation of MEK component leads to a temperature drop-off in the ambient gas, and, second, that insufficient exposure time for the HBP fuel to evaporate which results in an inferior heat transfer with the ambient gas. Both cause a lower evaporation for HBP fuel before the EOI. After the EOI, the evaporation of toluene component in E85 becomes faster due to the decreased influence of the MEK component. It also implied that for the actual E85 spray, the low boiling point (LBP) component in the gasoline would evaporate similarly to the ethanol component. While the mixture formation process of the heavy components with HBP are slow and remains in the spray before the EOI, and as a result, a dense gasoline vapor will form at the spray tip which will be discussed later. Also, the calculated result of the vapor distribution of MEK85/toluene15 indicates that the evaporation of E85 falls between the E0 and E100.
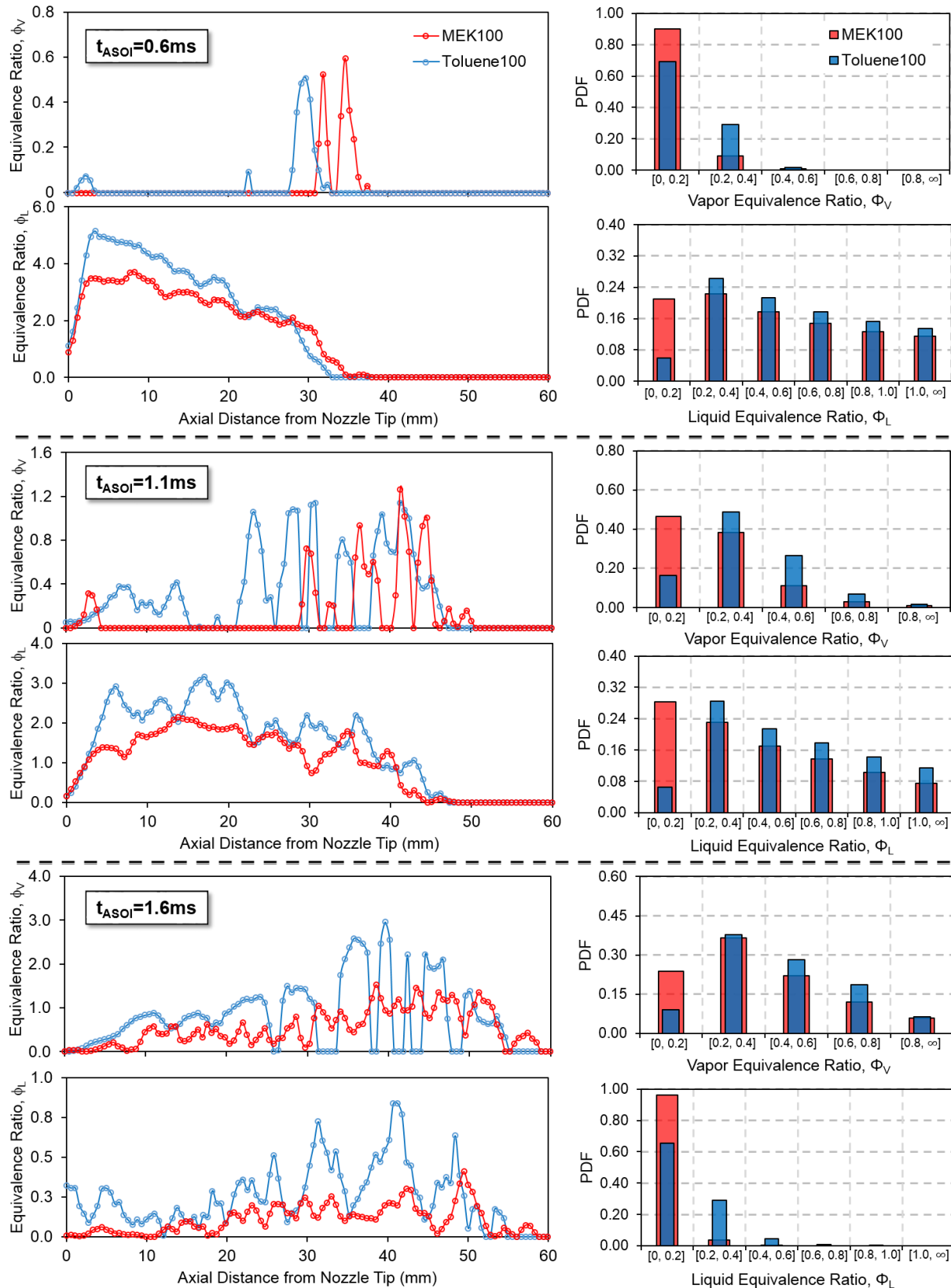
Figure 4.8 Axial Equivalence Ratio Distribution and Frequency Distribution for Pure Fuels

102

More detail of the local mixing for E0 and E100 is showed in Fig.4.8, where the axial equivalence ratio distributions of vapor and liquid are presented in the left column in temporally. Meanwhile, the probability distribution function (PDF) of liquid and vapor equivalence ratio in whole spray is shown in the right column. Before the EOI (t_{ASOI}=0.6ms), both of E0 and E100 obviously begin to evaporate at the downstream of spray along spray axis. While the presence of vapor at the upper region, especially in near nozzle for MEK100, can be found in Fig.4.7. In consider to this fact, it implies that before EOI, the evaporation speed at spray axis is much slow due to the existed large liquid droplets as shown in Fig.4.8 and probably less air entrainment introduced inside the spray.
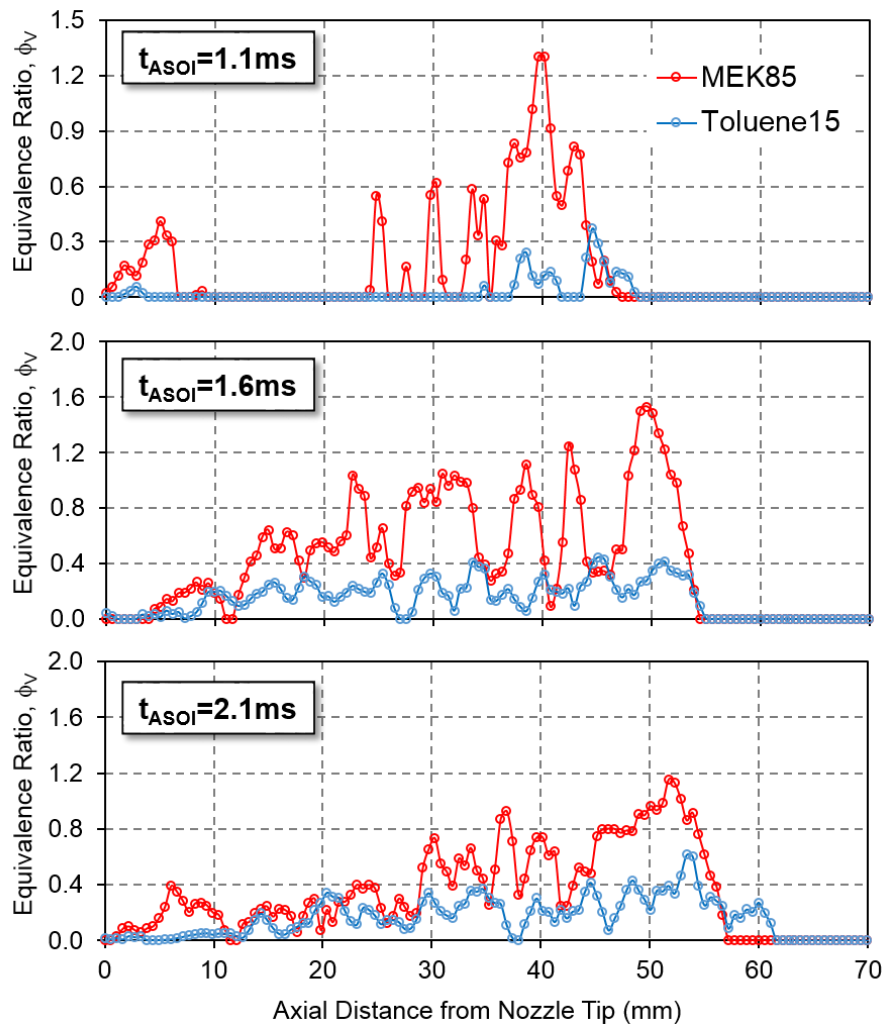

Figure 4.9 Axial Equivalence Ratio Distribution of Different Component in E85 Spray

After EOI, the evaporation process becomes more faster than before for both fuels. From t_{ASOI}=1.1ms to 1.6ms, it is noticeable that the vapor equivalence ratio of toluene100 seems to higher than MEK100 along the spray axis. However, this 'false' fact does not mean the toluene would evaporate faster than MEK with the time escape. Since the liquid equivalence ratio distribution demonstrates a denser liquid droplets still

103

present in spray for toluene100. One hypothesis for the low vapor of MEK along spray axis is that the mixing of MEK with ambient gas progresses quickly and its vapor becomes leaner after EOI. The evidence can be found in the PDF distribution map in the right column of Fig.4.8, where shows a majority share (>70%) of lean mixture (Φ<0.5) for MEK100 in either the vapor or liquid equivalence ratio distribution range after EOI in the whole spray. Therefore, the faster mixing of MEK100 also indicates its faster evaporation speed and more air entrainment which will discussed in the next section.
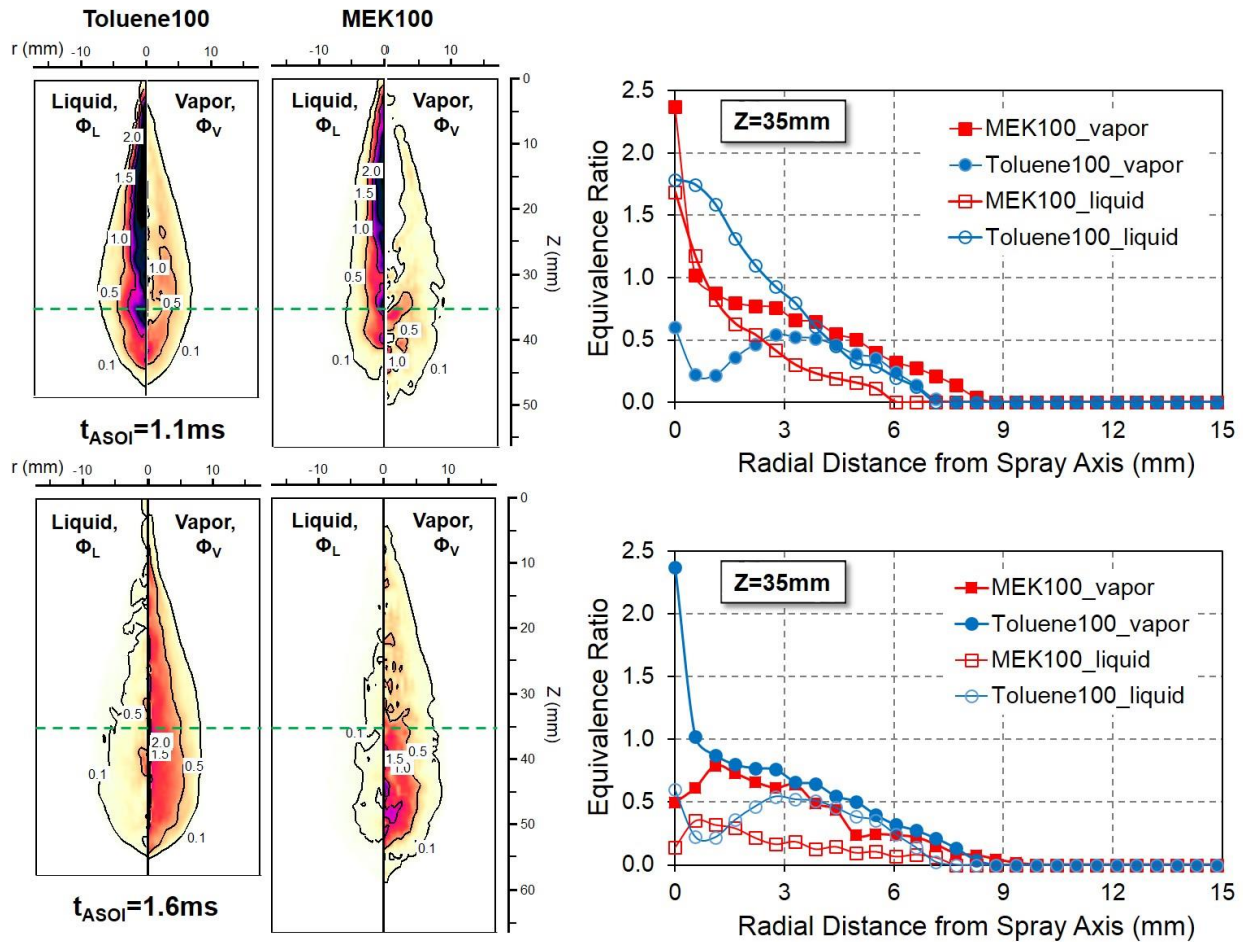

Figure 4.10 Radial Equivalence Ratio Distribution of Toluene100 and MEK100 at Z=35mm

For the E85 spray, the axial equivalence ratio distributions of vapor phase for different component (MEK85 represents the MEK component in E85, toluene15 represents the toluene component in E85 mixture) extracted the data from the spatial distribution maps in Ethanol85/toluene15 and MEK85/iso-octane15, are showed in Fig.4.9. A trend of vaporization stagnation of toluene component with high boiling point is observed before EOI at t_{ASOI}=1.1ms where reveals a negligible vapor at near nozzle region. As discussed previously, this may resulted from the evaporation of LBP component at the early injection. With the spray evolution, both MEK and toluene component distribute their vapor mixture more homogenously

along the spray axis that indicates an improved evaporation. For further development of spray, especially at t_{ASOI}=2.1ms, toluene component takes up a longer vapor propagation than MEK component along spray axis in their binary spray. More detail discussion on this phenomenon will be presented latter.

At 35mm axial distance, the radial distributions of equivalence ratio for pure fuels, toluene100 and MEK100, are shown in Fig.4.10. Both of vapor and liquid concentration decrease with increasing radial distance from spray axis until the r=7 to 8mm. It is obvious to find that the vapor concentration of MEK100 is much greater than that of toluene100, in particular at the spray axis where MEK fuel shows a four times over the toluene. This result reveals a faster evaporation of MEK during the injection, also indicated by the lower liquid concentration and more contracted liquid phase. After the EOI, the vapor equivalence ratio of MEK falls down quickly, yet a dense vapor of toluene still exists at the spray axis and shows a higher concentration than MEK along the radial distance. It provides the fact that the LBP fuel, MEK becomes leaner due to its faster mixing as discussed before.
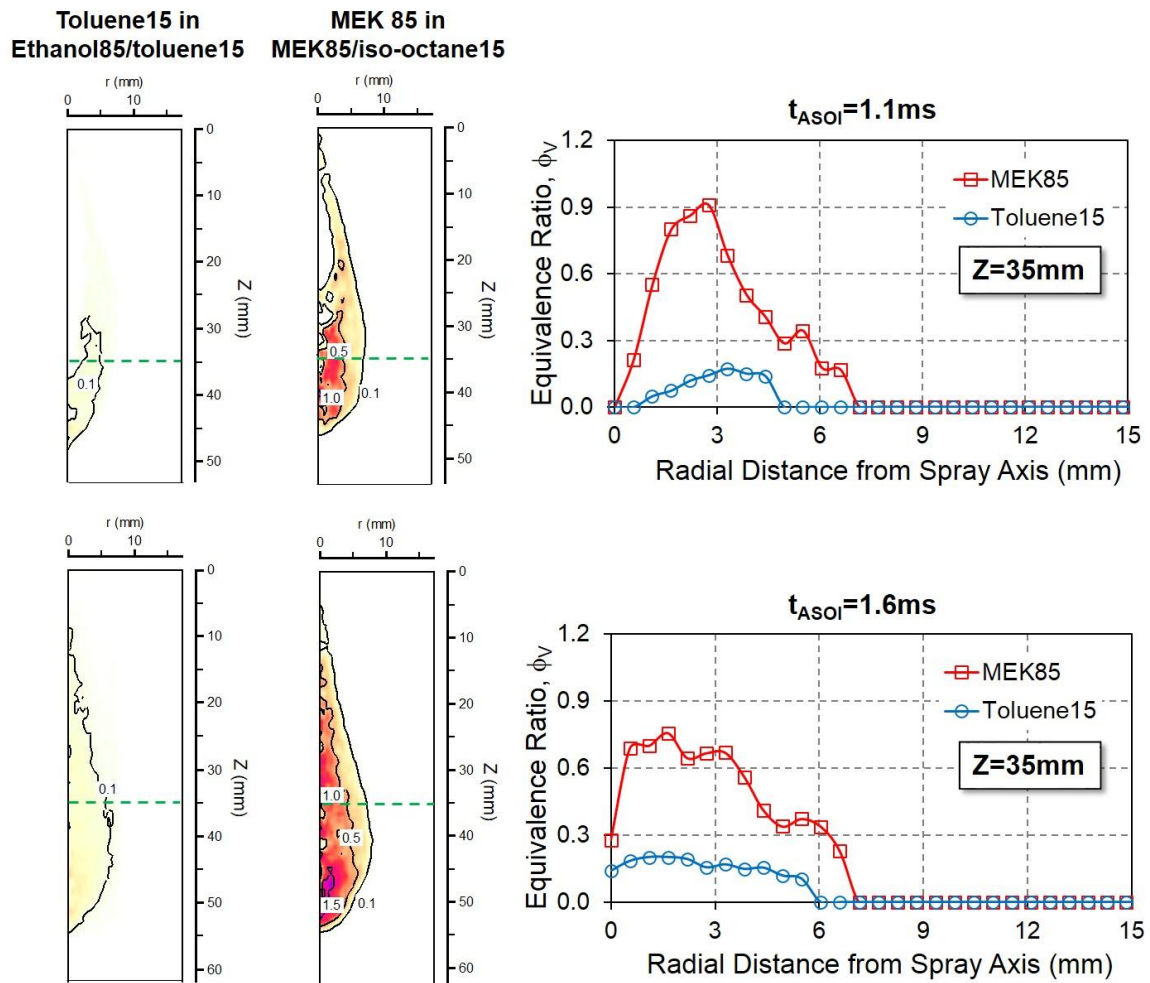

Figure 4.11 Radial Equivalence Ratio Distribution of Toluene15 and MEK85 at Z=35mm

105

Figure 4.11 shows the result of radial equivalence ratio distribution of toluene and MEK component in E85. Either at early or later stage of injection, the wider dispersion of MEK vapor than toluene component indicates that the vapor of LBP fuel covers the HBP component inside the spray totally. The dense LBP component locating at the outer region of spray also prevents the HBP fuel from mixing with ambient gas, hence blocking the vaporization of HBP fuel. Furthermore, the result in this figure implies that in real E85 spray, a pure ethanol vapor concentration may appear at the peripheral region of spray and cover the gasoline vapor inside the spray. This fact can be found in the later analysis.

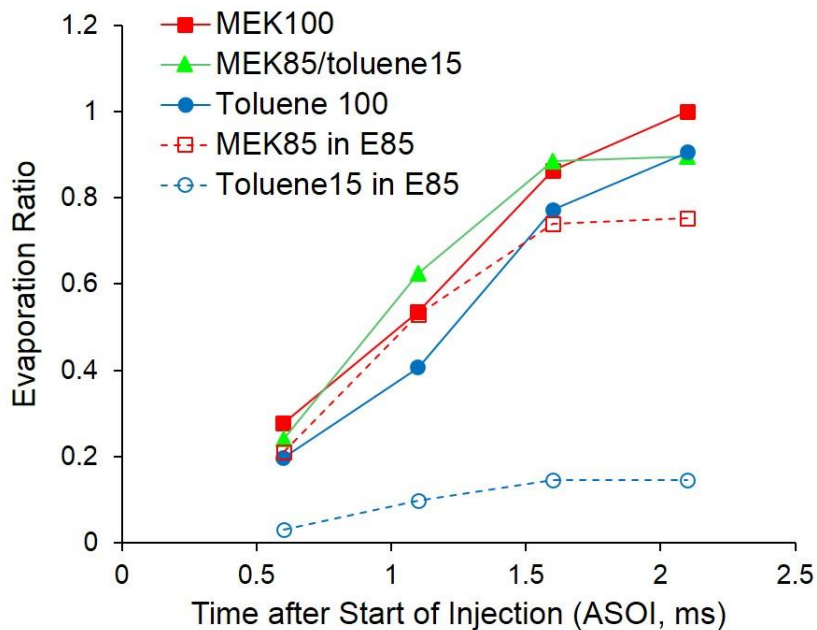### 4.2.4 Evaporation Characteristics

Figure 4.12 Evaporation Ratio of Ethanol-Gasoline Blends and Different Components

Figure 4.12 demonstrates the evaporation ratio of E0, E85, E100 and different components in E85. The vapor mass extracted from MEK85/iso-octane15 and Ethanol85/toluene15 can obtained to calculate the evaporation ratio of ideal E85 groups (MEK85/toluene15). The result of the lower evaporation ratio of toluene15 in E85 again proves the fact that the evaporation stagnation of toluene component (HBP fuel) inducing by the MEK component (LBP fuel), especially at the early injection (t_{ASOI}=0.6 to 1.1ms) at which shows the faster increased rate of the MEK85 than that of the toluene15. While for the pure fuels of MEK100 and toluene100, the increased tendencies of the evaporation ratio are seem to the similar with each other during the whole spray and atomization. It should be noticed that the mixing in a binary spray

(E85) produces mid-boiling point, as well as a closed vapor pressure to E100 estimated by Raoult's Law in previous study [244], which indicates a similar evaporation of E85 to E100 as shown in the figure.
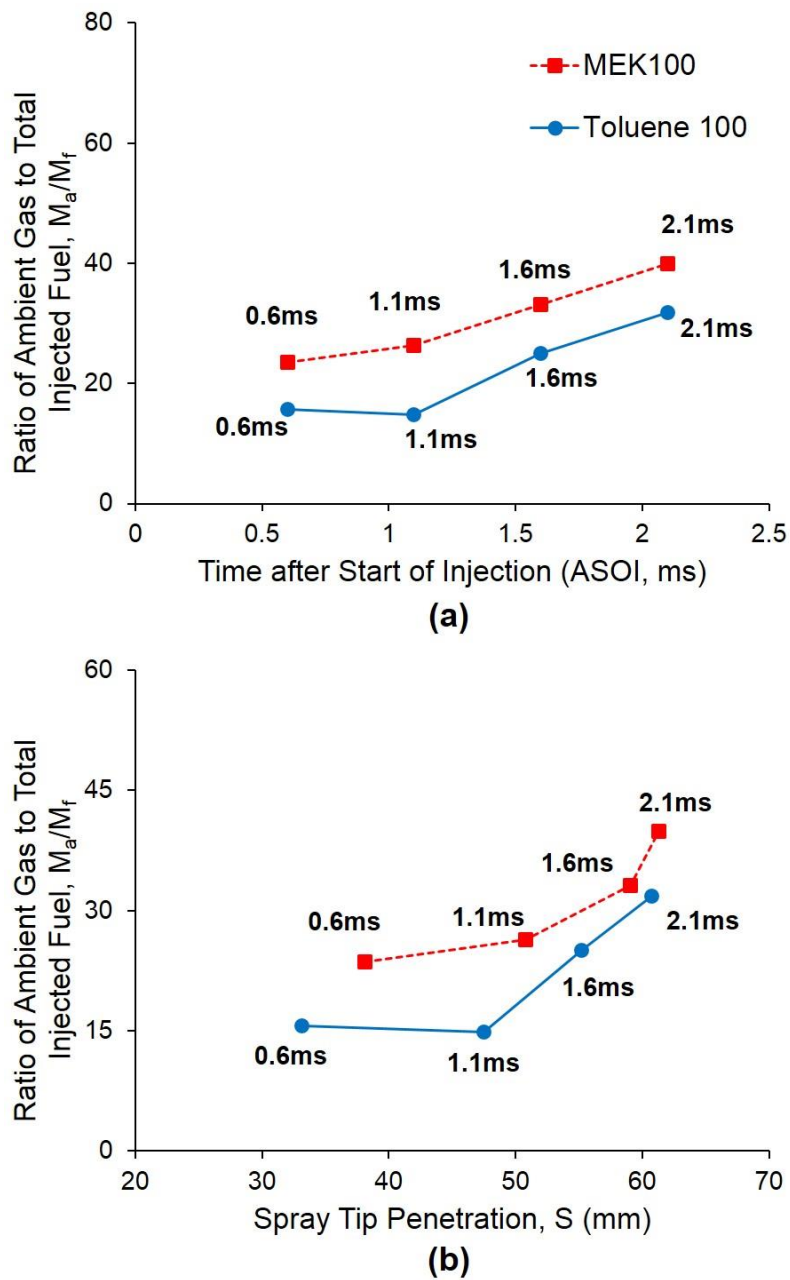
Figure 4.13 Ratio of Air Entrain Gas to Total Fuel Mass versus (1) time escape and (2) Spray Tip Penetration for E100 and E0

The ratio of the mass of air entrainment M_a to total injected fuel mass M_f is able to describe the mixing process. In Fig.4.13, this mixture formation interacted with ambient gas has been shown for E0 and E100. Different processes in mixing are presented in this section. The top in Fig.4.13 is the result of the mixing

rate M_a/M_f versus time escape, while the beneath one (see Fig.4.13 (b)) presents this ratio versus spray tip penetration. It can be found that air entrains increases with time escape for both fuels. For this tendency, more amount of ambient gas is introduced into the MEK spray compared with toluene, again proves that a faster mixing for LBP fuel under high temperature condition.

At temporal evolution, the increased air entrains shows an almost linear trend with the spray development, even after EOI. However, a significant difference for fuels occurs at the early injection. The greater ambient gas introduction over than that in toluene100 at the same injection timing. Two facts can be well explained in, first that the LBP fuel evaporates faster at early injection, and, second that the improved mixing process leads to a decreased local equivalence ratio for LBP vapor. Furthermore, the result of smaller sauter mean diameter (SMD) for MEK100 in Fig.4.14 also implies the well atomization is possible to be achieved when using the LBP fuels, in which shows at least 12% reduction by SMD during spray in this study. In consideration to this, the result in the Fig.4.13 (a) indicates that the mixing process can be enhanced with the increased of ethanol in gasoline fuel.
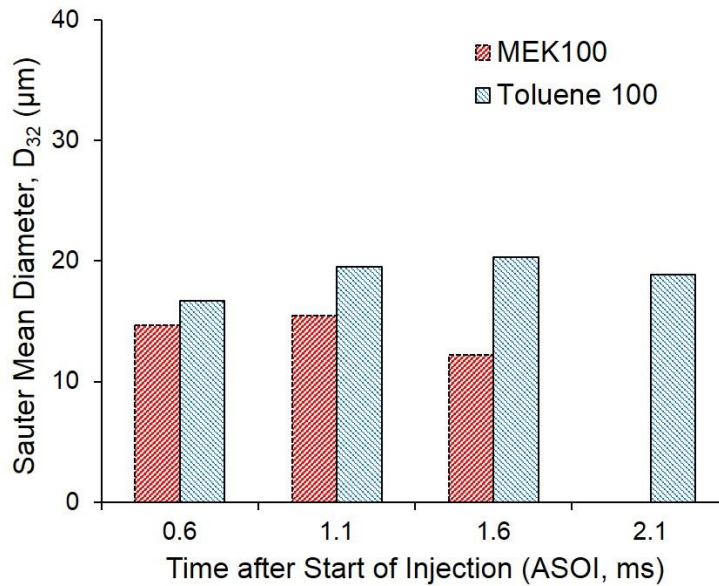
Figure 4.14 Sauter Mean Diameter of Pure Fuels

On the other hand, Fig.4.13 (b) shows that the variation of mixing rate with spray propagation. The result suggests that although the LBP fuel has a more air entrainment than HBP fuel before EOI due to its vaporization and mixing with ambient, this tendency will becomes smaller with the spray downstream propagation. An explanation for this could be addressed to the increased evaporation of HBP fuel after EOI. In terms of Fig.4.13 (a) and (b), the mixing rate, denoted by $M_a/M_{f,}$ is totally improved at the time when the injection is ended, probably as a result of not only the enhanced vaporization with vapor dispersion but also

the entrainment wave formed at near nozzle region during EOI transient and transporting towards downstream [245].

4.2.5 Blending Ratio in Fuel Vapor Ambient-Gas Mixture of E85 Spray

In order to provide added insight into the E85 evaporation, the temporal variation and spatial distribution of the blending ratio in MEK85/toluene15 (E85) were calculated and shown in Figs.4.15 and 4.16.
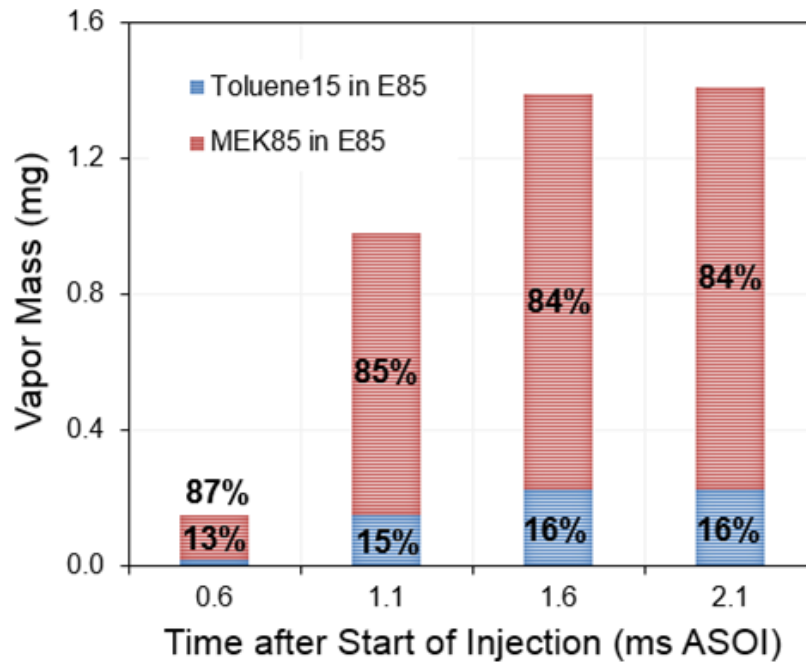

Figure 4.15 Temporal Variation of Blending Ratio for Different Components in MEK85/toluene15

Although the MEK and toluene mixed in the ratio of 85:15, the vapor mass fraction shows the different evolution for each component with the time escape. The faster and earlier evaporation of MEK85 produces a block mixing on the toulene15 as mentioned in the previous sections, leading a more vapor mass of MEK85 in the E85 mixture compared with the vapor mass fraction of the toluene15. However, this tendency becomes into the opposite side when the injection is ended. After the EOI, because of the enhanced evaporation of the toluene component as shown a more homogeneous vapor distribution in Fig.4.7, the ratio of MEK component vapor to the toluene components finally comes to the balance of 85:15, even a slight below that.
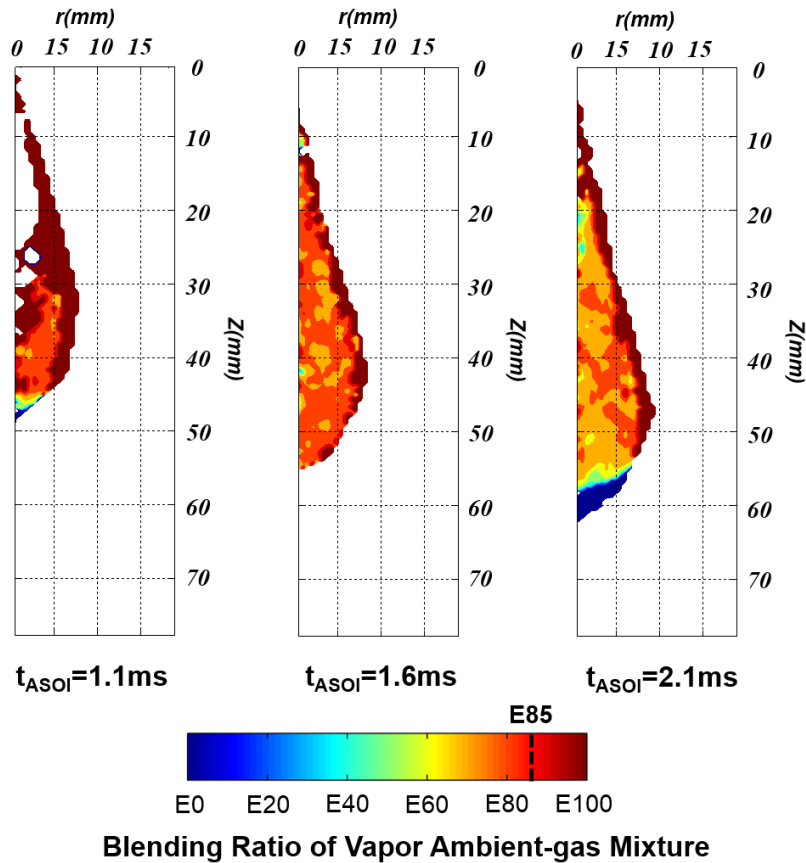
109

Figure 4.16 Spatial distribution of the blending ratio of vapor ambient-gas mixture in MEK85/toluene15

Combing the spatial distribution of MEK and toluene component, the blending ratio map of the vapor ambient-gas mixture in the E85 spray could be produced, which suggests a distinctly stratified vapor of different components due to the different boiling point. A pure MEK takes up the periphery region of the spray, also indicating its faster and earlier evaporation as previous discussion. While the toluene component forms a dense region inner the spray and even at the spray tip, especially for after the EOI where shows a blending ratio of E0 implying a high concentration of toluene as illustrated in t_{ASOI}=2.1ms in Fig.4.16.

Different mixing regimes are proposed her: (1) due to the fast and early evaporation before the EOI, the vapor of LBP component totally covers that of the HBP fuel, and (2) a dense HBP fuel vapor produces at the middle region of the spray, in turn transporting to the downstream spray or even at the spray tip after the EOI. In order to identify the dense region of the HBP fuel formed at the spray tip, the spray penetrations of the MEK in the MEK85/iso-octane15, and toluene in the Ethanol85/toluene15 at EOI timing are carefully measured by the LAS and shows the error in 4.7% and within 2mm in length. It is much smaller than the axial thickness of the dense HBP vapor which expresses approximately 5mm at t_{ASOI}=2.1ms. This result therefore demonstrates the error from the laser shot is less significant. The enhanced evaporation of toluene

component and the dilution of the MEK vapor after the EOI could be considered as the possible reasons for this phenomenon.

Previous study using laser induced fluorescence, conducted by Kawano and Senda et al [246], also reported a stratified vapor distribution in the multicomponent spray and suggested the vapor of HBP fuels mainly located at the downstream of the spray. Their results also indicated a dense region of the HBP fuel would occur at the spray tip because of its heterogeneous distribution along the spray axis. To some extent, the evaporation process of gasoline due to its multicomponent property, has somewhat difference from the toluene used in this study. However, the heavy component in gasoline, such as o-xylene, would still remain in fuel and evaporates after the EOI, thus locates at the spray tip [53, 223]. In spite of the less knowledge in the mechanism of the multicomponent evaporation, in particular for the distillation-like evaporation and co-evaporation regimes [247], this work in the section provides a more clear and useful information on the interaction between the spray mixture and the ambient gas in the E85 spray.

4.3 Fuel Distribution of Impinging Spray on a Low-Temperature Skew Wall

As mentioned at the beginning of this chapter, using ethanol-gasoline in SI engine is usually suffered from the cold start problem that causes a difficulty to start engine and over expected UHC emission. The reduced in-cylinder temperature by the vaporization of ethanol blends, and the sever impingement on a cold wall are regarded as the most significant reasons to responsible for those problems. In the case of DISI engine, although the ethanol-gasoline blend is injected into the in-cylinder condition with high ambient temperature (mainly over 450K), the wall temperature still is low at several early cycles, actually, at normal atmosphere (298K) or ultra-low temperature (about 273K) used in some cooler regions. This will result in a poor fuel evaporation and mixture formation, as well as producing a sever fuel film on cavity wall. Therefore, the fuel distributions of impinging spray by ethanol-gasoline blends on a low temperature skew wall which was selected as the typical impinging wall with 65°, were measured and discussed in this section as follow.

4.3.1 Time-Resolved Distribution of Vapor and Liquid Concentration

Figure 4.17 shows the images of impinging spray in optical thickness measured by LAS. The typical case using toluene100 spray injected towards the skew wall with the temperature of 298K, was selected to illustrate the spray evolution of impingement.
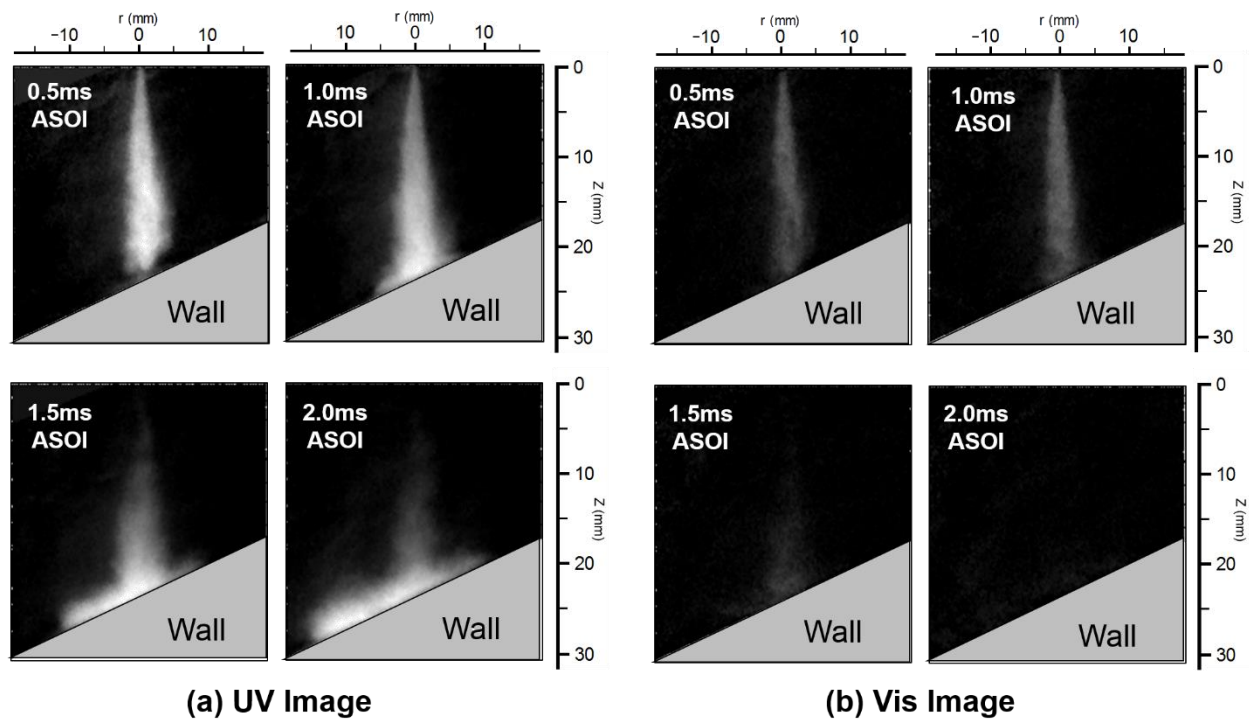
Figure 4.17 Time-Resolved Image of Spray in Optical Thickness for Impingement (Toluene100, P_a=1.0MPa, T_a=500K, P_{inj}=15MPa, t_{inj}=1.3ms, θ_w=65°, T_w=298K, D_{imp}=35mm)

The overall trend of impinging spray can be found in the figure. First, before impingement, less vapor exists at near the region of spray axis which is indicated by a large extinction in Vis image, in this case at t_{ASOI}=0.5ms. Until to the beginning of impingement, suggested by t_{ASOI}=1.0ms, a wider dispersion of spray in UV image compared with that in Vis one demonstrates somewhat concentration of vapor has presented. A dense liquid and vapor phase may locate at the impinge place near the wall that implied by the high brightness in the UV image. After impingement, the spray consisting of vapor and liquid spreads mainly towards downstream along the wall surface. Meanwhile, a portion of vapor and droplets would propagate to upstream, yet the concentration becomes weaker due to the resistance. With the spray further development, for example, at t_{ASOI}=2.0ms, the spray tip region tends to disperse widely as a result of bulk of air entrainment and vortex, hence more vapor form and concentrate near the wall. It should be noticed that the liquid still exist and move along the wall downstream due to the not sufficient heat flux from the wall for the vaporization, hence forms liquid films.
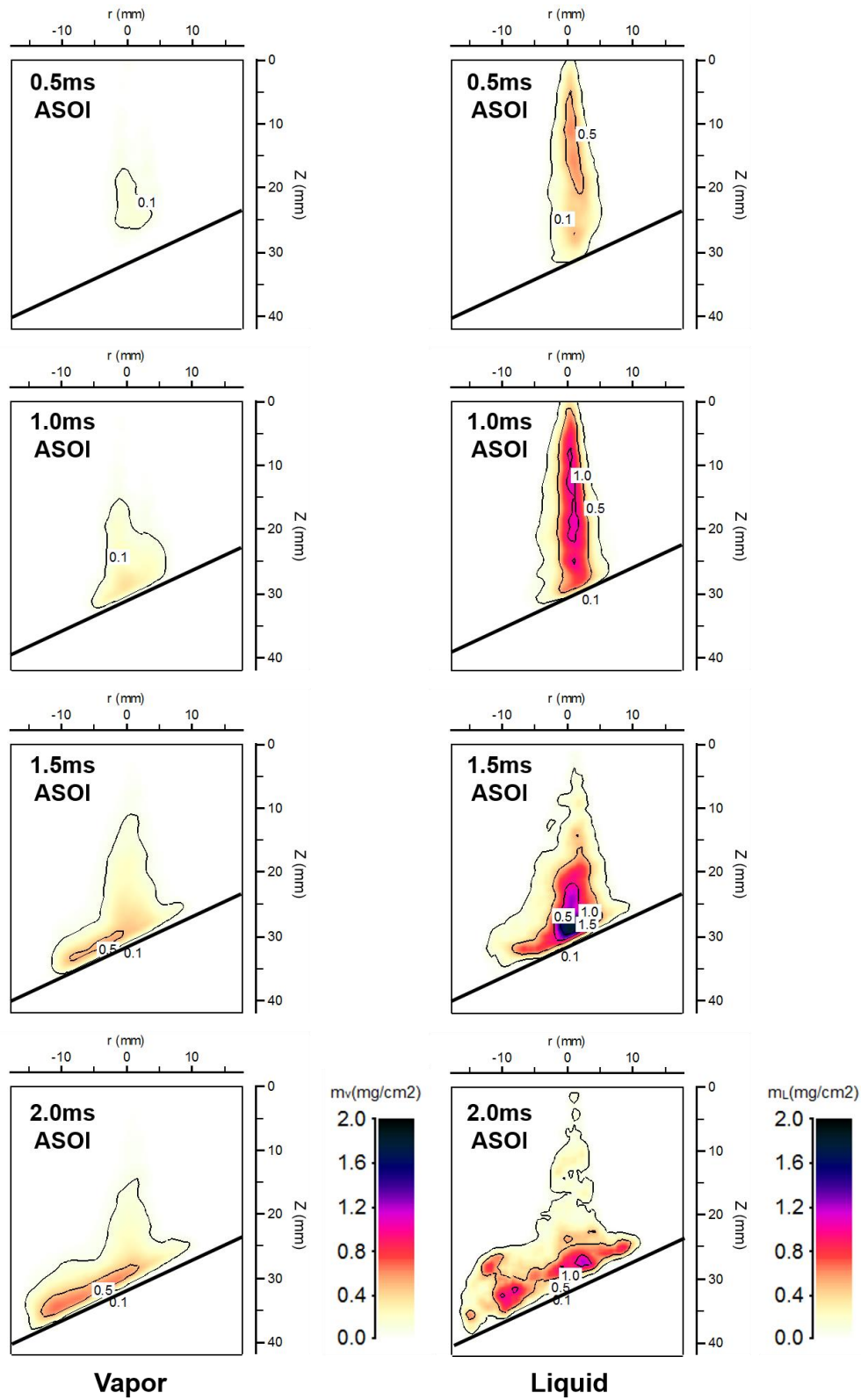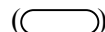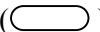
Figure 4.18 Time-Resolved Image of Vapor and Liquid Concentration for Impingement (Toluene100, Pa=1.0MPa, Ta=500K, P_{inj}=15MPa, t_{inj}=1.3ms, θ_w=65°, T_w=298K, D_{imp}=30mm)

Figure 4.18 gives the corresponded contour of line-of-sight integrated fuel concentration distribution of vapor and liquid during the injection and impingement for the case presented in Fig.4.17. For t_{ASOI}=0.5ms, the spray tip penetration just approaches to the wall with a large liquid droplets inside spray. Also, this dense droplets distributes still presents along the spray axis even after impingement, for example, at t_{ASOI}=1.5ms. While the vapor begins to form and mixed with ambient gas faster after impingement. Two facts should be noticed, first, that little fuel vapor exists in spray before impingement, and second, that a dense liquid droplet presents at the impinge point until to at least 1mms after EOI due to the poor evaporation, which shows a similar result revealed by Sakane [248] proposing an over stoichiometric equivalence ratio at those region in diesel spray. Furthermore, the both vapor and liquid droplets propagate along the skew wall towards downstream. Since the resistance from ambient and air entrainment at spray head, the spray tip propagation is blocked and spreads widely. This dispersion can be found in both vapor and liquid phase that promotes the mixing in further.

### 4.3.2 Effect of Impinge Distance on Fuel Distribution

The fuel concentrations of liquid and vapor phase of impinging spray under different impinge distance with the wall temperature of 298K, are shown in Fig.4.19. For every case, the top row presents the result of 30mm in impinge distance, while that of 45mm impingement is listed at the second row. In the case of 30mm impingement, the impinging timing begins at 1.0ms ASOI, while this timing for 45mm impingement was examined at t_{ASOI}=1.5ms.

The result reflects the fact the long distance impingement is able to reduce the formation of fuel film on the wall. In the figure, when the spray begins to interact with wall as shown in Fig.4.19 (a), a relative dense and wider vapor phase exists in the spray region, especially near the impinge point.

At the time of 1.0ms after impingement as shown in Fig.4.19 (b), the spray head propagates more sustainably towards downstream along the wall for 30mm impingement that presents a typical flat shape ( ). However, the longer impingement (D_{imp}=45mm) only has a slightly downstream movement, and demonstrates an obvious cone shape ( ). Two possible reasons may contribute those results. First, more quantity of liquid droplets remain in spray after impingement in the case of the 30mm impinging spray. Due to the shorter impact distances, these cluster liquid droplets with high momentum will move farther after interacting with the cool wall. Poor vaporization causes the contraction of spray, hence produces a flat shape ( ). On the contrary, the longer impingement losses momentum and has a faster evaporation. With the spray dispersion, more vapor takes up the peripheral region of spray. Combining with the slow propagation speed, a cone shape ( ) of vapor therefore can be observed at the case of 45mm impingement.

114
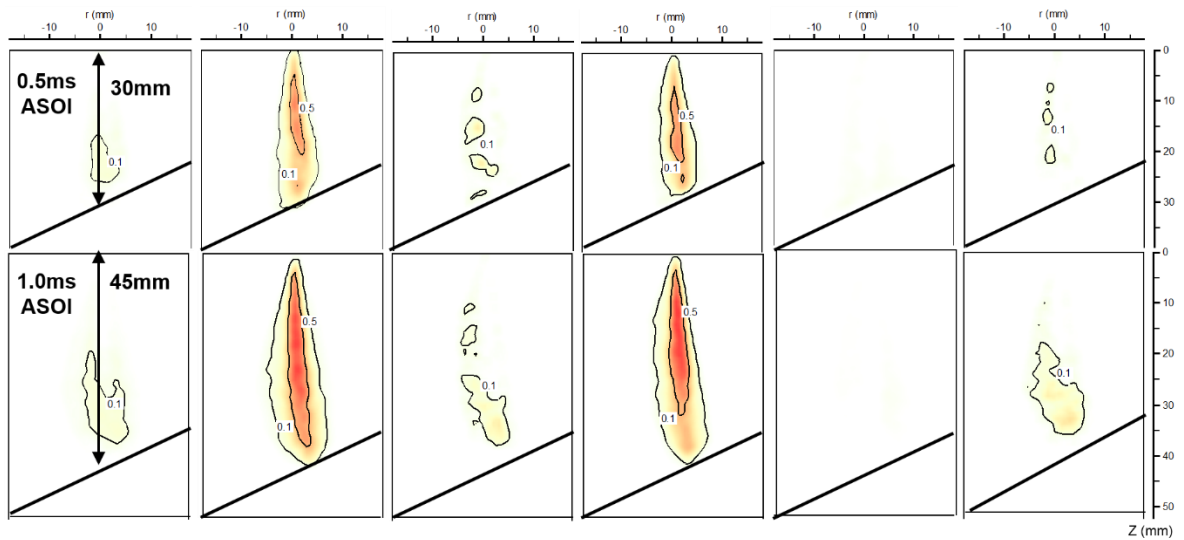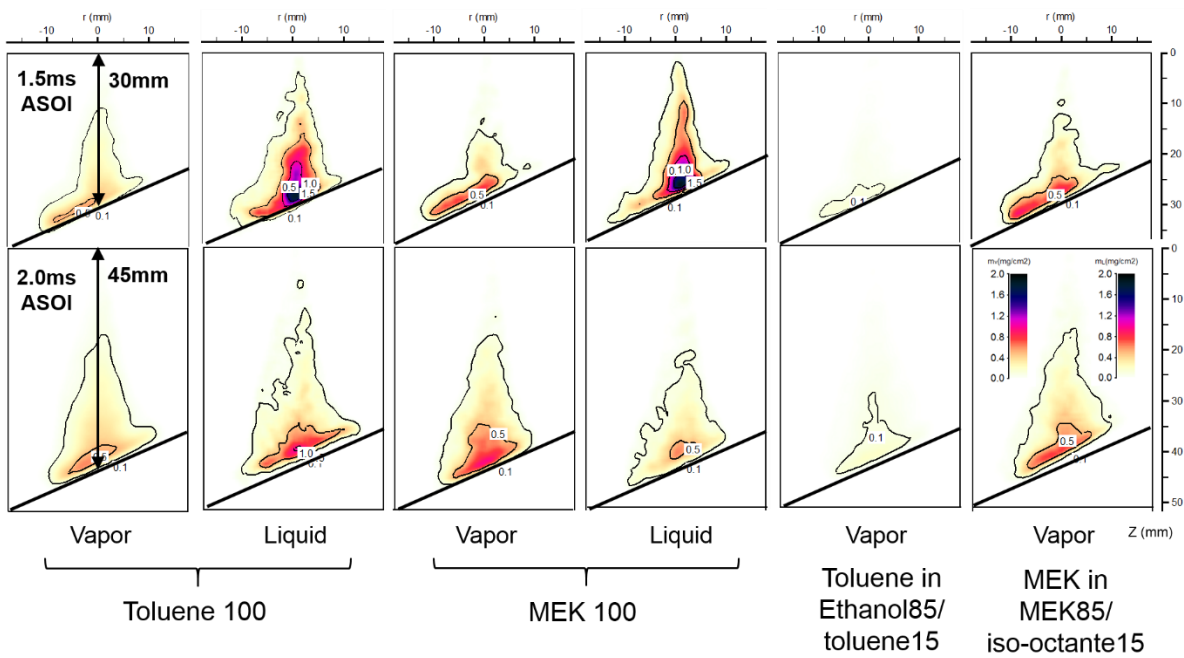
Figure 4.19 Fuel Distribution of Impinging Spray under Different Impinge Distance (T_w=298K)

For E85 spray, it is hardly to detect the observable vapor before impingement for both cases due to the delay evaporation of toluene affected by the faster evaporation of MEK as discussed previously. Also, the vapor phase distribution of toluene still reveals the fact that HBP fuel vapor locates inside of the binary spray, which is the same to the free spray. It should be noticed that the effect of impinge distance on different ethanol-gasoline blends seems similar to each other. However, the quantitative result of the ratio of vapor mass to total injected fuel mass shows somewhat difference between them as shown in Fig.4.20.

115
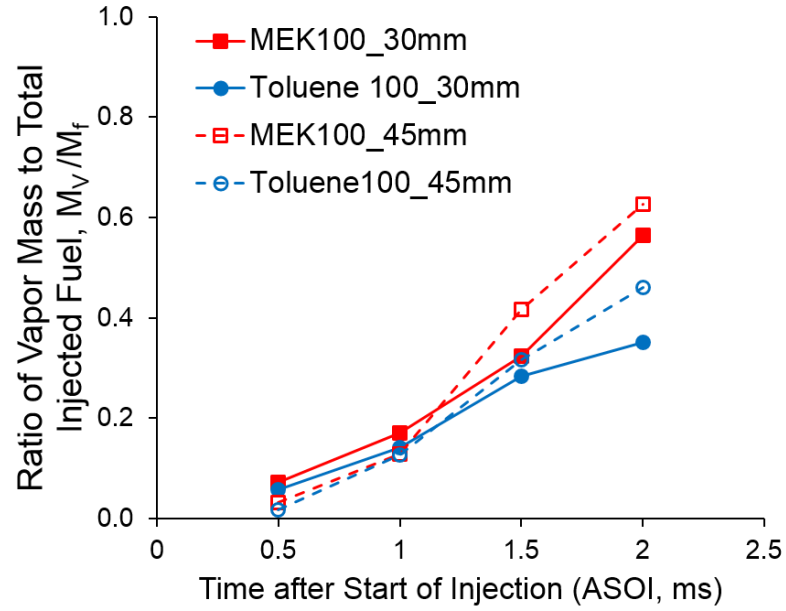
(a) E0 and E100
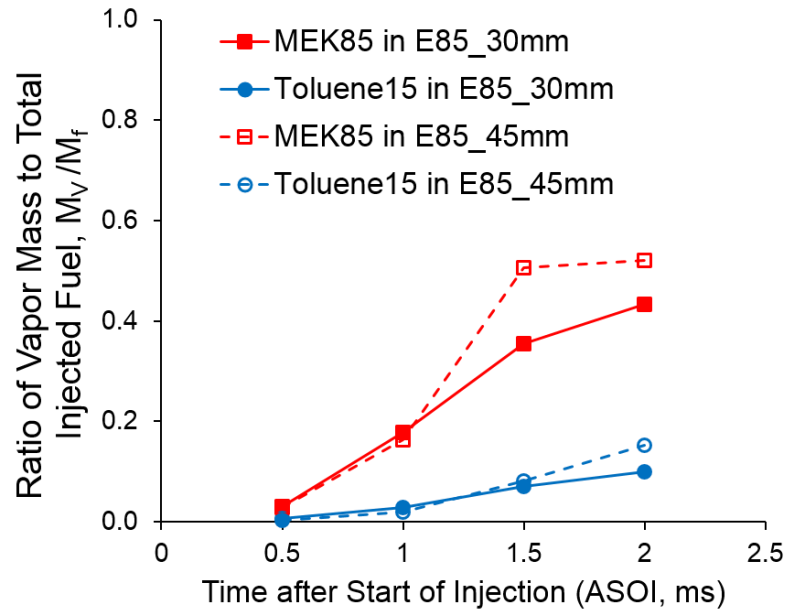
(b) Different Components in E85

Figure 4.20 Ratio of Vapor Mass to Total Injected Mass for Different Ethanol-Gasoline Blends under Different Impinge Distance (Pa=1.0MPa, Ta=500K, P_{inj}=15MPa, t_{inj}=1.3ms, θ_w=65°, T_w=298K)

A greater increased of fuel evaporation is observed after the impingement at both impinge distances for different fuels. While a distinct growth of vapor mass for MEK100 than toluene100 indicates that the effect of impingement on the improved evaporation is more efficient for LBP fuel than the HBP fuel. Furthermore, the

influences of impinge distance on the evaporation of pure fuel are similar to each other. The different components in E85, however, show a great distinguishable phenomenon. In Fig.4.20 (b), the MEK component begins to evaporates faster after impingement (t_{ASOI}=1.0ms), in comparison to a slightly increase of vapor mass for toluene component in E85 spray. Also, the longer impinge distance improve more (nearly five times) on the evaporation of MEK component than that of toluene in this study.
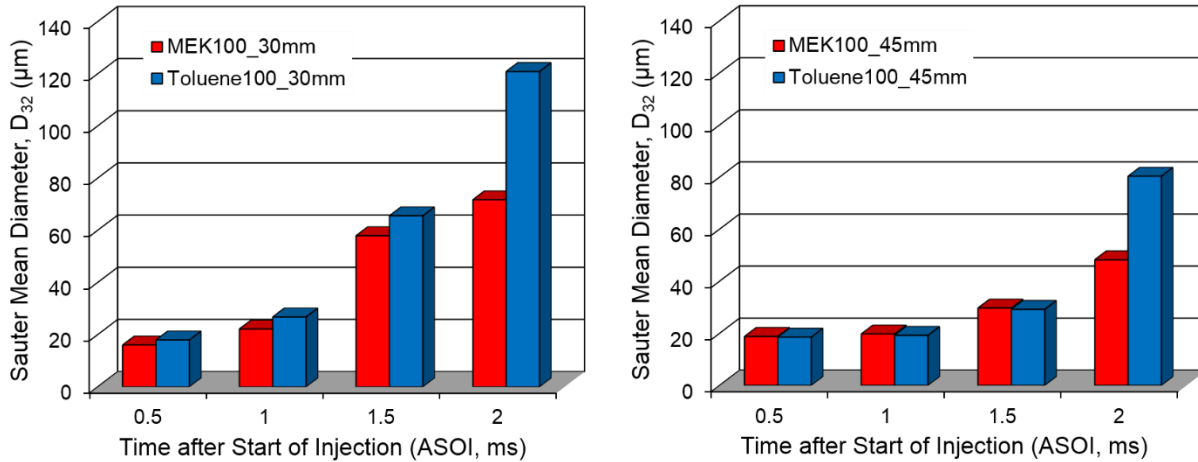
Figure 4.21 Effect of Impinge Distance on Sauter Mean Diameter (Pa=1.0MPa, Ta=500K, P_{inj}=15MPa, t_{inj}=1.3ms, θ_w=65°, T_w=298K)

The atomization characteristics of spray impingement on different distances is show in Fig.4.21. The tendency of spray disintegration process is obvious. Liquid droplet size increases when the fuel impinges on the surface of wall due to other large size of droplets forming by the droplet collide and coalescence. Before or at impinge time, for example, t_{ASOI}=0.5ms for D_{imp}=30mm and t_{ASOI}=1.0ms for D_{imp}=45mm, the size of droplet seems similar to each other indicating that the spray breakup before impingement has no significant influence by the shorter propagation space relative to the impinge wall. While a decrease droplet size with the increase of impinge distance can be found in the figure in the same time sequence. The sufficient time for the atomization of spray is reasonable as the key issues resulting in this trend.

However, one should be mentioned that if concerning the same time interval after impingement, it seems that longer impinging distance would cause an increase of SMD compared with the shorter one. For example, in the case of D_{imp}=30mm, the SMD increases about 3 times after impingement timing (from t_{ASOI}=0.5 to 1.5ms). While for the D_{imp}=45mm, the SMD of toluene increases an approximately four times after impinging timing (from t_{ASOI}=1.0ms to 2.0ms), except the MEK. It implies that HBP fuel may be influenced by the impinge interaction with wall because of more droplet remaining in the spray. On the other hand, MEK100 shows a favorable breakup process with a smaller droplet size due to its low boiling point as discussed before.

4.3.3 Effect of Wall Temperature on Fuel Distribution

The effects of wall temperature on the liquid and vapor phase of ethanol-gasoline blends are shown in Fig.4.22. Similar to Fig.4.19, a standard wall temperature of 25°C was selected as the benchmark to make the comparison with the ultra-low wall temperature with 0°C. The impinge distance was chosen under the same condition with D_{imp}=30mm. Two typical timing, at impingement and 1.0ms after impingement were set to investigate the mixture process interacting with the wall.

It can be observed that less vapor forms before the impingement for all fuels when the wall temperature is 273K, indicating a poor evaporation during the injection. This result implies a fact that the ultra-low temperature of wall may affect the ambient temperature distribution around the spray, then causing slow breakup and vaporization on fuels. One hypothesis is that the ultra-low temperature wall could lead to a much drop-off temperature and gradient from the near wall to nozzle tip compared with the standard wall temperature. Meanwhile, the shorter impinge distance, 30mm from the nozzle tip, also results in a relative narrower space from the nozzle tip to the wall, which is enable to highlight the effect of the heterogeneous distribution of ambient temperature. The long liquid-core containing lengths (high concentration over 0.5mg/cm^2) in both toluene100 and MEK100 at t_{ASOI}=0.5ms, also reveal the slow speed of vaporization at this space.

After impingement (at t_{ASOI}=1.5ms), more dense liquid droplets present at near the ultra-low temperature wall. Also, the less vapor forms around the liquid phase, especially in the toluene100 with a high boiling point. It can be found that the over low temperature of wall will reduce the vaporization speed for fuels. While in a binary spray, such as E85, the effect of ultra-low temperature of wall on the evaporation of individual component shows a difference. A more detail on this process is presented in Fig.4.23.
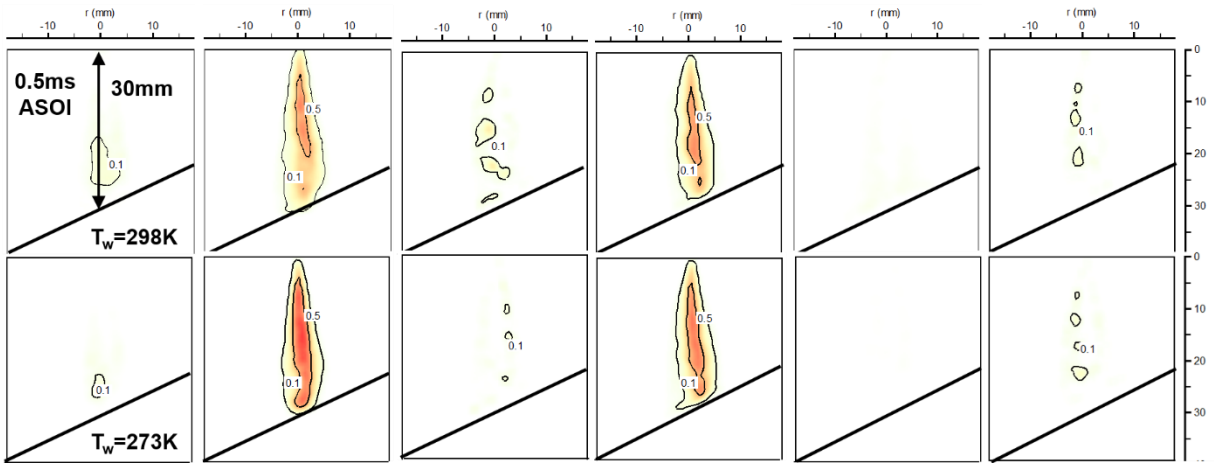
(a) At Impingement
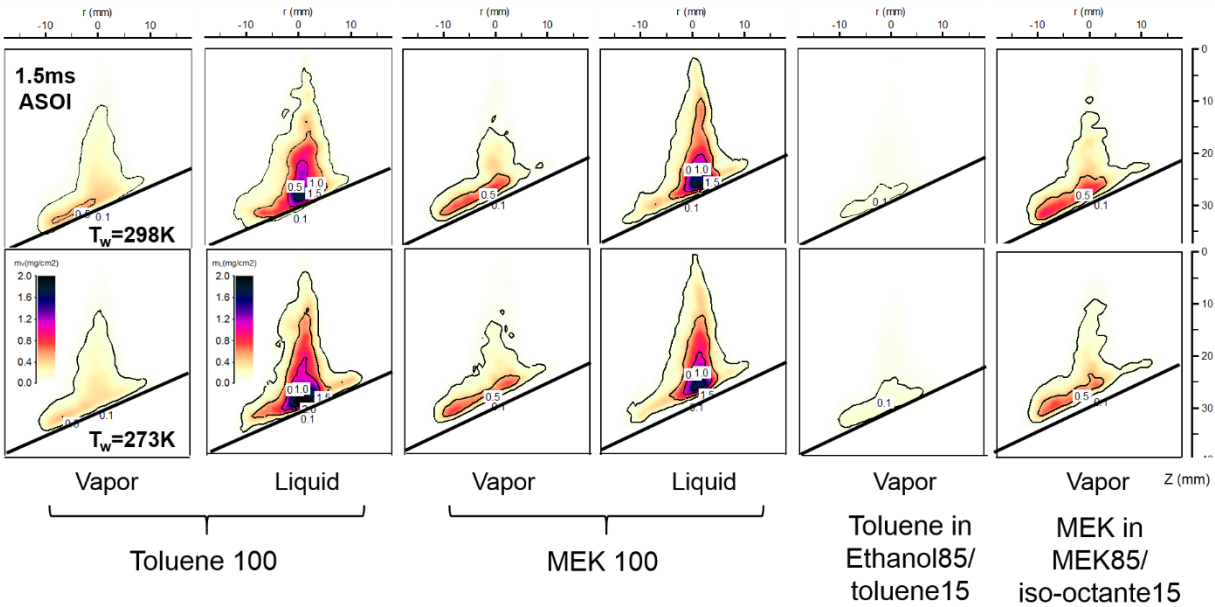
(b) 1.0ms After Impingement

Figure 4.22 Fuel Distribution of Impinging Spray under Different Wall Temperature

As expected, the over low temperature of wall reduces the evaporation speed for fuels, and this decrease becomes more sever with the time escape due to the low temperature preventing the evaporation. In addition, somewhat difference between individual components occurs when the E85 interacts with wall. As Fig.4.23 (b) shown, the vapor mixture is greatly decreased by the low wall temperature (T_w=273K) for MEK component in E85 spray. In the case of toluene component, it shows a similar evaporation for low temperature of wall to the standard condition. However, an opposite variation can be found after spray/wall interaction (after t_{ASOI}=0.5ms), which presents an increase vapor quantity compared with the MEK component. A possible reason is attributed to the enhanced mixing by the increased tangential velocity of

119

impinging fuel with decreased wall temperature [249]. Because the toluene vapor only locates at the middle to downstream of spray as presented previously. The effect of enhanced mixing induced by the increased tangential velocity may be significant for the increased vapor mass of toluene. Also, this result indicates that the E85 evaporation falls in between the E100 and E0 at both conditions.
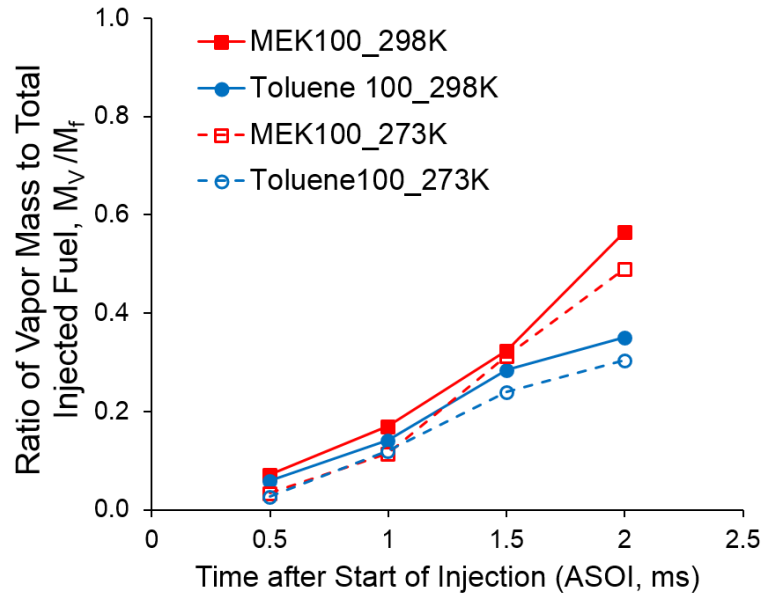
(a) E0 and E100
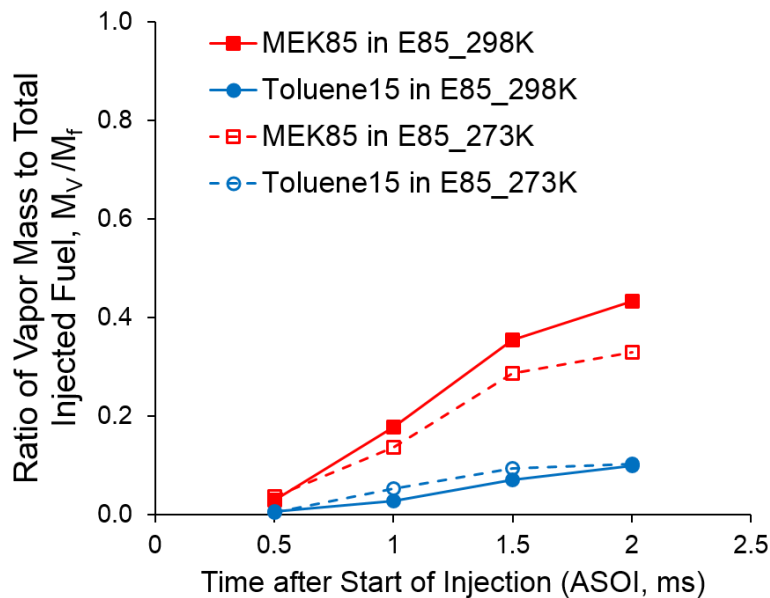
(b) Different Components in E85

Figure 4.23 Ratio of Vapor Mass to Total Injected Mass for Different Ethanol-Gasoline Blends under Different Wall Temperature (Pa=1.0MPa, Ta=500K, P_{inj}=15MPa, t_{inj}=1.3ms, θ_w=65°, D_{imp}=30mm)

120

The temperature effect of spray spreading on leading edge is investigated by the impinge spray penetration, which is shown in Fig.4.24. The overall tendency shows that the spray tip penetration is reduced by the decrease of wall temperature. This result is attributed to the enhanced head vortex appearance with increased wall temperature, hence improving the mixing rate and enable the spray propagating more sustainably [250].
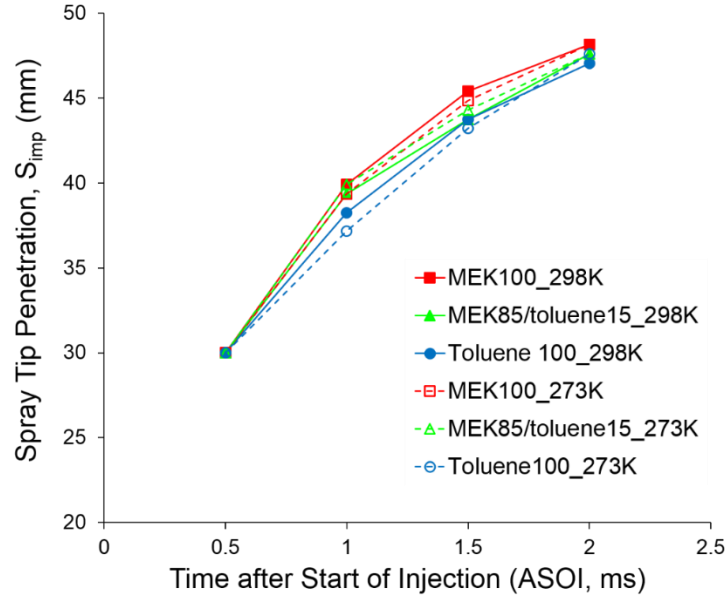
Figure 4.24 Impinged Spray Tip Penetration of Fuels under Different Wall Temperature (Pa=1.0MPa, Ta=500K, P_{inj}=15MPa, t_{inj}=1.3ms, θ_w=65°, D_{imp}=30mm)

4.4 Summary

In this section, the dual-wavelength ultraviolet-visible laser absorption scattering (LAS) was employed to investigate the mixture formation of ethanol-gasoline blends in free spray and impinge spray. Not only the pure fuel, such as E100 and E0, but also the binary fuel, E85 were able to be quantitatively measured using the substitute fuels in LAS system to determine the spray behavior. A standard wall temperature of 298K and ultra-low temperature of 273K were used to study the spray mixture formation of impingement for ethanol-gasoline blends under cold start condition. The main conclusions can be summarized as follows.

Free spray:

1. Liquid phase penetration has no significant differences for different ethanol ratios mixing with gasoline. While the vapor spray penetration length becomes longer with the increase of ethanol ratio, due to reduction of boiling point in blended fuel by the ethanol content.

2. The quantitative result of liquid and vapor phase distribution suggests that E100 has a faster evaporation speed than other fuels due to its lower boiling point. In the case of E85 spray, according to the spray behavior of individual component, it implies that the low boiling point (LBP) components in gasoline may evaporate similarly to the ethanol that showing a homogenous distribution of vapor along the spray axis. While the high boiling point (HBP) components in gasoline will only locate at the middle to downstream due to its evaporation blocked by the LBP components at early stage of injection.

3. Based on the analysis of the evaporation characteristic of different components in E85 spray, a dense gasoline vapor would form at the middle to downstream of spray, especially at the spray tip region after EOI. While the data of radial concentration distribution reveals the fact that the vapor of LBP fuel totally covers the HBP fuel vapor inside the spray, which implies that a high concentration of ethanol vapor would present at the peripheral region of spray. Although the ethanol and gasoline mixed in the ratio of 85:15, a distinctly different evolution of vapor mass demonstrated that the ethanol took up a larger portion of total vapor mass (87%) than mixing ratio (85%) before EOI due to its fast evaporation, yet decreased after EOI (84%) as a result of the enhanced evaporation of gasoline. Therefore, owing to the different vapor behavior of components, a typical stratified mixture distribution would form in E85 spray.

Impinging Spray:

1. The increased impinge distance can reduce the potentiality of liquid film on the wall, mainly due to some portion of liquid droplets evaporating before impingement. Because of the poor evaporation, the shorter impinge spray tends to form a flat shape along the wall after impingement in terms of momentum losses. While for the impinging spray at long impinge distance, lots of fuel vapor takes up the peripheral region of spray, hence generates a cone-shape fuel vapor. Furthermore, E100 has a faster evaporation speed after impingement than E0. In the E85 spray, the evaporation of LBP fuel component is accessible to be influenced by the impingement and becomes vigorous, as apposes to no significant effect on the HBP fuels.

2. In the case of the spray impingement under ultra-low wall temperature, the ambient temperature field in the space from nozzle tip to wall, is influenced by the heat transfer from the wall, and as a result, reduces the evaporation speed of fuel in this region. Therefore, a denser liquid core remains along the spray axis during the spray/wall interaction. Furthermore, the decreased evaporation

becomes more severe than the standard condition with time escape. Owing to the reduced head vortex, the spray tip penetration length of ultra-low impingement is slightly shorter.

CHAPTER 5 IGNITION PROCESS OF ETHANOL-GASOLINE BLENDS

5.1 Experimental Condition

Ignition robustness plays a key role on the mass production of SG-DISI engines. Due to the short time interval between the injection and ignition, the clarification of spray-ignition and its effect on the initial flame formation is important to improve the combustion performance of this type of engine. In this chapter, the ignition process of ethanol-gasoline blends was clarified by shadowgraph and OH* chemiluminescence. The experimental condition is shown in Table 5.1. The ambient condition was set similarly to the LAS measurement, except the ambient gas was changed by air. The same VCO injector with a nozzle hole of 0.15mm, was centrally mounted in the top of the vessel cover and pressurized by an accumulator of 20MPa. Ignition and combustion process were determined by the real gasoline and ethanol, consisting of E100 (100% ethanol), E85 (85% ethanol and 15% gasoline) and E0 (100% gasoline). For the ethanol in the ignition and combustion imaging, due to its lower air/fuel ratio (AFR) in stoichiometry and less lower heating value (LHV) than gasoline (typical AFR of 9.0 and LHV of 26.99MJ/kg for ethanol, 14.7 and 44.4MJ/kg for gasoline), the longer injection pulses of 1.42ms and 1.43ms were set for E85 and E100 respectively to maintain the same calorific value compared with the E0.
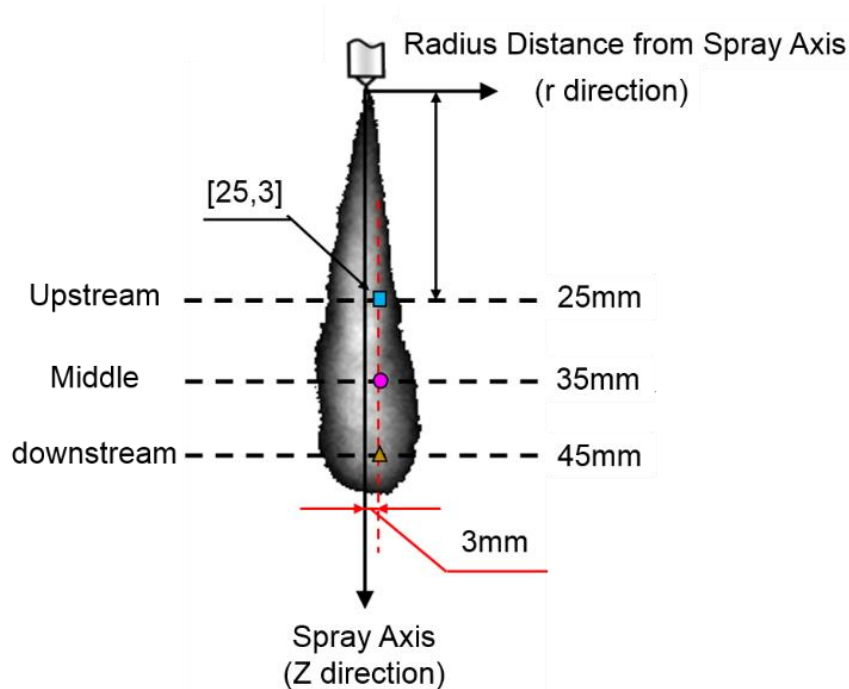
Figure 5.1 Definition of Ignition Location

Because of the special igniter available for flexibility arranging, the ignition position is able to be adjust to the location of interest. The definition of ignition location is shown in Fig.5.1. The spray axis distance from the nozzle tip was denoted Z, while the radial distance from the spray axis was denoted r. Three typical locations along the spray axis, Z=25, 35 and 45, were selected to represent the upstream, middle and downstream of the spray. Various radial distance away from the spray axis were chosen to clarify the ignition map. Also, the ignition timing was set to -0.5, -0.25, 0, 0.25, and 0.5ms time after end of injection (AEOI). Furthermore, several ignition dwell times (2~6ms) were chosen to study the effect of ignition energy on the ignition process and initial flame formation and development.

Table 5.1 Experiment Condition of Ignition and Combustion

Ignition Process			
Specific Items	Shadowgraph		OH* Chemiluminescence
Ambient Condition			
Ambient Gas	Air		
Ambient Temperature, T_a (K)	500		500
Ambient Pressure, P_a (MPa)	1.0		1.0
Injection Condition			
Hole Diameter, D (mm)	0.15		0.15
Injection Pressure, P_{inj} (MPa)	20		20
Injection Duration, t_{inj} (ms)	E0	E85	E100
	1.1	1.42	1.43
Test Fuel			
E0	Gasoline 100 (100% Gasoline)		
E85	Ethanol 85 (85% ethanol) + Gasoline 15 (15% gasoline)		
E100	Ethanol 100 (100% ethanol)		
Ignition Condition			
Ignition Position, [Z,r]	[25,1], [25,2], [25,3] [35,1], [35,2], [35,3], [35,4] [45,1], [45,2], [45,3], [45,4]		[25,3], [35,3], [45,3]
Ignition Dwell Time, t_d (ms)	2, 3, 4, 5, 6		2, 3, 4, 5, 6
Ignition Timing, (AEOI, ms)	-0.5, -0.25, 0, 0.25, 0.5		

5.2 Ignition Probability

5.2.1 Temporal Image of Ignition Process

In order to judge the initial spark and flame development, the special setting for the camera is considered. Since the higher flame luminosity of E0 and E85 is distinct under a bright-background (high illumination) condition and sufficient to be detect, due to them containing the long-chain carbon content. Therefore, the black-white camera (FASTCAM-APX RS, Photron Co.) setting of ignition probability measurements for E0 and E85 was set by using a Nikkon F=105mm lens, f/4.0. While for the E100, a dark-background (low illumination) was employed to detect the ignition process, because of the less luminosity from E100. Hence the aperture of camera was set to f/2.8. In the case of spray imaging, the bright background and small aperture were used to produce a high quality with the clear spray edge.

The ignition process is classified as three types: (1) successful ignition that expresses the initial flame kernel produced after spark and the subsequent full development of flame propagation; (2) partial ignition that shows the initial flame kernel can be formed, yet prevented from the next propagating; (3) failure ignition which exhibits the unsuccessful formation of flame kernel and the losses of observable flame luminosity. Figure 5.2 shows the schematic definition of ignition process based on the shadowgraph. When the back light passes through the spray area, the spray structure can be captured due to the extinction of spray liquid droplets, and the vapor phase by the reduced ambient density. The "schlieren-like" background is observed in the shadowgraph image due to the heterogamous distribution of ambient density.

In Fig.5.2 (a), the successful ignition shows a consecutive process from initial flame kernel formation after spark, to a distinct flame evolution with a high luminosity, for example, at 1.5ms time after ignition (t_{aign}). Due to the variation of ignition would appear in the case of the high temperature and high pressure, especially in the non-uniform ambient where tends to cause somewhat deviation of spray structure at every cycle, hence the spark fluctuation becomes inevitable. As shown in Fig.5.2 (b), provided the mixture ignited after spark, and extinguished within a short time without a widely flame propagation, this ignition is regarded as the partial spark, regardless of some dark smoke region can be found in the images. Furthermore, it is reasonable to define the spark process as failure ignition in according to neither presence of ignition or flame development, as shown in Fig.5.2 (c).
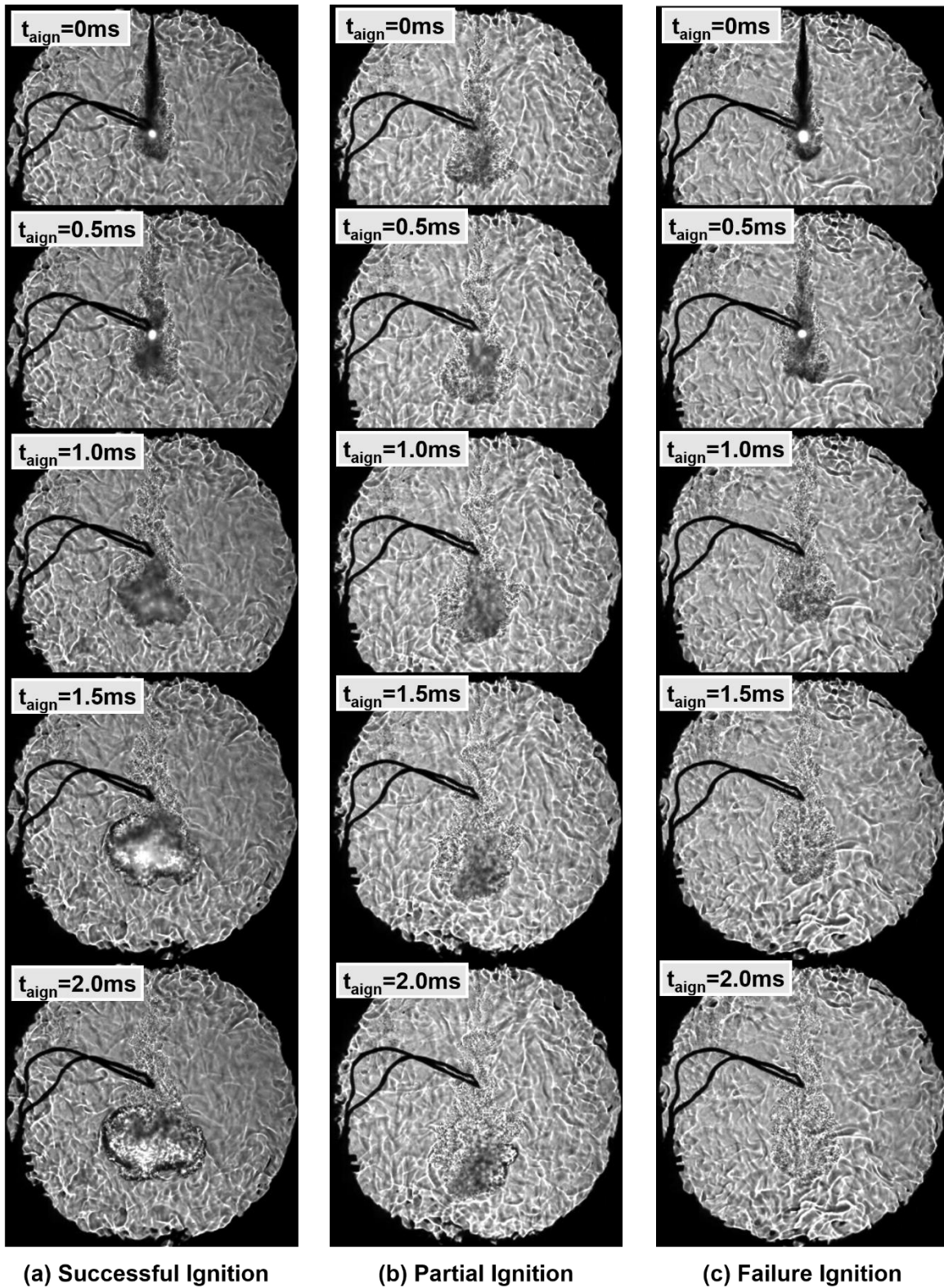
Figure 5.2 Definition of Ignition Process (E85, P_a=1.0MPa, T_a=500K, P_{inj}=20MPa, t_{inj}=1.42ms, t_d=6ms, [Z,r]=[35,3], t_{ign}=-0.25 ms AEOI for (a) and (c), 0.5ms AEOI for (b))

5.2.2 Ignition Probability of Ethanol-Gasoline Blends

Due to the sufficient heat and energy from the initial flame kernel transferring to the ambient ignitable mixture, the flame propagation and luminosity can be captured if the fuel is ignited successfully as discussed previously. Therefore, the ignition probability was clarified in this way whether a visible flame could be observed or not and obtained by the 50 times testing at every ignition position and timing, that means only the successful ignition is considered in the ignition probability calculation.
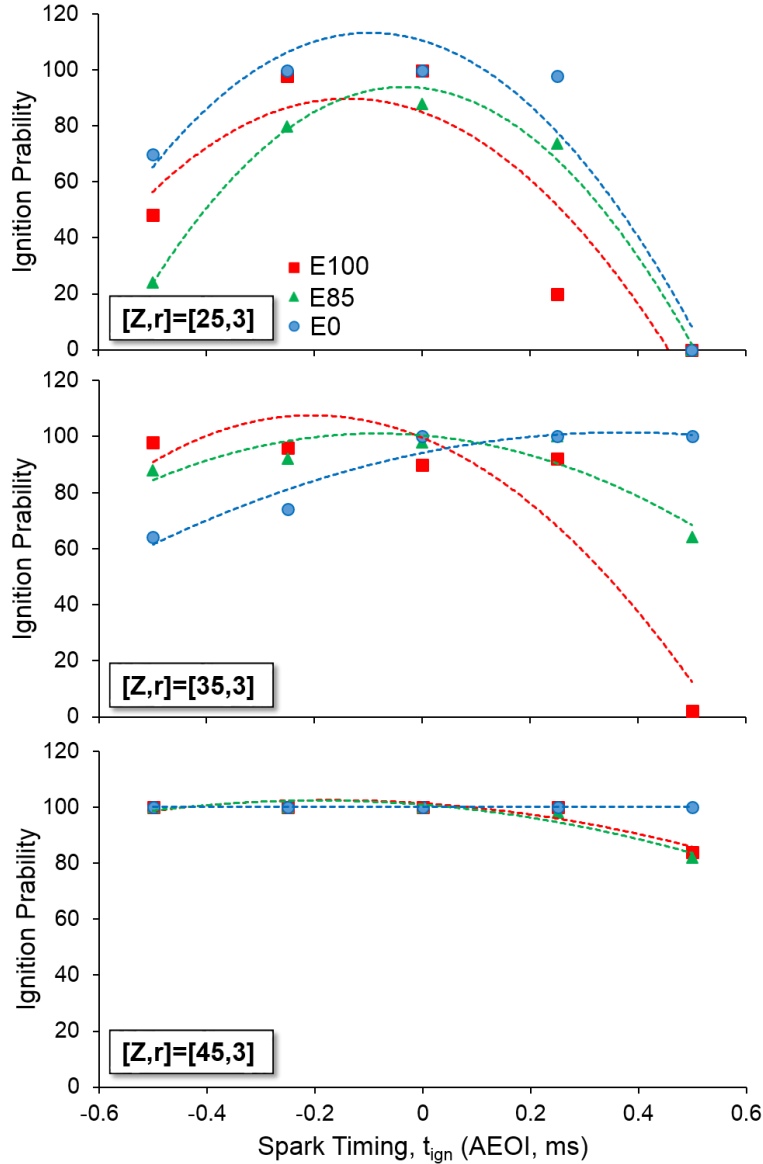
Figure 5.3 Stable Ignition Range of Spark Timing at Typical Local Positon. The trends was given by the solid line. (P_a=1.0MPa, T_a=500K, P_{inj}=20MPa, t_d=6ms)
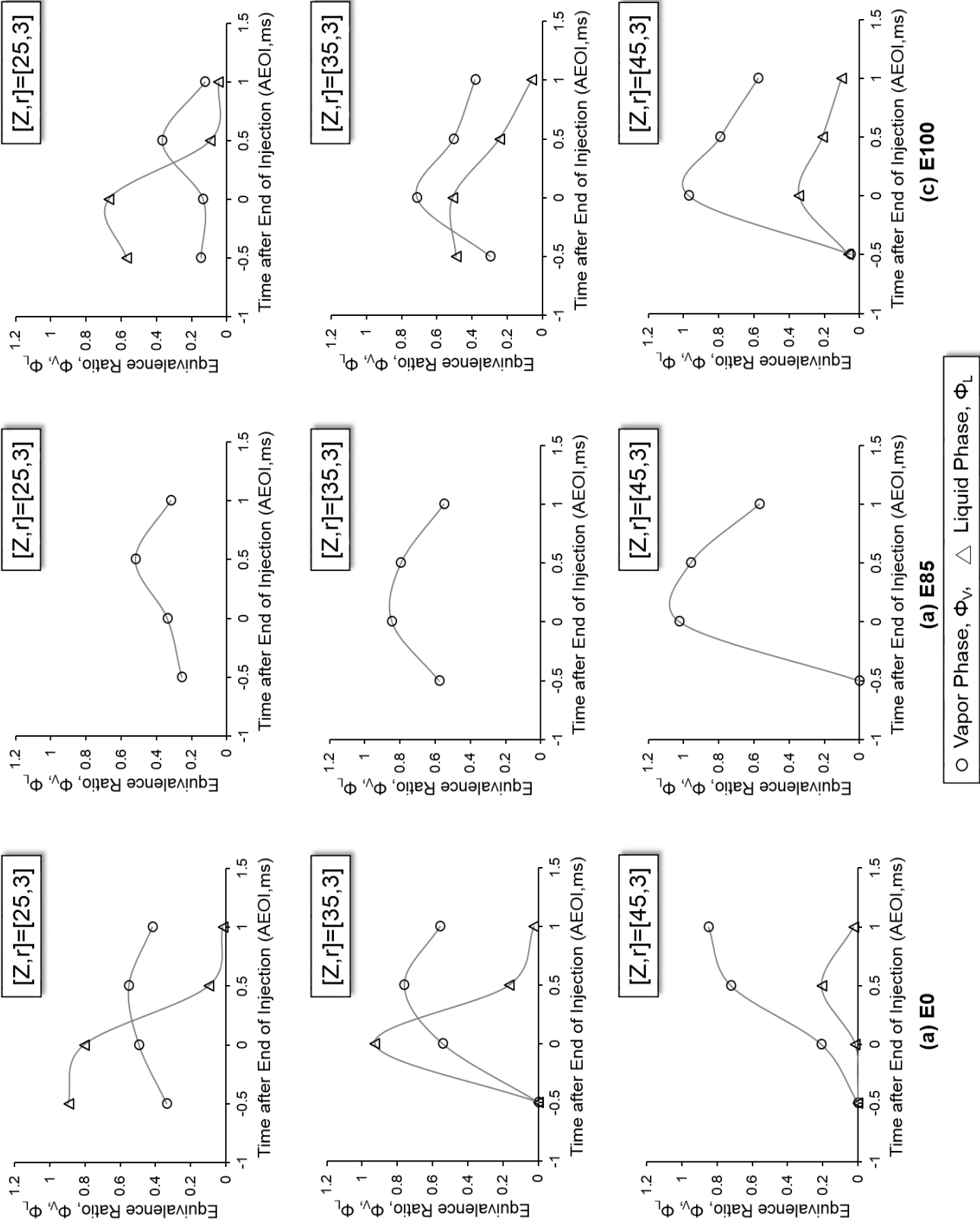
Figure 5.4 Equivalence Ratio of the Liquid and Vapor Phases for Typical Local Positions under Different Ignition Timings.

Figure 5.3 shows the results of ignition probability varied with ignition timing at three representative spray regions (upstream, middle and downstream). Meanwhile, the liquid and vapor phase distributions at these locations shifted with time escape also are presented follow in Fig.5.4 to explain the ignition process.

According to these figures, the ignition stability was much dependent on the local air-fuel mixing at the spark gap based on the evidences (1) more closed to the spray axis, less stability of spark is observed in this study, due to the presence of a dense liquid phase resulting in a carbon fouling on the spark electrodes, and (2) the ignition became difficult as the spark was close to the later ignition timing (t_{ign}=0.5ms AEOI) where the surrounding mixture is on the diluting, especially at the upstream ignition. When the fuel is ignited at upstream of spray, the ignition stabilities seems similar to each other since large liquid phase and less vapor exists. It should be noticed that it is more difficult to ignite the ethanol than gasoline even if the similar mixture concentration exists at the local ignition place, which is proven by a lower ignition probability for E100/E85 under early ignition at upstream as shown in the figures.

The middle region ignition shows somewhat differences from fuels. With the time escape, the fuel with ethanol addition evaporates faster and lead to a lean mixture at the later ignition, especially the E100 shows a lower vapor equivalence ratio at [Z,r]=[35,3] in t_{AEOI}=0.5ms. This local mixing dilution tends to result in a reduced ignition stability as the fuel is ignited at the later timing after EOI. The negative effect of leaner mixture on the spark robustness can be found in the middle region and downstream ignition for E100 and E85.

In the case of downstream ignition, a favorable ignition stability is observed since most vapor propagates downstream and the liquid fuel evaporates sufficiently. One should be pointed out that the reason of the higher ignition probability for E0 at later ignition timing, may be attributed to the still presence of fuel vapor as shown in Fig.5.4 (a). While the vapor of E85 and E100 is decreasing at the downstream when the late ignition takes place.

The results of the ignition probability varied with radial distance are shown in Fig.5.5. An extremely lower ignition stability can be found in E0 at near the spray axis, probably as a result of a dense liquid presents. Because the onset of faster flame development usually begins 0.5ms to 1.0ms after spark which will be shown in next chapter. Therefore, the dense liquid phase near 0ms AEOI at spark position (see Fig.5.6 (a)) would have a great impact on the initial flame kernel formation, and result in a failure/partial ignition. On the contrary, the existed larger amount of fuel vapor and lower liquid phase at 0.5ms AEOI (see Fig.5.6 (b)) allows the combustible mixture to be ignited successfully and developed in further, which reveals a higher ignition probability in Fig.5.5.

130
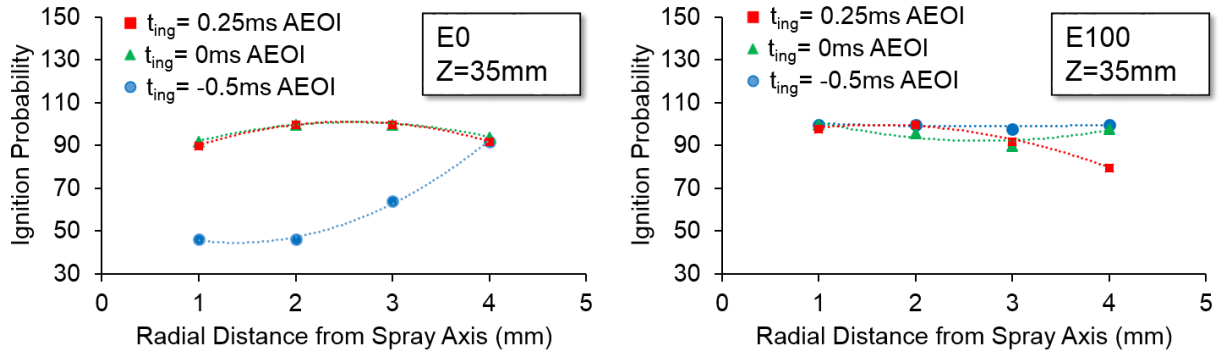
Figure 5.5 Ignition Probability Varied with Radial Distance for E0 and E100

(a) E0

(b) E100
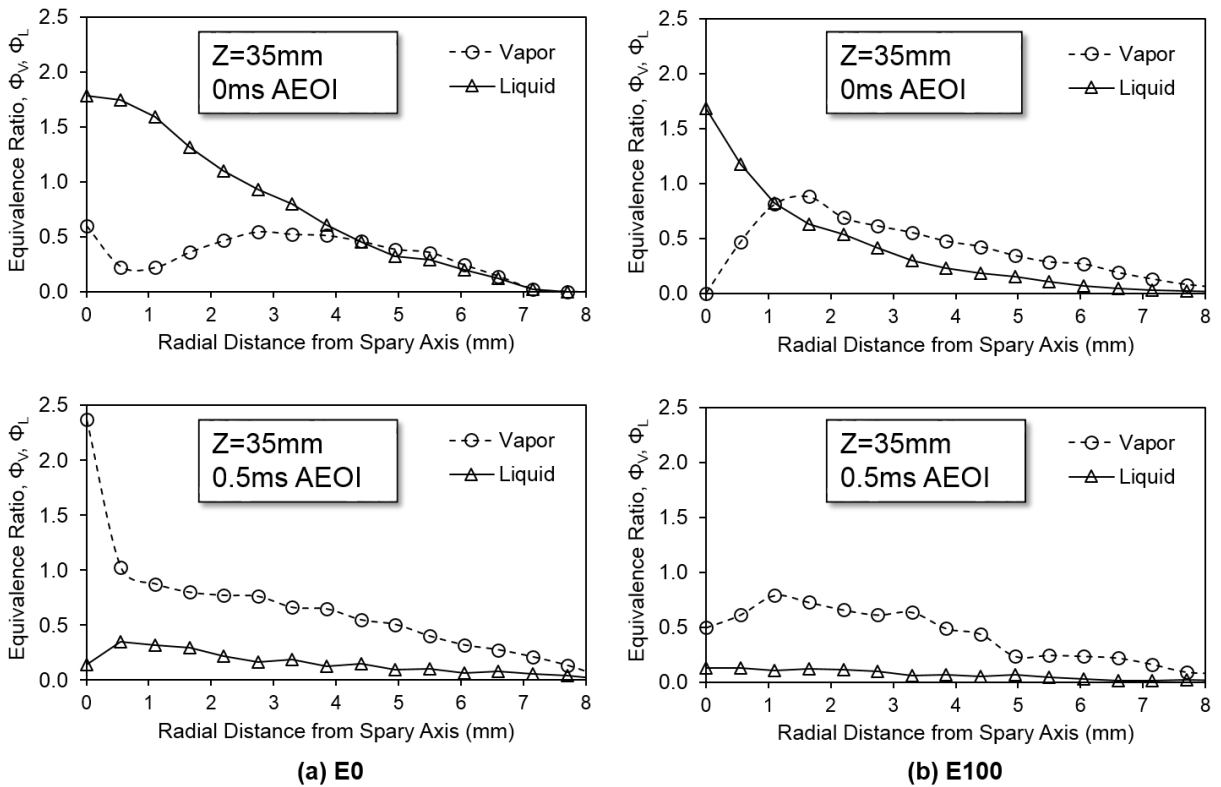
Figure 5.6 Equivalence Ratio of Liquid and Vapor Phases at Z=35mm for E0 and E100

In the case of E100, the presence of more vapor concentration (near stoichiometry) than liquid along the radial distance promotes an improved ignition robustness at early ignition, compared with the E0. Also, when the E100 is ignited in the wider position at later ignition (t_{ign}=0.25ms AEOI), a decreased local equivalence ratio results in a lower ignition probability.
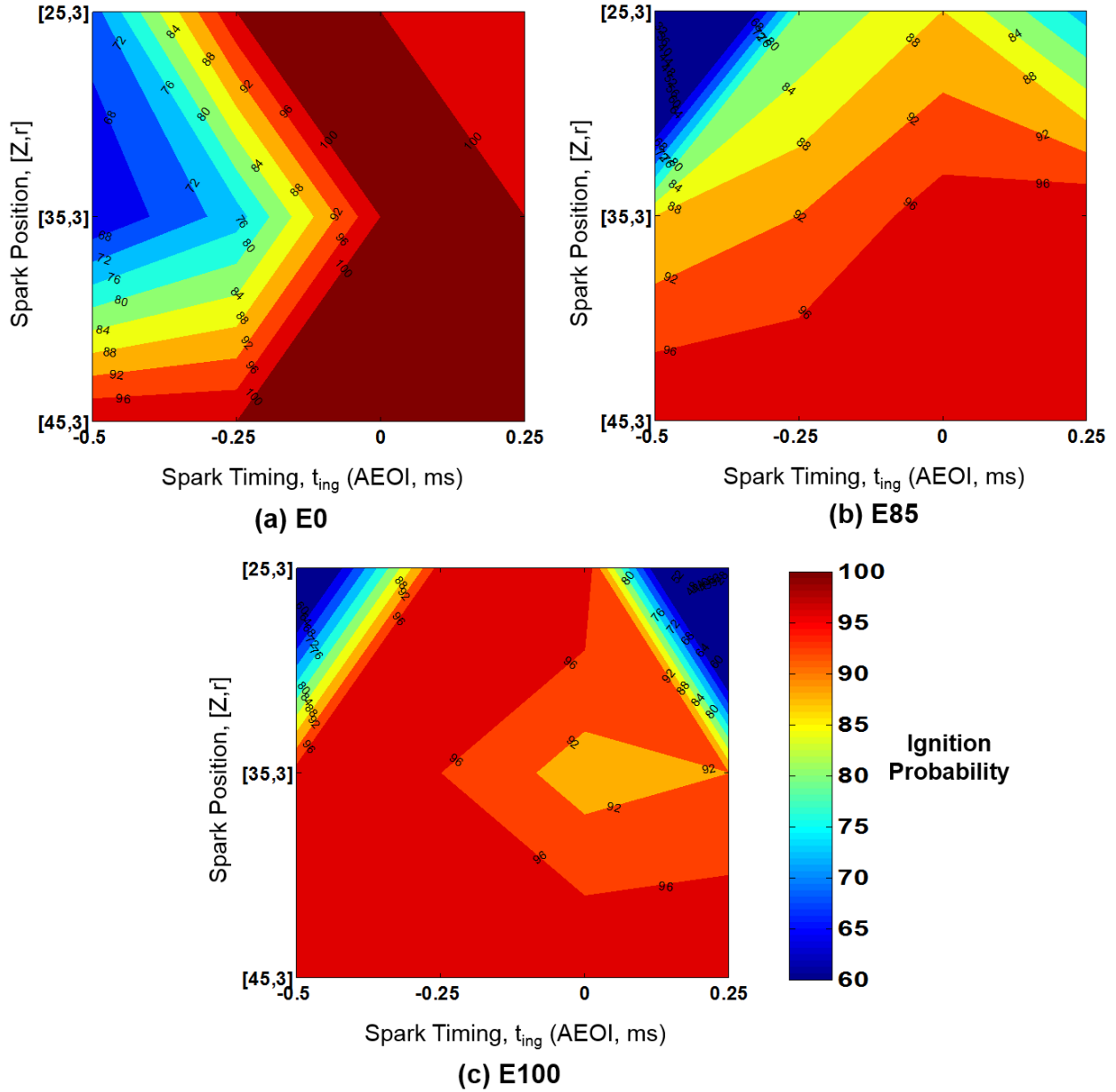
Figure 5.7 Ignition Stable Window for Different Fuels under Same Conditions

In order to provide a deep and clear insight into the effect of fuel on the ignition probability, the color maps of spark stability are produced in Fig.5.7. The level of ignition probability is illustrated in the color bar. For E0, the high probability of successful ignition is found when the fuel is ignited at near or after end of injection (see Fig.5.7 (a)), possible as a result of slow evaporation of gasoline that is discussed in Chapter four. Also, by this reason, more unstable ignition, such as partial ignition and misfire, occurs usually when the ignition takes place at advanced timing. While the added ethanol shows an improvement on the ignition process for expanding the stable ignition window which presents a range from -0.5ms to 0.25ms AEOI for

middle and downstream ignition. Furthermore, E100 also suggests a desirable ignition robustness that expressed by a large region of orange-red color in Fig.5.7 (c). In addition, because of the faster evaporation of ethanol, the extremely poor ignition at upstream for E0 is moderated with ethanol addition. The result indicates that fact the ignition stability is able to be improved with the increased of ethanol ratio in gasoline. However, one should be mentioned that due to the increase of mixing rate leading to a faster local mixture dilution, the ethanol-gasoline blends would tend to result in a lower ignition stability at upstream late ignition, especially the spark happens in E100 at [Z,r]=[25,3], 0.25ms AEOI.

5.3 Ignition Energy

In spark ignition engines, the initial flame kernel formation does not formed sustainably unless a sufficient energy transports from spark charge to compensate the heat losses in flame kernel. Since the ethanol has a lower heating value than gasoline in its physical property, it is necessary to clarify the effect of ignition energy on the flame formation and development for ethanol-gasoline blends.

5.3.1 Measurement of Ignition Energy
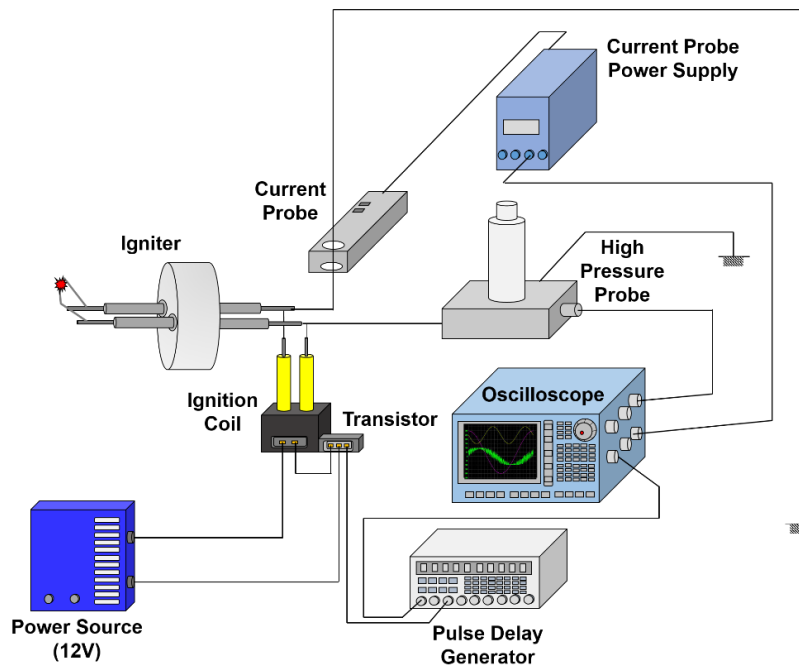
Figure 5.8 Schematic of Ignition Energy Measurement

133

Figure 5.8 shows a schematic of ignition energy measurement. A 12V power source was used to provide the circuit power. The ignition controlling signal from pulse delay generator was guided to the ignition coil by the transistor. The current probe (YOKOGAWA Co., 701934 Power Supply) was used to detect the ignition current and converted to electrical signal sending to the oscilloscope. A high pressure probe (IWATUS Co., SK-301 HP-P60 HV Probe Stand) was employed to trap the transient variation of the ignition voltage. The oscilloscope (YOKOGAWA Co., DL750P Scope Corder) was set to record the curve of both current and voltage. The typical spark current and voltage averaged by 128 times, as well as the definition of spark duration is shown in Fig.5.9.
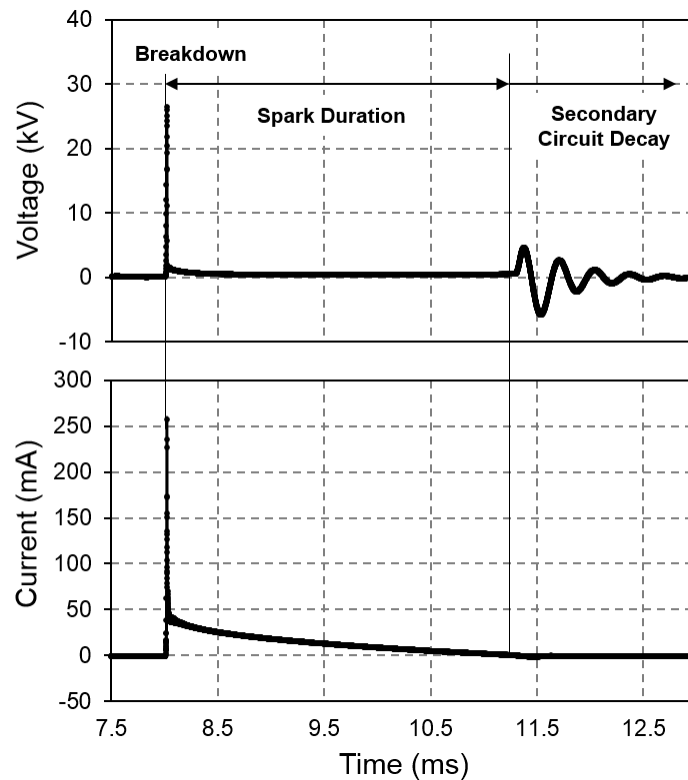
Figure 5.9 Voltage and Current Histories of Averaged Spark Discharge (Measured at atmospheric pressure, t_d=6ms, spark duration: 3.24ms, energy: 35.96mJ)

5.3.2 Effect of Ignition Energy on Ignition Process and Flame Development

Figure 5.10 shows the typical single-run results of OH* chemiluminescence when fuels are ignited by different spark dwell time (t_d=2ms for 25.42mJ and 6ms for 35.96mJ), in order to clarify the effect of spark energy on the flame development. Because of the amplified background noise resulted from the image intensifier, an appropriate threshold of 12 (5% of the maximum intensity of 255) was carefully chosen to acquire more reliable image. The false-color maps of the spatial flame evolution were generated to show

134

the combustion intensity and behavior in convenience. Each case was obtained by 6 times in order to ensure the reliable quantitative analysis.

(a) E0

(b) E85

(c) E100
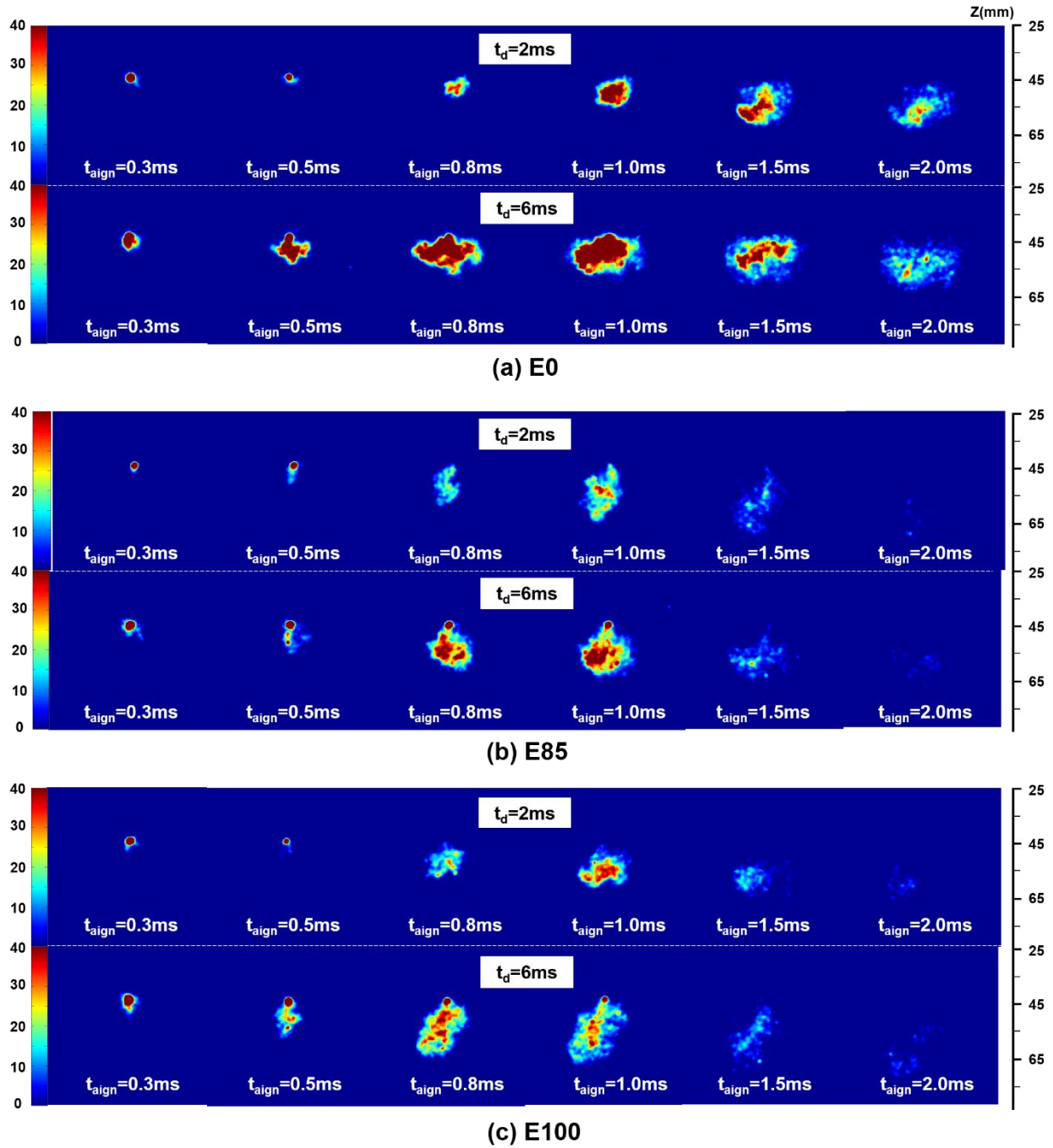
Figure 5.10 Effect of Spark Charge Time on Flame Propagation by OH* Chemiluminescence
(P_a=1.0MPa, T_a=500K, P_{inj}=20MPa, [Z,r]=[45,3], t_{ign}=0ms)

From t_{aign} (time after start of ignition) =0.3ms to t_{aign}=1.0ms, a distinct difference of flame development can be found for all fuels under different ignition dwell time. When the fuel is ignited by a short dwell time (low spark energy), more time is required for the initial flame development compared to the longer dwell time (high spark energy). A spark offered by the lower energy only shows a typical tiny flame area at t_{aign}=0.5ms. However, the mixture ignited by a high energy is burned faster and exhibits a greatly dispersion of flame propagation, which is illustrated by a comparably large projected area of flame at t_{aign}=0.5ms. An explanation for this is that expect the heat compensation of early flame development, whether a more remained energy in initial flame kernel plays a key role on its growth in further. More energy from spark charge would promote the chemical thermal pyrolysis, hence make it easier to burn the ambient combustible mixture. On the other hand, although the smaller flame area produced by the low spark energy, it shows almost the same combustion duration for t_d=2ms and 6ms. This result implied the fact that the spark energy has no distinguishable effect on the combustion period, but great impact on the combustion intensity and flame propagation. Furthermore, a reduced combustion duration with increasing ethanol addition is observed in the figure.

The quantitative result extracted from Fig.5.10 is analyzed to provide detail information on the flame propagation with different spark dwell time as shown in Fig.5.11. The overall trend shows that increased combustion intensity (also represents rate of heat release), for example, at least 35% improved from t_d=2ms to 6ms for all fuels, occurs with the increase of spark dwell time (increased spark energy) as shown in Fig.5.11 (a). Due to more time needed to sustain the initial flame formation, the flame propagation under low energy ignition has an obvious delay, approximately 0.2ms in contrast to that under the higher energy spark.

The equivalent flame radius, R, (defined as the radius of a cycle with the same area for the flame [251]), was used to characterize the flame progress as shown in Fig.5.11 (b). Also, the stagnation of flame early development can be found clearly when the fuel is ignited at the spark dwell time of 2ms. The slope of radius curve, defined as dR/dt, represents the flame velocity. The flame velocity at early kernel formation increases with higher spark energy due to the faster growth of flame kernel supported by more energy from spark charge as discussed previously. In contrast to the early stage formation of flame, there is no significant difference in flame growth at the steady flame development (defined as a constant in the slope of radius curve) for t_d=2ms to 6ms. In addition, the initial growth of E0 flame under t_d=4ms is almost the same with that under t_d=6ms in contrast to the distinct difference from t_d=2ms to t_d=6ms in E100. This result implied that the E100 has the higher sensibility to the spark energy than E0 due to the increase of ethanol in gasoline leading itself more difficulty to be ignited.
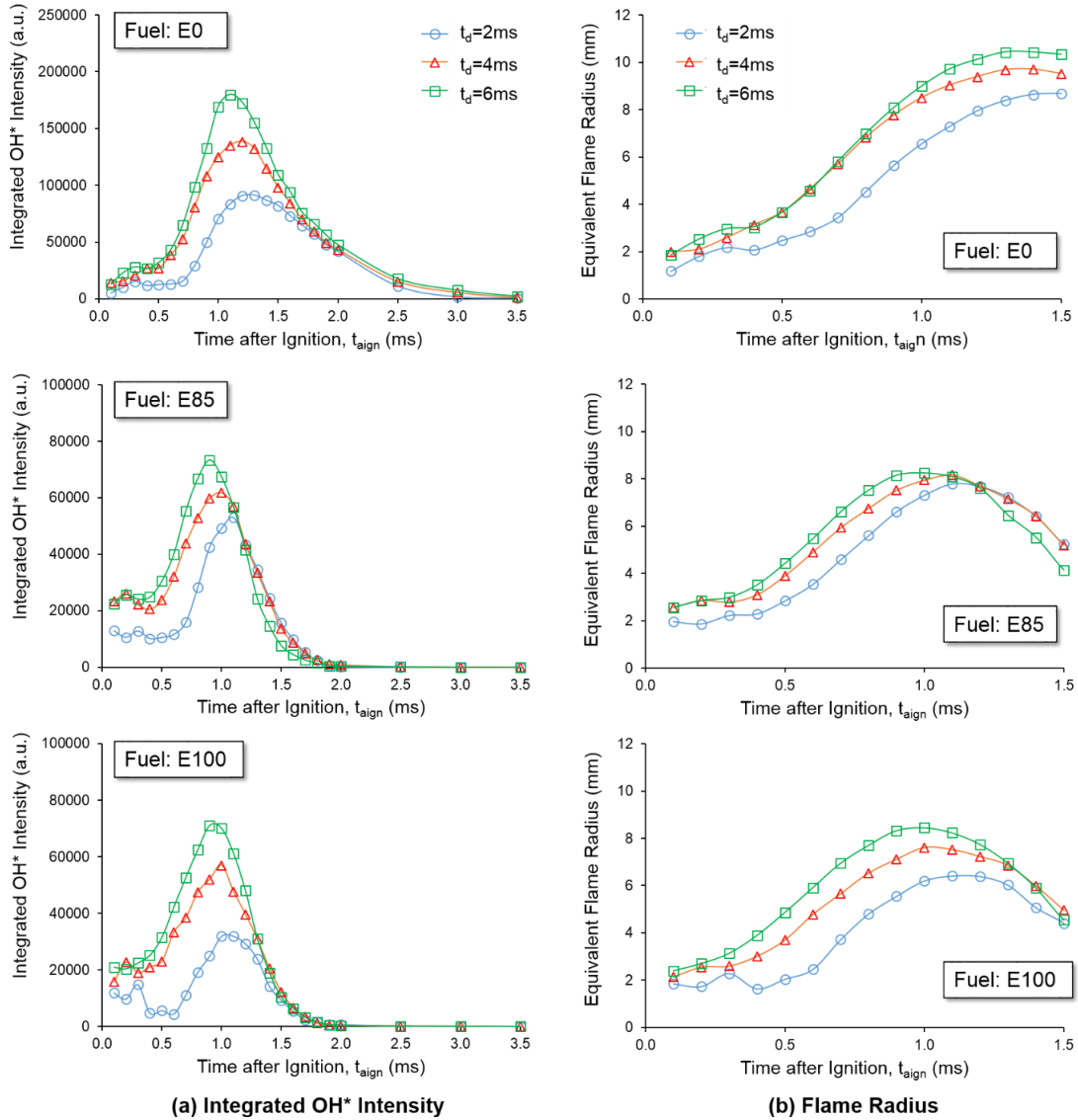
Figure 5.11 Integrated OH* Intensity and Equivalent Flame Radius (P_a=1.0MPa, T_a=500K, P_{inj}=20MPa, [Z,r]=[45,3], t_{ign}=0ms)

Generally, the lower spark energy has a negative effect on the flame development, suggesting not only a decreased growth rate on the earl flame, but also a lower combustion intensity during the flame fully development. While there is nearly no effect of spark energy on the combustion duration and the flame velocity at steady evolution of flame. With increasing ratio of ethanol in gasoline, more sensitive to the spark energy of fuels can be found due to the lower heating value of ethanol content.

5.4 Summary

The ignition process of ethanol-gasoline blends used under a high temperature and high pressure ambient condition was clarified in this chapter. The real gasoline and ethanol were employed by shadowgraph and OH* chemiluminescence. Various conditions, consisting of ignition location, ignition timing and spark energy, were considered to be investigate those effects on ignition process for ethanol-gasoline blends. Three typical locations of spray, defined as upstream, middle and downstream of spray, were chosen as the ignition locations. Different injection durations for E0, E85 and E100 were set respectively in order to maintain the same calorific value. The conclusions can be summarized as follows.

1. Based on the shadowgraph, three types of ignition process consisting of successful ignition, partial ignition and failure ignition were defined. And the ignition probability can be clarified in this way that whether a visible flame could be observed or not and obtained by the enough sample testing at every ignition position and timing.

2. The ignition probability has much dependent on the local mixture formation. In general, the presence of dense liquid phase or leaner mixture (mixture dilution) result in a lower ignition probability for fuels, especially in the central region of spray along the spray axis or peripheral region along the radial distance of spray.

3. In according to the ignition probability map, the result indicates that with increasing the ratio of ethanol in gasoline, the stable combustion window is improved, in particular the advanced ignition due to the faster evaporation and mixing of ethanol. However, the local mixture dilution of ethanol addition also enables to reduce the ignition robustness at upstream or late ignition for E85 and E100.

4. The effect of spark energy on the ignition process and flame propagation were investigated by OH* chemiluminescence. Lower spark energy will block the initial flame growth, then reduce the flame velocity at the early stage. This effect cause about 0.2ms delay for the flame development. In addition, because the longer ignition delay, the combustion intensity by lower spark energy also becomes weaker than that by higher energy.

5. Ethanol addition increases the sensibility of flame development on the spark energy due to its lower heating value leading itself difficulty to be burnt. However, the flame velocity at the steady development and the combustion duration seems does not affected by the spark energy.

CHAPTER 6 FLAME DEVELOPMENT AND COMBUSTION PERFORMANCE OF ETHANOL-GASOLINE BLENDS

6.1 Experimental Condition

Flame development and combustion characteristics are essential to the application of ethanol-gasoline blends in DISI engines, due to their unique physical properties different from those of gasoline. Several properties, such as lower heating value and air-fuel ratio (AFR) enable to have consequence to the distinguishable combustion behavior due to different local mixture around spark plug and the flame propagation characteristics. Therefore, the optical visualization and the corresponded analysis of flame development and combustion performance are considered as an effective way to deeper understand the combustion of ethanol-gasoline blends under DISI-like conditions.

In this chapter, various optical diagnostic methods, including shadowgraph, Mie scattering, OH* chemiluminescence, flame natural luminosity were employed and combined together to clarify the combustion and flame propagation of E0, E85 and E100. The experimental conditions are shown in Table 6.1. Ambient conditions were set to similar to the LAS measurement. The fuels of real gasoline and ethanol were used and their injection pulses were set to the same calorific value.

A robust ignition process is necessary for combustion evaluation. Therefore the ignition locations of ethanol-gasoline fuel with different blending ratios should be carefully chosen. Previous chapter demonstrated that ignition probability decreased when the fuel was ignited either closed to the spray axis (dense liquid area) or to the periphery of the spray (lean mixture). In order to eliminate such influences on the spark, the appropriate ignition locations defined by the same way as last chapter, namely [Z,r]=[25,3], [35,3] and [45,3] (which represent ignition position upstream, middle region and downstream of the spray respectively), were selected for all fuels due to those positons have a higher ignition probability as already presented in Chapter 5. Thus it is possible to investigate the effects of the ignition position and timing on the combustion characteristics. The ignition timing were set -0.5, -0.25, 0, 0.25 and 0.5ms after end of injection. Spark dwell time was maintained in 6ms to provide a sufficient spark energy for the formation of initial flame kernel.

Table 6.1 Experimental Conditions

Ambient Condition			
Ambient Gas	Air		
Ambient Temperature, T_a (K)	500		
Ambient Pressure, P_a (MPa)	1.0		
Injection Condition			
Injector	VCO Single Nozzle		
Hole Diameter, D (mm)	0.15		
Injection Pressure, P_{inj} (MPa)	20		
Injection Duration, t_{inj} (ms)	E0	E85	E100
	1.1	1.42	1.43
Test Fuel			
E0	Gasoline 100 (100% Gasoline)		
E85	Ethanol 85 (85% ethanol) + Gasoline 15 (15% gasoline)		
E100	Ethanol 100 (100% ethanol)		
Ignition Condition			
Ignition Position, [Z,r]	[25,3], [35,3], [45,3]		
Ignition Dwell Time, t_d (ms)	6		
Ignition Energy (mJ)	36		
Spark Duration (ms)	3.2		
Ignition Timing, (AEOI, ms)	-0.5, -0.25, 0, 0.25, 0.5		

6.2 Visualization of Combustion and Flame Development for Ethanol-Gasoline Blends

6.2.1 Overall Flame Development

In this section, the flame as already mentioned in Chapter 2, the liquid and vapor phases of fuel spray can be detected by using shadowgraph, even if the separation of those two phases is impossible due to the same appearance color of liquid droplets and the liquid-vapor interface in image. However, based on this optical method, the flame development with existed fuel vapor is able to be observed. The fuel vapor at

upstream of spray is important to clarify the flame propagation. Since the refractive index gradient induced by the temperature distinction exists in the ambient gas and boundary layer of the window, it is hard to observe the fuel vapor boundary in the raw shadowgraph images as shown in the left column (I_n) of Fig.6.1at each image timing.
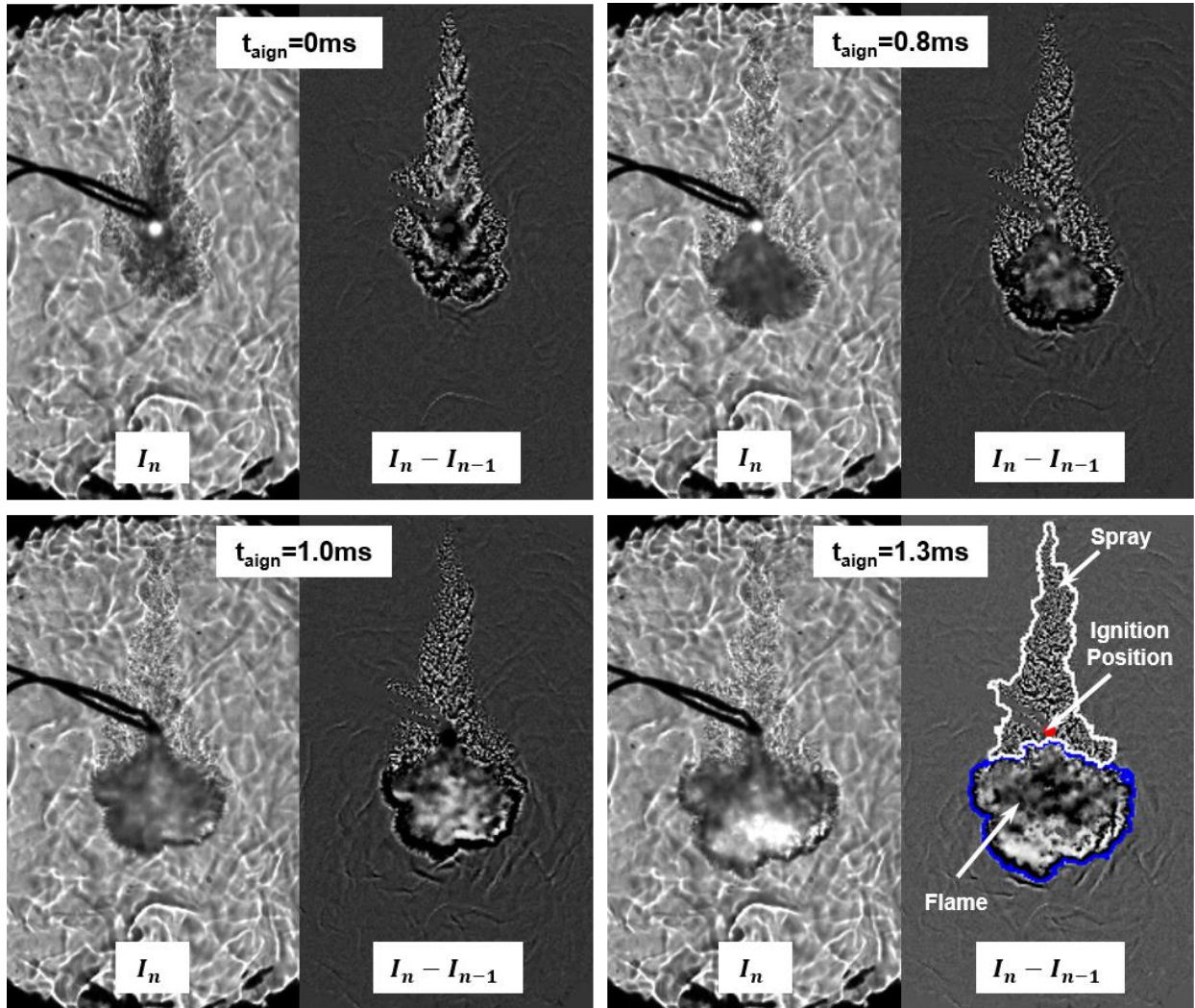
Figure 6.1 Schematic of Flame Development by Shadowgraph (At each timing, the left column is the original shadowgraph image, the right column is the produced by the post process. Fuel: E85, P_a=1.0MPa, T_a=500K, P_{inj}=20MPa, [Z,r]=[35,3], t_{ign}=0ms, t_d=6ms)

An effective way to resolve this issue is using the background from the preceding image to moderate the influence from ambient noise [227]. The right column of Fig. 6.1 exhibits the correction results utilizing the intensity of the current image (I_n) to subtract that of the preceding image (I_{n-1}). The appropriate brightness and contrast are necessary to compensate and highlight the spray and combustion features more clearly. The corrected shadowgraph images show the vapor boundary of E85 spray unambiguously and

almost no place-to-place variation at the successive frame. For the combustion, the black area around the flame edge shows the burning region because of the most distinct refractive index gradient forming at the combustion interface.

For the flame propagation, firstly the spark discharge ironizes the surrounding ignitable mixture, thus an initial flame kernel forms. The downstream evaporating fuel generates a favorable locally air-fuel mixture that sustains a subsequent flame propagation. With the fuel being ignited continuously, the flame quickly expands to the mixture edge and produces a shock-wave like appearance in ambient, especially at the downstream flame tip.

It should be mentioned that unlike gasoline, a 'black' and transparent appearance of E85 flame at the early stage of combustion as shown in Fig.6.1 at t_{aign}=0.8~1.0ms, corresponds to a region with smooth texture in the corrected image ($I_n - I_{n-1}$). This reveals the fact of E85 flame with a pronounced non-luminous flame at the early combustion period. While after that, somewhat high luminous flame can be found with the flame at the fully developing as shown in t_{aign}=1.3ms. Meanwhile, the burnt products mixing with upstream unburnt vapor presents at the region closed to the ignition position and upper of the luminous flame. The flame visualization characteristics of ethanol-gasoline blends will be discussed at the latter section.

Another of interest as shown in Fig.6.2, is that the combustion region demonstrates that the flame propagates towards the downstream of the spray rather than to the upstream, which is similar to the free reacting spray in diesel [227]. There are two important reasons of this tendency. First, the upstream mixture becomes diluted during the flame rapid propagation due to the bulk air entrainment introduced into this region after the EOI [150, 252]. The upstream mixture becomes leaner can be demonstrated in Fig.6.2, where shows a steep decrease of vapor equivalence ratio (from Z=35 to 20mm, Φ_V reduces quickly from 0.6 to 0.2) at the upper of ignition location. Over-lean air-fuel mixing is not sufficient for the burning. In the contrast, the presence of dense air-fuel vapor locates at below the spark position, and transports towards downstream from 0ms AEOI to 1.0ms AEOI. Second, the high flow velocity above the ignition position, estimated as 20 to 30 m/s at the SOIg timing by the numerical calculation [253], is faster than the maximum flame growth speed of about 14 m/s which will be discussed in the latter. Locally speedy flow is more accessible to increase the heat dissipation, and then quench the flame front progress at the interface between the burned and unburned mixture.
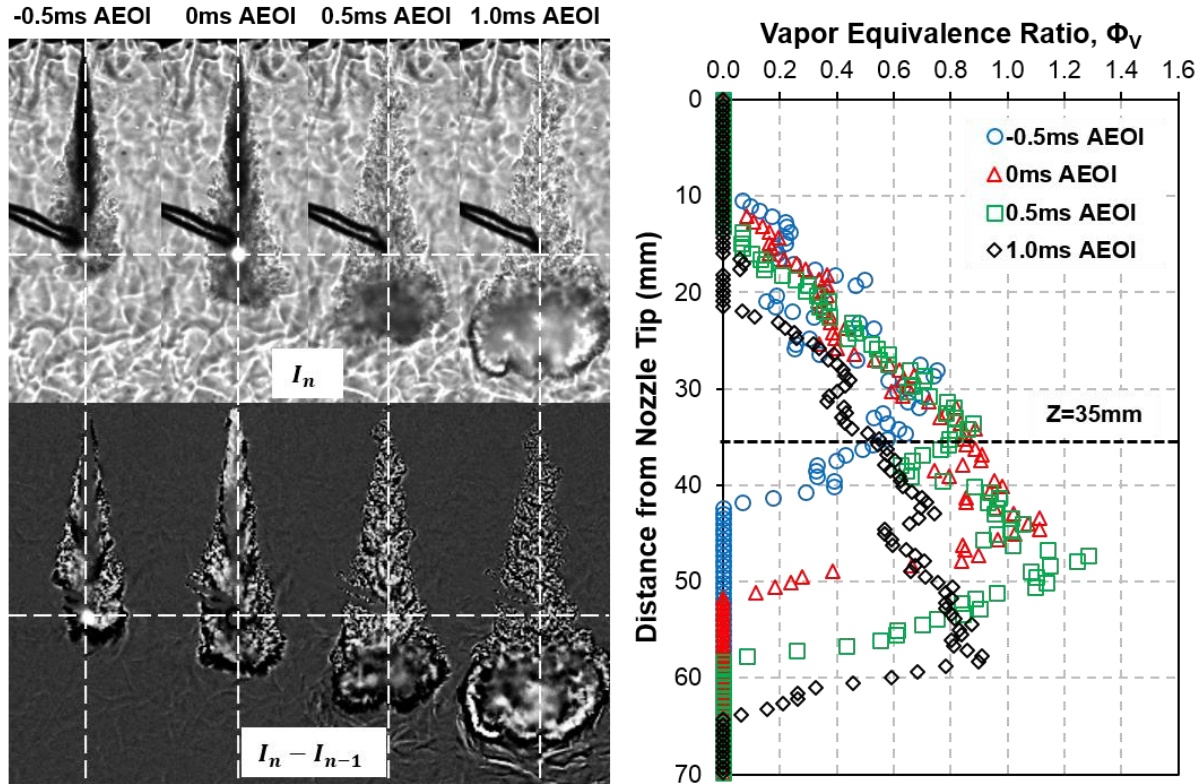
Figure 6.2 Comparison of Vapor Equivalence Ratio along Spray Axis at [Z,r]=[35,3], (Fuel: E85, P_a=1.0MPa, T_a=500K, P_{inj}=20MPa, t_{ign}=-0.5ms, t_d=6ms)

6.2.2 Visualization of Flame for Ethanol-Gasoline Blends Combustion

Since the blending of ethanol and gasoline together alters the physical and chemical characteristics of the original fuels, somewhat resulting changes may occur. One of the noticeable differences in the blended fuel versus gasoline is the visual difference of smoke and flame characteristics, as shown in Fig.6.3. The original shadowgraph and its corrected image also were used to compare the natural luminosity for the explanation of flame visualization. A typical signal-run case of combustion ([Z,r]=[45,3], t_{ign}=0ms) was chosen in Fig.6.3.
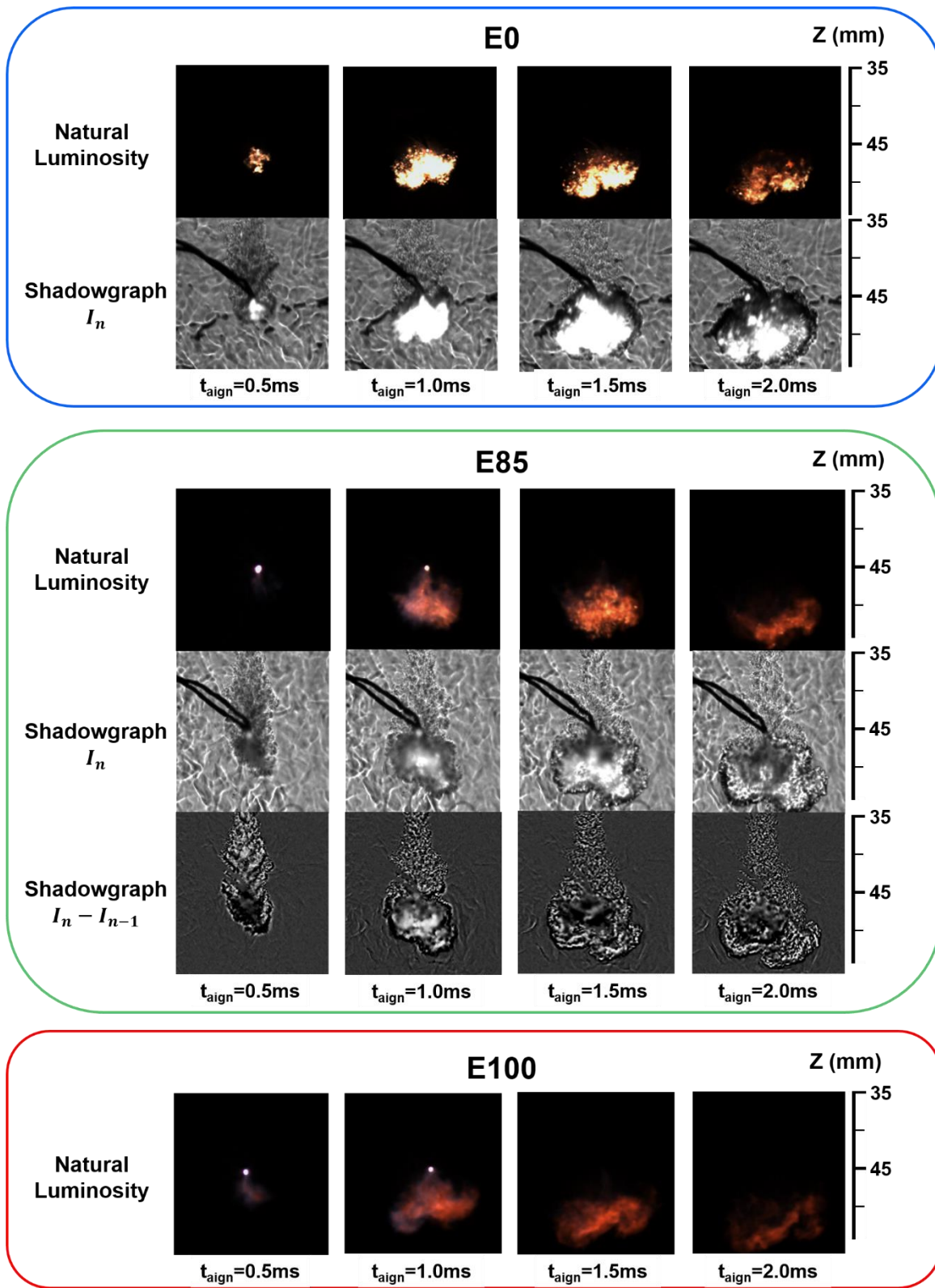
Figure 6.3 Visualization of Flame for Ethanol-Gasoline Blends (P_a=1.0MPa, T_a=500K, P_{inj}=20MPa, [Z,r]=[45,3], t_{ign}=0ms, t_d=6ms)

The flame formation and evolution of all fuels are similar for each other. The natural luminosity (NL) of E0, however, reveals the remarkable luminous flame even with a saturation at the burning region which also is exhibited in the shadowgraph image. Obviously, this result is greatly attributed to the soot incandescence because of the higher carbon atom contained in hydrocarbon fuel.

In contrast to E0, the E85 and E100 suggests a lower luminous intensity in NL image that indicates the increase of ethanol ratio in gasoline will reduce the soot production (less smoke generation) and decrease the visible flame color. In detail, the flame color of ethanol-gasoline seems a more 'opaque' appearance during the combustion, especially the E100 which presents a smoke-like flame almost without any soot incandescence. For the E85, the obvious non-luminous flame, dominated by the blue color, occurs at the early stage of combustion (i.e., t_{aign}=0.5ms). Thereafter, a less luminous flame appears with the flame fully developing. Therefore, there are two significant results are found in NL image. First, the E0 produces more soot than the E85 and E100. Secondly, E0 produces soot more early than E85 and E100. It implies that for the pre-soot matter in E0 combustion, such as the soot precursor, would occur when the fuel is ignited. No reports have been found in the literature that describe the mechanism of the soot formation for the ethanol-gasoline blends used in the engine test or volume vessel experiment. One possible explanation for the result related to the soot occurrence, could be attributed to the oxygen content in ethanol contributing the different level of the particulate matter formation at the early combustion.

On the other hand, the visualization of flame evolution by shadowgraph also reveals one noticeable difference about the appearance of non-luminous flame. From the image of E85 in Fig.6.3, a gray-smooth texture in original shadowgraph and its corrected image is observed when the fuel is ignited after 0.5ms, which is corresponded to the blue flame in NL image. The low flame temperature of blue flame causes the difference of temperature distribution, hence leads to a gradient of ambient density presenting a dark region. Because of the back light, this blue flame is too weak to be differential from the gray-smooth region. One should be mentioned that at the upper tip of flame, a gray-smooth texture also exists. However, this region cannot be recognized as non-luminous flame due to the entrainment of combustion products which also has a lower temperature to result in a fluctuation of ambient gas density.

6.2.3 Non-Luminous and Luminous Flame

The natural luminosity of the flame is well known to consist of two primary sources: soot incandescence and chemiluminescence. Different regimes leads to these two kinds of emission. The soot incandescence produced from the hot soot particles with a broad band thermal radiation. While the chemiluminescence is non-thermal radiation of relatively narrow spectral ranges emitted from the intermediate species during

combustion. The captured combustion images of E85 in Fig.6.3 shows a non-luminous and luminous flame in the combustion region. The non-luminous flame shows a relatively lower luminosity dominated by blue color. While the luminous flame presents the bright yellow-orange color that could be distinguished from the former one. These different visual characteristics can be used to interpret the combustion behavior. The non-luminous flames are observed under the non-sooting condition, for example, premixed combustion. This emission is known as the chemiluminescence signals from various intermediate species, in particular predominantly given off by the relaxation of CO_2^* to its ground state, following excitation in the reaction $CO+O \rightarrow CO_2^*$. While the luminous flames signal in IC engine is regarded to be governed by soot incandescence and as the evidence of diffusion flame model. Therefore, luminous and non-luminous flame shown in Fig.6.3 represents the sooting and non-sooting flame respectively. Also, the captured color images suggests a profile of red-green-blue (RGB) for the flame characteristics.

Figure 6.4 shows the flame characteristics of RGB channel for different ethanol-gasoline blends. For E0, the profile of RBG shows similar to each other due to its existed high luminous flame, which is also represented by a high intensity at R channel. In the case of E85, a distinct difference in color channel occurs especially at the early stage of combustion where the presence of the obvious blue flame appears. This character also is revealed by a higher value at B channel compared with R channel at t_{aign}=1.0ms in Fig.6.4 (b). The feature tends to weak similar to E0 with the flame development since the soot incandescence becomes dominant and emits the high luminosity as expressed by the region with a black dot line in the subsequent timing of t_{aign}=1.6 to 2.2ms. While the E100 has a non-sooting flame indicated by the RGB profile in Fig.6.4 (c), where shows a relative stable R channel without large number pixels locating at near the intensity of 255. Meanwhile, the increased blue channel in E100 demonstrates more non-luminous flame. It is worth noticing that some bright 'spot' existing in the E100 flame highlights the presence of droplet burning.
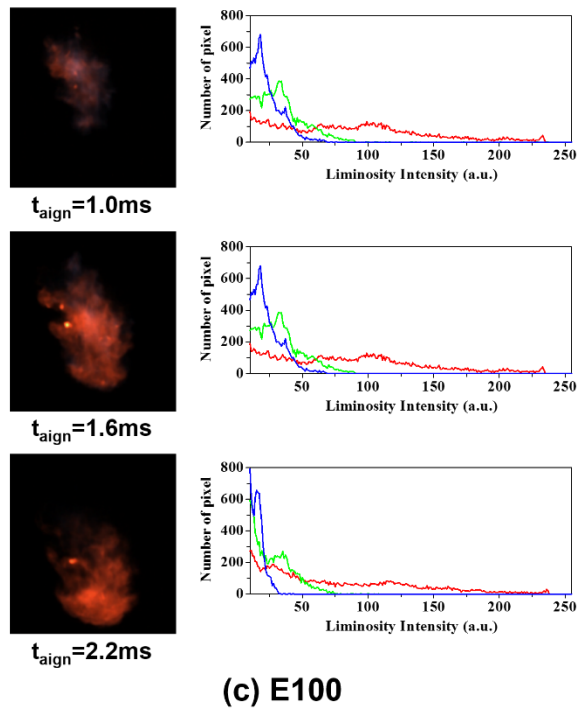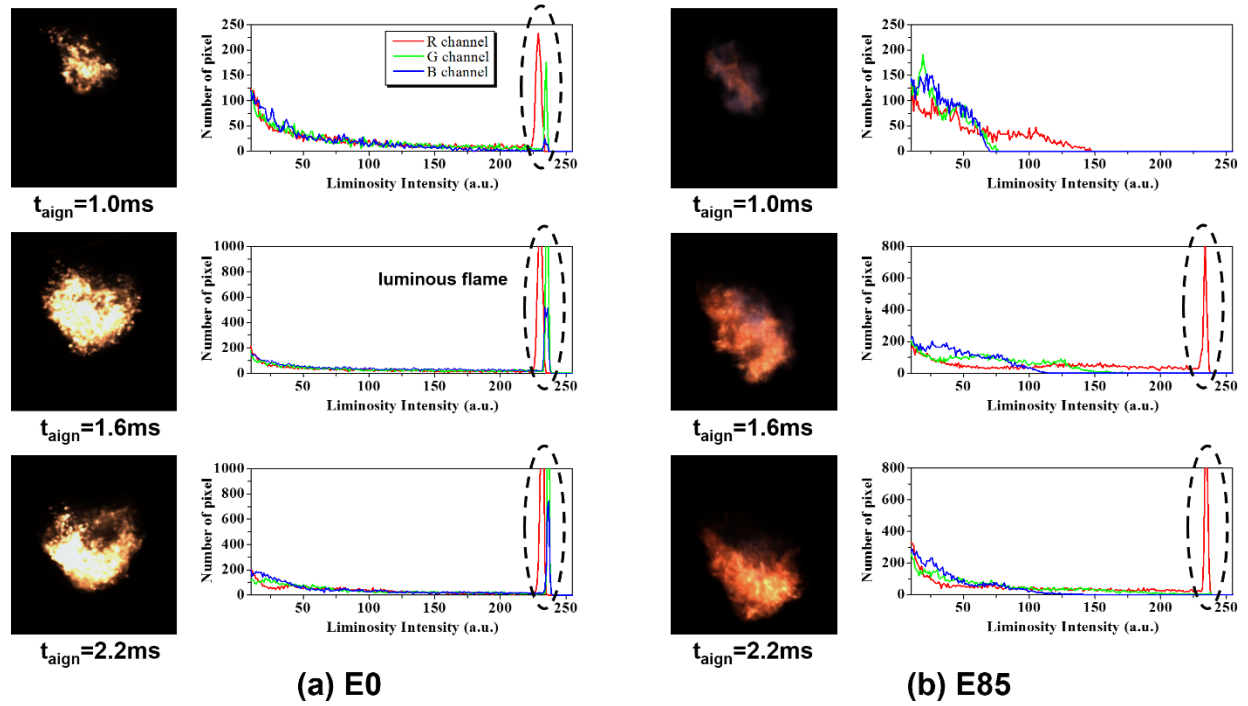
Figure 6.4 Flame Characteristics of RGB Channel for Fuels (P_a=1.0MPa, T_a=500K, P_{inj}=20MPa, [Z,r]=[35,3], t_{ign}=-0.5ms, t_d=6ms)

The luminous flame is mainly described by the R channel accompanying with the lower intensity level in B and G channel [254]. Thereby the different type of flames, luminous and non-luminous flame, could be distinguished from each other in a color RGB image if using a suitable threshold of the R channel as an effective way to characterize the flame visualization and the quantitative analysis.
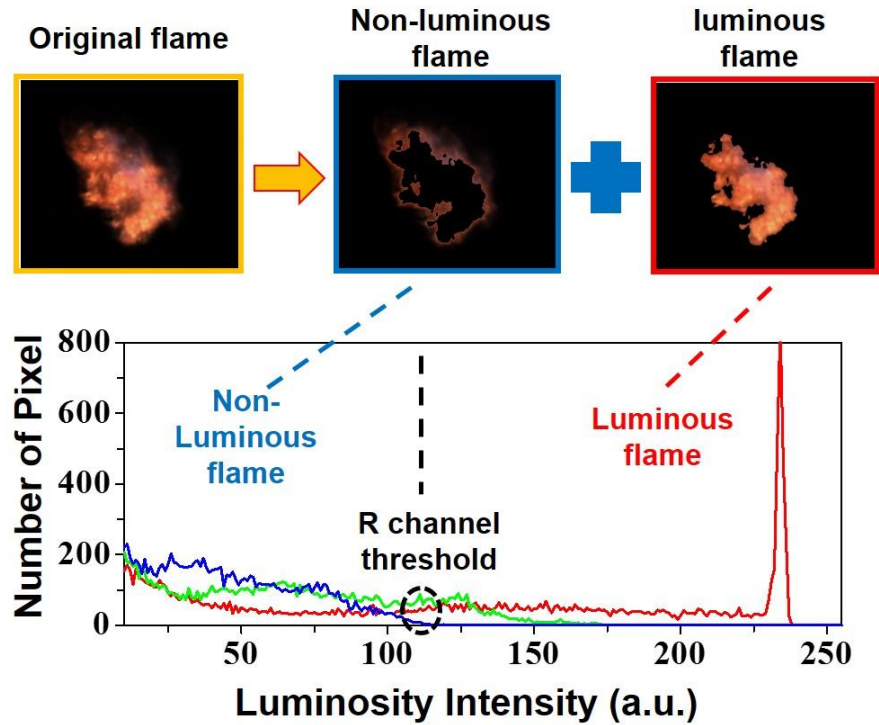
Figure 6.5 Separation of the luminous flame and non-luminous flame

In this study, the threshold for every image is chosen as this way when the R channel becomes dominant and the B channel firstly comes to zero as shown in Fig.6.5, in order to separate the luminous flame completely. Therefore, the non-luminous and luminous flame can be separated by the thresholding as shown in Fig.6.5. Based on this method, a comparison of flame development in according to the visualization is shown in Fig.6.6, where a typical single-run case (ignition at [Z,r]=[35,3], t_{ign}=-0.5ms) is used as the illustration.

As the figure shown, the non-luminous flame grows fast and becomes a dominance in the flame evolution at the early combustion, even until to the time when the flame comes to the fully developed state. More non-luminous flame of E85, i.e., almost three times over E0 at t_{aign}=0.6ms, produces at the early combustion. At the fully developed burning, the E0 shows a dominant development of the luminous flame, compared with the E85. Also, a lower level of non-luminous flame (~50% projected area in the E85 combustion) is demonstrated in the characteristics of the E0 flame. One should be mentioned that for both

E0 and E85, the first appearance of luminous flame occurs closed to the t_{aign}=0.6ms. While for the E0, the luminous flame has a steep increase at t_{aign}=0.9ms and becomes the main flame type after t_{aign}=1.2ms due to the large amount of soot incandescence.
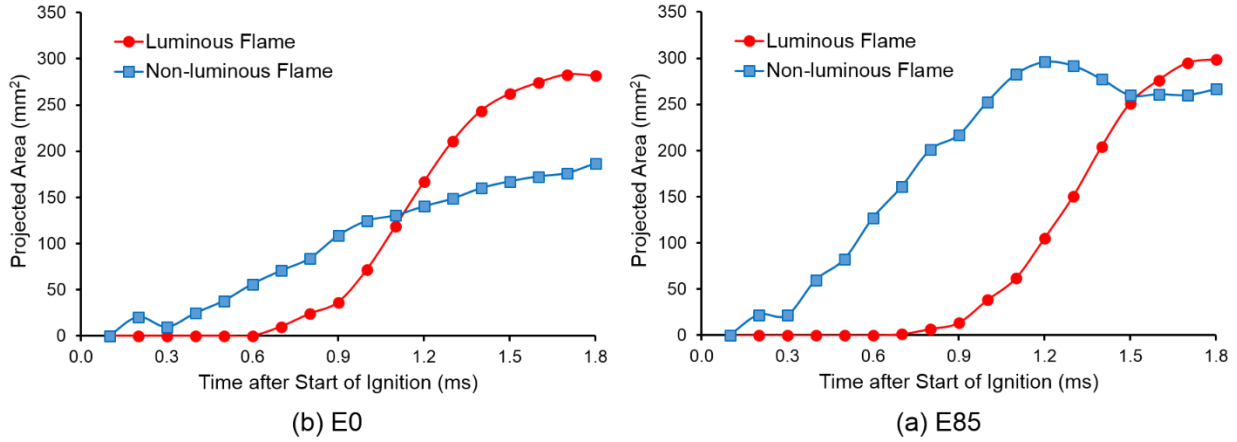
Figure 6.6 Temporal Variation of Luminous Flame and Non-luminous Flame for E0 and E85
(P_a=1.0MPa, T_a=500K, P_{inj}=20MPa, [Z,r]=[35,3], t_{ign}=-0.5ms, t_d=6ms)

6.3 Interference Analysis of Soot Incandescence on OH* Chemiluminescence

As already mentioned, the natural luminosity consists of the non-luminous and luminous flame. The former is mainly governed by the narrow-band chemiluminescence. While the latter is greatly dependent on the soot incandescence with a broad band wavelength. When the sooting flame occurs, especially the E0 combustion, it has the two or three times of strong intensity than the non-luminous flame, hence possibly leading to an interference on the chemiluminescence. In order to quantitatively analyze the OH* chemiluminescence in the latter section, the interference of soot incandescence from the natural luminosity on OH* signal at the simultaneous imaging of NL and OH* emission should be carefully examined in this study. According to the requirement of both high OH* emission and NL intensity, thereby the case of E0 (ignited at [Z,r]=[35,3] and 0ms AEOI) was chosen as the typical example.
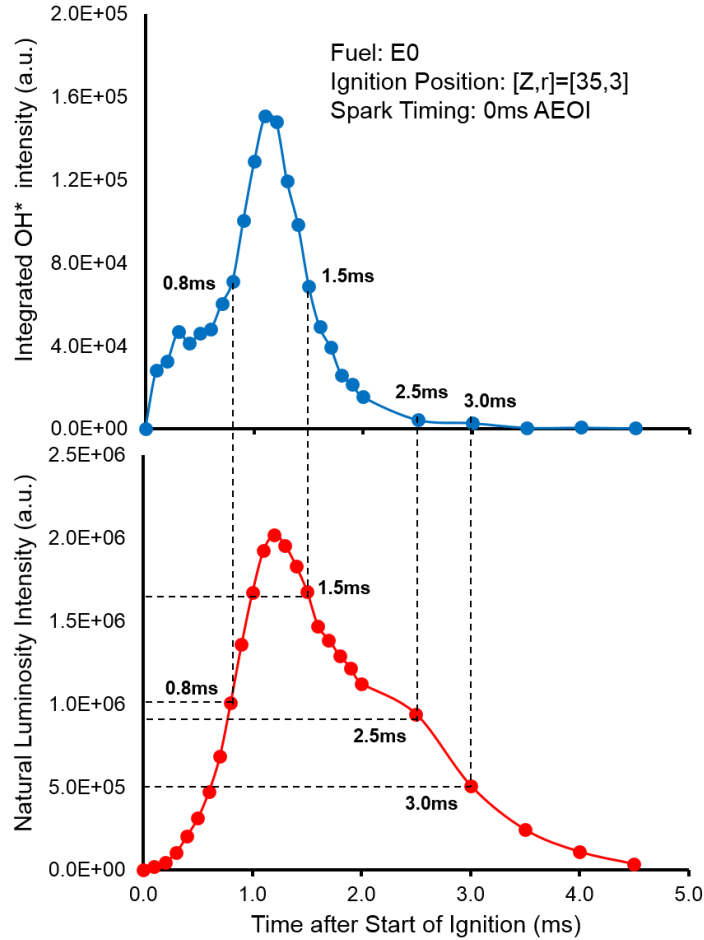
Figure 6.7 Comparison of OH* Intensity and Flame Natural Luminosity

Figure 11 shows the temporal variation of the integrated OH* intensity and the flame natural luminosity. It can be noticed that the OH* intensity at 0.8ms after SOIg shows a similar total amount to that at 1.5ms after SOIg. Meanwhile, the corresponded value of the NL intensity for the latter has a 1.6 times (10^5 level) over than the former one. Also, when the OH* signal approaches nearly disappearance as expressed at 2.5ms and 3.0ms SOIg. A large amount of NL intensity still presents in the combustion phase. According to this result, it can be considered that the influence of NL intensity on the OH* signal is enough weak to be neglected in this study.

6.4 Spatial and Temporal Distribution of Flame Development

6.4.1 Time Resolved Image

To investigate the effect of spray evaporation on the combustion characteristics, the OH* chemuluminescence of E0, E85 and E100 was measured under the same ambient conditions with the LAS

test. Real gasoline and ethanol were employed in the combustion experiment. Spark processes for all fuels were taken at the same ignition timings (t_{ign}= -0.5ms, 0ms and 0.5ms AEOI) and regions in the spray (upstream, middle and downstream of the spray). And the spark charge time was selected as 6ms to provide the enough spark energy. Since the heating value of ethanol is lower in volume basis as compared with gasoline, the injection durations were corrected to be the same calorific value, defined as 1.1ms for E0, 1.42ms for E85 and 1.43ms for E100. Also, the vapor distributions of ethanol-gasoline blends under the corresponded condition of same calorific value were measured by LAS to interpret the combustion behavior. The thresholding method (13 of the maximum intensity of 255) which is mentioned in Chapter 5, is also employed to produce the clear false-color map to show the combustion intensity and flame behavior in convenience. Typical single-run images of the EOI ignition upstream, in the middle and downstream of the spray, and of the middle-region ignition at -0.5ms, 0ms and 0.5ms AEOI, are selected to demonstrate the flame characteristics as shown in Figs. 6.8 and 6.9. The ignition location was marked by the yellow-dot lines.

For all fuels, an unambiguous distinction between the different combustion behaviors is observed in the pronounced long narrow flame shape and relatively lower OH* chemiluminescence in the EOI ignition at [25,3] and the middle region spark at 0.5ms AEOI. In contrast, in the case of good combustion, the profiles of the flame are quite continuous, which indicates the smooth progress of the flame front and the effect of less turbulence due to the quiescent ambient. The higher OH* production at the axial distance of 15-25mm (about 130-170 times the nozzle orifice diameter) below the ignition position suggests that the stoichiometric or slightly rich combustion in those regions. The impeded flame propagation toward upstream is proven again by the OH* distribution.

In order to interpret the flame behavior more effectively, the local variation of vapor equivalence ratio from which the average data in every four shot images are extracted by the LAS technique, is shown in Fig.6.10. In the specific time interval of 0.5ms, the concentrating mixture vapor is marked by from the black to red (0~1.0). While the diluting mixture vapor is illustrated as by the color from black to blue (0~-1.0).

151

Figure 6.8 Spatial Distribution of OH* Chemiluminescence Image for Different Ignition Location

(P_a=1.0MPa, T_a=500K, P_{inj}=20MPa, t_{ign}=0ms AEOI, t_d=6ms)

152

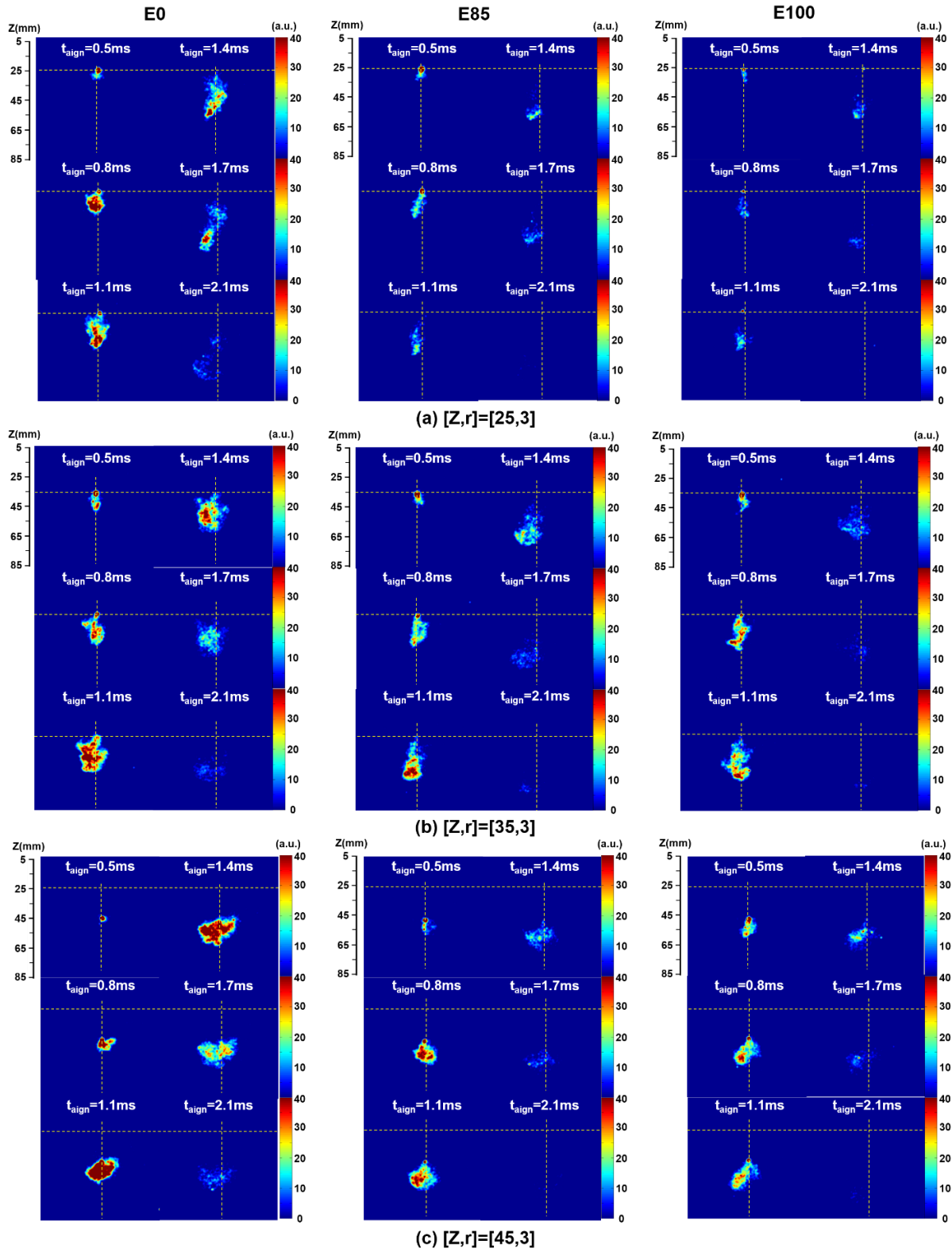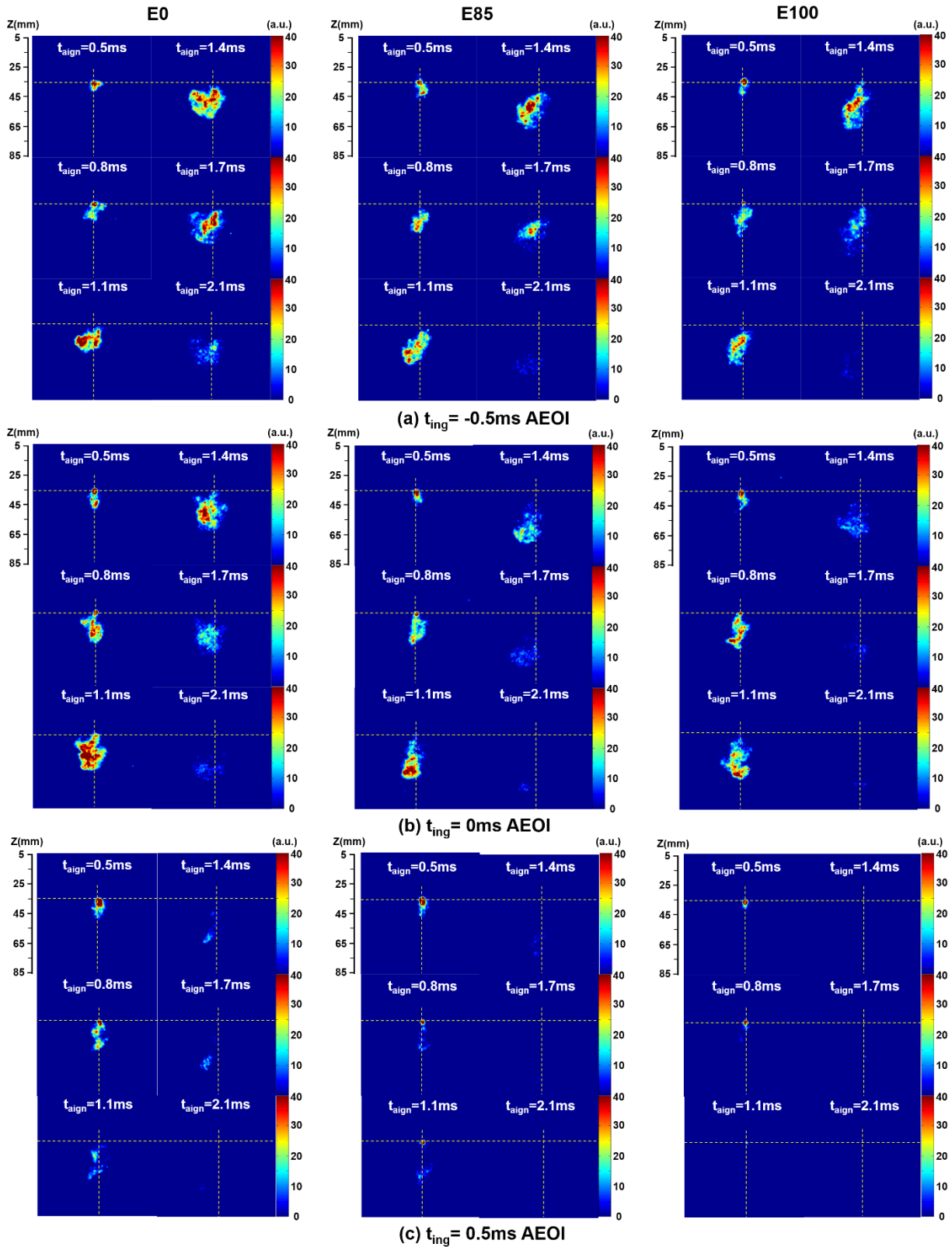**Figure 6.9** Spatial Distribution of OH* Chemiluminescence Image for Different Ignition Timing

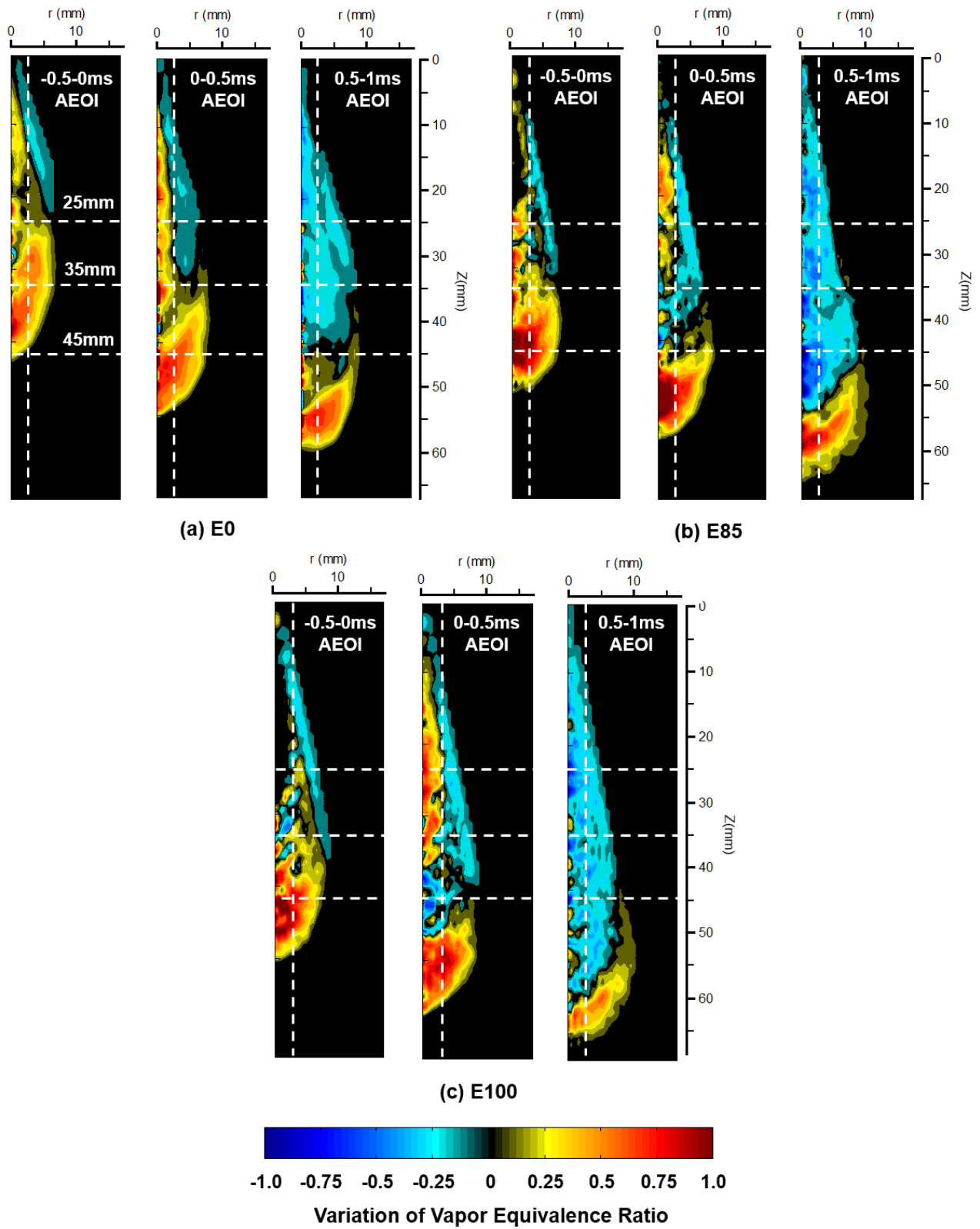$(P_a=1.0MPa,\ T_a=500K,\ P_{inj}=20MPa,\ [Z,r]=[35,3],\ t_d=6ms)$

Figure 6.10 Spatial Distribution of the Variation of Vapor Equivalence Ratio (ignition position was marked by the white dot lines, P_a=1.0MPa, T_a=500K, P_{inj}=20MPa, t_{ign}=0ms AEOI, t_d=6ms)

At actual, the time interval from the start of ignition to fast flame propagation is about 0.5ms which will be discussed at the next section. The rich mixture forms at the ignition position ([Z,r]=[25,3]) from -0.5ms to 0ms AEOI as shown a yellow region near that location in Fig.6.10. However, for t_{ing}=0ms AEOI, this dense mixture region becomes leaner gradually within 0.5ms after SOIg which is demonstrated by a blue color in Fig.6.10. Especially the E85 and E100 show a severe decreased fuel vapor at the peripheral region of spray near [25,3]. Moreover, the presence of comparatively dense liquid droplets (nearly twice over than vapor concentration) demonstrated in Fig.5.4 also leads to a larger amount of carbon fouling on the electrodes and has a great impact on the initial flame kernel growth owing to the higher vaporization heat losses [1]. Both of the above reasons contribute the relative incomplete combustion with the long narrow flame shape and lower OH* signal for the case of [25,3], t_{ign}=0ms AEOI, especially the E85 and E100 where have a wider region of decreasing local mixture concentration along the spray axis as expressed in Fig.6.10.

The local mixture dilution is also considered as the primary factor in determining the undesirable burning process for the late ignition (0.5ms AEOI) in the middle region of the spray. As shown in Figs.6.9 and 6.10, a distance of predominant leaner mixture along the spray axis, about 10mm for E0, 20mm for E85 and E100 downstream of the ignition location ([Z,r]=[35,3]) is considered as the most significant reason to cause an incomplete combustion at the case of [35,3], t_{ign}=0.5ms AEOI. More lean local mixing would result in a poorer flame development, in particular the E100 which only demonstrates a little OH* intensity after the ignition.

One phenomenon of interest can be found at the onset of flame fast development. The flame seems propagates closed to the spray axis during its evolution with time escape, especially the upstream ([Z,r]=[25,3]) and early (t_{ign}= -0.5ms AEOI) ignition. Combined the spatial variation of fuel vapor in Fig.6.10, an enrichment of local vapor mixture at the inner region of spray (a positive variation marked by yellow color along the spray axis in Fig.6.10) is found at the time when the flame begins to spread quickly at the upstream and early ignitions. This result indicates the fact that the flame is prone to direct to the regions in which the local mixture becomes denser.

In general, the behavior of flame propagation suggests that the flame development depends on the progress of the flame front, which is greatly sensitive to the local equivalence ratio of fuel vapor, and is governed by the amount of sufficiently ignitable mixture downstream of the ignition positon.

Compared with E0, a shorten combustion duration of ethanol-gasoline blends with the increased of ethanol ratio can be found in Figs.6.8 and 6.9, which is similar to the result of Turner et al. [255]. The intensity of OH* chemiluminescence for different ethanol-gasoline blends also implied that the E0 has a

higher OH* emission than E85 and E100 under the comparison at the same ignition locations and timings. The lower OH* with ethanol addition will be discussed in the following section.

6.4.2 Quantitative Analysis of OH* Chemiluminescence
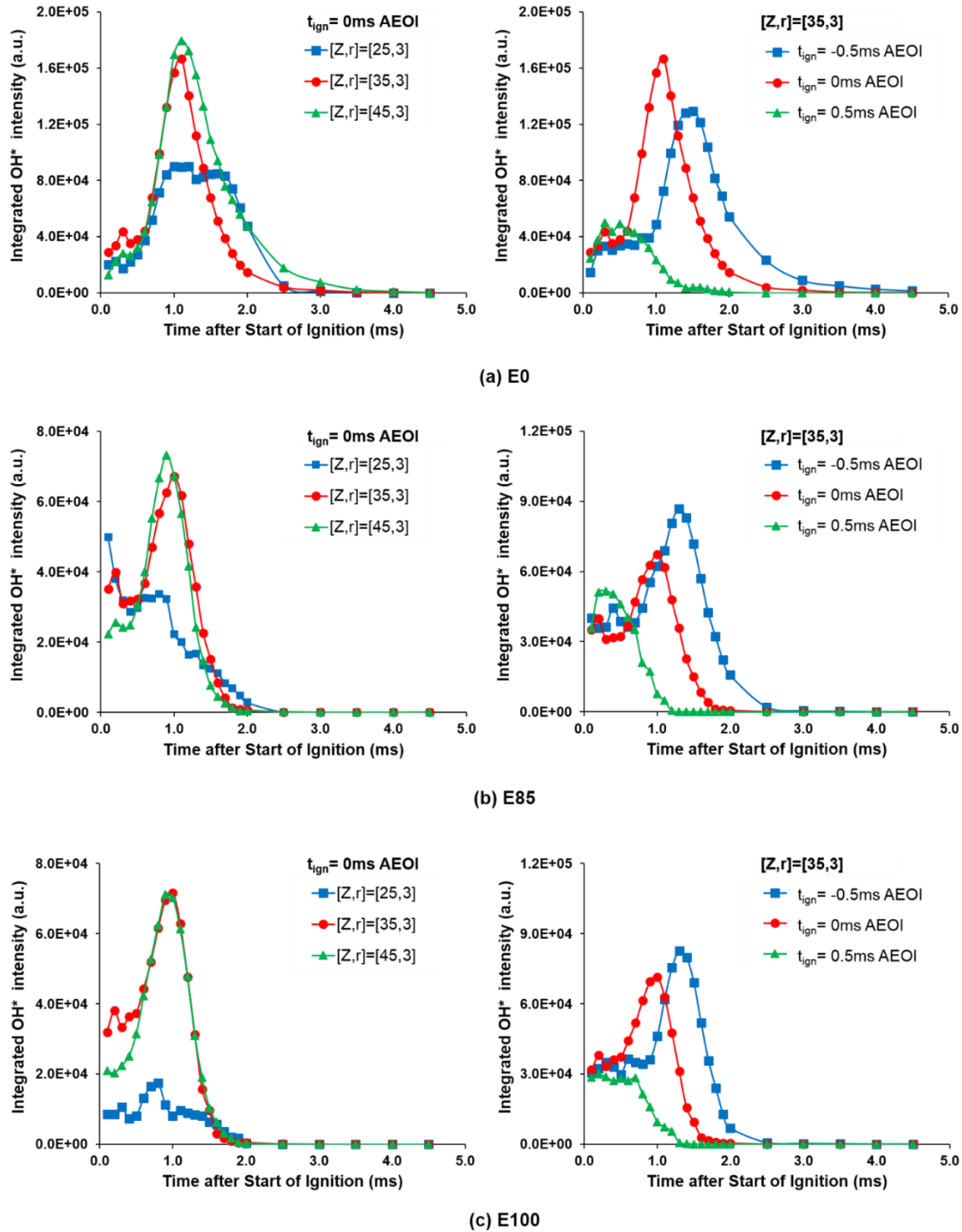

(a) E0

(b) E85

(c) E100

Figure 6.11 Temporal Variation of OH* Chemiluminescence

The temporal variation of the integrated OH* intensity is quantitatively analyzed in Fig.6.11. Every case was obtained by six times to ensure the reliability for the quantitative combustion analysis. The averaged results were used in this section and it can provide the comparable variation on combustion evolution after the start of ignition. The typical ignition cases of E0, E85 and E100 were selected in the discussion.

A first peak of OH* which is dependent on the concentration of the CH radical is observed, particularly in the case of adding ethanol, probably as a result of spark charge. Similar result was found for the CH* emission taken by a photomultiplier in an engine test, in which a temporarily increased CH* signal appeared at the spark duration [256]. For all fuels, the upstream ignition shows a poor burning behavior as a result of dense liquid phase and the dilution of local vapor concentration as already discussed previously, which tends to an unstable flame propagation. E0 presents a favorable combustion with a higher OH* intensity at the EOI timing, which is also reported in the previous study [257]. However, a higher OH* intensity for E85 and E100 flames is observed under the advanced ignition, as opposed to the worse burning in E0. An explanation for this is the downstream mixture concentrations of E85 and E100 becomes denser from the time of -0.5ms to 0ms AEOI. This tendency also is indicated by the vapor equivalence ratio in Fig.5.4 where shows the presence of higher fuel vapor at the 0ms AEOI at the ignition location ([Z,r]=[35,3]). The local variation of fuel vapor for E85 and E100 in Fig.6.10 also demonstrates an enrichment of fuel vapor from -0.5ms to 0ms AEOI at [35,3], in comparison to the decreased tendency at that positon from 0ms to 0.5ms AEOI. All the above is regarded as the evidence for the higher OH* emission for E85 and E100 ignited at advanced timing.

The lower OH* emission at the upstream and late ignition also are revealed in Fig.6.11 as mentioned already in the previous section. Furthermore, one should be noticed that E100 lows the OH* intensity extremely as the fuel is ignited at [25,3] and 0.5ms AEOI, compared with E0 and E100. The much decreased heating value by pure ethanol is considered as the result of the reduced OH* emission, due to the diluting local mixture at upstream and late ignition condition leading difficulty for the flame propagation. On the other hand, there is no significant difference of OH* intensity at both middle region and downstream ignition, since a favorable concentrating of fuel vapor at those region as shown in Fig.6.10. Furthermore, adding ethanol into gasoline does not change the combustion phase, which indicates that the ignition and timing is possible adjusted based on using gasoline. From Fig.6.11, the higher OH* emission of E0 (about 2~3 times) than that of E85 and E100 is observed, probably as a result of the locally richer mixture zones in the combustion chamber for E0.

6.4.3 Effect of Stratified Vapor Distribution on Ethanol-Gasoline Blends

The spray mixture formation of E85, as already mentioned in Chapter 4, tends to produce a stratified vapor distribution due to its different boiling point for individual components. Especially, a region of rich high boiling point component in gasoline will form at the downstream of spray after EOI. In order to investigate the potential effect of the stratified vapor distribution, the impact of this vapor ambient-gas mixture formation on the E85 combustion and its comparison to the E100 were clarified in this section.

Since the dense vapor region of gasoline at downstream occurs at the near 1.0ms AEOI for E85 under the same calorific value condition, the specific two cases of ignition ($[Z,r]=[35,3]$, $t_{ign}=0.5$ms AEOI and $[Z,r]=[45,3]$, $t_{ign}=0.5$ms AEOI) were chosen to make the comparison between E85 and E100. The left column in Fig. 6.12 shows the temporal variation of OH* intensity under those two cases for E85 and E100. While the figure at right column demonstrates the vapor fraction of toluene (represent gasoline in E85) in MEK85/toluene15 (represent E85) along the spray axis at different timings.
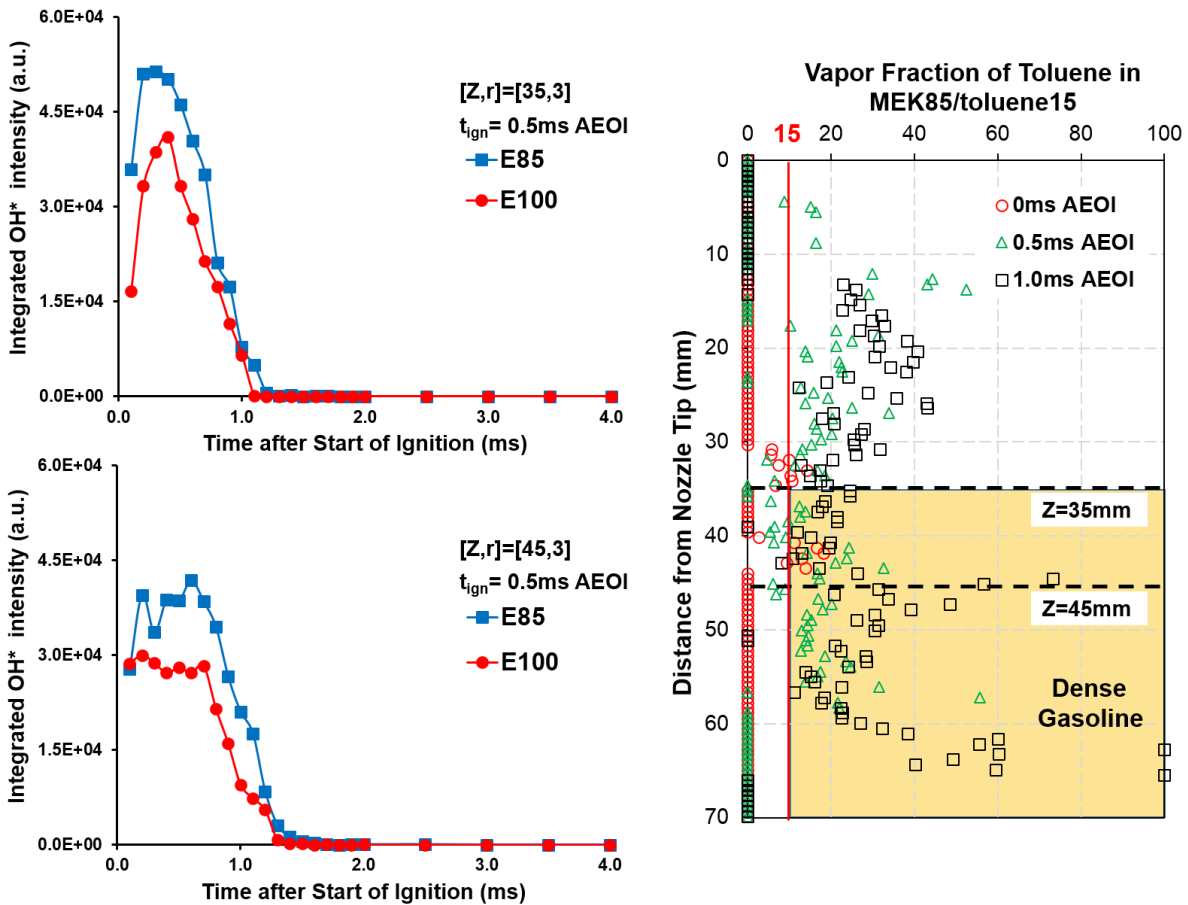

Figure 6.12 Effect of Downstream Dense Gasoline on Combustion for E85 Compared with E100

158

It is obvious to notice that a higher combustion intensity of E85 than that of E100 occurs at those region of spray. However, less remarkable distinction of equivalence ratio at ignition along the spray axis is detected from the LAS (not presented here). Therefore, one possible reason causing this significant difference can be considered as the result of the downstream dense gasoline. As shown in Fig.6.12, a distinct dense area of toluene (>15%, marked by an orange color) occurs at the middle to downstream of the spray from 0.5ms to 1.0ms AEOI. When the flame starts to fast propagation, the flame front would probably encounter the dense gasoline vapor formed at the downstream during the fast development. It has been well known that the laminar flame speed of ethanol is higher than that of gasoline and iso-octane, however, all of those researches were conducted in a homogenous mixture condition [258-260]. Recent studies proposes the fact that gasoline can potentially achieve a faster flame propagation than ethanol addition in DISI engines [263-264]. For the ethanol-gasoline combustion, the latent heat of ethanol should be considered as the significant factor that influences the flame speed during the fast combustion period. The high enthalpy of vaporization and low energy density of ethanol would reduce the combustion temperature and hence decrease the flame speed. In consideration of this effect, the flame speed of ethanol is potentially lower than that of the gasoline. On the other hand, the late evaporation of high boiling point component in E85 induces a relatively increased vapor concentration at downstream compared with E100 as shown from 0.5ms to 1.0ms AEOI in Fig.6.10. Therefore, the E85 would show a faster burning velocity than pure ethanol, which results in the maximum projected area of E85 about 2.7 times larger than that of E100 at those cases presented in Fig.6.12. This result is similar to the author's previous studies [261-262] by using the injection pressure of 10MPa for ethanol-gasoline blends.

6.5 Flame Growth of Ethanol-Gasoline Fuels

6.5.1 Flame Radius

Similar to the analysis method mentioned in Chapter 5, the equivalent flame radius, R, can be extracted from the images of OH* chemiluminescence to characterize the flame development under different ignition strategies as shown in Fig.6.13. The larger equivalent flame radius of E0 over than E85 and E100 is found for all ignition cases due to the presence of locally rich mixture and sustainable combustion period. Moreover, a desirable shorter combustion duration is observed with the increase of ethanol ratio. This is important because favorable combustion is necessary not only so that there is sufficient burning activity to ensure heat release but also because the shorter combustion period maintains a higher thermal efficiency of the cycle. Therefore, adding ethanol is possible to achieve the fast burning in cylinder to avoid the higher pollutant emission and reduced heat efficiency at post combustion.
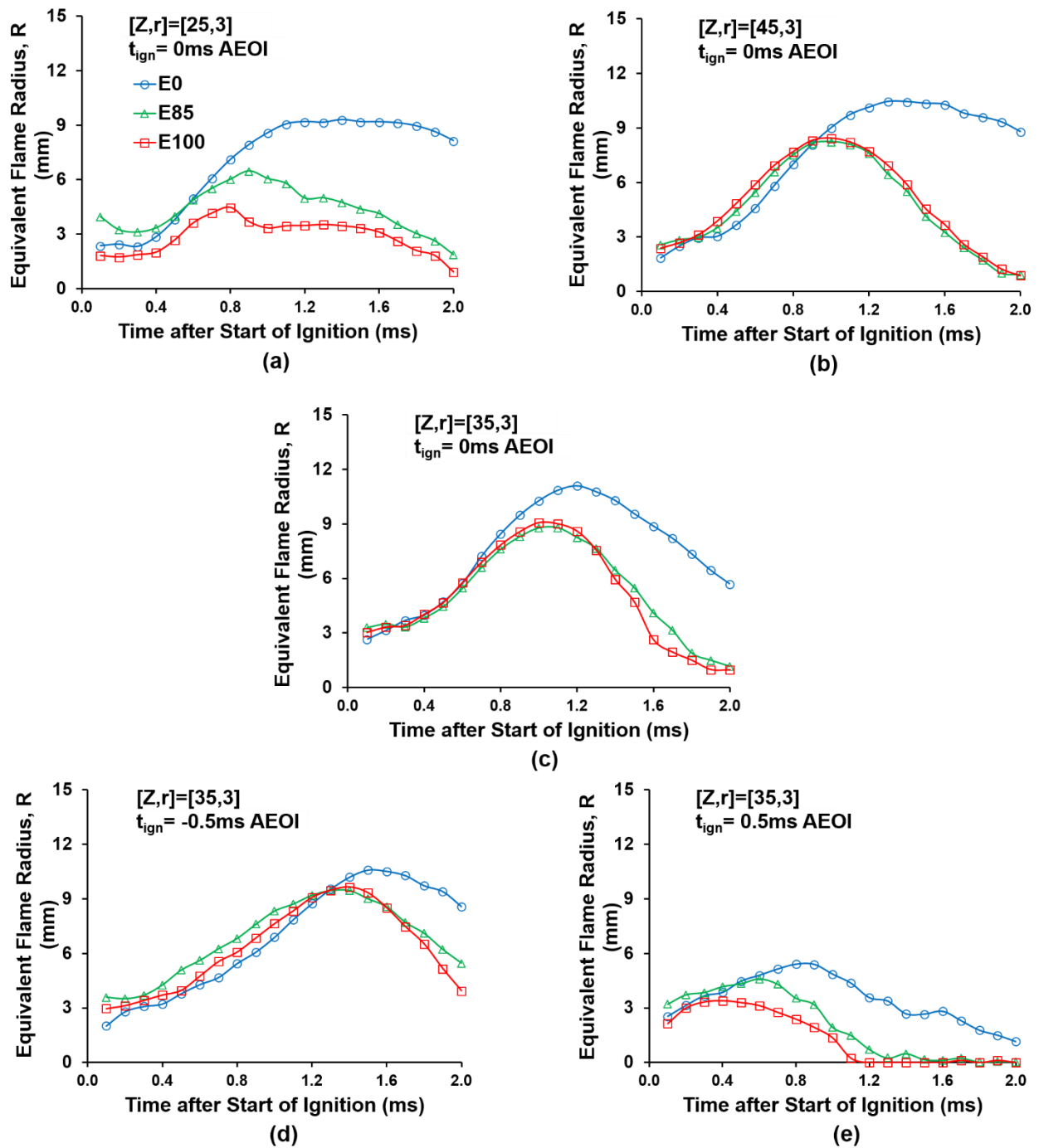
Figure 6.13 Flame Radius for Ethanol-Gasoline Blends

From Figs.6.13 (a) to (c), the variations of flame radius at the middle region and downstream ignitions for E85 and E100 are nearly the same, which show a regular curve and higher value of flame radius compared with the case of upstream ignition. This result indicates that for ethanol-gasoline blends, the

middle-downstream ignition enable the flame to propagate smoothly, as a result, it is believed that the stable flame evolution and heat release rate can be achieved when the ethanol-gasoline blends is ignited under those conditions. As seen from Fig.6.13 (c) to (e), when the ignition is taken place at the period from the advanced timing (t_{ign}= -0.5ms AEOI) to EOI, the enough flame radius is observed about R=9mm, which is able to provide the normal flame propagation as proven by the imaging of OH* chemiluminescence distribution in Fig.6.9. While for the late ignition, the extremely unstable flame formation, especially the E85 and E100, occurs due to the decreased vapor concentration at downstream of ignition positon as shown in Fig.6.10.

The flame growth speed (dR/dt) of E0, E85 and E100 seems to increase slowly (see Fig.6.13) at the early stage of combustion for the ignition cases ([Z,r]=[25,3], t_{ign}=0ms and [Z,r]=[35,3], t_{ign}=-0.5ms), approximately less than 5m/s at a time of 0.45ms after the spark. Irrespective of the facts that there are notable liquid droplets at the ignition position [25,3] for all fuels or that no liquid and vapor are present at the ignition position [35,3] for E0, when the fuel is ignited at those timings, growth of the flame also occurs. Two significant factors give rise to these results. First, Solomon [263] has shown that, even if the spark gap is immersed in a slightly rich cloud of fuel or vapor, the initial flame kernel can also persistently grow until the ambient mixture becomes sufficiently lean to sustain progress of the flame. Second, a spark discharge duration of about 3.2ms is a sufficient time for local fuel transport and mixing with ambient gas, so that an ignitable mixture exists at the spark gap during the discharge as shown in Fig.5.4.

6.5.2 Ignition Delay

When the ignitable mixture around spark plug is ignited, the initial flame kernel formation is greatly governed by the spark breakdown, arc and glow phases. Thereafter, the initial flame development stage occurs and usually is defined as the burned mass fraction up to 1 or 2%. As long as the heat release of chemical reaction is larger than the heat dissipation of the flame kernel, the flame tends to the steady propagation. Therefore, the ignition delay, which represents the duration between the SOIg to the flame steady propagation (a constant of dR/dt during flame propagation), offers a significant way to evaluate the combustion characteristics. In terms of the equivalent flame radius R, the ignition delay τ can be defined as the SOIg to the cross point which formed by the two trend lines of initial flame development and the stable flame growth respectively during the flame development, as shown in Fig.6.14.
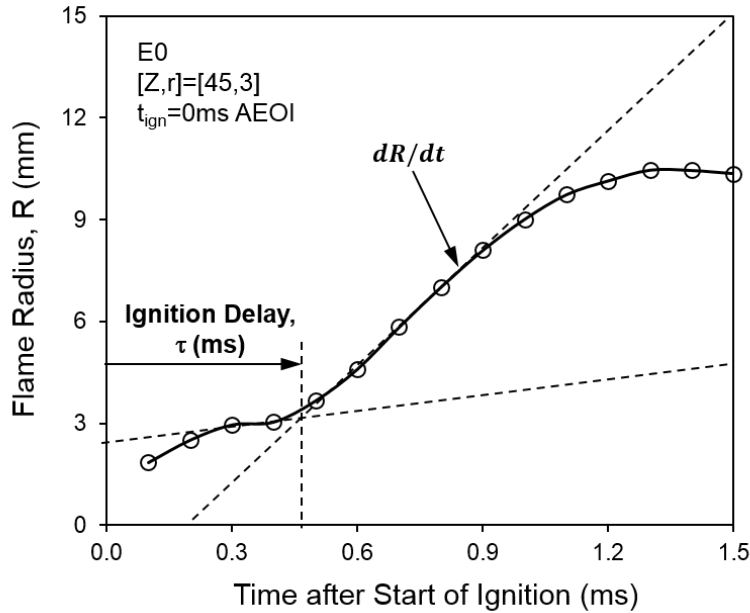
Figure 6.14 Definition of Ignition Delay

For all fuels, the effect of spark location and timing on the ignition delay are plotted in Fig.6.15. Generally, the ignition delay is reduced with retarded ignition timing, from t_{ign}= -0.5ms to 0.25ms AEOI in the figure. Several reasons, such as the local flow field and liquid droplet of fuel, are considered as the predominant factors. First, when the fuel is sparked at the intensive flow field (induced by spray), in particular the upstream or early ignition, the ignition delay is catalytic to increase as a result of the reduced spark energy and flame kernel stretching by the spray-flow interaction. Thus the resistant time of initial flame development is extended (approximately above 0.6ms), due to the less heat transported from the spark charge and the excess of the heat dissipation. Secondly, the existed large amount of liquid droplet also delays the initial flame propagation since the initial flame kernel does not start to propagate faster unless the local mixture around spark plug becomes ignitable.

On the other hand, the increased of ethanol ratio in gasoline will decrease the ignition delay (below 0.6ms at advanced ignition) from the start of ignition to fast development. An explanation for this is the higher laminar flame speed for ethanol than gasoline during the initial flame growth, with respect to the less significant effect of turbulent on this period than the laminar flame speed which enables the local burning velocity of fuel to reach the its laminar value [264].

162
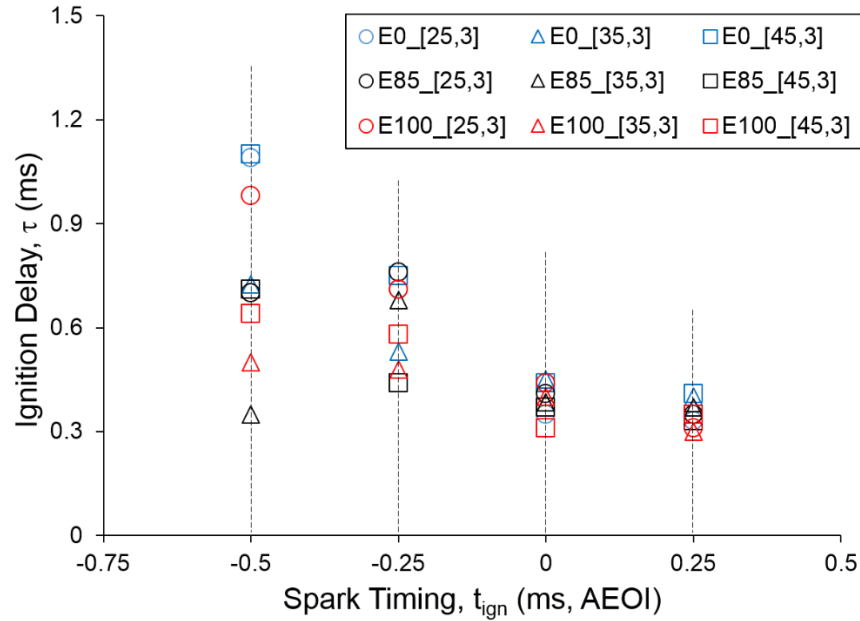
Figure 6.15 Ignition Delay of Fuels under Different Spark Locations and Timings

The time needed for the subsequence development of flame after ignition has no significant difference when the fuel is ignited at the EOI or slightly after EOI, expressing about 0.3~0.4ms as shown in Fig.6.15. The higher vapor concentration of fuel around the ignition location (see Fig.5.4) is responsible for this result, especially the E85 and E100 due to the ethanol content reducing the high boiling point component in fuel and resulting in a faster evaporation.

6.6 Jet-to-Jet Variation

The coefficient of variation (CoV) is usually used as a good indicator to analyze the engine performance, especially for the indicated mean effective pressure or the maximum in-cylinder pressure in the internal combustion engine. Also it is employed to describe the fluctuation in the flame area during the combustion by measurement of the planar laser-induced fluorescence [265]. In this section, the jet-to-jet variation in the peak integrated OH* intensity is used to represent the cyclic variability of the heat release rate and combustion pressure of the ethanol-gasoline blends as presented in Fig.6.16. Turner et al. [255] reported that the coefficient of variability of the indicated mean effective pressure decreased with the increase of ethanol content and advanced ignition. In addition, this study reveals that the combustion stability is greatly affected by not only the spark timing but also the ignition location.

163
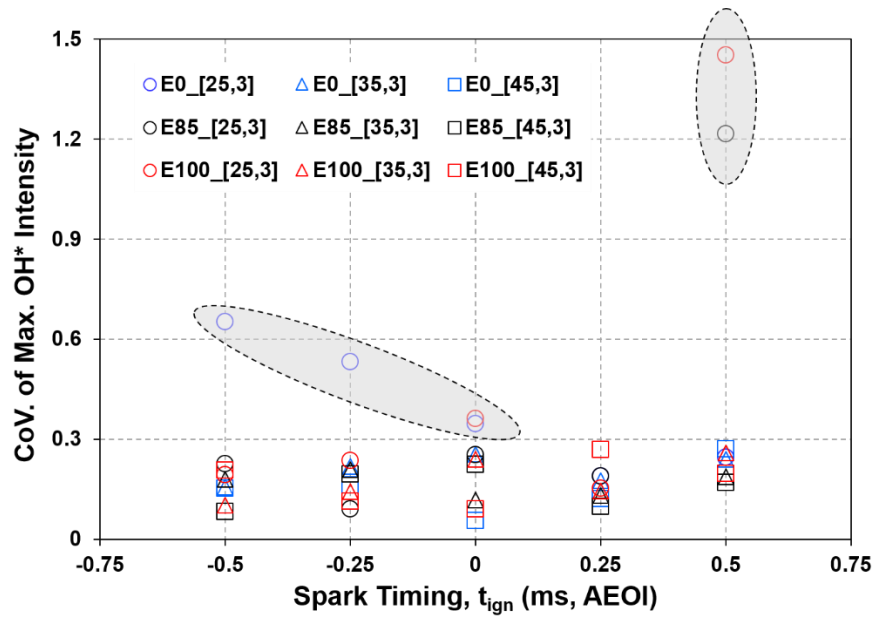
Figure 6.16 CoV of Max. OH* Intensity
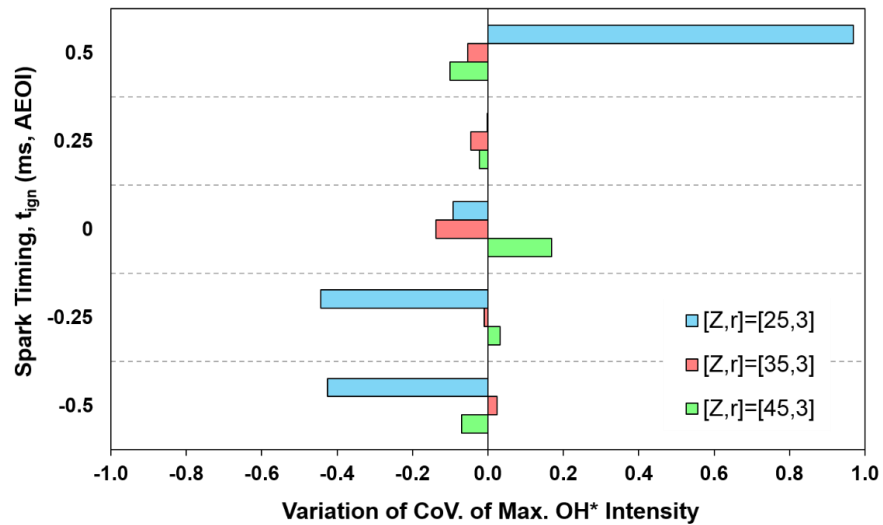
Figure 6.17 CoV of Max. OH* Intensity Varied with Fuels from E85 to E0

In general, the combustion stability of E0, E85 and E100 is located in the range below 0.3 under different ignition locations and timings. Moreover, the favorable combustion stability presents at the middle and downstream ignition for all fuels, especially in the advanced ignition for E100 which achieves the jet-to-jet variation less than 0.2. Also, an increase of CoV value of combustion occurs when the ignition is taken place at the retarded timing, especially the increase of ethanol content in gasoline. While the E0 shows

164

a higher unstable combustion at the upstream ignition as marked by a gray cycle in Fig.6.16. The detail information of the comparison between using E0 and E85 on the combustion stability is shown in Fig.6.17. The negative value indicates the improvement of combustion robustness by using E85 instead of the E0.

It can be found that the combustion stability is greatly improved by the ethanol addition under the early ignition at upstream ignition, which is enhanced up to 60%. While the disadvantage of increasing ethanol ratio in gasoline is that it will lead to much worse combustion when the fuel is ignited at t_{ign}=0.5ms, [Z,r]=[25,3] in this study. The possible reason is attributed to the fast mixing ratio of ethanol addition and the dilution of local mixture as discussed previously. Figure 6.10 demonstrates E85 has a pronounced decreased vapor concentration below the ignition location [Z,r]=[25,3] at t_{ign}=0.5ms AEOI, compared with E0. Therefore, the initial flame growth becomes difficulty, which is evidenced by a lower ignition probability as expressed in Fig.5.3, also leads to the severe unstable combustion.

Furthermore, it should be noticed that ethanol-gasoline has a potential to extend the ignition timing range of the stable combustion in DISI engine, especially for the advanced ignition. An explanation for this is that the combustion efficiency generally improves with the increase of ethanol in gasoline which produces more oxygen content and favorable local mixing resulting from a faster evaporation. With the advantage of the stable combustion under advanced ignition, the utility of ethanol-gasoline blends allow more flexible arrangement of ignition timing in the DISI engines, even in the case of spray-guided concept.

6.7 Soot Formation

In high-speed imaing method, the soot formation and flame temeprature in diesel or gasoline ususally is evaluated by the two-color pyrometry [266-267]. The previous study using gasoline under the same ambient condition has proposed the results of (1) the large soot amount produced by the locally over-rich mixture and (2) not much significant differrence in the time required for the onset of the soot oxidation [257]. With the addtion of ethanol, the noticable difference of the flame visulation for ethaonl-gasoline blends is the decreased of flame color, indicating the much lower soot formation than gasoline. Therefore, the measured error would be enlarged if using the conventional two-color pyrometry to detect the soot formation of ethanol-gasoline blends.

As describd in section 1.2.3, the luminous flame which is primary produced by the soot incandenscence, can be used to characterize the soot formation in this section. Based on the RGB analysis method to differential the luminous flame from the NL signal, the luminos intensity ratio (LIR) is proposed and defined as below.

$$LIR = \frac{\int I_l dN_l}{\int I_t dN_t} \tag{6.1}$$

Where I_l and I_t indicate the light intensity of luminous flame and that of total flame respectively. N_l and N_t represent the corresponded pixel number of lumnious flame and the total flame. Therefore, the soot formation can be simply described by the LIR in according to the NL image.
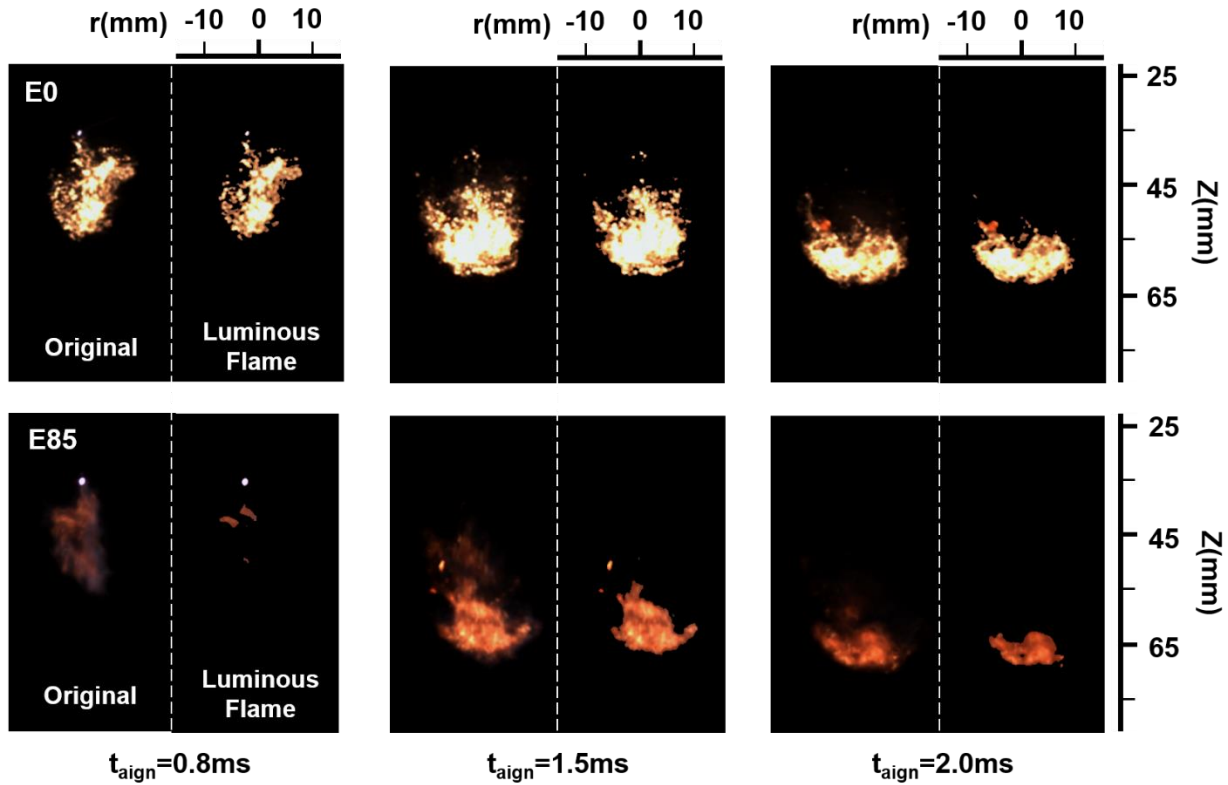
Figure 6.18 Comparison of Liminous Flame between E0 and E85 (P_a=1.0MPa, T_a=500K, P_{inj}=20MPa, [Z,r]=[35,3], t_{ign}=0ms AEOI, t_d=6ms)

Figure 6.18 illustrates the comparison of luminous flame for E0 and E85 under the same condition. Due to the hydrocarbon content, the E0 shows a high intensity with the yellow color in the flame. In contrast to E0, the flame of E85 has a moderate orange color which is seems to be transparent as discussed in the section 1.2.2. By this seperation, the lately production of soot can be found in the E85 combustion at t_{aign}=0.8ms, probably as a result of the ethanol content impeding the formation of soot at the early stage of combustion. A large area of non-luminous flame, dominated by the blue color is observed in E85 flame. During the flame development, the E85 also shows a soot incandencse at downstream of spray with a less luminosity instead of the higher brightness in E0 flame.
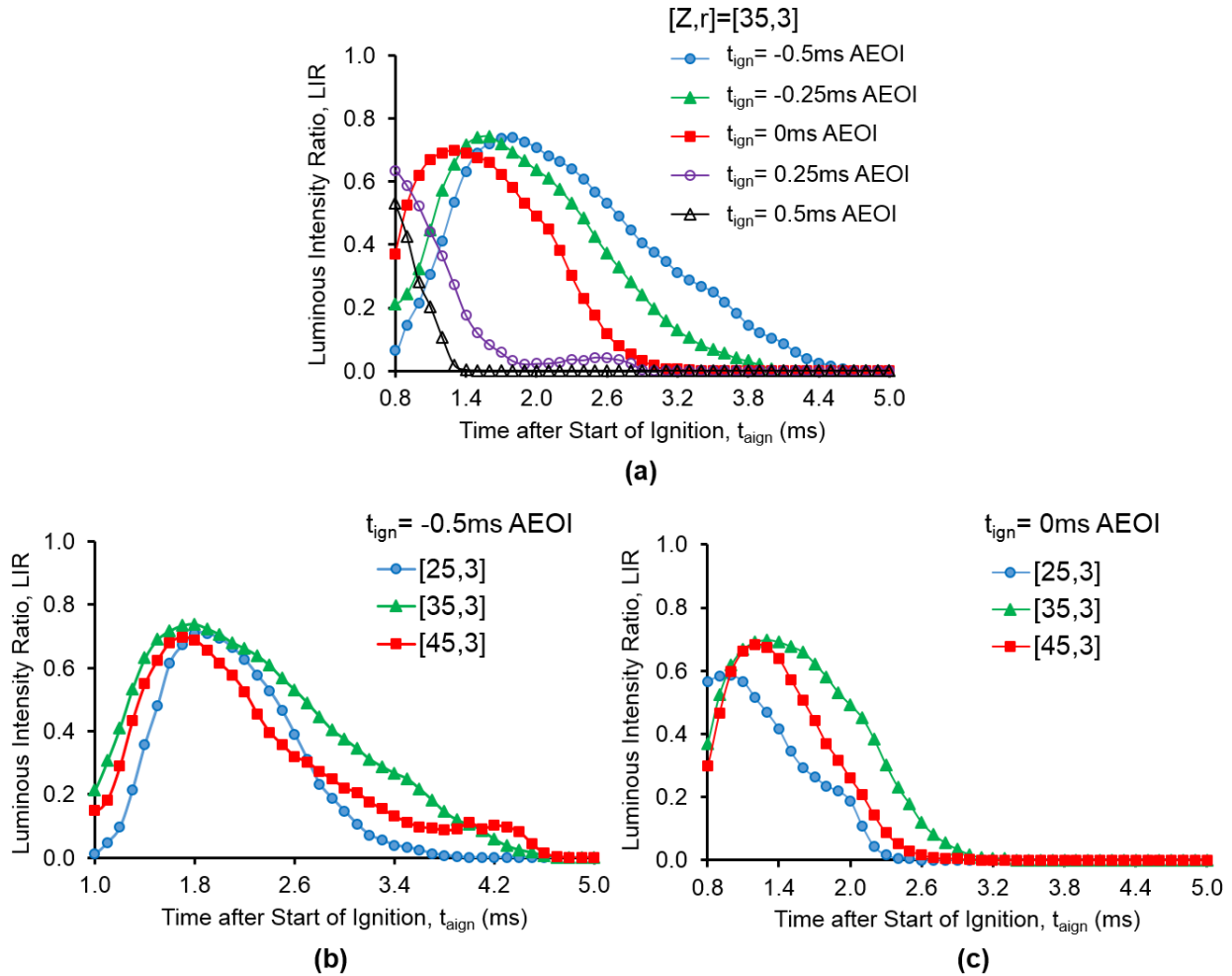
Figure 6.19 Comparison of Luminous Intensity Ratio in E85 Combustion under Different Ignition Location and Timing

This section focuses on the luminous flame (based on the LIR) of E85 in order to investigate the soot formation in the case of ethanol addition compared with the pure gasoline (E0). Differnet variations of LIR for E85 combustion under different igntion positons and timings are shwon in Fig.6.19. The differences of maximum LIR are not so large when the fuel is sparked under the different ignition timing as shwon in Fig.6.19 (a), which shows a vaule about 0.7. It should be noticed that the pahse of soot production becomes earlier at the late ignition because of the reduced ignition delay. Also, the ealier igntion timing can give rist to an increased of LIR, meanig that the luminous sooting flame increases as the time interval between end of injection and start of ignition was shorten. On the other hand, the variation of LIR shows a similar tendency with the OH* chemiluminescence in Fig.6.11 under the given igntiion timing as shwon in Figs 6.19 (b) and (c). It should be mentioned that a slightly retarded of maximum soot formation compared with the peak OH* intensity is found in the range of 0.2~0.3ms. Based on this anlaysis, the soot formation of

167

E85 is able to be measured quanlitatively. Also, a further discussion of using E85 in DISI engine can be realized in consideration of the above overall discussion of the flame characteristics analysis, which will be showed in the followint section.

6.8 Discussion on Using Ethanol-Gasoline Blend (E85) in DISI Engines
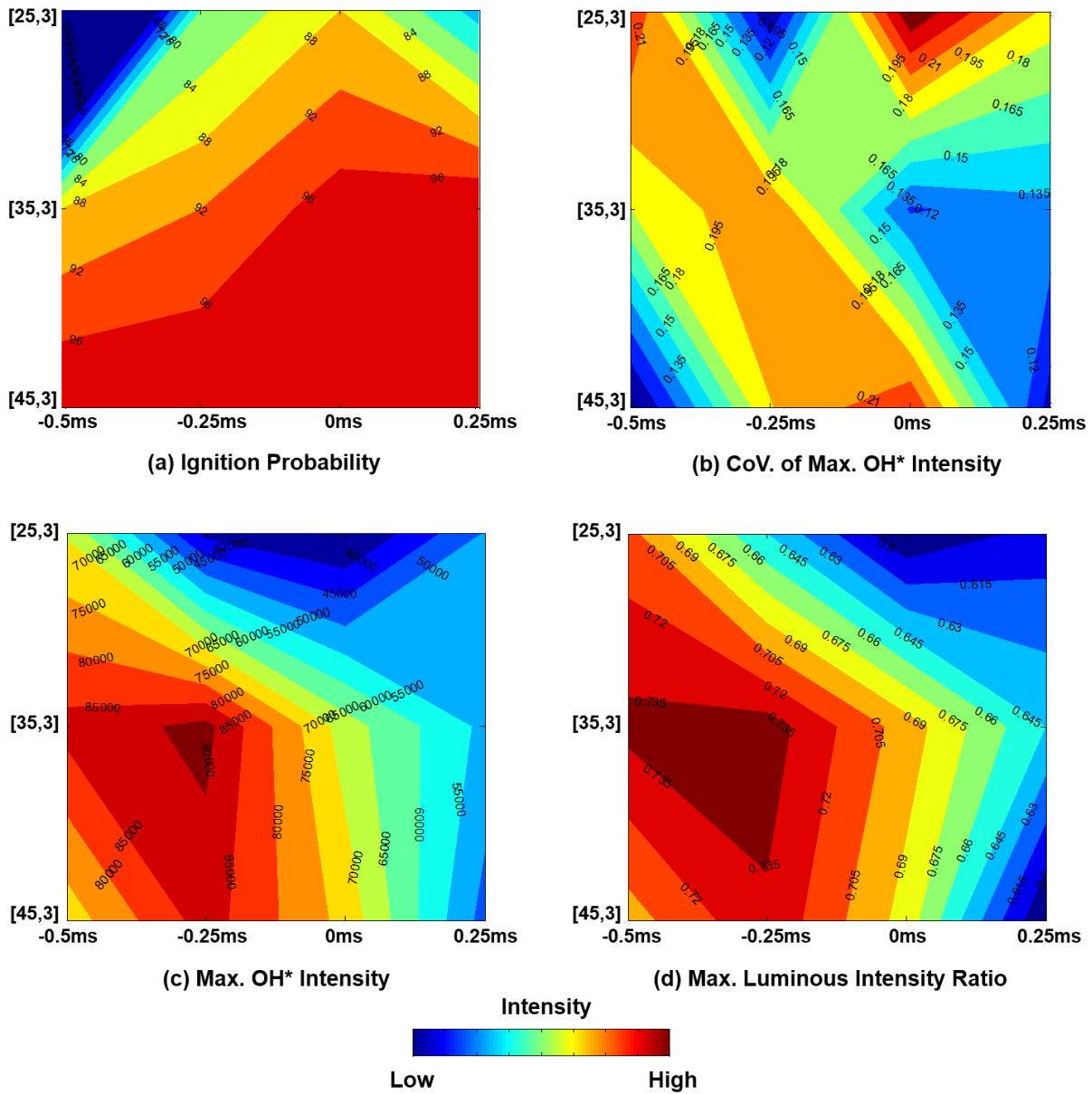
Figure 6.20 Maps Distribution of (1) Ignition Probability, (2) CoV. of Max. OH* Intensity, (3) Max. OH* Intensity and (4) Max. Luminous Intensity Ratio for E85 Combustion

In order to moderate the dependence on petroleum fuels and reduce the CO2 emission, using ethanol-gasoline blends in SI engines, or recent advanced concept of D.I. stratified combustion, has been achieved comparable attention in automobile industry. The promise of this technique, especially the SG-DISI system, is to gain the diesel engine-like efficiency and improve fuel economy. This section is focused on the further discussion of using ethanol-gasoline blend, typically the E85 which has been introduced into market for many years to replace the petroleum, in the SG-DISI engine-like condition based on the experiment results presented previously.

Data extracted from the Chapters 5 and 6 shows the maps of ignition probability, CoV. of max. OH* intensity (represents combustion stability), max. OH* intensity (represents heat release rate) and max. luminous intensity ratio (represents soot production) for E85 in Fig.6.20. According to these maps, it is possible to investigate and discuss the optimum combustion and burning activity of E85.

The striking feather of E85 ignition process is the extension of ignition probability from t_{ign}= -0.5ms to 0.25ms AEOI at middle to downstream spark in this study, compared with gasoline. While owing to the presence of dense liquid phase and high momentum of droplets in spray by a more injection mass, the spark discharge loses the robustness induced by the spray-spark interaction, hence increase the proportion of partial or misfire cycles, in turn resulting in a lower ignition probability at early-upstream ignition as expressed by a distinct blue color in Fig.6.20 (a). In addition, an typical unstable combustion zone (higher CoV. of max. OH* intensity above 20%) is revealed from [Z,r]=[25,3], t_{ign}= -0.5ms to [Z,r]=[45,3], t_{ign}=0ms AEOI in Fig.6.20 (b). Meanwhile, the ignition [Z,r]=[25,3], t_{ign}=0.5ms AEOI shows a severe cycle variability because of the dilution at local mixture, which can be indicated by a greatly decrease of vapor equivalence ratio at [25,3], 0~0.5ms AEOI in Fig.6.10. The interpretation of heat release rate in combustion is dependent on the OH* chemiluminescence which primary produces at the near stoichiometric condition. A favorable range of E85 burning activity concentrates at the region where the fuel is ignited before EOI and the middle to downstream of spray. Figure 6.20 (d) shows the similar tendency distribution of soot production to the Max. OH* intensity.

In terms of the above results and the previous study using E0 [257], the striking feather of the differences between the fuels (E85 and E0) is the shift in the optimal ignition timing relative to the start of injection, which can achieve the favorable ignition and combustion (higher ignition robustness and heat release, lower soot formation) by using E85 in DISI-like condition. Moreover, the optimal spark location is found at the middle to downstream of spray, where expresses a better local mixing with an increase of fuel vapor along the direction of flame propagation. The results of this study is used to make the comparison with the recent studies of Sjöberg and Reuss [268-269] in Sandia Nation Laboratories whose have found some gains about the achievements of ultra-low NO_x and soot formation by using E85 in a single cylinder four-valve SG-

DISI engine. They proposed the near-TDC injection and the ignition prior to injection, in order to realize the purpose of (1) fully utilizing the enhanced mixing rate of E85 under an intense in-cylinder turbulent and (2) avoid the severe interaction between spark discharge and one of the fuel jets adjacent to the spark plug. This study also demonstrates that the faster evaporation for E85 than gasoline under the DISI-like near TDC condition due to its lower boiling point, implying the local mixture is able to be improved in the case of middle to downstream ignition as shown in Fig.6.10. Moreover, the study reveals the advantage of advanced ignition (-0.5ms to 0ms AEOI) for E85 combustion, similar to the result from Sjöberg and Reuss which showed the most stable combustion was achieved if the spark timing was set to the first half or in the middle of injection event. It should be mentioned that this study suggests the optimal combustion of E85 can be realized when the fuel is ignited from middle to downstream of spray at advanced ignition. In this case, the interest is found that the ignition happens when the E85 spray just arrives at the spark plug. This is greatly in consistent with Sjöberg and Reuss's result. However, one significant difference is that they used the ignition prior to the injection and longer spark discharge duration lasting until to SOI, as a result, the strong interaction between the spark discharge and spray plume can be avoided because of the fully development of the spark plasma. In contrast to the narrow distance of only 13mm between injector and spark plug in their experimental engine, this study demonstrates the optimal ignition location is about 35 to 45mm distance along spray axis which implies the decreased spray momentum at spray axis when the spray penetrates at ignition location. Therefore, the effect of spray-spark interaction at this ignition location is much less significant than that in the Sjöberg and Reuss's experiment.

For the soot formation, a lower soot formation (LIR≈0.7) is observed under the optimal ignition timing and spark position in this study. Sjöberg and Reuss also expressed that the ultra-low NO and soot were able to be realized if using the near-TDC injection and advanced ignition. They used a flame model by means of CHEMKIN to propose that the strong vaporization cooling of ethanol would suppress the flame speed in rich area, hence reducing the soot formation of E85. The effect of higher enthalpy of vaporization for ethanol on the limitation of flame propagation also is assumed by the author and evidenced by the lower flame radius of E85 than that of gasoline under the optimum ignition strategy in Fig.6.13.

In consequence, the result of this study demonstrates the fact that it is potential to achieve the high combustion efficiency without decreasing the stable combustion, and lower pollutant emission by using E85 in SG-DISI engine, if combing with the fast evaporation and the advantage of advanced ignition.

6.9 Summary

In this chapter, the flame development process and combustion characteristics of ethanol-gasoline blends were investigated under the typical ambient conditions with high temperature and pressure simulating the near TDC environment in DISI engine. By means of combing the optical methods of the shadowgraph, high-speed imaging of OH* chemiluminescnece and natural luminosity, the characteristics of flame and combustion were able to be analyzed quantitatively. The corresponded mixture formation under the same condition with combustion also was measured by the LAS technique in order to interpret the effect of spray evaporation on the combustion. Different blending ratio of ethanol, E0, E85 and E100 were used in this chapter. Like the chapter 5, longer injection mass of ethanol-gasoline blends was corrected due to the lower stoichiometric air/fuel ratio than gasoline. Some gains were found and summarized as follows.

1. Local mixture formation plays a pivotal role on the flame development and evolution. Especially the flame propagates towards downstream of the ignition position instead of in the upstream direction as a consequence of the upstream diluted mixture and locally high flow velocity which is greater than the flame growth speed. Also, the decreased local fuel vapor leads to the results of an incomplete combustion with a pronounced long-narrow flame shape as the fuel is ignited at upstream/early timing and downstream/late timing. On the other hand, the flame front is sensitive to the local mixture and prone to direct to the regions in which the local mixture becomes denser.

2. The flame visualization was characterized by the high-speed imaging of natural luminosity and its appearance in shadowgraph. E0 shows a brilliant luminosity than the fuels mixed with ethanol, which demonstrates a mild-luminosity signal and 'opaque-like' appearance of flame. Since different type of flames shows different visualization in the RGB image, the non-luminous and luminous flames can be distinguished from each other based on the proper thresholding by R channel. The qualitative result expresses the non-luminous, as the predominant flames in the early stage of combustion in E85 and E100, is governed by a blue color, or revealed a gray-smooth texture in the shadowgraph image. Also, the soot formation (luminous flame) occurs earlier for E0 than E85 and E100, probably as a result of the ethanol content with oxygen preventing the soot precursor formation at the initial flame formation.

3. In order to quantitatively analyze the OH* chemiluminescence, the effect of natural luminosity on the OH* signal is examined. The result shows that there is no significant impact of natural

luminosity on the OH* emission for ethanol-gasoline blends, because of those soot incandescence much lower than that in diesel combustion.

4. The analysis of integrated OH* intensity suggests that the favorable heat release for E0 occurs when the fuel is ignited at the end of injection (EOI). In contrast to this, with the increase of ethanol ratio, the improved combustion behavior is achieved at the advanced spark. In addition, E0 has a higher OH* intensity than those fuels mixed with ethanol due to the local rich region. Compared with the E100, the stratified vapor distribution of different components in E85 spray has a potential impact on its combustion characteristics, owing to the lower enthalpy of vaporization for gasoline than that for ethanol. When the propagating flame encounters the dense gasoline vapor at the downstream of E85 spray, the flame has the potential to burn faster, and hence induces a higher combustion intensity than E100.

5. Based on the OH* chemiluminescense, the characteristics of flame growth is possible to be analyzed. Smaller flame radius of E85 and E100 than E0 is found, probably as a result of the relatively local rich mixture for E0 and the limitation of flame propagation by the higher enthalpy of vaporization for E85 and E100. Furthermore, in the case of ethanol-gasoline blends, the ignition before EOI could provide a sustainable flame development with a regular shape of flame radius. Moreover, adding ethanol into gasoline is able to greatly decrease the ignition delay (defined by the start of ignition to the steady development of flame) at advanced ignition, indicating that the improvement of flame propagation. Also, the combustion stability is found to be extended with the increase of ethanol ratio. Meanwhile, the shorten combustion duration and lower soot formation also is observed when the ethanol is introduced into the gasoline, due to the increase of oxygen content.

6. In according to the analysis results from flame development and combustion characteristics, both the stable ignition and favorable combustion performance are able to be realized if using the advanced ignition strategy at the middle to downstream of spray (about 230-300 times the nozzle orifice diameter). This condition also is corresponded to the situation that the ignition happens at the head of penetrating spray under the acceptable spray-spark interaction.

CHAPTER 7 CONCLUSTIONS

This study is lain emphasis on the clarification of mixture formation, ignition and combustion characteristics by using ethanol-gasoline blends spray injected by a hole-type nozzle in a quiescent constant volume vessel with high temperature and pressure. The comparison of gasoline and fuels with different ethanol blending ratios were taken in terms of the difference of spray mixture formation and ignition and combustion process. The typical thermodynamic environment of direct-injection spark ignition (DISI) engine at near top dead center (TDC) conditions with the ambient temperature of 500K and backpressure of 1.0MPa, was used in the experiment. A valve-covered-orifice (VCO) nozzle with a hole diameter 0.15mm, was mainly pressurized up to 20MPa in this study to investigate the mixing process and combustion characteristics. Three typical ethanol-gasoline blends, E0 (100% gasoline), E85 (85% ethanol and 15% gasoline) and E100 (100% ethanol) were clarified in this study. Various optical methods, including Mie scattering and laser absorption scattering (LAS) technique were employed to investigate the spray evolution and quantitatively measure the mixture formation of ethanol-gasoline blends under free spray and impinging spray conditions. Meanwhile, the combustion feathers, such as ignition process, flame development and soot emission, were characterized by using the shadowgraph, OH* chemiluminescence and direct imaging on natural luminosity. The general findings in this research are summarized in this chapter as follows.

7.1 Spray Evolution of Ethanol-Gasoline Blend (E85)

In order to clarify the development of E85 spray in DISI engine, the characteristics of the spray evolution was measured by Mie scattering under various conditions, consisting of injection pressure (4~20MPa), ambient gas density (2~10kg/m^3) and ambient temperature (300~500K) that simulates the typical DISI-like environment. Several characteristics of spray in liquid phase, such as spray tip penetration, spray angle and spray volume were quantitatively analysis by the proper binarized images.

Both injection pressure and ambient gas density were considered as the primary factors to control the liquid spray tip penetration S_L. In detail, it has a more sustainable propagation with increasing injection pressure because of high momentum. While the increased ambient gas density would cause an opposite effect on the spray tip penetration. However, those trend became weak, or not so much significant under high- injection pressure and surrounding gas density. An interest was found that the liquid spray penetration was not sensitive to the increase of injection pressure (>15MPa) under a given ambient gas density, which allowed the utility of high injection pressure system for E85 spray in DISI engine without worry about the severe impacts of spray-wall interaction and fuel film formation.

The correlations of liquid spray angle θ_L and ambient gas density/injection pressure were also characterized. Several previous studies about diesels conducted by Siebers et al. were used to make the comparison with some findings in this study. For non-evaporating spray, unlike the spray angle of diesel giving a 0.19 power dependence on ambient gas density, the E85 has a unique correlation of spray angle and gas density under different injection pressure: 0.1 for high injection pressure (>10MPa) and 0.15 for low injection pressure (<5MPa) power dependence on gas density respectively. In the case of vaporizing condition, the spray angle was reduced with increasing ambient temperature (i.e., maximum reduction in 20% under low ambient gas density condition). This trend, however, became so unobvious that can be neglected under high surrounding gas density. For both non-vaporizing and vaporizing spray of E85, the common was found that the spray angle had a stronger dependence on the ambient gas density under low injection pressure less than 5MPa. However, this tendency became weaker under injection pressure over 10MPa.

For the spray volume of liquid phase, it was greatly dominated by injection pressure and ambient temperature, and in detail, it had a growth with the increase of injection pressure (i.e., expansion at least 3.6 times under the injection pressure from 4MPa to 20MPa) and opposite effect by the increasing ambient gas density. On the other hand, the effect of ambient temperature on spray volume was negligible at the early stage of injection due to the presence of liquid ligament or large droplets. Furthermore, the quantitative analysis of spray volume showed that it is potential to improve evaporation of E85 spray under high injection pressure with elevated ambient temperature and gas density.

To improve the utility of Hiroyasu-Arai empirical equation in the prediction of E85 spray under DISI-like conditions, an impact index of ambient gas factor was introduced to correct the effect of ambient gas density on the spray tip penetration at the early stage of injection. The new empirical equations of spray tip penetration length at primary injection period ($t < t_{break}$) and breakup time were proposed. The result showed that the corrected equation had a good agreement to the experimental data and was useful to improve the predict model in numerical simulation.

7.2 Mixture Formation of Ethanol-Gasoline Blends

The mixture formations of ethanol-gasoline blends under free and impinging spray were measured by a dual-wavelength ultraviolet-visible laser absorption scattering (LAS). The ambient temperature of 500K and pressure of 1.0MPa were chosen as the conditions to create a similarly typical environment at near TDC in DISI engine. The ethanol-gasoline blends, E0, E85 and E100 were able to be quantitatively measured by using the surrogate fuels in LAS technique. The vapor distribution of gasoline was determined by toluene,

which had similar physical properties to gasoline and high absorption for ultraviolet. Likewise, the vapor behavior of ethanol was determined by methyl ethyl ketone (MEK). On the other hand, a standard wall temperature of 298K and ultra-low temperature of 273K were used to study the spray mixture formation of spray-wall interaction for ethanol-gasoline blends under cold start condition, in order to clarify the effect of wall temperature and vapor behavior on the utility of E85 in DISI engine.

For free spray, the liquid phase penetration had no significant difference for different mixing ratio of ethanol in gasoline. However, the vapor penetration length became longer with the increase of ethanol blending ratio, as a result of the ethanol content reducing the boiling point. Under the high temperature condition, E100 (represented by MEK100 in LAS), due to its low boiling point, showed a faster evaporation than the E0 (represented by toluene in LAS). In the case of E85 spray, based on the results from the liquid and vapor phase distribution, it could be deducted that the low boiling point (LBP) components in gasoline would evaporate similar to ethanol, and distributed homogeneously along the spray axis. While the high boiling point (HBP) components in gasoline mainly located from the middle to downstream of the spray due to its evaporation blocked by the LBP components at early stage of injection. Therefore, a dense gasoline vapor would form at those regions, especially at the spray tip after EOI. In addition, the radial distribution of vapor phase indicated the vapor of LBP components would totally cover that of HBP components inside the spray, which implied that a high concentration of ethanol vapor presented at the peripheral region of spray in comparison to gasoline in the mixture formation of E85 spray. On the other hand, although the ethanol and gasoline mixed in the ratio of 85:15, a distinctly different evolution of vapor mass demonstrated that the ethanol took up a larger portion of total vapor mass (87%) than mixing ratio (85%) before EOI due to its fast evaporation, yet decreased after EOI (84%) as a result of the enhanced evaporation of gasoline. According to the results mentioned above, a typical stratified mixture distribution would form in E85 spray.

In the case of impinging spray, the increased impinge distance is able to reduce the effect of spray-wall interaction and the liquid fuel film formation on the wall, mainly due to some portion of liquid droplets evaporating before impingement. Because of the poor evaporation, a flat shape of vapor after impingement was induced by a shorter impinge distance in terms of momentum losses. While for the long-distance impinging spray, lots of fuel vapor primary took up the peripheral region of spray, hence generated a cone-shape fuel vapor. Furthermore, E100 had a faster evaporation after impingement than E0. In the case of E85, the spray/wall interaction had an effect on the evaporation process of LBP component that became more vigorous, compared to no significant difference on the HBP component. On the other hand, the ultra-low wall temperature would lower the temperature field between the wall and nozzle tip, as a result, reduced the evaporation speed of fuel locating in this region. Therefore, a denser liquid core remained along the

spray axis during the spray/wall interaction. Owing to the reduced head vortex, the spray tip penetration length of the spray impinge at ultra-low wall temperature was slightly shorten.

7.3 Ignition Process of Ethanol-Gasoline Blends

The ignition processes of ethanol-gasoline blends also were investigated under the same ambient conditions with the LAS experiment. In this study, the real gasoline and ethanol were employed and measured by shadowgraph and OH* chemiluminescence. Various conditions, such as ignition position, ignition timing and energy, were chosen as the impact factors to investigate their effects on the ignition robustness of ethanol-gasoline blends. Three typical location of spray, defined as upstream, middle and downstream of spray, were selected as ignition locations in this study. Different injection duration for E0, E85 and E100 were set respectively in order to maintain the same calorific value.

According to the shadowgraph imaging, three types of ignition process, namely successful, partial and failure ignition, were defined. The successful ignition showed a consecutive flame development from initial flame kernel to a fully growth flame with a high luminosity. Partial ignition expressed a fact that after the mixture was ignited, the initial flame extinguished within a short time without a widely flame propagation regardless of some dark smoke region could be found in the image. While an absence of initial flame and its downstream development was considered as the failure ignition case. Therefore, the ignition probability could be clarified in this way that whether a visible flame could be observed or not and obtained by 50 times testing at every ignition position and timing. The ignition probability was greatly dependent on the local mixture. In general, the presence of dense liquid phase or leaner mixture tended to result in an unstable ignition for fuels, especially in the region closed to the spray axis or peripheral region of spray. With respect to the map of ignition probability, it indicated that the stable combustion window was improved with the increase of ethanol ratio in gasoline, in particular the advanced ignition because of the faster evaporation and mixing of ethanol. However, the local mixture dilution of ethanol addition also enabled to decrease the ignition robustness at the upstream or late ignition for E85 and E100.

The effect of spark energy on the ignition process and flame propagation were investigated by OH* chemiluminescence. Lower spark energy blocked the initial flame growth, hence reduce the flame velocity at the early stage of combustion. This effect generally would lead to a 0.2ms delay for the flame development, as well as resulted in a lower combustion intensity and poor flame behavior than high spark energy. It should be mentioned that ethanol addition increased the sensibility of flame development on the spark energy, because of ethanol content reducing the heating value and leading itself difficulty to be burnt.

176

While the flame velocity at the steady development period, and the combustion duration did not affected by the spark energy so much.

7.4 Flame Development and Combustion Characteristics of Ethanol-Gasoline Blends

The flame development and combustion characteristics of ethanol-gasoline blends were investigated under the same ambient conditions with LAS and ignition experiments. The similar near TDC condition was used to examine the combustion performance of ethanol-gasoline blends (E0, E85 and E100). By means of shadowgraph, high-speed imaging of OH* chemiluminescence and natural luminosity, the characteristics of flame and combustion evolution was able to be quantitatively analysis. Also, the corresponded mixture formation under the same experimental condition was measured by LAS to make the clearly interpretation about the effect of spray evaporation on the combustion. Longer injection masses were corrected for E85 and E100 which was similar to the last section.

The result showed that the flame development and evolution were greatly determined by the local mixture formation. The flame tended to propagate towards downstream of the ignition position instead of in the upstream direction as a consequence of the upstream diluted mixture and locally high flow velocity which was greater than the flame growth speed. In addition, the decreased local fuel vapor caused an incomplete combustion with a pronounced long-narrow flame shape as the fuel was ignited at upstream/early timing and downstream/late timing. Moreover, the flame front was sensitive to the local mixing and prone to direct to the regions where the local mixture became denser.

By means of the high-speed imaging of shadowgraph and natural luminosity, the flame visualization was characterized. A distinct brilliant luminosity was found in E0 burning. While the E85 and E100 demonstrated a moderate luminosity or nearly transparent appearance of flame. Since the color in RGB image was found to correspond the different type of flames, the non-luminous and luminous flame were able to be differential from each other based on the proper chosen threshold in R channel. Different types of flame during the combustion revealed the fact that the non-luminous flame was the dominant flame in the early stage of combustion for E85 and E100, which was mainly expressed as a blue color in natural luminosity imaging or a gray-smooth texture in shadowgraph. The luminous flame (represents soot incandescence) occurred earlier for E0 than E85 and E100, probably resulted from the oxygen content in ethanol.

The less significant effect of natural luminosity on OH* signal was proven in this study. E0 showed a higher intensity of OH* emission than E85 and E100. On the other hand, the favorable combustion was found for E0 when the fuel was ignited at the end of injection (EOI). In contrast, with the increase of ethanol ratio, the improved combustion behavior is achieved at the advanced spark. One should be noticed that compared with E100, the stratified vapor distribution of different components in E85 spray had a potential impact on its combustion characteristics, owing to the lower enthalpy of vaporization for gasoline than that for ethanol. The flame would burn faster when it encountered the dense gasoline vapor at downstream of E85 spray, thus induced a higher combustion intensity than E100.

E0 had a larger flame radius than other fuels due to the locally rich mixture and a potential limitation of flame propagation by the higher enthalpy of vaporization with ethanol addition. For E85 and E100, the early ignition (before EOI) could provide a sustainable flame development with a regular shape of flame radius. In addition, the ignition delay under advanced ignition was decreased by increasing ethanol ratio, which indicated the improvement of subsequent flame development. The combustion stability was extended with the aid of ethanol content in E85 and E100, compared with E0. Meanwhile, due to the oxygen content, a shorten combustion duration and reduced soot formation also were observed by adding ethanol.

A further discussion of using E85 in DISI engine was conducted and compared with other previous studies. The result showed that the optimal ignition strategies proposed by this study (advanced timing and middle to downstream ignition) was able to achieve the favorable combustion performance. This condition also was relative to the situation that the ignition happened at the head of penetrating spray under an acceptable spray-spark interaction.

7.5 Recommendations for Future Works

To clarify the spray mixture formation, ignition and combustion process of ethanol-gasoline blends are being played attention by automobile industry, aiming to meet the strict legislated emission level and improve the fuel economy. Further works should be focused on several aspects as shown following.

First, the precision of measurement of the mixture formation by LAS technique needs to be improved, especially the verification of the used surrogate fuels and the liquid phase concentration of impinging spray. Utility of another test fuels with more similar physical properties to the gasoline and ethanol would enhance the measurement precision. The stratified vapor distribution and dense region of gasoline at downstream of spray should be more carefully examined because the error during the laser shoting or spray fluctuation may somewhat lead to the different result.

Secondary, the ignition probability is needed to be clarified by a commercial spark plug, in order to simulate the practical operation in SI engine and offer the more stable ignition energy for the ignition process. The spray-spark interaction with different ethanol-gasoline blends should be verified in further because the spray with high momentum would lead to a stretch or distortion on the spark discharge that has a great impact on the initial flame formation. Moreover, other advanced ignition strategies, such as new ignition system (laser ignition) or advanced ignition prior to injection, are needed to be clarified.

On the other hand, in consideration of the turbulent effect on the combustion in real DISI engine, it is recommended to study the spray evaporation and combustion characteristics using ethanol-gasoline blends in the production optical SG-DISI engine. Also, since the local mixing process and heat release rate play a significant role on the evaluation of flame development and combustion performance, some radical emissions, such as OH* , CH* or HCO et al., should be considered as an effective way to measure the in-flame equivalence ratio and heat release rate. Also, the proper numerical models for ethanol-gasoline blends should be developed to more effectively predict their spray or combustion behaviors in engines.

REFERENCE

[1]Drake, M.C., Haworth, D.C. Advanced gasoline engine development using optical diagnostics and numerical modeling. *Proc Combust Inst* 2007; 31: 99–124.

[2] Heywood J.B. *Internal Combustion Engine Fundamentals*, McGraw-Hill, NY, 1988.

[3] Maly, R.R. State of the art and future needs in S.I. engine combustion. *Proc. Combust. Inst.* 25 (1994) 111–124.

[4] Zhao, F., Lai, M-C., Harrington, D.L. Automotive spark-ignited direct-injection gasoline engines. *Prog Energy Combust Sci* 1999; 25: 437–562.

[5] Preussner, C., Kampmann, S. Gasoline direct injection, a new challenge for future gasoline control systems – part 2: injector and mixture formation. *MTZ* 1997;58.

[6] Iwamoto, Y., Noma, K., Nakayama, O., Yamauchi, T., Ando, H. Development of direct injection gasoline engine. SAE Paper 970540, 1997.

[7] Tomoda, T., Sasaki, S., Sawada, D. Development of direct injection gasoline engine-study of stratified mixture formation. SAE Paper 970539, 1997.

[8] Tagaki, Y., Itoh, T., Muranaka, S., Iiyama, A., Iwakiri, Y., Urushihara, Y., Naitoh, K. Simultaneous attainment of low fuel consumption, high output power and low exhaust emissions in direct injection SI engines. SAE Paper 980149, 1998.

[9] Hentschel, W., Block, B., Hovestadt, T., Meyer, H., Ohmstede, G., Richter, V., Stiebels, B., Winkler, A. Optical diagnostics and CFD simulations to support the combustion process development of the Volkswagen FSI direct-injection gasoline engine. SAE Paper 2001-01-3648, 2001.

[10] Herrenschmidt, T., Souhaite, P. "New PSA HPI 2 liter gasoline direct injection engine". 9 Aachner Kolloquium, 2000.

[11] Han, Z., Yi, J., Trigui, N. Stratified mixture formation and piston surface wetting in a DISI engine. SAE Paper 2002-01-2655, 2002.

[12] Stevens, E., Steeper, R. Piston wetting in an optical DISI engine: fuel films, pool fires, and soot generation. SAE Paper 2001-01-1203, 2001.

[13] Drack, M.C., Fansler, T.D., Solomon, A.S., Szekely, G.A. Piston fuel films as a source of smoke and hydrocarbon emissions from a wall-controlled spark-ignited direct-injection engine. SAE Paper 2003-01-0547, 2003.

[14] Eichlseder, H., Baumann, E., Muller, P., Neugebauer, S. Potential and risks of gasoline direct injection engines for passenger cardrivelines. *MTZ worldwide*, 2000; 61:2–5.

[15] Katashiba, H., Honda, T., Kawamoto, M., Sumida, M., Fukutomi, N., Kawajiri, K. Improvement of center injection spray guided DISI performance. SAE Paper 2006-01-1001; 2006.

[16] Koch, T., Schanzlin, K., Boulouchos, K. Characterization and phenomenological modeling of mixture formation and combustion in a direct injection spark ignition engine. SAE Paper 2002-01-1138, 2002.

[17] Schanzlin, K., Koch, T., Tzannis, A.P., Boulouchos, K. Characterization of mixture formation in a direct injected spark ignition engine. SAE Paper 2001-01-1909, 2001.

[**18] Van Der Wege, B.A., Han, Z., Iyer, C.O. Munoz, R.H., Yi, J.** Development and analysis of a spray-guided DISI combustion system concept. SAE Paper 2003-01-3105, 2003.

[19] Iyer, C.O., Han, Z., Yi, J. CFD modeling of a vortex induced stratification combustion (VISC) system. SAE Paper 2004-01-0550, 2004.

[20] Szekely, G.A., Alkidas, A. Combustion characteristics of a spray-guided direct-injection stratified-charge engine with a high-squish piston. SAE Paper 2005-01-1937, 2005.

[21] Marchi, A., Nouri, J.M., Yan, Y., Arcoumanis, C. Internal flow and spray characteristics of pintle-type outwards opening piezo injectors for gasoline direct-injection engines. SAE Paper 2007-01-1406, 2007.

[22] Schwarz, C., Schunemann, E., Durst, B., Fischer, J., Witt, A. Potentials of the spray-guided DI combustion system. SAE Paper 2006-01-1265, 2006.

[23] Sick, V., Drake, M.C., Fansler, T.D. High-speed imaging for direct-injection gasoline engine research and development. *Exp Fluids* 2010; 49: 937–947.

[24] Nishida, K., Tian, J.P., Sumoto, Y., Long, W.Q., Sato, K., Yamakawa, M. An experimental and numerical study on sprays injected from two-hole nozzles for DISI engines. *Fuel* 2009; 88: 1634–1642.

[25] Smith, J.D., Sick, V. Factors influencing spark behavior in a spray-guided direct-injected engine. SAE paper 2006-01-3376, 2006.

[26] Kawamura, K., Saito, A., Kanda, M., Kashiwagura, T., Yamamoto, Y. Spray characteristics of slit nozzle for DI gasoline engines. JSME 2003; 46:10-16.

[**27] Hayakawa, M., Takada, S., Yonesige, K., Nagaoka, M., Takeda, K.** Fuel spray simulation of slit nozzle injector for direct-injection gasoline engine. SAE Paper 2002-01-1135.

[28] DeCorso, S.M., Kemeny, G.A. Effect of ambient and fuel pressure on nozzle spray angle. *Trans. of ASME*, 1957; 79-3: 607-615.

[29] Saito, A., Ohsawa, K., Kawamura, K., Shirakawa, S., Tanasawa, Y. Spray characteristics of swirl nozzle used for diesel engines. *International Conference on Liquid Atomization and Spray Systems*, London, 1985; 1-11.

[30] Nouri, J.M., Hamid, M.A., Yan, Y., Arcoumanis, C. Spray characterization of a piezo pintle-type injector for gasoline direct injection engines. *Proceedings of Third International Conference on Optical and Laser Diagnostics (ICOLAD 2007)*, London, 2007.

[31] Skogsberg, M., Dahlander, P., Denbratt, I. Spray shape and atomization quality of an outward-opening piezo gasoline DI injector. SAE Paper 2007-01-1409, 2007.

[32] Skogsberg, M. A Study on Spray-guided stratified charge systems for gasoline DI engines, PhD Thesis, Chalmers University of Technology, Gothenburg, Sweden, 2007.

[33] Marchi, A., Nouri, J., Yan, Y., Arcoumanis, C. Spray stability of outwards opening pintle injectors for stratified direct injection spark ignition engine operation. *Int. J. Engine Res.* 2010;11: 413-437.

[34] Mitroglou. N., Nouri, J.M., Yan, Y., Gavaises, M., Arcoumanis, C. Spray structure generated by multi-hole injectors for gasoline direct-injection engines. SAE Paper 2007-01-1417, 2007.

[35] Ortmann R, Arndt S, Raimann J, Grzeszik R, Würfel G. Methods and analysis of fuel injection, mixture preparation and charge stratification in different direct injected SI engines. SAE Paper 2001-01-0970, 2001.

[36] Mitroglou, N., Nouri, J.M., Gavaises, M., and Arcoumanis, C. Spray characteristics of a multi-hole injector for direct-injection gasoline engines. *Int. J. Engine Res*. 2006; 7: 255-270.

[37] Stach, T., Schlerfer, J., Vorbach, M. New generation multi-hole fuel injector for direct-injection SI engines-optimization of spray characteristics by means of adapted injector layout and multiple injection. SAE Paper 2007-01-1404.

[38] Dahlander, P., Lindgren, R. Multi-hole injectors for DISI engines: nozzle hole configuration influence on spray formation. SAE Paper 2008-01-0136.

[39] Skogsberg, M., Dahlander, P., Lindgren, R., Denbratt, I. Effects of injector parameters on mixture formation for multi-hole nozzles in a spray-guided gasoline DI engine. SAE Paper 2005-01-0097.

[40] Alperstein. M., Schafer, G.H., Villforth, III. FJ. Texaco's stratified charge engine- multi fuel, efficient, clean, and practical. SAE Paper 740563, 1974.

[41] Scussei. A.J., Simko, A.O., Wade, W.R. The Ford PROCO engine update. SAE Paper780699, 1978.

[42] Smith, J., Szekely Jr, G., Solomon, A., and Parrish, S. A comparison of spray-guided stratified-charge combustion performance with outwardly-opening piezo and multi-hole solenoid injectors. SAE paper 2011-01-1217.

[43] International Energy Agency (IEA), World Energy Outlook 2010, http://www.worldenergyoutlook.org/publications/weo-2010.

[44] American Petroleum Institute. Alcohols and ethers: a technical assessment of their application as fuels and fuel components, 3rd, API Publication 4261, 2001.

[45] Zhao, H. Advanced direct injection combustion engine technologies and development. Gasoline and gas engines. Vol. Woodhead Publication, 2010.

[46] Kim, S., Dale, B.E. Environmental aspects of ethanol derived from no-tilled corn grain: nonrenewable energy consumption and greenhouse gas. *Biomass Bioenergy* 2005; 28: 475-489.

[47] Rossilo-Calle, F., Corte L.A.B. Towards pro-alcohol II-a review of the Brazilian bio-ethanol program. *Biomass Bioenergy* 1998; 14(2): 115-124.

[48] Varde, K., Jones, A., Knutsen, A., Mertz, D., Yu, P. Exhaust emissions and energy release rates from a controlled spark ignition engine using ethanol blends. *Proc IMechE Part D: J Autom Eng* 2007; 221(8): 933-941.

[49] Al-Farayedhi, A.A., Al-Dawood, A.M., Gandhidasan, P. Effects of blending crude ethanol with unleaded gasoline on exhaust emissions of SI engine. SAE paper 2000-01-2857.

[50] Wallner, T., Miers, S.A. Combustion behavior of gasoline and gasoline/ethanol blends in a modern direct-injection 4-cylinder engine. SAE Paper 2008-01-0077, 2008.

[51] Brinkman, N., Halsall, R., Jorgensen, S.W., Kirwan, J.E. The development of improved fuel specifications for methanol (M85) and ethanol (E85). SAE Paper 940764, 1994.

[52] **Farrell, J.T., Johnston, R.J., Androulakis, I.P.** Molecular structure effects on laminar burning velocities at elevated temperature and pressure. SAE Paper 2004-01-2936, 2004.

[53] **Aleiferis, P.G., Van Romunde, Z.R.** An analysis of spray development with iso-octane, n-pentane, gasoline, ethanol and n-butanol from a multi-hole injector under hot fuel conditions. *Fuel* 2013; 105: 143-168.

[54] **Serras-Perelra, J., Aleiferis, P.G., Richardson, D., Wallace, S.** Characteristics of ethanol, butanol, iso-octane and gasoline spray and combustion from a multi-hole injector in a DISI engine. SAE Paper 2008-01-1591, 2008.

[55] **Aleiferis, P.G., Serras-Pereira, J., Van Romunde, Z., Caine, J., Wirth, M.** Mechanisms of spray formation and combustion from a multi-hole injector with E85 and gasoline. *Combust Flame* 2010; 157: 735-756.

[56] **Aleiferis, P.G., Serras-Pereira, J., Augoye, A., Davies, T.J., Cracknell, R.F., Richardson, D.** Effect of fuel temperature on in-nozzle cavitation and spray formation of liquid hydrocarbons and alcohols from a real-size optical injector for direct-injection spark-ignition engines. *Int. J. Heat Mass Transfer* 2010; 53: 4588-4606.

[57] **Oh, H., Bae, C., Min, K.** Spray and combustion characteristics of ethanol blended gasoline in a spray guided DISI engine under lean stratified operation. SAE Paper 2010-01-2352, 2010.

[58] **Park, S.H., Kim, H.J., Suh, H.K., Lee, C.S.** Atomization and spray characteristics of bioethanol and bioethanol blended gasoline fuel injected through a direct injection gasoline injector. *Int. J. Heat Mass Transfer* 2009; 30: 1183-1192.

[59] **Gao, J., Jiang, D., Huang, Z.** Spray properties of alternative fuels: A comparative analysis of ethanol-gasoline blends and gasoline. *Combust Flame* 2007; 86: 1645-1650.

[60] **Chen, L., Braisher, M., Crossley, A., Stone, R., Richardson, D.** The influence of ethanol blends on particulate matter emissions from gasoline direct injection engines. SAE Paper 2010-01-0793.

[61] **Chen, L., Richard, S., Richardson, D.** A study of mixture preparation and PM emissions using a direct injection engine fuelled with stoichiometric gasoline/ethanol blends. *Fuel* 2012; 96: 120-130.

[62] **Turner, D., Xu, H., F. Cracknell, R., Nararajan, V., Chen, X.** Combustion performance of bio-ethanol at various blend ratio in a gasoline direct injection engine. *Fuel* 2011; 90: 1999-2006.

[63] **Al-Farayedhi, A.A., Al-Dawood, A.M., Gandhidasan, P.** Effects of blending crude ethanol with unleaded gasoline on exhaust emissions of SI engine. SAE Paper 2000-01-2857, 2000.

[64] **Krämer, H., Einecke, S., Schulz, C., Sick, V., Nattrass, S.R., Kitching, J.S.** Simultaneous mapping of the distribution of different Fuel volatility classes using tracer-LIF tomography in an IC engine. SAE Paper 982467, 1998.

[65] **Zhang, R., Sick, V.** Multi-component fuel imaging in a spray-guided spark-ignition direct-injection engine", JSAE Paper 20077146, 2007.

[66] **Andersson, M., Wärnberg, J., Hemdal, S., Dahlander, P., Denbratt, I.** Evaporation of gasoline-like and ethanol-based fuels in hollow-cone sprays investigated by planar laser-induced fluorescence and Mie scattering. SAE Paper 2011-01-1889.

[67] **Andersson, M., Wärnberg, J.** Application of laser-induced fluorescence for imaging sprays of model fuels emulating gasoline and gasoline/ethanol blends. *Proceeding of 11*[th] *International Congress Liquid Atomization and Spray Systems,* Paper ID ICLASS2009-189, 2009.

[68] **Sementa, P., Vagieco, B.M., Catapano, F.** Thermodynamic and optical characteristics of a high performance GDI engine operating in homogeneous and stratified charge mixture conditions fueled with gasoline and bio-ethanol. *Fuel* 2012; 96: 204-219.

[69] **Catapano, F., Sementa, P., Vagieco, B.M.** Optical characterization of bio-ethanol injection and combustion in a small DISI engine for two wheels vehicles. *Fuel* 2013; 106: 651-666.

[70] **Baumgarten, C.** Mixture formation in internal combustion engines. Berlin Heidelberg, Germany, Publisher: Springer, 2006.

[71] **Wu, P.K., Faeth, G.M.** Onset and end of drop formation along the surface of turbulent liquid jets in still gases. *Phys. of fluids* 1995; 7(11): 2915-2917.

[72] **Arai, M., Shimizu, M., Hiroyasu, H.** Similarity between the breakup lengths of a high speed liquid jet in atmospheric and pressurized conditions. Los Alamos National Laboratory.

[73] **Hiroyasu, H., Shimizu, M., Arai, M.** Breakup length of a liquid jet and internal flow in a nozzle. *Proc. ICLASS-91*, 275-282.

[74] **Soterious, C., Andrews, R., Smith, M.** Direct injection diesel sprays and the effect of cavitation and hydraulic flip on atomization. SAE Paper 950080, 1995.

[75] **Nurick, W.H.** Orifice cavitation and its effects on spray mixing. *ASME J. Fluids Eng.* 1976; 681-687.

[76] Reitz, R.D., Bracco, F.V. Mechanisms of breakup of round liquid jets. *Enzyclopedia of Fluid Mechanics*, Gulf Publishing, Houston, Texas 3: 233–249.

[77] Hiroyasu, H., Arai, M. Structure of fuel sprays in diesel engines. SAE Paper 900475, 1990.

[78] Wakuri, Y., Fujii, M., Amitani, T., Rsuneya, R. Studies on the penetration of fuel spray of diesel engine (in Japanese). *Trans. JSME* 1957, 25: 820-826.

[79] Naber, J.D., Siebers, D.L. Effects of gas density and vaporization on penetration and dispersion of diesel sprays. *SAE Trans* 1996; 105(3): 82-111.

[80] Siebers, D.L. Recent development on diesel fuel jest under quiescent conditions. In: Arcoumanis, C., and Kaminoto, T., Editors. *Flow and Combustion in Reciprocating Engines*. Berlin Heidelberg, Springer-Verlag.

[81] Zhao, F.F., Harrington, D.L., Lai, M.C. Automotive gasoline direct-injection engines. SAE 2002.

[82] Zhao, F., Yoo, J.H., Lai, M.C. In-cylinder spray/wall interactions of a gasoline direct-injection engine. *Proceedings of ILASS-America*, 1997.

[83] Dodge, L.G. Fuel preparation requirements for direct-injected spark ignition engines. *Proceedings of ILASS-America*, 120–124, 1996.

[84] Dodge, L.G. Fuel preparation requirements for direct-injected spark ignition engines. SAE Paper, No. 962015, 1996.

[85] Tomoda, T., Sasaki, S., Sawada, D., Saito, A., Sami, H. Development of direct injection gasoline engine—study of stratified mixture formation. SAE Paper 970539, 1997.

[86] Hochgreb, S., VanDer Wege, B. The effect of fuel volatility on early spray development from high pressure swirl injectors. In Direkteinspritzung im Ottomotor, Editor: Spicher U, Expert-Verlag, Rennigen-Malmsheim, 1998.

[87] Hochgreb, S., VanDer Wege, B. Investigation of the effect of fuel volatility on operating conditions on DISI sprays. In Direkteinspritzung im Ottomotor II, Editor: Spicher U, Expert-Verlag, Rennigen-Malmsheim, 1999.

[88] Lai, M.C., Yoo, J.H., Kim, S.K. High pressure gasoline spray structure and its implications to in-cylinder mixture formation. Tagung Direkteinspritzung im Ottomotor, Haus der Technik, Essen, Germany, 1997.

[89] Preussner, C., Döring, C., Fehler, S., Kampmann, S. GDI: Interaction between mixture preparation, combustion system and injector performance. SAE paper 980498, 1998.

[90] Lefebvre, A.H. Atomization and Sprays. Hemisphere Publishing Corporation, New York, Washington, Philadelphia, London, 1989.

[91] Gindele, J. Untersuchung zur ladungsbewegung und gemischbildung im ottomotor mit direkteinspritzung (in German). Ph.D. Thesis, University of Karlsruhe, Germany, Logos-Verlag, Berlin, ISBN 3-89722-727-4, 2001.

[92] Homburg, A. Optische untersuchungen zur strahlausbreitung und gemischbildung beim DI-Benzin-Brennverfahren (in German). Ph.D. Thesis, University of Braunschweig, Germany, 2002.

[93] Rotondi, R., Bella, G. Gasoline direct injection spray simulation. *Int. J. Therm. Sci.* 2006; 45: 168-179.

[94] Han, Z., Parrish, S., Farrel, P.V., Reitz, R.D. Modeling atomization processes of pressure swirl hollow-cone fuel sprays. *Atomization Sprays* 1997; 7: 663–684.

[95] Allocca, L., Bella, G., De Vita, A., Di Angelo, L. Experimental validation of a GDI spray model. SAE Paper 2002-01-1137, 2002.

[96] Nagaoka, M., Kawamura, K. A deforming droplet model for fuel spray in direct-injection gasoline engines. SAE 2001-01-1225, 2001.

[97] Hayakawa, M., Takada, S., Yonesige, K., Nagaoka, M., Takeda, K. Fuel spray simulation of a slit nozzle injector for direct-injection gasoline engine. SAE 2002-01-1135, 2002.

[98] Das S., Vanbrocklin, P.G. Effect of design and operating parameters on the spray characteristics of an outward opening injector. Proceeding of 13th International Multidimensional Engine Modeling User's Group Meeting. March 2, Detroit, 2003.

[99] Xu, M., Markle, L. CFD-Aided development of spray for an outwardly opening direct injection gasoline injector. SAE Paper 980493, 1998.

[99] Lippert, A., Reitz, R. Modeling of multicomponent fuels using continuous distributions with application to droplet evaporation and sprays. SAE Paper 972882, 1997.

[100] Senda, J., Fujimoto, H., Kobayashi, M., Enomoto, Y. Heat transfer characteristics of a diesel spray impinging on a wall. Bulletin of the M.E.S.J. 1995; 23(2): 67-76.

[101] Senda, J., Kobayashi, M., Iwashita, S., Fujimoto, H. Modeling of diesel spray impinging on flat wall. *Int. J. JSME Series B: Fluids and Thermal Engineering* 1996; 39(4): 859-866.

[102] Senda, J., Kanda, T., Al-Roub, M., Farrell, P.V., Fukami, T., Fujimoto, H. Modeling spray impingement considering fuel film formation on the wall. SAE Paper 970047, 1997.

[103] Bai, C.X., Gosman, A.D. Development of methodology for spray impingement simulation. SAE Paper 950283, 1995.

[104] Lindgren, R., Denbratt, I. Modeling gasoline spray-wall interaction-A review of current models. SAE Paper 2000-01-2808, 2000.

[105] Walkins, A.P., Park, K. Assessment and application of a new spray wall impaction model. *Proc. Inst. Mech. Eng. Conf. Comput. Reciprocating Gas Turbines* 1996: 1–10.

[106] Bai, C.X., Rusche, H., Gosman, A.D. Modeling of gasoline spray impingement. *Atomization Spray* 2002; 12:1-27.

[107] Senda, J., Ohnishi, M., Takahashi, T., Fujimoto, H., Utsunomiya, A., Wakatabe, M. Measurement and modeling on wall wetted fuel film profile and mixture preparation in intake port of SI engine. SAE Paper 1999-01-0798, 1999.

[108] Park, J., Xie, X., Im, K.S., Kim, H., Lai, M.C., Yang, J., Han, Z., Anderson, R.W. Characteristics of direct injection gasoline spray wall impingement at elevated temperature conditions. SAE Paper 1999-01-3662.

[109] Habchi, C., Foucart, H., Baritaud, T. Influence of the wall temperature on the mixture preparation in DI gasoline engines. *Oil & Gas Sci. Tech.* 1999; 54(2): 211-222.

[110] Shim, Y.S., Choi, G.M., Kim, D.J. Numerical and experimental study on effect of wall geometry on wall impingement process of hollow-cone fuel spray under various ambient conditions. *Int. J. Multiphase Flow* 2009; 35: 885-895.

[111] Moriyoshi, Y., Uchida, R., Takagi, M., Kubota, M. Numerical and experimental analyses of mixture formation process using a fan-shaped DI gasoline spray: Examinations on effects of crosswind and wall impingement. SAE Paper 2009-01-1502.

[112] Lindgren, R., Denbratt, I. Influence of wall properties on the characteristics of a gasoline spray after wall impingement. SAE Paper 2004-01-1951, 2004.

[113] Serras-Pereira, J., Aleiferis, P.G., Walmsley, H.L., Davies, T.J., Cracknell, R.F. Heat flux characteristics of spray wall impingement with ethanol, butanol, iso-octane, gasoline and E10 fuels. *Int. J. Heat Fluid Flow* 2013; 44: 662-683.

[114] Serras-Pereira, J. Aleiferis, P.G., Richardson, D. Imaging and heat flux measurement of wall impingement sprays of hydrocarbons and alcohols in a direct-injection spark-ignition engine. *Fuel* 2012; 264-297.

[115] Salber, W., Wolters, P., Esch, T., Gelger, J., Dllthey, J. Synergies of variable valve actuation and direction injection. SAE Paper 2002-01-0706.

[116] Alkidas, A.C., El Tahry, S.H. Contributors to the fuel economy advantage of DISI engines over PFI engines. SAE Paper 2003-01-3101, 2003.

[117] Harada, J., Tomita, T., Mizuno, H., Mashiki, Z., Yasushi I. Development of direct injection gasoline engine. SAE Paper 970540, 1997.

[118] Wirth, M., Piock, W.F., Fraidl, G.K., Schoeggl, P., Winklhofer, E. Gasoline DI engines: the complete system approach by interaction of advanced development tools. SAE Paper 980492, 1998.

[119] Fuerhapter, A., Piock, W.F., Fraidl, G.K. CSI – controlled auto ignition –The best solution for the fuel consumption – versus emission tradeoff? SAE Paper 2003-01-0754, 2003.

[120] Frohlich, K., Borgmann, K. Potentials of future fuel consumption technologies. *Proceeding of 24th Internationales Weiner Motoren-symposium* 2003, 220–235.

[121] Wirth, M., Zimmermann, D., Friedfeldt, R., Caine, J., Schamel, A., Storch, A. The next generation of gasoline direct injection: improved fuel economy and optimized system cost. *Proceeding of Advance Engine Design and Performance GPC'03*; 2003, 139–152.

[122] Szekely, G.A., Alkidas, A.C. Combustion characteristics of a spray-guided direct injection stratified-charge engine with high-squish piston. SAE Paper 2005-01-1937, 2005.

[123] Christensen, M., Johansson, B., Einewall, P. Homogeneous charge compression ignition (HCCI) using iso-octne, ethanol and natural gas- A comparison with spark ignition operation. SAE 972874, 1997.

[124] Kulzer, A., Christ, A., Rauscher, M., Sauer, C., Würfel, G., Blank, T. Thermodynamic analysis and benchmark of various gasoline combustion concepts. SAE Paper 2006-01-0231, 2006.

[125] Fuerhapter, A., Unger, E., Piock, W.F., Fraidl, G.K. The new AVL CSI engine-HCCI operation on a multi cylinder gasoline engine. SAE Paper 2004-01-0551, 2004.

[126] **De Zilwa, S., Steeper, R.** Predicting NOx emissions from HCCI engines using LIF imaging. SAE Paper 2006-01-0025.

[127] **Thring, R.H.** Homogeneous-charge compression-ignition (HCCI) engines. SAE Paper 890264, 1983.

[128] **Oakley, A., Zhao, H., Ladommatos, N., Ma, T.** Experimental studies on controlled auto-ignition (CAI) combustion in a 4-stroke multi cylinder gasoline engine. SAE Paper 2001-01-1030, 2001.

[129] **Najt, P.M., Foster, D.E.** Compression ignited homogeneous charge combustion. SAE Paper 830264, 1983.

[130] **Hiraya, K., Haseqawa, K., Urushihara, T., Iiyama, A., Itoh, T.** A study on gasoline fueled compression ignition engine – a trial of operation region expansion. SAE Paper 2002-01-0416, 2002.

[131] **Yang, J., Culp, T., Keney, T.** Development of gasoline engine system using HCCI technology – the concept and test results. SAE Paper 2002-01-2832, 2002.

[132] **Hyvonen, J., Haraldsson, G., Johansson, B.** Operating conditions using spark assisted HCCI combustion during combustion mode transfer to SI in a multi-cylinder VCR-HCCI engine. SAE Paper 2005-01-0109, 2005.

[133] **Bunting, B.G.** Combustion, control, and fuel effects in a spark assisted HCCI engine equipped with variable valve timing. SAE Paper 2006-01-0872, 2006.

[134] **Kalian, N., Standing, R., Zhao, H.** Effects of ignition timing on CAI combustion in a multi-cylinder DI gasoline engine. SAE Paper 2005-01-3720, 2005.

[135] **Stolz, W., Köhler, J., Lawrenz, W., Meier, F., Bloss, W.H., Maly, R.R., Herweg, R., Zahn, M.** Cycle resolved flow field measurement using a PIV movies technology in a SI engine. SAE Paper 922354, 1992.

[136] **Müller, S.H.R., Böhm, B., Gleißneer, M., Grzeszik, R., Arndt, S., Dreizleer, A.** Flow field measurements in an optically accessible, direct-injection spray-guided internal combustion engine using high-speed PIV. *Exp. Fluids* 2010; 48:281-290.

[137] **Fajardo, C., Sick, V.** Flow field assessment in a fired spray-guided spark-ignition direct-injection engine based on UV particle image velocimetry with sub crank angle resolution. *Proc. Combust. Inst.* 2007; 3023-3031.

[138] **Fajardo, C., Sick, V.** Development of a high-speed UV particle image velocimetry techinique and application for measurements in internal combustion engines. *Exp Fluids* 2009; 46: 43-53.

[139] **Fajardo, C., Sick, V.** Kinetic energy and dissipation rate spectra of high- and low- swirl internal combustion engine flows. SAE Paper 2009-01-0651, 2009.

[140] **Fajardo, C.M, Smith, J.D, Sick, V.** PIV, high-speed PLIF and chemiluminescence imaging for near-spark-plug investigations in IC engines. *J Phys Conf Ser* 2006; 45:19–26.

[141] **Fajardo, C.M., Smith, J.D., Sick, V.** Sustained simultaneous high-speed imaging of scalar and velocity fields using a single laser. *Appl Phys B* 2006; 85(1):25–31.

[142] **Hung, D.L.S., Harrington, D.L., Gandhl, A.H., Markle, L.E., Parrish, S.E., Shakal, J.S., Sayar, H., Cummings, S.D., Kramer, J.L.** Gasoline fuel injector spray measurement and characterization-A new SAE J2715 recommended practice. SAE 2008-01-1068, 2008.

[143] **Fansler, T.D., Drake, M.C., Düwel, I., Zimmermann, F.P.** Fuel-spray and spark-plug interactions in a spray-guided direct-injection gasoline engine. Proceeding of 7th international symposium on internal combustion diagnostics 2006, Baden-Baden.

[144] **Smith, J.D., Sick, V.** Real-time imaging of fuel injection, ignition and combustion in a direct-injected spark-ignition engine. *Proceeding of ILASS 2006*, Toronto, Canada.

[145] **Settles, G.S.** Schlieren and Shadowgraph Techniques: Visualizing Phenomena in Transparent Media. Berlin, Spring, 2001.

[146] **Kook, S., Le, M.K., Padala, S., Hawkes, E.** Z-type Schlieren setup and its application to high-speed imaging of gasoline sprays. SAE Paper 2011-01-1981.

[147] **Durão, D.F., Moreira, A.L.N., Panão, M.R.O.** The effect of a cross-flow on secondary atomization in multipoint fuel injection systems. *Proceeding of 13th International Symposium of Application of Laser Techniques to Fluid Mechanics 2006*, Lisbon, Portugal.

[148] **Panão, M.R.O., Moreira, A.L.N., Durão, D.F.** Effect of a cross-flow on spray impingement with port fuel injection systems for HCCI engines. *Fuel* 2013; 106:249-257.

[149] **Moon, S., Nishida, K., Matsumoto, Y.** Gas entrainment characteristics of diesel spray during end of injection. *Atomization Spray* 2009; 19(11): 1013-1029.

[150] **Zhu, J., Nishida, K., Kuti, O.A., Moon, S.** Quantitative analysis of fuel spray-ambient gas interaction by means of LIF-PIV technique. *Atomization Spray* 2011; 21(6): 447-465.

[151] Rottenkolber, G., Gindele, J., Raposo, J., Dullenkopf, K., Hentschel, W., Witting, S., Spicher, U., Merzkirch, W. Spray analysis of a gasoline direct injector by means of two-phase PIV. *Exp. Fluids* 2002; 32: 710-721.

[152] Andresen, P., Meijer, G., Schliter, H., Voges, H., Koch, A., Hentenschel, W., Opperaman, W., Rothe, E. Fluorescence imaging inside an internal combustion engine using tunable excimer laser. *Applied Optics* 1990; 29: 2392-2402.

[153] Meyer, J., Haug, M., Schreiber, M., Unverzagt, S. Controlling combustion in a spark ignition engine by quantitative fuel distribution. SAE Paper 950107.

[154] Smith, J.D., Sick, V. Crank-angle resolved imaging of biacetyl laser-induced fluorescence in an optical internal combustion engine. *Appl Phys B* 2005; 81(5): 579-584.

[155] Smith, J.D., Sick, V. Quantitative, dynamic fuel distribution measurements in combustion-related devices using laser-induced fluorescence imaging of biacetyl in iso-octane. *Proc. Combust. Inst.* 2007; 31: 747-755.

[156] Schulz, C., Sick, V. Tracer-LIF diagnostics: quantitative measurement of fuel concentration, temperature and fuel/air ratio in practical combustion systems. *Prog Energy Combust Sci* 2005; 31: 75-121.

[157] Aldén, M., Bood, J., Li, Zhong, Richter, M. Visualization and understanding of combustion processed using spatially and temporally resolved laser diagnostic techniques. *Proc. Combust. Inst.* 2011; 33: 69-97.

[158] Pterson, B., Sick, V. Simultaneous flow field and fuel concentration imaging at 4.8 kHz in an operating engine. *Appl. Phys.* B 2009; 97: 887-895.

[159] Fajardo, C.M., Smith, J.D., Sick, V. PIV, high-speed PLIF and chemiluminescence imaging for near-spark-plug investigations in IC engines. *J. Phys. Confer. Seri.* 2006: 45:19-26.

[160] Peterson, B., Reuss, D.L., Sick, V. High-speed imaging analysis of misfire in a spray-guided direct injection engine. *Proc. Combust. Inst.* 2011; 33: 3089-3096.

[161] Peterson, B., Sick, V. High-speed flow and fuel imaging study of available spark energy in a spray-guided direct-injection engine and implications on misfires. *Int. J. Engine Res.* 11: 313-329.

[162] Fansler, T.D., Drake, M. "Designer diagnostics" for developing direct-injection gasoline engines. *J. Phys. Conf. Seri.* 2006; 45: 1-17.

[163] **Fansler, T.D., Stojkovic, B., Drake, M.C., Rosalik, M.E.** Local fuel concentration measurements in internal combustion engines using spark-emission spectroscopy. *Appl. Phys. B* 2002; 75: 577-590.

[164] **Dahms, R., Fansler, T.D., Drake, M.C., Kuo, T-W., Lippert, A.M., Peters, N.** Modeling ignition phenomena in spray-guided spark-ignited engines. *Proc. Combust. Inst.* 2009; 32: 2743-2750.

[165] **Dahms, R.N., Drake, M.C., Fansler, T.D., Kuo, T-W., Peters, N.** Understanding ignition processes in spray-guided gasoline engines using high-speed imaging and the extended spark-ignition model SparkCIMM. Part A: Spark channel processes and the turbulent flame front propagation. *Combust. Flame* 2011; 158: 2229-2244.

[166] **Dahms, R.N., Drake, M.C., Fansler, T.D., Kuo, T-W., Peters, N.** Understanding ignition processes in spray-guided gasoline engines using high-speed imaging and the extended spark-ignition model SparkCIMM. Part B: Importance of molecular fuel properties in early flame front propagation. *Combust. Flame* 2011; 158: 2245-2260.

[167] **Melton, L.A., Verdieck, J.F.** Vapor/liquid visualization in fuel sprays. *The 20ᵗʰ Symposium (International) on Combustion* 1985; 20: 1283-1290.

[168] **Leach, B., Zhao, H., Li, Y.F., Ma, T.** Two-phase fuel distribution in an air-assisted DI gasoline engine. *The international symposium on diagnostics and modeling of combustion in internal combustion engines* 2004; 6: 497-504.

[169] **Froba, A., Rabenstein, F., Munch, K., Leipertz, A.** Mixture of triethylamine and benzene as a new seeding material for quantitative two-dimensional laser-induced exciplex fluorescence imaging of vapor and liquid fuel inside SI engine. *Combust. Flame* 1998; 112: 199-209.

[170] **Kramer, H., Munch, K., Leiperts, A.** Investigation of fuel evaporation inside the intake of a SI engine using laser induced exciplex fluorescence with a new seed. SAE Paper 961930, 1996.

[171] **Zhang, G., Xu, M., Zhang, Y., Zeng, W.** Quantitative measurement of liquid and vapor distributions in flash boiling fuel sprays using planar laser induced exciplex technique. SAE Paper 2011-01-1879.

[172] **Desantes, J.M., Pastor, J.V., Pastor, J.M., Juliá, J.E.** Limitation on the use of the planar laser induced exciplex fluorescence technique in diesel sprays. *Fuel* 2005; 84: 2301-2315.

[173] **Charplyve, A.R.** Non-intrusive measurements of vapor concentrations inside sprays. *App. Opt.* 1991; 20: 63-88.

[174] Drallmeier, J.A., Peters, R.E. Experimental investigation of fuel spray vapor phase characterization. *Atomization Spray* 1991; 1:63-88.

[175] Billings, T.P., Drallmeier, J.A. A detailed assessment of the infrared extinction technique for hydrocarbon vapor measurements in a controlled two-phase flow. *Atomization Spray* 1994; 4: 99-121.

[176] Li, T., Yamakawa, M., Nishida, K. Zhang, Y., Hiroyasu, H. Spray and mixture formation processes by high-pressure swirl injector for DISI engine-analyses based on laser absorption scattering (LAS) measurements. *Proceeding of ILASS 2003*, 2003.

[177] Nishida, K., Tian, J., Sumoto, Y., Long, W., Sato, K., Yamakawa, M. An experimental and numerical study on sprays injected from two-hole nozzles for DISI engines. *Fuel* 2009; 88: 1634-1642.

[178] Suh H.K., Park, S.W., Lee, C.S. Effect of piezo-driven injection system on the macroscopic and microscopic atomization characteristics of diesel fuel spray. *Fuel* 2007; 86: 2833-2845.

[179] VanDerWege, B., Hochgreb, S. Effects of fuel volatility and operating conditions on fuel sprays in DISI engines: (2) PDPA investigation. SAE Paper 2000-01-0536.

[180] Wigley, G., Hargrave, G.K., Heath, J. A high power, high resolution LDA/PDA system applied to gasoline direct injection sprays. *Part. Part. Syst. Charact.* 1999; 16: 11-19.

[181] Soid, S.N., Zainal, Z.A. Spray and combustion characterization for internal combustion engines using optical measuring techniques- A review. *Energy* 2011; 36: 724-741.

[182] Zeng, W., Xu, M., Zhang, Y., Wang, Z. Laser sheet dropsizing of evaporating sprays using simultaneous LIEF/MIE techniques. *Proc. Combust. Inst.* 2013; 34: 1677-1685.

[183] Wang, Y., Liu, X., Im, K-S., Lee, W-K., Wang, J., Fezzaa, K., Hung, D.L.S., Winkelman, J.R. Ultrafast X-ray study of dense-liquid-jet flow dynamics using structure-tracking velocimetry. *Nat. Phys.* 2008; 4: 305-309.

[184] Wang, Y., Im, K-S., Fezzaa, K. Similar between the primary and secondary air-assisted liquid jet breakup mechanisms. *Physical Review Letters.* 2008; 100: 154502.

[185] Monn, S., Tsujimura, T. Advanced spray analysis technique using synchrotron X-ray sources. *J. ILASS-Japan.* 2013; 22(77): 180-188.

[186] Oh, H., Bae, C. Effects of the injection timing on spray and combustion characteristics in a spray-guided DISI engine under lean-stratified operation. *Fuel* 2013; 107: 225-235.

[187] Gaydon, A.G. *The Spectroscopy of Flames*, 2nd Ed. Chapman and Hall, London.

[188] Xiong, Y., Roberts, W.L. Investigation of pre-mixed flame-kernel/vortex interactions via high-speed imaging. *Combust. Flame* 2001; 126: 1827-1844.

[189] Stojkovic, B. D., Fansler, T.D., Drake, M.C., Sick, V. High-speed imaging of OH* and soot temperature and concentration in a stratified-charge direct-injection gasoline engine. *Proc. Combust. Inst.* 2005: 30: 2657-2665.

[190] Tinaut. F.V., Melgar, A., Gimenez, B., Reyes, M. Characterization of the combustion of biomass producer gas in a constant volume combustion bomb. *Fuel* 2010; 89: 724-731.

[191] Hardalupas, Y., Orain, M. Local measurements of the time-dependent heat release rate and equivalence ratio using chemiluminescnece emission from a flame. *Combust. Flame* 2004; 139: 188-207.

[192] Tinaut, F.V., Reyes, M., Giménez, B., Pastor, J.V. Measurements of OH* and CH* chemiluminescnece in pre-mixed flames in a constant volume bomb under autoignition conditions. *Energy Fuels* 2011; 25: 119-129.

[193] Aleiferis, P.G., Hardalupas, Y., Taylor, A.M.K.P., Ishii, K., Urata, Y. Flame chemiluminescence studies of cyclic combustion variations and air-to-fuel ratio of the reacting mixture in a lean-burn stratified-charge spark-ignition engine. *Combust. Flame* 2004; 136: 72-90.

[194] Becker, H., Arnold, A., Suntz, R., Monkhouse, P., Wolfrum, J., Maly, R., Prister, W. Investigation of flame structure and burning behavior in an IC engine simulator by 2D-LIF of OH radicals. *Appl. Phys. B* 1990; 50: 473-478.

[195] Kaminski, C.F., Hult, J., Richer, M., Nygren, J., Franke, A., Aldén, M., Lindenmaier, S., Dreizler, A., Maas, U., Williams, R.B. Development of high speed spectroscopic imaging techniques for the time resolved study of spark ignition phenomena. SAE Paper 2000-01-2833.

[196] Müller, S.H.R., Böhm, B., Gleißner, M., Arndt, S., Dreizler, A. Analysis of the temporal flame kernel development in an optically accessible IC engine using high-speed OH-PLIF. *Appl. Phys. B* 2010; 100: 447-452.

[197] Schießl, R., Maas, U., Hoffmann, A., Wolfrum, J., Schulz, C. Method for absolute OH-concentration measurements in premixed flames by LIF and numerical simulation. *Appl. Phys. B*. 2004; 79: 795-766.

[198] Sadanandan, R., Meier, W., Heinze, J. Experimental study of signal trapping of OH laser induced fluorescence and chemiluminescnece in flames. *Appl. Phys. B*. 2012; 106: 717-724.

[199] **Paul, P.H., Najm, H.N.** Planar laser-induced fluorescence imaging of flame heat release rate. *Proc. Combust. Inst.* 1998; 27: 43-50.

[200] **Najm, H.B., Paul, P.H., Muller, C.J., Wyckoff, P.S.** On the adequacy of certain experimental observables as measurements of flame burning rate. *Combust. Flame* 1998; 113: 312-332.

[201] **Najm, H.N., Knio, O.M., Paul, P.H., Wyckoff, P.S.** A study of flame observables in premixed methane-air flames. *Combust. Sci. Technol.* 1998; 140(1-6): 369-403.

[202] **Gordon, R.L., Masri, A.R., Mastorakos, E.** Heat release rate as represented by $[OH] \times [CH_2O]$ and its role in autoignition. *Combust. Sci. Technol.* 2009; 13(4): 645-670.

[203] **Röder, M., Dreier, T., Schulz, C.** Simultaneous measurement of localized heat-release with OH/CH2O-LIF imaging and spatially integrated OH* chemiluminescence in turbulent swirl flames. *Proc. Combust. Inst.* 2013; 34: 3549-3556.

[204] **Matsuti, Y., Kamimoto, K., Matsuoka, S.** A study on the time and space resolved measurement of flame temperature and soot concentration in a D.I. diesel engine by the two-color method. SAE Paper 790491, 1979.

[205] **Kobayashi, S., Sakai, T., Nakahira, T., Komori, M., Tsujimura, K.** Measurement of flame temperature distribution in D.I. diesel engine with high pressure fuel injection. SAE Paper 920692, 1992.

[206] **Wang, X., Huang, Z., Zhang, W., Kuti, O.A., Nishida, K.** Effects of ultra-high injection pressure and micro-hole nozzle on flame structure and soot formation of impinging diesel spray. *Appl. Energy* 2011; 1620-1628.

[207] **Aizawa, T., Kosaka, H., Matsui, Y.** 2-D imaging of soot formation process in a transient spray flame by laser-induced fluorescence and incandescence techniques. SAE Paper 2002-01-2669.

[208] **Kosaka, H., Aizawa, T., Kamimoto, T.** Two-dimensional imaging of ignition and soot formation processes in a diesel flame. *Int. J. Engine. Res.* 2005; 6(1): 21-42.

[209] **Vander Wal, R.L., Jensen, K.A., Choi, M.Y.** Simultaneous laser-induced emission of soot and polycyclic aromatic hydrocarbons within a gas-jet diffusion flame. *Combust. Flame* 1997; 109: 399-414.

[210] **Manin, J., Pickett, L.M., Skeen, S.A.** Two-color diffused back-illumination imaging as a diagnostic for time-resolved soot measurements in reacting sprays. SAE Paper 2013-01-2548.

[211] **Bohren, C.F., Huffman, D.R.** Absorption and scattering of light by small particles. New York, John Wiley and Sons; 1983.

[212] **Yamakawa, M., Takaki, D., Li, T., Zhang, Y., Nishida, K.** Quantitative measurement of liquid and vapor phase concentration distribution in a D.I. gasoline spray by the laser absorption scattering (LAS) technique. SAE Paper 2002-01-1644.

[213] **Gumprecht, R.O., Sliepcevich, C.M.** Scattering of light by large spherical particles. *J. Phys. Chem* 1953; 57(1): 90-95.

[214] **Sato, K.** Measurement and numerical analysis of mixture formation process of spray injected by hole-type injector for direct injection gasoline engine. PhD thesis, 2008.

[215] **Hanmmond, D.C., Jr:** Deconvolution technique for line-of-sight optical scattering measurements in axisymmetric sprays. *Appl. Optic.* 1981; 20(3): 493-498.

[216] **Tadokoro, T., Sato, K., Gao, J., Matsumoto, Y., Nishida, K.** Analysis of evaporation process of non-axisymmetrically wall impinging spray by means of laser absorption scattering technique. *Proceeding of the 15th ILASS-Japan Symposium*, Kanagawa, 2006; 101-106.

[217] **Gaso, J., Matsumoto, Y., Nishida, K.** Effects of group-hole nozzle specifications on fuel atomization and evaporation of direct injection diesel sprays. SAE Paper 2007-01-1889, 2007.

[218] **Zhang, Y., Nishida, K.** Imaging of vapor/liquid distributions of split-injected diesel sprays in a two-dimensional model combustion chamber. *Combust. Sci. Technol.* 2004; 176: 1465-1491.

[219] **Zhang, Y.** A study on mixture formation in diesel sprays with split injection strategy. PhD thesis, 2001.

[220] **Zhang, Y., Kotani, Y., Yoshida, A., Nishida, K.** A challenge to vapor distribution measurement of multi-component evaporating fuel spray via laser absorption-scattering (LAS) technique. SAE Paper 2007-01-1892, 2007.

[221] **Hiroyasu, H., Arai, M., Tabata, M.** Empirical equations for the sauter mean diameter of a diesel spray. SAE paper 890464, 1989.

[222] **Naber, J.D., Siebers, D.L.** Effects of gas density and vaporization on penetration and dispersion of diesel sprays. SAE paper 960034, 1996.

[223] **Matsumoto, A., Moore, W.R., Lai, M-C., Zheng, Y., Foster, M., Xie, X.B., Yen, D., Confer, K., Hopkins, E.** Spray characteristics of ethanol gasoline blends and comparison to a CFD model for a gasoline direct injector. *SAE Int. J. Engines* 2010; 3(1): 402-425.

[224] Kook, S., Pickett, L.M., Musculus, P.B. Influence of diesel injection parameters on end-of-injection liquid length recession. *SAE Int. J. Engines* 2009; 2(1): 1194-1210.

[225] Pastor, J.V., Garcia, J.M., Pastor, J.M., Zapat, L.D. Evaporating diesel spray visualization using a double-pass shadowgraph/schlieren imaging. SAE Paper 2007-24-0026, 2007.

[226] Petersen, B.R., Ghandhi, J.B. Transient high-pressure hydrogen jet measurements. SAE Paper 2006-01-0652, 2006.

[227] Pickett, L.M., Kook, S., Williams, T.C. Visualization of diesel spray penetration, cool-flame, ignition, high-temperature combustion, and soot formation using high-speed imaging. *SAE Int. J. Engines* 2009; 2(1): 439-459.

[228] Durox, D., Ducruix, S. Concerning the location of the schlieren limit in premixed flame. Combust. Flame 2000; 120: 595-598.

[229] Marshall, S.P., Taylor, S., Stone, C.R., Davies, T.J., Cracknell, R.F. Laminar buring velocity measurement of liquid fuels at elevated pressures and temperatures with combustion residuals. *Combust. Flame* 2011; 158: 1920-1932.

[230] Lawes, M., Ormsby, M.P., Sheppard, C.G.W., Woolley, R. The turbulent burning velocity of iso-octane/air mixtures. *Combust. Flame* 2012; 159: 1949-1959.

[231] Eisazadeh-Far, K., Parsinejad, F., Metghalchi, H., Keck, J.C. On flame kernel formation and propagation in premixed gases. *Combust. Flame* 2010: 157: 2211-2221.

[232] Parsinejad, F., Matlo, M., Metghalchi, M. A mathematical model for schlieren and shadowgraph images of transient expanding spherical thin flames. *J. Eng. Gas Turb. Power* 2004; 126: 241-247.

[233] Phrsinejad, F., Keck, J.C., Metghalchi, H. On the location of lame edge in shadowgraph pictures of spherical flames: a theoretical and experimental study. *Exp. Fluids* 2007: 43(6): 887-894.

[234] Gao, J., Moon, S., Zhang, Y., Nishda, K., Matsumoto, Y. Flame structure of wall-impinging diesel fuel sprays injected by group-hole nozzles. *Combust. Flame* 2009; 156(6): 1263-1277.

[235] Mueller, C., Martin, G. Effects of oxygenated compounds on combustion soot evolution in a DI diesel engine: broadband natural luminosity imaging. SAE Paper 2003-01-1631.

[236] Siebers, D.L., Higgins, B.S. Measurement of the flame lift-off location on DI diesel sprays using OH chemiluminescence. SAE Paper 2001-01-0918.

[237] Lee, S., Park, S. Experimental study on spray break-up and atomization processes from GDI injector using high injection pressure up to 30MPa. *Int. J. Heat Fluid Flow* 2014; 45: 14-22.

[238] Varde, K., Popa, D., Varde, L. Spray angle and atomization in diesel sprays. SAE Paper 841055, 1984.

[239] Dent, J.E. A basis for the comparison of various experimental methods for studying spray penetration. SAE Paper 710571, 1971.

[240] Zhu, J. Characterization of mixing and combustion processes of diesel spray in high ambient gas density. PhD thesis, 2012.

[241] Charalampous, G., Hadjiyiannis, C., Hardalupas, Y., Taylor, A.M.K.P. Measurement of continuous liquid jet length in atomizers with optical connectivity, electrical conductivity and high-speed photography techniques. *Proceeding of 23th ILASS-Europe*, September, Brno, 2010.

[242] Salters, D.G. A conductivity probe technique for investigating the breakup of diesel sprays. *Atomization Sprays* 1994; 4: 253-262.

[243] Yule, A.J. On the break-up times and lengths of diesel sprays. *Int. J. Heat and Fluid Flow* 1992; 13(2): 197-206.

[244] Chato, M., Fukuda, S., Sato, K., Fujikawa, T., Chen, R., Li, Z., Tian, J., Nishida, K. Fuel spray evaporation and mixture formation processes of ethanol-gasoline blend injected by hole-type nozzle for DISI engine. *SAE Int. J. Engines* 5(4): 1836-1846.

[245] Moon, S., Nishida, K., Matsumoto, Y., Lee, J. Gas entrainment characteristics of diesel spray during end of injection transient. *Atomization Sprays* 2009; 19(11): 1013-1029.

[246] Kawano, D., Senda, J., Wada, Y., Fujimoto, H. Numerical Simulation of Multicomponent Fuel Spray. SAE Paper 2003-01-1838, 2003.

[247] Zigan, L., Schmitz, I., Flügel, A., Knorsch, T., Wensing, M., Leipertz, A. Effect of Fuel Properties on Spray Breakup and Evaporation Studied for A Multihole Direct Injection Spark Ignition Injector. *Energy Fuels* 2010; 24: 4341-4350.

[248] Sakane, A., Hamamoto, Y. Behavior of diesel spray impinging on a wall. *JSME Transactions (B)* 1988; 54(503): 1861-1865.

[249] Lindgren, R., Denbratt, I. Influence of wall properties on the characteristics of a gasoline spray after wall impingement. SAE paper 2004-01-1951.

[250] **Arcoumanis, C., Chang, J-C.** Flow and heat transfer characteristics of impinging transient diesel sprays. SAE paper 940678.

[251] **Aleiferis, P.G., Taylor, A.M.K.P., Ishii, K., Urata, Y.** The nature of early flame development in a lean-burn stratified-charge spark-ignition engine. *Combust. Flame* 2004; 136: 283-302.

[252] **Musculus, M.P.B., Kattke, K.** Entrainment waves in diesel jets. SAE paper 2009-01-1355, 2009.

[253] **Kataoka, H., Tian, J.P., Sato, K., Kitamitsu, K., Nishida, K.** Mixture distribution and ignition probability of gasoline spray injected by hole-type nozzle. In Proceeding of the Nineteenth Symposium (ILASS-Japan) on Atomization, Tokyo, Japan, 21-22 December 2010, pp. 129-136.

[254] **Huang, H., Zhang, Y.** Flame colour characterization in the visible and infrared spectrum using a digital camera and image processing. *Means. Sci. Technol.* 2008: 19(8): 085409.

[255] **Turner, D., Xu, H., Cracknell, R.F., Natarajan, V., Chen, X.** Combustion performance of bio-ethanol at various blend ratios in a gasoline direct injection engine. *Fuel* 2011; 90:1999-2006.

[256] **Ohyama, Y., Ohsuga, M., Kuroiwa, H.** Study on mixture formation and ignition process in spark ignition engine using optical combustion sensor. SAE Paper 901712, 1990.

[257] **Run, C., Nishida, K., Kataoka, H.** Characterization of the ignition and combustion processes of spray injected by a hole-type nozzle for a direct-injection spark ignition engine. *Proc. IMechE. Part D: J. Automobile Engineering* 2014; 228(6): 617-630.

[258] **Van Lipzig, J.P.J., Nilsson, E.J.k., De Gody, L.P.H., Konnov, A.A.** Laminar burning velocities of n-heptane, iso-octane, ethanol and their binary and tertiary mixtures. *Fuel* 2011; 90: 2773-2781.

[259] **Bradley, D., Lawes, M., Mansour, M.S.** Explosion bomb measurements of ethanol-air laminar gaseous flame characteristics at pressure up to 1.4MPa. *Combust. Flame* 2009; 156: 1462-1470.

[260] **Broustail, G., Seers, P., Halter, F., Moréac, G., Mounaim-Rousselle, C.** Experimental determination of laminar burning velocity for butanol and ethanol iso-octane blends. *Fuel* 2011; 90: 1-6.

[261] **Run, C., Nishida, K.** Spray evaporation of ethanol-gasoline-like blend and combustion of ethanol-gasoline blend injected by hole-type nozzle for direct-injection spark ignition engines. *Fuel* 2014; 134: 263-273.

[262] **Run, C., Chato, M., Nishida, K., Ogata, Y., Bao, S.** Mixture formation process of gasoline/ethanol blended fuel spray injected by hole-type nozzle for D.I. Gasoline engines. *Proceeding of 16th ILASS-Asia, 2013*, Nagasaki, Japan.

[263] Solomon A.S.P. A photographic study of fuel spray ignition in a rapid compression machine. SAE Paper 860065, 1986.

[264] Ozdor, N., Dulger, M., Sher, E. Cyclic variability in spark ignition engines a literature survey. SAE Paper 940987, 1994.

[265] Müller, S.H.R., Böhm, B., Gleißner, M. Arndt, S., Dreizler, A. Analysis of the temporal flame kernel development in an optically accessible IC engine using high-speed OH-PLIF. *Appl. Phys. B* 2010; 100: 447-452.

[266] Matsuti, Y., Kamimoto, K., Matsuoka, S. A study on the time and space resolved measurement of flame temperature and soot concentration in a D.I. diesel engine by the two-color method. SAE Paper 790491, 1979.

[267] Kobayashi, S., Sakai, T., Nakahira, T., Komori, M., Tsujimura, K. Measurement of flame temperature distribution in D.I. diesel engine with high pressure fuel injection. SAE Paper 920692, 1992.

[268] Sjöberg, M., Reuss, D.L. High-speed imaging of spray-guided DISI engine combustion with near-TDC injection of E85 for ultra-low NO and soot. *Proc. Combust. Inst.* 2013; 34: 2933-2940.

[269] Sjöberg, M., Reuss, D.L. NOx-reduction by injection-timing retard in a stratified-charge DISI engine using gasoline and E85. SAE Paper 2012-01-1643, 2012.

ACKNOWLEDGMENTS